Density Functional Calculations

Recent Progresses of Theory and Application

Edited by Gang Yang

DENSITY FUNCTIONAL CALCULATIONS - RECENT PROGRESSES OF THEORY AND APPLICATION

Edited by **Gang Yang**

Density Functional Calculations - Recent Progresses of Theory and Application
Edited by Gang Yang

Contributors

Ataf Ali Altaf, Amin Badshah, Samia Kausar, Burkhard Kirste, Florian Senn, Issaka Seidu, Young Choon Park, Jaime Gustavo Rodriguez-Zavala, Zuriel Natanael Cisneros-Garcia, Francisco J Tenorio, David Alejandro Hernández-Velázquez, M. Leonor Contreras, Roberto Rozas, Nageh K. Allam, Warjeet S. Laitonjam, Lokendrajit Nahakpam, Alimi Kamel, Dalila Khlaifia, Gang Yang, Madhulata Shukla, Indrajit Sinha, Jia Fu, Daniel Glossman-Mitnik, Norma Flores-Holguín, Juan Frau

Notice

Statements and opinions expressed in the chapters are these of the individual contributors and not necessarily those of the editors or publisher. No responsibility is accepted for the accuracy of information contained in the published chapters. The publisher assumes no responsibility for any damage or injury to persons or property arising out of the use of any materials, instructions, methods or ideas contained in the book.

We are IntechOpen,
the first native scientific
publisher of Open Access books

3,450+
Open access books available

110,000+
International authors and editors

115M+
Downloads

151
Countries delivered to

Our authors are among the
Top 1%
most cited scientists

12.2%
Contributors from top 500 universities

WEB OF SCIENCE™

Selection of our books indexed in the Book Citation Index
in Web of Science™ Core Collection (BKCI)

Interested in publishing with us?
Contact book.department@intechopen.com

Meet the editor

Dr. Yang is now a full professor of Southwest University (China). He obtained his PhD degree from Chinese Academy of Science in 2006, and after being an associate professor for 5 years in Northeast Forestry University, he moved to Eindhoven University of Technology to continue his studies as a postdoc researcher. His research interests focus on molecular modeling, computational soil chemistry, and theoretical catalysis. He has coauthored more than 100 peer-reviewed papers and 7 book chapters. He has delivered speeches in many international and domestic conferences. He serves as the editor for *PLOS One*, *Colloid*, and *Surface Science* as well as the referee for more than 40 international journals, books, proposals of European Research Council, etc.

Contents

Preface

Density functional theory (DFT) is a method of obtaining approximate solutions to Schrödinger equation for many-body systems, where electron density rather than wave function is the central variable. Although DFT can be traced back to 1927 when the Thomas-Fermi model was developed, it was first put on a firm theoretical footing in 1964 by Kohn and Hohenberg in the framework of two Hohenberg-Kohn theorems.

DFT owes its popularity in the predictive power for physical and chemical properties and the ability to handle large systems accurately and efficiently. Now, DFT ranks as the most widely used quantum mechanical method, and its success is clearly demonstrated by the overwhelming amount of research articles in the past decades that report results by means of *DFT* methods. A vast number of DFT software packages are available to us, such as Gaussian, VASP, DMOL, ADF, and Wien. Some of them are easy to use, which significantly promotes the popularization of DFT methods.

There are numerous books and reviews that showcase the contemporary advances of DFT methods, while DFT is always being developed toward higher accuracy and larger systems with less computational costs. In addition, DFT has expanded its business rapidly and plays an increasingly larger role in a number of disciplines such as chemistry, physics, material, biology, and pharmacy. A major goal of this book is to draw together contributors from the various research fields, to spread knowledge of current capabilities and new possibilities, and to stimulate the exchange of information between disparate disciplines. This book is divided into five sections that include original chapters written by experts in their fields. The first section describes the recent developments of DFT methods and the validation of these computational techniques that is equally important. The following sections are the applications of DFT methods in the various domains: Section 2 includes spectra and thermodynamics that establish direct contacts with experiments such as spectral assignments, Section 3 focuses on catalysis and mechanism that identifies short-time intermediates and presents complicated reaction processes at the atomic level, Section 4 involves material and molecular designs that see the power of DFT methods by predicting the properties of existing and new materials with hitherto unprecedented accuracy, and Section 5 (multidisciplinary integration) is to broaden the insights with respect to DFT applications. This section contains only one chapter from our lab, showing the tremendous advantages and bright prospects in computational soil science. As a matter of fact, DFT methods have been widely used and bring forth a number of interdisciplines that are probably better known to us, such as computational biology, molecular pharmacy, and computational nanoscience.

I would like to express my sincere gratitude to all authors who have contributed to this book. They are Ataf Ali Altaf, Amin Badshah, Basant A. Ali, Burkhard Kirste, Chang Zhu, Daniel

Southwest University Chongqing preface acknowledgement

Glossman-Mitnik, David Alejandro Hernández-Velázquez, Florian Senn, Francisco J. Tenorio, Gang Yang, Hossam A. Almossalami, Issake Seidu, I. Sinha, Jaime Gustavo Rodríguez-Zavala, Jia FU, Jiena Yun, Juan Frau, Kareem M. Gameel, Lokendrajit Nahakpam, Madhulata Shukla, M. Leonor Contreras, Nageh K. Allam, Norma Flores-Holguín, Qian Wang, Roberto Rozas, Samia Kausar, Sarah A. Tolba, Warjeet S. Laitonjam, Young Choon Park, and Zuriel Natanael Cisneros-García. Thank you very much for your excellent contributions!

Gang Yang
College of Resources and Environment &
Chongqing Key Laboratory of Soil Multi-scale Interfacial Process
Southwest University
Chongqing 400715, China

Method Development and Validation

The DFT+U: Approaches, Accuracy, and Applications

Sarah A. Tolba, Kareem M. Gameel, Basant A. Ali,
Hossam A. Almossalami and Nageh K. Allam

Additional information is available at the end of the chapter

http://dx.doi.org/10.5772/intechopen.72020

Abstract

This chapter introduces the Hubbard model and its applicability as a corrective tool for accurate modeling of the electronic properties of various classes of systems. The attainment of a correct description of electronic structure is critical for predicting further electronic-related properties, including intermolecular interactions and formation energies. The chapter begins with an introduction to the formulation of density functional theory (DFT) functionals, while addressing the origin of bandgap problem with correlated materials. Then, the corrective approaches proposed to solve the DFT bandgap problem are reviewed, while comparing them in terms of accuracy and computational cost. The Hubbard model will then offer a simple approach to correctly describe the behavior of highly correlated materials, known as the Mott insulators. Based on Hubbard model, DFT+U scheme is built, which is computationally convenient for accurate calculations of electronic structures. Later in this chapter, the computational and semiempirical methods of optimizing the value of the Coulomb interaction potential (U) are discussed, while evaluating the conditions under which it can be most predictive. The chapter focuses on highlighting the use of U to correct the description of the physical properties, by reviewing the results of case studies presented in literature for various classes of materials.

Keywords: first principles, Hubbard U correction, GGA+U, DFT+U, LDA+U, spin crossover, metal organic framework, solid defects, band structure

1. Introduction

Density functional theory (DFT) is one of the most convenient computational tools for the prediction of the properties of different classes of materials [1, 2]. Although its accuracy is acceptable as long as structural and cohesive properties are concerned, it dramatically fails in the prediction of electronic and other related properties of semiconductors up to a factor of

two [3]. However, reaching a correct description of electronic structure is critical for predicting further electronic-related properties, including intermolecular interactions and formation energies. In order to solve this problem, computationally heavier jobs must be employed, using either larger basis sets or hybrid functionals, which include the solution of the exact Hartree-Fock (HF) equations, in order to reach relatively higher accuracies [4]. Nevertheless, in some cases, even solving exact HF equations can fail in correctly predicting the bandgap for a certain class of semiconductors that possess strong correlations between electrons, such as Mott insulators [5, 6]. Consistent research efforts have been employed in order to formulate more accurate functionals, by using corrective approaches or alternatives to the density functionals. The applicability of these alternatives and corrections has large dependence on the type of the system studied, its size and complexity, and the computational cost required. One of the corrective approaches employed to relieve the DFT electronic bandgap problem is the DFT+U correction method, which is the focus of this chapter. Compared to the alternative approaches, such as the hybrid functionals and the post-Hartree-Fock methods, DFT+U correction has proved to be as reliable as the other methods, but with a critical advantage of considerably lower computational cost. By successfully correcting the electronic structure of the studied system using the U correction, further accurate predictions of intermolecular interactions and formation energies can be reached [6]. In addition, the U correction can further enhance the description of physical properties, other than the electronic structure, including magnetic and structural properties of correlated systems, the electron transfer energetics, and chemical reactions. However, one of the drawbacks of the Hubbard method is that it fails in predicting the properties of systems with more delocalized electrons, such as metals. The relative success of the DFT+U method is related to its straightforward approach to account for the underestimated electronic interactions by simply adding a semiempirically tuned numerical parameter "U" [5]. This interaction parameter can be easily controlled, making the DFT+U method a tool to give a qualitative assessment of the influence of the electronic correlations on the physical properties of a system.

One of the mostly implemented methods in the DFT+U realm is the LDA+U method. It is widely used due to its simple implementation on the existing LDA codes, which makes it only slightly computationally heavier than the standard DFT computations [6]. In this chapter, we discuss the fundamental formulation of the LDA+U method and examine its applicability for practical implementations for different classes of materials, where DFT is usually found to be impractical. Popular cases of DFT shortage are discussed including materials with strong correlations, defective solid-state materials, and organometallics, while reviewing literature case studies that studied these classes of materials with DFT+U calculations. The methodology of optimizing the U correction is inspected, where it can be either formulated from first principles or achieved empirically by tuning the U value, while seeking an agreement with experimental results of the system's physical properties. In this chapter, we also present a review of the practical implementation of U, while assessing its corrective influence on improving the description of a variety of physical properties related to certain classes of materials. In addition, the effect of the calculation parameters on the chosen U value is discussed, including the choice of the localized basis set and the type of DFT functional employed.

2. Theoretical formulation

2.1. Standard DFT problem

Using exact HF or DFT solutions, the aim is always to reach, as close as possible, the exact description of the total energy of the system. Unluckily, reaching this exact energy description is impossible and approximations have to be employed. In DFT, electronic interaction energies are simply described as the sum of classical Columbic repulsion between electronic densities in a mean field kind of way (Hartree term) and an additive term that is supposed to encompass all the correlations and spin interactions [1]. This additive term, namely the exchange and correlation (xc), is founded on approximations that have the responsibility to recover the exact energy description of the system. This approximated xc functional is a function of the electronic charge density of the system, and the accuracy of a DFT calculation is strongly dependent on the descriptive ability of this functional of the energy of the system [2]. It is generally difficult to model the dependence of the xc functional on electronic charge density, and thus, it can inadequately represent the many-body features of the N-electron ground state. For this reason, systems with physical properties that are controlled by many body electronic interactions (correlated systems) are poorly described by DFT calculations. For these systems, incorrect description of the electronic structure induces the so-called "bandgap problem," which in turn, imposes difficulties in utilizing DFT to predict accurate intermolecular interactions, formation energies, and transition states [7].

The problem of DFT to describe correlated systems can be attributed to the tendency of xc functionals to over-delocalize valence electrons and to over-stabilize metallic ground states [5, 6]. That is why DFT fails significantly in predicting the properties of systems whose ground state is characterized by a more pronounced localization of electrons. The reason behind this delocalization is rooted to the inability of the approximated xc to completely cancel out the electronic self-interaction contained in the Hartree term; thus, a remaining "fragment" of the same electron is still there that can induce added self-interaction, consequently inducing an excessive delocalization of the wave functions [5]. For this reason, hybrid functionals were formulated to include a linear combination of a number of xc explicit density and HF exact exchange functionals, that is self-interaction free, by eliminating the extra self-interaction of electrons through the explicit introduction of a Fock exchange term. However, this method is computationally expensive and is not usually practical when larger, more complex systems are studied. Nonetheless, HF method, which describes the electronic structure with variationally optimized single determinant, cannot describe the physics of strongly correlated materials such as the Mott insulators. In order to describe the behavior of these systems, full account of the multideterminant nature of the N-electron wave function and of the many-body terms of the electronic interactions is needed [6]. Therefore, it is predicted that applying DFT calculations using approximate xc functionals, such as LDA or GGA, will poorly describe the physical properties of strongly correlated systems.

2.2. Mott insulators and the Hubbard model

According to the conventional band theories, strongly correlated materials are predicted to be conductive, while they show insulating behavior when experimentally measured. This serious

flaw of the band theory was pointed out by Sir Nevil Mott, who emphasized that interelectron forces cannot be neglected, which lead to the existence of the bandgap in these falsely predicted conductors (Mott insulators) [8]. In these "metal-insulators," the bandgap exists between bands of like character i.e., between suborbitals of the same orbitals, such as 3d character, which originates from crystal field splitting or Hund's rule. The insulating character of the ground state stems from the strong Coulomb repulsion between electrons that forces them to localize in atomic-like orbitals (Mott localization). This Coulomb potential, responsible for localization, is described by the term "U," and when electrons are strongly localized, they cannot move freely between atoms and rather jump from one atom to another by a "hopping" mechanism between neighbor atoms, with an amplitude t that is proportional to the dispersion (the bandwidth) of the valence electronic states. The formation of an energy gap can be settled as the competition between the Coulomb potential U between 3d electrons and the transfer integral t of the tight-binding approximation of 3d electrons between neighboring atoms. Therefore, the bandgap can be described by the U, t and an extra z term that denotes the number of nearest neighbor atoms as [6]:

$$E_{gap} = U - 2zt \qquad (1)$$

Since the problem is rooted down to the band model of the systems, alternative models have been formulated to describe the correlated systems. One of the simplest models is the "Hubbard" model [9]. The Hubbard model is able to include the so-called "on-site repulsion," which stems from the Coulomb repulsion between electrons at the same atomic orbitals, and can therefore explain the transition between the conducting and insulating behavior of these systems. Based on this model, new Hamiltonian can be formulated with an additive Hubbard term that explicitly describes electronic interactions. The additive Hubbard Hamiltonian can be written in its simplest form as follows [6]:

$$H_{Hub} = t \sum_{\langle i,j \rangle, \sigma} \left(c_{i,\sigma}^{\dagger} c_{j,\sigma} + h.c. \right) + U \sum_{i} n_{i,\uparrow} n_{i,\downarrow} \qquad (2)$$

As predicted, the Hubbard Hamiltonian should be dependent on the two terms t and U, with $\langle i.j \rangle$ denoting nearest-neighbor atomic sites and $c_i^{\dagger}$, c_j, and n_i are electronic creation, annihilation, and number operators for electrons of spin on site i, respectively. The hopping amplitude t is proportional to the bandwidth (dispersion) of the valence electrons, while the on-site Coulomb repulsion term U is proportional to the product of the occupation numbers of atomic states on the same site [6]. The system's insulating character develops when electrons do not have sufficient energy to overcome the repulsion potential of other electrons on neighbor sites, i.e., when $t \ll U$. The ability of the DFT scheme to predict electronic properties is fairly accurate when $t \gg U$, while for large U values, DFT significantly fails the HF method, which describes the electronic ground state with a variationally optimized single determinant, that cannot capture the physics of Mott insulators.

2.3. DFT+U

Inspired by the Hubbard model, DFT+U method is formulated to improve the description of the ground state of correlated systems. The main advantage of the DFT+U method is that

it is within the realm of DFT, thus does not require significant effort to be implemented in the existing DFT codes and its computational cost is only slightly higher than that of normal DFT computations. This "*U*" correction can be added to the local and semilocal density functionals offering LDA+U and GGA+U computational operations. The basic role of the *U* correction is to treat the strong on-site Coulomb interaction of localized electrons with an additional Hubbard-like term. The Hubbard Hamiltonian describes the strongly correlated electronic states (*d* and *f* orbitals), while treating the rest of the valence electrons by the normal DFT approximations. For practical implementation of DFT+U in computational chemistry, the strength of the on-site interactions is described by a couple of parameters: the on-site Coulomb term *U* and the site exchange term *J*. These parameters "*U* and *J*" can be extracted from *ab initio* calculations, but usually are obtained semiempirically. The implementation of the DFT+U requires a clear understanding of the approximations it is based on and a precise evaluation of the conditions under which it can be expected to provide accurate quantitative predictions [5, 6].

The LDA+U method is widely implemented to correct the approximate DFT xc functional. The LDA+U works in the same way as the standard LDA method to describe the valence electrons, and only for the strongly correlated electronic states (the *d* and *f* orbitals), the Hubbard model is implemented for a more accurate modeling. Therefore, the total energy of the system (E_{LDA+U}) is typically the summation of the standard LDA energy functional (E_{Hub}) for all the states and the energy of the Hubbard functional that describes the correlated states. Because of the additive Hubbard term, there will be a double counting error for the correlated states; therefore, a "double-counting" term (E_{dc}) must be deducted from the LDA's total energy that describes the electronic interactions in a mean field kind of way [5].

$$E_{LDA} + U[\rho(r)] \ = \ E_{LDA}[\rho(r)] + E_{Hub}\left[\left\{n_{mm}^{I\sigma}\right\}\right] - E_{dc}[n^{I\sigma}] \tag{3}$$

Therefore, it can be understood that the LDA+U is more like a substitution of the mean-field electronic interaction contained in the approximate xc functional. Nonetheless, the E_{dc} term is not uniquely defined for each system and various formulations can be applied to different systems. The most dominant of these formulations is the FLL formulation [10–12]. It is based on the implementation of fully localized limit (FLL) on systems with more localized electrons on atomic orbitals. The reason for this formulation popularity is due to its ability to expand the width of the Kohn Sham (KS) orbitals and to effectively capture Mott localization. Based on this formulation, the LDA+U can be written as:

$$E_{LDA+U}\left[\rho(r)\right] + \sum_{l}\left[\frac{U^{l}}{2}\sum_{m,\sigma\neq m',\sigma'} n_{m}^{l\sigma} n_{m'}^{l\sigma'} - \frac{U^{l}}{2} n^{l}(n^{l}-1)\right] \tag{4}$$

where $n_{m}^{l\sigma}$ m are the localized orbitals occupation numbers identified by the atomic site index I, state index m, and by the spin σ. In Eq. (4), the right-hand side second and third terms are the Hubbard and double-counting terms, specified in Eq. (3). The dependency on the occupation number is expected as the Hubbard correction is only applied to the states that are most disturbed by correlation effects. The occupation number is calculated as the projection of occupied KS orbitals on the states of a localized basis set:

$$n_{m,m'}^{I\sigma} = \sum_{k,v} f_{kv}^{\sigma} \langle \Psi_{kv}^{\sigma} | \varphi_{m'}^{I} \rangle \langle \varphi_{m}^{I} | \Psi_{kv}^{\sigma} \rangle \tag{5}$$

where the coefficients f_{kv}^{σ} represent the occupations of KS states (labeled by k-point, band, and spin indices), determined by the Fermi-Dirac distribution of the corresponding single-particle energy eigen values. According to this formulation, the fractional occupations of localized orbitals is reduced, while assisting the Mott localization of electrons on particular atomic states [5].

Although the above approach described in Eq. (4) is able to capture Mott localization, it is not invariant under rotation of the atomic orbital basis set employed to define the occupation number of n in Eq. (5). This variation makes the calculations performed unfavorably dependent on the unitary transformation of the chosen localized basis set. Therefore, "rotationally invariant formulation" is introduced, which is unitary-transformation invariant of LDA+U [12]. In this formulation, the electronic interactions are fully orbital dependent, and thus considered to be the most complete formulation of the LDA+U. However, a simpler formulation that preserves rotational invariance, which is theoretically based on the full rotationally invariant formulation, had proved to work as effectively as the full formulation for most materials [11]. Based on the simplified LDA+U form, it has been customary to utilize, instead of the interaction parameter U, an effective U parameter: $U_{eff} = U - J$, where the "J" parameter is known as the exchange interaction term that accounts for Hund's rule coupling. The U_{eff} is generally preferred because the J parameter is proven to be crucial to describe the electronic structure of certain classes of materials, typically those subject to strong spin-orbit coupling.

3. Practical implementations of the Hubbard correction

DFT+U is applicable for all open shell orbitals, such as d and f orbitals for transition metal elements with localized orbitals existing in extended states, as in the case of many strongly correlated materials and perovskites, where localized $3d$ or $4f$ orbitals are embedded in elongated s-p states. A complicated many-electron problem is made of electrons living in these localized orbitals, where they experience strong correlations among each other and with a subtle coupling with the extended states. Isolating a few degrees of freedom relevant to the correlation is the idea in the Hubbard model, where screened or renormalized Coulomb interaction (U) is kept among the localized orbitals' electrons [13]. In other word, the localized orbitals in the bandgap, which are present as localized states (d- and f-states), are too close to the Fermi energy. From that aspect, the U value should be used to push theses states away from the Fermi level, such as that provided by the GGA+U theory, which adds to the Hamiltonian a term that increases the total energy preventing the unwanted delocalization of the d- or f-electrons, when two d- or f-electrons are located on the same cation [14]. It is worth mentioning that using too large values of U will over-localize the states and lead to an unphysical flattening of the appropriate bands, which unlike fitting to many other properties, will make the fit worse. Also, the increase in the U value can cause an overestimation of the lattice constants as well as a wrong estimation of the ground state energy due to the electronic interaction error. Therefore, applying Hubbard
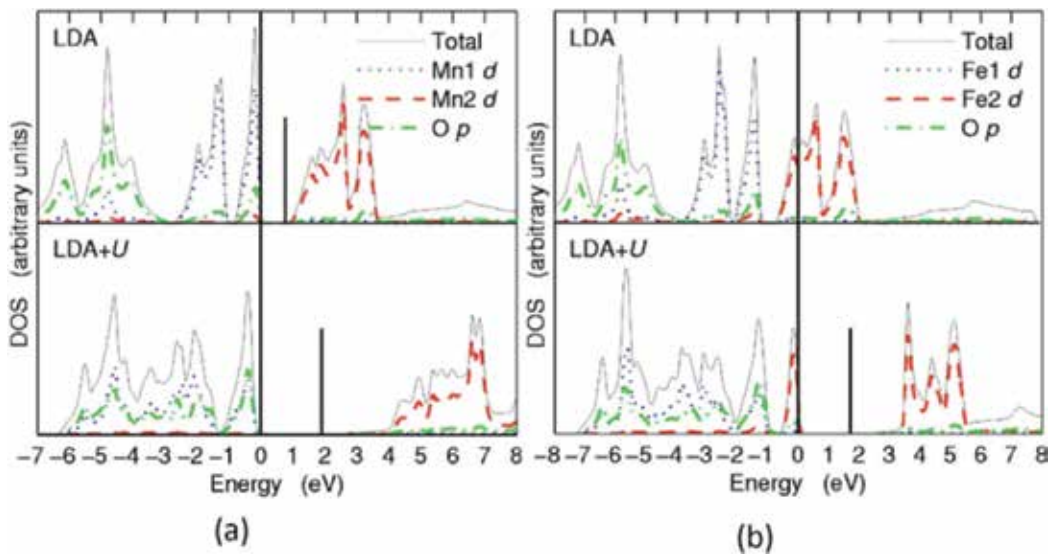
Figure 1. Comparison of theoretical DOS calculated by LDA and LDA+U for (a) MnO and (b) FeO. Adapted with permission from [15].

correction to solve the bandgap problem is necessary for predicting the properties of transition metal oxides. **Figure 1** shows the effect of U potential on correcting the failure of DFT to predict correct bandgaps for strongly correlated materials. Note the underestimation of the bandgap in case of MnO and the incorrect prediction of the metallic behavior of FeO [15].

3.1. Optimizing the U value

From the case studies and examples presented within this chapter, one can intuitively conclude that corrective functional LDA+U is particularly dependent on the numerical value of the effective potential U_{eff}, which is generally referred to in literature as "U" for simplicity. However, the U value is not known and practically is often tuned semiempirically to make a good agreement with experimental or higher level computational results. However, the semiempirical way of evaluating the U parameter fails to capture its dependence on the volume, structure, or the magnetic phase of the crystal, and also does not permit the capturing of changes in the on-site electronic interaction under changing physical conditions, such as chemical reactions. In order to get full advantage of this method, different procedures have been addressed to determine the Hubbard U from first principles [13]. In these procedures, the U parameter can generally be calculated using a self-consistent and basis set in an independent way. These different *ab initio* approaches for calculating U have been applied to different material systems, where the U value is calculated for individual atoms. For each atom, the U value is found to be dependent on the material specific parameters, including its position in the lattice and the structural and magnetic properties of the crystal, and also dependent on the localized basis set employed to describe the on-site occupation in the Hubbard functional. Therefore, the value of effective interactions should be re-computed for each type of material

and each type of LDA+U implementation (e.g., based on augmented plane waves, Gaussian functions, etc.). Most programs these days use the method presented by Cococcioni et al. [16], where the values of U can be determined through a linear response method [17], in which the response of the occupation of localized states to a small perturbation of the local potential is calculated. The U is self-consistently determined, which is fully consistent with the definition of the DFT+U Hamiltonian, making this approach for the potential calculations fully *ab initio*. The value of U implemented by Cococcioni et al. is $U_{eff} = U–J$, where J is indirectly assumed to be zero in order to obtain a simplified expression [17]. Nonetheless, J can add some additional flexibility to the DFT+U calculations, but it may yield surprising results including reversing the trends previously obtained in the implemented DFT+U calculations [18].

Despite the limitations of choosing the U value semiempirically for systems, where variations of on-site electronic interactions are present, it is found to be the most common practice used in literature, where the value of U is usually compared to the experimental bandgap. This semiempirical trend in practical implementation of U is present because of the significant computational cost of *ab initio* calculation of U, and in the cases of studying static physical properties, the results of computed U are not necessarily found to be better than the empirical ones. Within this practice, however, caution should be taken while pursuing the semiempirical method [19]. If it will be possible to describe all the relevant aspects of a system, except the bandgap, with a reasonable U, one might then look into using a scissor operator or rigid shift to the bandgap [20, 21]. However, in particular cases, where calculations aim at understanding catalysis, it is natural to choose U to fit the energy of the oxidation-reduction, as catalysis is controlled by energy differences [14]. Conversely, one of the possible solutions is to venture into a negative value for the Hubbard U parameter, there is no obvious physical rationale for that yet, but the results may match with experiment for both the magnetic moment and structural properties, as illustrated later in this chapter.

To elaborate the numerical U tuning procedure, three quick examples are presented below that can show the correlation between the value of U and the predicted physical properties:

- The compilation of the correlated nature of cobalt *3d* electrons in the theoretical studies of Co_3O_4 gives a good picture of the significant difference in the U value with the difference in most of the calculated properties. The variety of U values have been used ranging from 2 to 6 for the properties including bandgap [22], oxidation energy [23], and structural parameters [24], which affect the choice of the value of U for each of these properties uniquely. The calculated bandgap at the generalized gradient approximation (GGA)+U agrees well with the experimental value of 1.6 eV. On the other hand, the calculated value using the PBE0 hybrid functional (3.42 eV) is highly overestimated, due to neglecting the screening problem of the Hartree-Fock approximation [25].

- From the study made by Lu and Liu [26] on cerium compounds presented some characteristics for U values for Ce atoms in different configurations as isolated atoms and ions. They illustrated that the ion charge (Ce atoms, Ce in $Ce_3H_xO_7$ clusters, or CeO_2) does not significantly affect the value of U and that when ions are isolated, the values are much larger (close to 15 for $Ce^{2.5+}$ and 18 eV for $Ce^{3.5+}$).

- Within the study of $BiMnO_3$ that has strongly distorted perovskite structure with the GGA+U method, calculations show that distortions of the MnO_6 octahedral, which is considered the main unit in the crystal structure, are very sensitive to the value of the Coulomb repulsion U. The study showed that large U value decreases the $3d$-$2p$ hybridization, and therefore decreases the bonding effects, which in turn distortion increases the short Mn-O distances, and thus overly expands the MnO_6 octahedral [27].

3.2. Variation of U with calculation methods and parameters

The parameters assigned for DFT calculations can significantly affect the choice of the optimum U value. These parameters include pseudopotentials, basis sets, the cutoff energy, and k-point sampling. As pseudopotentials are used to reduce computational time by replacing the full electron system in the Columbic potential by a system only taking explicitly into account the "valence" electrons [28], the pseudopotential will strongly affect the U value. Thus, calculations have to be converged very well with respect to the cutoff energy and k-point sampling, while taking into account that the symmetry used in DFT+U calculations, because adding the U parameter often lowers the crystallographic symmetry, thereby the number of k-points needs to be increased.

Not only is the U value affected by the parameters applied, but it is also strongly dependent on the DFT method used. In a published review [29], a comparison of different calculated U values using different approaches was highlighted for several transition metal oxides. It was reported that with small U values, the electrons were still not localized, and that the U value depends on the used exchange-correlation functionals (LDA or GGA), the pseudopotential, the fitted experimental properties, and projection operators [30]. In the computational study of strongly correlated systems, it can be usually found in literature that researchers refer to the utilization of (DFT+U) method in their calculations, which may include generalized gradient approximation (GGA+U) [8], local density approximation (LDA+U) [31], or both [32]. To be able to choose the proper method of calculation for a studied system, one should know the limitation of each of the two methods for that specific system and to what extent is each method approved to be closer to the experimental values. Knowing the optimum U value can be reached empirically by applying different values of U for either GGA or LDA. From the following list of examples from literature, an assessment of the performance of different values of U when applied to both GGA and LDA for the same system can be realized:

- Griffin et al. [33] studied the FeAs crystal comparing the GGA+U and LDA+U levels of accuracy, using $U_{eff} = -2$ to 4 eV. The results showed that for the bond distances and angles in the crystal, the GGA+U gave results close to the experimental values when $U \leq 1$ eV, whereas using LDA, the structural properties were poorly predicted. It was observed that increasing the value of U in the GGA+U increased the stabilization energy for antiferromagnetic ordering. Both GGA+U and LDA+U overestimated the value of magnetic moment. However, only the GGA+U could attain the experimental values of magnetic moment for negative U_{eff} [5].

- Cerium oxides (CeO_2 and Ce_2O_3) were tested by Christoph et al. [34] comparing GGA+U and LDA+U level of theory meanwhile studying the effect of the U_{eff} value on the calculated properties. It was found that the value of U_{eff} is dependent on the property under examination. The sensitivity toward U_{eff} values was especially high for properties of Ce_2O_3, because it has an electron in the *4f* orbital, which is sensitive to the change in the effective on-site Coulomb repulsion due to the strong localization, in contrary to the CeO_2 that has an empty *4f* orbital. The GGA+U showed an acceptable agreement with experiment at lower energies of U_{eff} than LDA did, with values of U_{eff} 2.5–3.5 eV for LDA+U and 1.5–2.0 eV for GGA+U, which can be due to the more accurate treatment of correlation effects within the GGA potential. On the other hand, the structural properties were better represented by the LDA+U method for CeO_2. Regarding Ce_2O_3 electronic structure, both LDA+U and GGA+U results showed a similarly good accuracy, while for the calculated reaction energies, LDA+U results showed better accuracy. [34]

- Sun et al. [35] studied PuO_2 and Pu_2O_3 oxides using both GGA+U and LDA+U methods. Although PuO_2 is known to be an insulator [36], its ground state was reported experimentally to be an antiferromagnetic phase [37]. For PuO_2, at $U = 0$, the ground state was a ferromagnetic metal, which is different from experimental results. Upon increasing the amplitude of U to 1.5 eV, the LDA+U and GGA+U calculations correctly predicted the antiferromagnetic insulating ground-state characteristics. For the lattice parameters, it was found that higher values of U ($U = 4$ eV) were needed with the LDA+U than for GGA+U. At $U = 4$ eV, it is expected that both LDA+U and the GGA+U would show a satisfactory prediction of the ground-state atomic structure of Pu_2O_3. However, the study showed that above the metallic-insulating transition, the reaction energy decreases with increasing U for the LDA and the GGA schemes. Therefore, for both Pu_2O_5 and PuO_2, the LDA+U and GGA+U approaches, with U as large as 6 eV, failed to describe the electronic structure correctly. When the energy gap increases, the electrons gain more localization that causes a difficulty of making any new reactions, consequently increasing the reaction energy. When U exceeds 4 eV, the conduction band electrons approximately considered to be ionized; thus, the atoms (cores or ions) have got a better chance to react with other atoms which, resulting in a reduction in the reaction energy.

As noticed in the previous studies, the U value is material dependent, besides being variable among the level of theory used. In general, the more localized the system is, the more sensitive it is to the value of U. The estimated value of U for a system of material using a specific level of calculation should not be extended to another system; rather, it should be recomputed each time for each material and even upon change of the level of calculation. Researchers will need to perform calculations using different U values within different xc functionals to get the best prediction of the calculated properties in comparison with the experimental measurements or with the other computational results as benchmark.

3.3. The effect of U on pure and defected systems

The chemical properties of transition-metal systems with localized electrons, mainly within *d* or *f* orbitals, are typically governed by the properties of the valence electrons. Experimentally,

these electrons are observed to be localized in their orbitals due to strong correlations [38], whereas computationally, DFT approximated xc functionals tend to overly delocalize them while over-stabilizing metallic ground states, and thus underestimating the bandgap for semiconductors, and may reach false prediction of metallic behavior for systems like the Mott insulators. U can induce electronic localization due to the explicit account for the on-site electronic interactions. Another common problem that DFT calculations can impose is the prediction of the properties of materials with defects, as the underestimation of the bandgap by DFT can cause the conduction band (CB) or the valence band (VB) to kind of mask the true defect states. This is because defects can cause unpaired electrons and holes to form, which are overly delocalized by DFT, as it attempts to reduce the Coulomb repulsion due to self-interaction error.

Ref. [39] discusses an example of this problem studying the anatase TiO_2, where they showed that the description of the distribution of electrons in the unit cell, created from oxygen vacancies and hydrogen impurities, is wrongly predicted using GGA-PBE scheme of DFT calculations. In the case of oxygen vacancies, their calculations predicted a 2.6 eV bandgap, which is about 0.6 eV smaller than that reported experimentally. The electrons left in the system upon vacancy formation are completely delocalized over the entire cell. These electrons are incorrectly shared over all the Ti atoms of the cell, and as a result, the atomic displacements around the vacancies are predicted to be symmetric. All these findings indicate the difficulty of DFT methods to describe the properties of defects in wide bandgap metal oxides. Also, the accuracy of the description of the electronic structure of the partially reduced oxide systems was reviewed and discussed within the first principle methods [40].

The electronic structure of TiO_2–both pristine and doped–is one of the examples that is frequently studied in literature. Typically, in the anatase and rutile phases, computational studies encountered the problem of considerable underestimation of the bandgap, which presented a barrier in the prediction of further related properties. Titania is widely studied in various photoelectrochemical applications, and accurate theoretical assessment is required to be able to enhance its catalytic properties. In addition, to further improve the properties of TiO_2 as a photocatalyst, an optimization of the band structure is required, including narrowing the bandgap (Eg) to improve visible light absorption, and proper positioning of the valence band (VB) and the conduction band (CB) [41]. Efforts on narrowing the bandgap of the TiO_2 have been done through doping with metallic and nonmetallic elements that typically replace Ti or O atoms, and thus change the position of the VB and or the CB leading to a change in the bandgap [42]. In the following subsections, titania will be used as an example to assess the effect of U correction by presenting results from literature for both pristine and doped cases. We will monitor the behavior of the materials before and after U correction, while assessing the significance of the U correction for correct prediction of the material's properties.

3.3.1. The Bandgap problem: pristine TiO_2 with U correction

Regarding the electronic structure of titania, the bandgap was underestimated by the standard DFT, while found to be overestimated when the hybrid functional Heyd-Scuseria-Ernzerhof (HSE06) was applied. However, the bandgap prediction was markedly improved by adding

the Hubbard U correction. The obtained band structures using GGA-PBE showed bandgaps of 2.140 and 1.973 eV for anatase and rutile, respectively. However, upon applying the localization of the excess electronic charge using +U correction, the predicted bandgaps are accurate and in a good agreement with the experimental and the computationally expensive hybrid functional (HSE06) results [43], **Figure 2**. In another study, for rutile TiO2, the prediction of the experimental bandgap is achieved with a U value of 10 eV, whereas the crystal and electronic structures were better described with $U < 5$ eV [19].
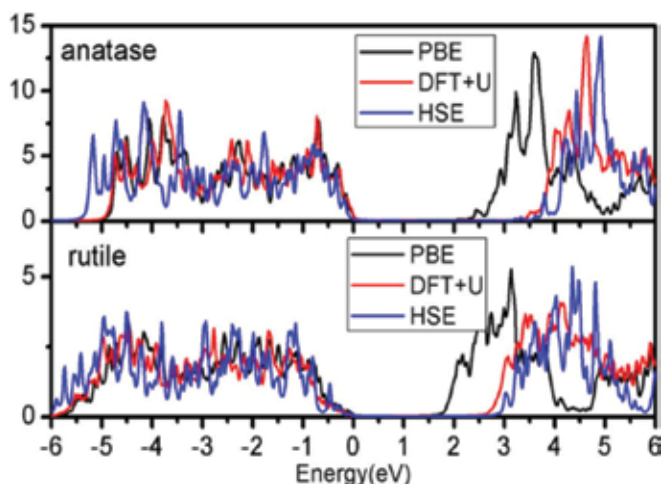
Figure 2. Total DOS of pure TiO$_2$ (anatase and rutile) [43]. Copyright (2014)—American Chemical Society.

Dompablo et al. [19] compared the effect of the U parameter value ($0 < U < 10$ eV) within the LDA+U and the GGA+U on the calculated properties of anatase TiO$_2$. Both LDA+U and GGA+U required a small value of U (3 and 6 eV, respectively) to reproduce the experimental measurements, **Figure 3**. However, using very large U values leads to mismatching, where the lattice parameters (a and c) and the volume of unit cell are increasing with increasing U, due to the Coulomb repulsion increase. Note that standard DFT and the hybrid functional HSE06 failed to calculate the crystal lattice.

On the other hand, the calculated bandgap within the GGA+U and LDA+U methods was found to be in better agreement with experiments compared to the conventional GGA or LDA, with small difference in the required U value. The bandgap was shown to increase by increasing the U value till 8.5 eV, which gave a result close to the experimental bandgap and in agreement with those obtained in previous DFT studies [44]. For values of U larger than 8.5, the bandgap was overestimated. It is worth to mention that this value (8.5 eV) is considered high when compared to other U values for other transition metal oxides [29]. In all these calculations, the Hubbard U parameter was used for the d or f orbitals of transition metals. However, when the Ti-O bonding is considered, while applying the correction only to the $3d$-states, it can be estimated that this correction might have an influence over the Ti−O covalent bonding, where the Ti states are shifted and the $2p$ states of oxygen are not changed [45]. In this regard, several first principle calculations were derived to study the electronic,

structural, and optical properties of TiO_2 polymorphs by applying the U correction for the oxygen's *2p* orbitals and titanium's *3d* orbitals [46]. In order to correct the bandgap, while avoiding the use of large U values and the bonding problem, Ataei et al. [47] reported that with values of 3.5 eV for both O *2p* and Ti *3d*-states, the results for the lattice constants, bandgap, and gap states are in good agreement with the experimental reports.
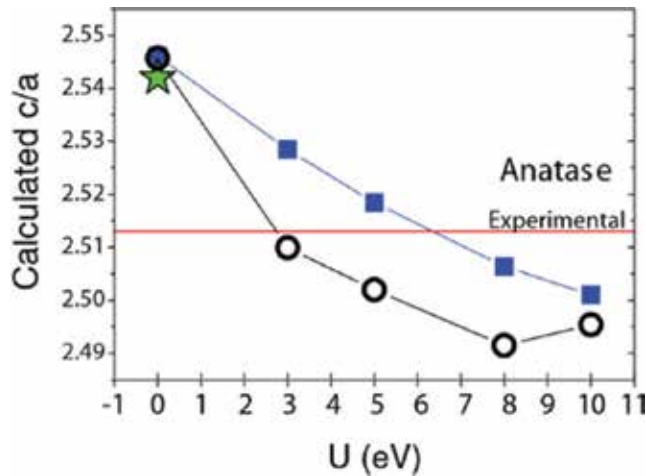
Figure 3. Calculated c/a ratio vs. U value. Reproduced from [19], with the permission of AIP Publishing.

3.3.2. Doped-TiO$_2$ with U correction

In a recent study [40], a comparison was performed to elucidate the effect of different U values in representing the bandgap states produced by interstitial hydrogen atom and oxygen vacancy within the bulk Ti anatase structure. The dependence on the method used was observed, beside the value of U within GGA+U scheme, see **Figure 4**. When the U correction was not applied, the bandgap is underestimated, as expected, and the electrons caused by the oxygen vacancy or the hydrogen impurity are fully delocalized and have conduction band character. Upon applying the U correction, the states start to localize and are became deeply localized in the gap with increasing the value of U. In all these calculations, the Hubbard U correction was applied for the Ti *3d* orbitals only; by applying the correction for the *2p* oxygen orbitals with $U = 3.5$, the results were in agreement with previous results [47].

The intrinsic defects in TiO_2 (vacancies) have been computationally studied, providing a fast-cheap method to guide researchers in choosing the defect position in the solid crystal. The oxygen vacancy in the rutile crystal was investigated [48] using the DFT+U with U value of 4.0 eV, indicating that oxygen vacancy in the rutile crystal introduces four local states with two occupied and two unoccupied states, with no change in the bandgap (2.75 eV) [48]. The Ti vacancy effect on the bandgap (E_g) was also studied [49] using the GGA+U with U values of 7.2 eV. It was found that Ti vacancy caused ferromagnetism besides widening the valence band, and switching the TiO_2 from n-type to p-type semiconductor with higher charge mobility [49].

Oxygen vacancy
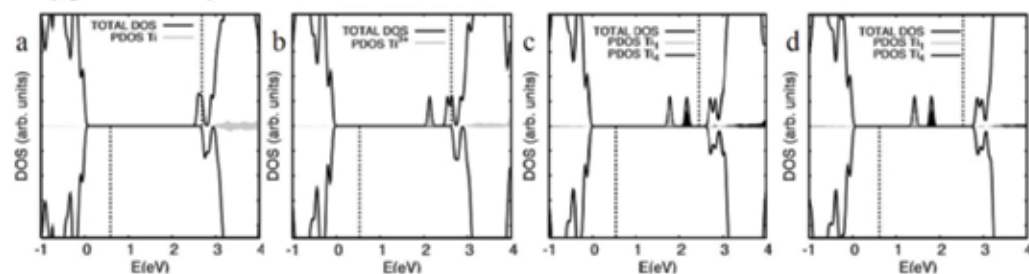
Hydrogen interstitial
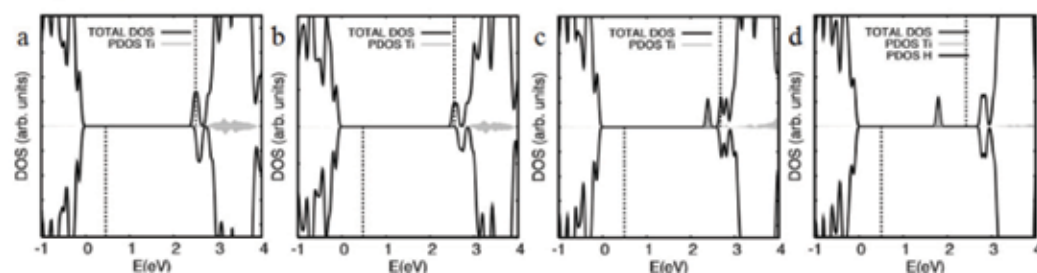
Figure 4. Total and partial density of states DOS for anatase TiO_2 doped with (oxygen vacancies and interstitial H atom) obtained with GGA-PBE+U. Adapted with permission from [39]; (a) U = 0, (b) U = 2, (c) U = 3, (d) U = 4.

4. Modeling of organometallics using the (+U)

Hubbard correction is a computational tool that can be applied widely not only to crystals but also to the strongly correlated metals attached to other noncorrelated systems such as organic moieties. One of these important systems is metal organic framework (MOF).

4.1. Metal organic frameworks (MOFs)

MOFs are crystalline nanoporous materials where a centered transition metal is linked to different types of ligands, which provide a very large surface area [50] that can allow their use in supercapacitors and water splitting applications. Most of the MOFs have open metal sites, which are coordinative unsaturated metal sites with no geometric hindrance. While the whole material remains as a solid, the structure allows the complex framework to be used in gas capturing and storage, and the binding energy between the MOFs and the gas or water molecules allows the prediction of the capturing mechanism. The cage shape of the MOFs and the organic moiety allow their use in many applications such as drug delivery and fertilizers, while the magnetic behavior of MOFs allows the researchers to correctly predict how it can be used in applications. Quantum mechanics frame of work is usually used to describe the full interaction between the centered metal ion and the surrounding ligands, due to the fact that the synthesis of these materials is both time and money consuming. The complex geometry

resulted from the computational calculations is important to predict the small change in electronic structure upon application of external stimuli [51].

Density functional theory (DFT) has been used to model the MOFs as it allows the "mapping" of a system of N interacting electrons onto a system of N noninteracting electrons having the same ground state charge density in an effective potential. However, DFT fails to describe electrons in open *d*- or *f*-shells [8]. The pure DFT calculations usually wrongly estimate the bandgap and the ferromagnetic (FM) or antiferromagnetic (AFM) coupling for the centered metal in the MOFs. The reason for this wrong estimation is the localized spin and itinerant spin density that are coupled via the Heisenberg exchange interaction [52, 53]. In this interaction, the ferromagnetic sign is assumed if the hybridization of the conduction electrons (dispersive LUMO band) with a doubly occupied or empty *d* orbital of the magnetic center is sufficiently strong. Owing to Hund's rule, in the *d* shell, it is energetically favorable to induce spin polarization parallel to the *d*-shell spin. The itinerant spin density, however, forms at an energy penalty determined by the dispersion of the conduction band; the larger the density of states at the Fermi level, the easier is for the itinerant spin density to form. The addition of an extra interaction term that accounts for the strong on-site coulomb U correction has proved to lead to good results [54]. One more advantage of the DFT+U is that it can be used to model systems containing up to few hundred atoms [55]. The U parameter affects the predicted electronic structure and magnetic properties; in the following paragraphs, we will discuss some of the MOF applications and how to fit a proper magnitude of U in DFT+U calculations:

- The magnetic properties of the MOF of the complex dimethyl ammonium copper format (DMACuF) were predicted correctly [56] using the (GGA+U) with convenient U values ($U = 4$–7 eV) for Cu $3d$-states to describe the effect of electron correlation associated with those states. Also, the magnetic properties of MOFs of TCNQ (7,7,8,8-tetracyanoquinodimethane) and two different (Mn and Ni) $3d$ transition metal atoms were predicted correctly without synthesizing. But in this case to properly describe the d electrons in Ni and Mn metal centers, spin-polarized calculations using the DFT+U with U value of ($U = 4$ eV) were performed [53]. It can be claimed that the varying of U in the range of 3 to 5 eV does not appreciably change the values of the Ni and Mn magnetic moments, nor the corresponding $3d$ level occupations, in particular, that of the Ni ($3dxz$) orbital that crosses the Fermi level [53].

- The binding energy of CO_2 to a Co-MOF-74 was predicted [57] using DFT+U with U values ($U = 0$–6 eV), and it was found that the value of U between 2 and 5 eV gives lattice parameters matching with experiment due to the fact that the Co-O bond length decreases with U, since U localizes the Co d-states, which allows the CO_2 molecule closer to the charged open metal site, increasing the electrostatic contribution to the binding energy [57].

- The Cu-BTC [58], a material consisting of copper dimers linked by 1,3,5-benzenetricarboxylate $C_6O_9H_3$ (BTC) units, was studied for its ability to absorb up to 3.5 H_2O per Cu as the Cu binds to the closest oxygen of the water molecule [59]. The U parameter in the meta-GGA+U calculation of the Cu-BTC was adjusted with the experimental crystallographic structure and the bandgap by minimizing the absorption at 2.3 eV. The U values gave the best results at 3.08 eV for Cu and 7.05 eV for O because those values reduced the calculated

root mean square residual forces on the ions at their experimental fixed positions to its minimum value. The nonzero U of oxygen greatly reduces the residual forces, while the value of U for Cu ions controls the splitting in the Cu d levels, which have a great effect on calculated bandgap [59].

4.2. Spin-crossover (SCO)

Spin-crossover (SCO) is a unique feature in which the centered transition metal ion linked to the surrounding ligand has the ability to attain different spin states with different total spin quantum numbers (S), while keeping the same valence state [47]. This property allows MOFs and organometallics generally to reversibly switch between spin states upon application of temperature, pressure, light, or magnetic field, such as changing between low spin and high spin [60, 61]. The SCO can be predicted effectively using the U correction as well as the effect of temperature on the SCO. The use of DFT+U to model SCO was first done by Lebègue et al. [62]. SCO is generally appealing for metals that have availability to change between high spin and low spin due to the small difference between the HOMO and LUMO levels. Iron (Fe) is one of the most important examples for this property. Fe is important since it can be found in many ores and can be used in many applications such as solar cells. Besides, Fe can be called the source of life, which is the heme molecule in the blood and which is responsible for the transfer of oxygen and carbon dioxide to and from the cell, respectively, consist of Fe-porphyrin molecule. Modeling of those molecules and their reaction mechanisms provides information about drug reactions inside the blood stream. Unfortunately, the common exchange-correlation functional fails to predict the properties of the deoxygenated active site of hemoglobin and myoglobin and Fe-porphyrin molecules [63, 64]. Some of the examples of SCO in Fe complexes are listed below:

- The SCO of $[TiFe(CN)_6]^{2-}$, $[CrFe(CN)_6]^{2-}$, $[MnFe(CN)_6]^{2-}$, and $[CoFe(CN)_6]^{2-}$ frameworks has been studied [65] using the DFT+U. It was found that high U values > 8 eV should be applied to the low spin Fe site, while low U value should be applied to the high spin ion. The results showed a great agreement with other DFT calculations. The generally used DFT-GGA failed to predict the high spin of the five coordinate Fe complexes [68], but it could be obtained by the DFT+U with $U \sim$ 4 eV and J~ 1 eV. The complexes $Fe(phen)_2(NCS)_2$ and $Fe(btr)_2(NCS)_2$ were tested using a U value of 2.5 eV [62], with the energy difference between the low spin state and high spin state is in agreement with the experimental values and proved that the U coulomb term was needed. The study showed the importance of magneto elastic couplings through the correlation between the spin state and the structure [62].

- Another study on the complex $[Fe(pmd)-(H_2O)M_2(CN)_4].H_2O$ (pmd = pyrimidine and M = Ag or Au) showed an interesting SCO behavior according to temperature [66]. This complex forms chain polymers that contain two different Fe(II) ions Fe1 and Fe2. Through hydration/dehydration, temperature changes between 130 and 230 K for the Ag-based coordination polymer changing the SCO reversibly and this change is due to the structure change caused by the water molecules in the network. For the Au-based complexes, only the SCO transition was different in the hydrated framework [66]. Such behavior could be explained using the DFT+U calculations [67]. The low spin-high spin transition was found

to occur only on the sixfold nitrogen coordinate Fe_1 ion, while the Fe_2 ion coordinate with four nitrogen and two oxygen from the water molecules. For the dehydrated compounds, the effect of the Au atom caused a difference in the degree of the covalent bonding, which resulted in a distinct behavior of the Au network as compared to the Ag network. The hydrated and dehydrated Ag networks were predicted to exhibit a low spin-high spin transition, whereas the dehydrated Au network was predicted to remain in a high spin state [55].

- Fe-porphyrin molecules were found to have an intermediate spin state. The ground-state configuration was indicated to be $(d_{XY})^2(d_{\pi})^2(d_{z^2})^2$ using Mossbauer [68–70], magnetic [71] and NMR [72, 73] measurements. However, Raman spectroscopy predicted a ground state with a configuration $(d_{XY})^2(d_{\pi})^3(d_{z^2})^1$ [74]. Therefore, a computational calculation was important to predict the reason for those results. The DFT+U was used to predict the electronic structure and magnetic properties of Fe molecules for a range of Coulomb U parameters (U = 2–4 eV), which is reasonable for iron [10, 75], and then compared to available data in literature. It was found that GGA+U with U value of 4 eV provided an overall better comparison of the structural, electronic, magnetic properties, and energy level diagram of these systems [76, 77].

To summarize, DFT+U are good to predict the correlation in the centered metal in organometallics. The spin change between FM and AFM states or in SCO can all be well predicted by the Hubbard correction, while the pure DFT fails due to the correlation in the d or f orbitals of the centered metal.

5. Solving the CO adsorption puzzle with the U correction

Studying surface chemistry is of great significance for enhancing the overall efficiency of many electrochemical applications [78–80]. In catalysis, for example, understanding the adsorption mechanism of species on catalytic surfaces—mainly electrodes—is essential in order to formulate a design principle for the prefect catalyst that can reach the optimum efficiency for a desired electrochemical process [81–83]. Typically, the adsorption of CO on metal surface is widely acknowledged as the prototypical system for studying molecular chemisorption [84–87]. Despite the extensive experimental studies, grasping the complete theoretical description of the "bonding model" has not yet been reached, due to the inability of experimental tools to fully describe the details of molecular orbital interactions and to make a profound population analysis, which is based on studying the electronic structures of the substrate and surface particles [88, 89]. To this end, DFT can be utilized to explicitly describe electronic structures of the system particles in greater details, which can help in extending the conceptual model of CO chemisorption [90–94]. Unfortunately, due to the inherent wrong description of the electronic structure by DFT, wrong predictions of CO preferred adsorption sites are observed that contradict experimental results, especially for the (111) surface facets of transition metals, leading to the so-called "CO adsorption *Puzzle*" [95, 96]. The root of this DFT problem resides on the fact that both local density and generalized gradient approximation functionals underestimate the CO bandgap, predicting wrong positions of the CO frontier orbitals, which results in an overestimated bond strength between the substrate and surface molecules [97].

One of the popular solutions that has been exploited by researchers to resolve the adsorption site prediction puzzle is the DFT+U correction [97, 98]. In this approach, the position of the $2\pi^*$ orbital is shifted to higher values, by adding the on-site Coulomb interaction parameter. By doing so, the interaction of CO $2\pi^*$ orbital with the metallic d-band will no longer be over-estimated, bringing the appropriate estimation of the CO adsorption site. Kresse et al. [99] first implemented this method and successfully obtained a site preference in agreement with experiment, emphasizing that the use of such a simple empirical method is able to capture the essential physics of adsorption. DFT calculations utilizing GGA functionals predict adsorption on the threefold hollow site for Cu(111) and in the bridge site on Cu(001), instead of the experimental on-top site preference. Reference [98] implanted Kresse's method to investigate the adsorption of CO on Cu(111) and (001) surfaces with 1/4 monolayer (ML) coverage on different adsorption sites. In that study, the HOMO-LUMO gap of the isolated CO molecule was demonstrated to be increased by increasing the value of U. Also, upon changing the U value, the corresponding adsorption energies of the CO over the different adsorption sites were calculated.

Reviewing the Cu (111) surface results, five different U values (0.0, 0.5, 1.0, 1.25, and 1.5 eV) were used in the calculations. It was observed that only 20 meV changes in the adsorption energy (higher coordinated hollow sites) for $U = 1.25$ and 0.03 eV for $U = 1.5$ eV. Nonetheless, the absolute value of adsorption energy decreases linearly with increasing U, where the rate of reduction is found to be larger for higher coordinated sites. It was observed that the site preference between top and bridge sites to be reversed around the U value of 0.05 eV, while between the top and hollow sites around $U = 0.45$ eV. Concerning the adsorbate (surface) description in the study, the calculated interlayer relaxations were the same as that calculated using the GGA (PW91) functional without the U correction. Not only does the U correction help in solving the adsorption puzzle dilemma, but it can also enhance the description of other related properties, such as the calculated work function and the vibrational spectra for the CO-metal complexes, which are also demonstrated in Ref. [98] (**Figure 5**).
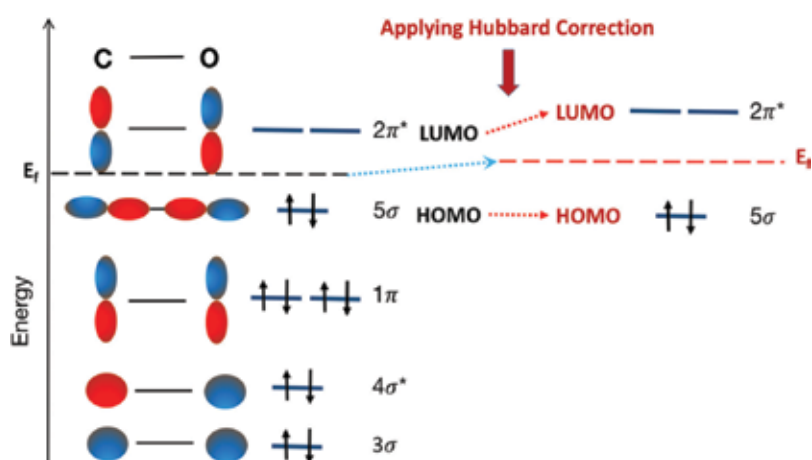

Figure 5. A schematic sketch of the molecular eigenstates of the CO molecule. The DFT+U technique shifts the LUMO orbitals to higher energies, but the energies of the occupied orbitals remain the same.

6. Summary and outlook

In this chapter, the corrective capability of the DFT+U is overviewed and evaluated for a number of different classes of materials. Generally, the addition of the on-site Coulomb interaction potential (U) to the standard DFT Hamiltonian proved to provide significant changes to the predicted electronic structures, which can solve the inherent DFT bandgap prediction problem. The value of U can either be theoretically calculated or semiempirically tuned to match the experimental electronic structure. For the various case studies and applications reviewed, the criticality of correcting the electronic structure predictions was manifested, as it leads to significant improvements for the prediction of further electronic-related properties. Prior to the practical assessment, the theoretical foundation of the DFT+U method is briefly discussed and is verified to be rather simple adding only marginal computational cost to the standard DFT calculations. Compared to other corrective approaches, the DFT+U formulation demonstrated to be simpler in terms of theoretical formulation and practical implementations with considerably lower computational cost, while having nearly the same predictive power; it can even capture properties of certain materials that cannot be captured by other higher level or exact calculations. One of the most popular implementations of the U correction is the description of the electronic structure for strongly correlated materials (Mott insulators). The behavior of these types of insulators cannot be captured by applying Hartree-Fock, band theory based, calculations, as the root of this problem resides on the deficiency of the band theory to capture such behavior, as it neglects the interelectron forces. One of the simple models, which explicitly accounts for the on-site repulsion between electrons at the same atomic orbitals, is the Hubbard model. Based on this model, the DFT+U method is formulated to improve the description of the ground state of correlated systems.

The theoretical and semiempirical techniques of the U optimization are discussed. The semiempirical tuning is found to be the most common practice employed by researchers due to the significant computational cost of *ab initio* calculations that U can have, and also, the computed U is not necessarily being better than the empirical ones. However, the semiempirical evaluation of U does not permit the capturing of changes in the on-site electronic interaction under changing physical conditions, such as chemical reactions. The practical implementations of U correction are discussed, while assessing the effect of the DFT scheme employed and the calculation parameters assigned on the numerical value of the optimum U utilized. The corrective influence of the U correction is validated by reviewing different examples and case studies in literature. Starting with the transition metal oxides, the effect of adding the U parameter to correctly describe the electronic structure of pure and defected TiO2 is reviewed, showing the different optimum values of U utilized for each level of calculation. Then, the implementation of the Hubbard correction to the systems that comprises molecules with solid-state crystals is reviewed, such as organometallics. The addition of U to the DFT calculation provides a better understanding of the behavior of the metals inside the organometallic systems. One of the most importantly studied organometallic systems is the metal organic frameworks (MOFs). Different examples in literature are reviewed, showing the effect of the U correction and how it can significantly improve the prediction of the magnetic properties of such systems. Also, one of the unique features of organometallics, which can be influenced the U correction, is the spin crossover (SCO). This property allows the MOFs and the organometallics generally to reversibly switch between spin states

upon changing the external parameters. The SCO is proved to be predicted more effectively by applying the *U* correction, as demonstrated in the results presented in literature. Finally, the significance of the DFT+U method is manifested upon describing the adsorption mechanism of CO on transition metal systems. The influence of *U* correction on solving the so-called adsorption *Puzzle* is demonstrated, which leads to the correct prediction of CO adsorption site preference, which was an unresolved problem when DFT calculations are applied alone.

Upon reviewing the presented applications and different case studies, where the *U* correction significantly improved the estimated results without changing the essential physics of the systems, we can estimate the potential of the Hubbard correction to gain a greater weight in the future of computational chemistry. Despite the convenience of the semiempirical tuning of *U*, the capabilities of the Hubbard correction in this way cannot be fully exploited, as it cannot be used to study systems with variations of on-site electronic interactions. On the other hand, despite the availability of theoretical *U* calculation methods, their computational costs are considerably large, compared to the semiempirical methods. Therefore, further improvements to the *ab initio* calculation of *U* is still required, with lower computational costs, in order to conceive full potential of the *U* correction that is able to capture phase changes and chemical reactions for the studied physical systems.

Acknowledgements

Author details

Sarah A. Tolba[†], Kareem M. Gameel[†], Basant A. Ali, Hossam A. Almossalami and Nageh K. Allam*

*Address all correspondence to: nageh.allam@aucegypt.edu

Energy Materials Laboratory, The American University in Cairo, New Cairo, Egypt

[†]These authors contributed equally

References

[1] Koch W, Holthausen MC. A Chemist's Guide to Density Functional Theory. New York, USA: John Wiley & Sons; 2001. DOI: 10.1002/3527600043

[2] Mattsson AE, Schultz PA, Desjarlais MP. Designing meaningful density functional theory calculations in materials science—A primer. Modelling and Simulation in Materials Science and Engineering. 13 R, 2005;**1**. DOI: 10.1088/0965-0393/13/1/R01

[3]   Levy M. Generalized Kohn-Sham schemes and the band-gap problem. Physical Review B. 1996;**53**(7):3764-3774. DOI: 10.1103/PhysRevB.53.3764

[4]   Sholl D, Steckel J. Density Functional Theory: A Practical Introduction. Density Functional Theory. New York, USA: John Wiley & Sons; 2009. pp. 83-112. DOI: 10.1002/9780470447710

[5]   Himmetoglu B, Floris A, De Gironcoli S, Cococcioni M. Hubbard-corrected DFT energy functionals: The LDA+U description of correlated systems. International Journal of Quantum Chemistry. 2014;**114**:14-49. DOI: 10.1002/qua.24521

[6]   Cococcioni M. The LDA+U approach: A simple hubbard correction for correlated ground states. Correlated Electrons: From Models to Materials Modeling and Simulation, Forschungszentrum Julich, Germany. 2012;**2**

[7]   Kryachko ES. Density Functional Theory and Molecular Interactions: Dispersion Interactions. 2013. DOI: https://doi.org/10.1007/978-3-642-32750-6_2

[8]   Anisimov VI, Zaanen J, Andersen OK. Band theory and Mott insulators: Hubbard U instead of stoner I. Physical Review B. 1991;**44**(3):943-954. DOI: 10.1103/PhysRevB.44.943

[9]   Bruus H, Flensberg K. Introduction to Many-Body Quantum Theory in Condensed Matter Physics. Oxford, UK: Oxford University Press; Aug 2002:152-183. DOI: 10.1088/0305-4470/38/8/B01

[10] Anisimov VI, Aryasetiawan F, Lichtenstein AI. First-principles calculations of the electronic structure and spectra of strongly correlated systems: The LDA +U method. Journal of Physics: Condensed Matter. 1997;**9**:767-808. DOI: 10.1088/0953-8984/9/4/002

[11] Dudarev SL, Botton GA, Savrasov SY, Humphreys CJ, Sutton AP. Electron-energy-loss spectra and the structural stability of nickel oxide. Physical Review B. 1998;**57**(3):1505-1509. DOI:10.1103/PhysRevB.57.1505

[12] Liechtenstein AI, Anisimov VI, Zaanen J. Density-functional theory and strong interactions: Orbital ordering in Mott-Hubbard insulators. Physical Review B. 1995;**52**(8): R5467-R5470. DOI: 10.1103/PhysRevB.52.R5467

[13] Aryasetiawan F, Karlsson K, Jepsen O, Schönberger U. Calculations of Hubbard U from first-principles. Physical Review B - Condensed Matter Material Physics. 2006;**74**(12):1-24. DOI: 10.1103/PhysRevB.74.125106

[14] Hu Z, Metiu H. Choice of U for DFT+U calculations for titanium oxides. Journal of Physical Chemistry C. 2011;**115**:5841-5845. DOI: 10.1021/jp111350u

[15] Tran F, Blaha P, Schwarz K, Novák P. Hybrid exchange-correlation energy functionals for strongly correlated electrons: Applications to transition-metal monoxides. Physical Review B - Condensed Material Physics. 2006;**74**(15):1-10. DOI: 10.1103/PhysRevB.74.155108

[16] Gulans A et al. QUANTUM ESPRESSO: A modular and open-source software project for quantum simulations of materials. Journal of Physics Condensed Matter. 2009;**21**(39): 395502. DOI: 10.1126/science.1244358

[17] Cococcioni M, de Gironcoli S. A linear response approach to the calculation of the effective interaction parameters in the LDA+U method. Physical Review B. 2004:1-16. DOI: 10.1103/PhysRevB.71.035105

[18] http://hjkgrp.mit.edu/content/readers-choice-dftu

[19] Arroyo-De Dompablo ME, Morales-Garca A, Taravillo M. DFTU calculations of crystal lattice, electronic structure, and phase stability under pressure of TiO_2 polymorphs. The Journal of Chemical Physics. 2011;**135**(5). DOI: 10.1063/1.3617244

[20] Tian F, Liu C. DFT description on electronic structure and optical absorption properties of anionic S-doped anatase TiO_2. The Journal of Physical Chemistry. B. 2006;**110**(36):17866-17871. DOI: 10.1021/jp0635462

[21] Guo M, Du J. First-principles study of electronic structures and optical properties of Cu, Ag, and au-doped anatase TiO_2. Physica B Condensed Matter. 2012;**407**(6):1003-1007. DOI: 10.1016/j.physb.2011.12.128

[22] Walsh A, Wei S, Yan Y, Turner JA, Woodhouse M, Parkinson BA. Structural, magnetic, and electronic properties of the Co-Fe-Al oxide spinel system: Density-functional theory calculations. Physical Review B. 2007:1-9. DOI: 10.1103/PhysRevB.76.165119

[23] Wang L, Maxisch T, Ceder G. Oxidation energies of transition metal oxides within the GGA+U framework. Physical Review B - Condensed Matter Material Physics. 2006; **73**(19):1-6. DOI: 10.1103/PhysRevB.73.195107

[24] Chen J, Wu X, Selloni A. Electronic structure and bonding properties of cobalt oxide in the spinel structure. Physical Review B. 2011;**245204**:1-7. DOI: 10.1103/ PhysRevB.83.245204

[25] Anisimov VI, Poteryaev AI, Korotin MA, Anokhin AO, Kotlia G. First-principles calculations of the electronic structure and spectra of strongly correlated systems: The LDA +U method. Journal of Physics. Condensed Matter. 1997;**9**:767-808. DOI: 10.1088/ 0953-8984/9/35/010

[26] Lu D, Liu P. Rationalization of the Hubbard U parameter in CeO_x from first principles : Unveiling the role of local structure in screening Rationalization of the Hubbard U parameter in CeO_x from first principles. 2014;**84101**. no. May 2015:pp. 3-10. DOI: http:// dx.doi.org/10.1063/1.4865831

[27] Boukhvalov DW, Solovyev IV. Defects of the crystal structure and Jahn-Teller distortion in $BiMnO_3$. Physical Review B. 2010;**82**(August):pp. 1-2. DOI: https://doi.org/10.1103/ PhysRevB.82.245101

[28] Kresse G, Joubert D. From ultrasoft pseudopotentials to the projector augmented-wave method. Physical Review B. 1999;**59**(3):11-19. DOI: 10.1103/PhysRevB.59.1758

[29] Capdevila-Cortada M, Łodziana Z, López N. Performance of DFT+U approaches in the study of catalytic materials. ACS Catalysis. 2016;**6**(12):8370-8379. DOI: 10.1021/ acscatal.6b01907

[30] Stekolnikov AA, Bechstedt F. Shape of free and constrained group-IV crystallites: Influence of surface energies. Physical Review B. Sept 2005:1-9. DOI: 10.1103/PhysRevB.72.125326

[31] Anisimov VI, Solovyev IV, Korotin MA, Czyżyk MT, Sawatzky GA. Density-functional theory and NiO photoemission spectra. Physical Review B. 1993;**48**(23). DOI: 10.1103/PhysRevB.48.16929

[32] Zhou F, Cococcioni M, Marianetti CA, Morgan D, Ceder G. First-principles prediction of redox potentials in transition-metal compounds with LDA+U. Physical Review B. 2004;**70**(23). DOI: 10.1103/PhysRevB.70.235121

[33] Griffin SM, Spaldin NA. A density functional theory study of FeAs comparing LDA+U, GGA+U and hybrid functionals. arXiv preprint. 2014. DOI: arXiv:1401.2277v1

[34] Loschen C, Carrasco J, Neyman KM, Illas F. First-principles LDA+U and GGA+U study of cerium oxides: Dependence on the effective U parameter. Physical Review B. 2007;**75**(3). DOI: 10.1103/PhysRevB.75.035115

[35] Sun B, Zhang P, Zhao XG. First-principles local density approximation+U and generalized gradient approximation+U study of plutonium oxides. The Journal of Chemical Physics. 2008 Feb 28;**128**(8):084705. DOI: 10.1063/1.2833553

[36] McNeilly CE. The electrical properties of plutonium oxides. Journal of Nuclear Materials. 1964 Jan;**11**(1, 1):53-58. DOI: 10.1016/0022-3115(64)90120-5

[37] Santini P, Lemanski R, Erdős P. Magnetism of actinide compounds. Advances in Physics. 1999 Sep 1;**48**(5):537-653. DOI: 10.1080/000187399243419

[38] Jepsen O. Electronic structure of Nio: Correlation and band efFects. Physics Review. 1991;**44**(8, 8). DOI: 10.1103/PhysRevB.44.3604

[39] Finazzi E, Di Valentin C, Pacchioni G, Selloni A. Excess electron states in reduced bulk anatase TiO_2:Comparison of standard GGA, GGA+U, and hybrid DFT calculations. The Journal of Chemical Physics. 2008;**129**(15). DOI: 10.1063/1.2996362

[40] Hofmann A, Sauer J. Oxygen vacancies in transition metal and rare earth oxides: Current state of understanding and remaining challenges. Surface Science Reports. 2007;**62**:219-270. DOI: 10.1016/j.surfrep.2007.03.002

[41] Wu Y, Lazic P, Hautier G, Persson K, Ceder G. First principles high throughput screening of oxynitrides for water-splitting photocatalysts. Energy & Environmental Science. 2013;**6**(1):157-168. DOI: 10.1039/C2EE23482C

[42] Liu G, Wang L, Yang HG, Cheng HM, Lu GQ. Titania-based photocatalysts—Crystal growth, doping and heterostructuring. Journal of Materials Chemistry. 2010;**20**(5):831-843. DOI: 10.1039/B909930A

[43] Ju M, Sun G, Wang J, Meng Q, Liang W. Origin of high photocatalytic properties in the mixed-phase TiO2: A first-principles theoretical study. ACS Applied Materials & Interfaces. 2014;**6**(15):12885-12892. DOI: 10.1021/am502830m

[44] Beltrán JA, Sambrano JR, Longo E. Density functional theory study on the structural and electronic properties of low index rutile surfaces for $TiO_2/SnO_2/TiO_2$ and $SnO_2/TiO_2/SnO_2$ composite systems. The Journal of Physical Chemistry. A. 2008;**112**(38):8943-8952. DOI: 10.1021/jp801604n

[45] Park S, Magyari-köpe B, Nishi Y. Electronic correlation effects in reduced rutile TiO_2 within the LDA +U method. Physical Review B. 2010:1-9. DOI: 10.1103/PhysRevB.82.115109

[46] Vu NH, Le HV, Cao TM, Pham VV, Le HM. Anatase – rutile phase transformation of titanium dioxide bulk material : A DFT+U approach. 2012;**405501**. DOI: 10.1088/0953-8984/24/40/405501

[47] Ataei SS, Mohammadizadeh MR, Seriani N. Ab initio simulation of the effects of hydrogen concentration on Anatase TiO_2. Journal of Physical Chemistry C. 2016;**120**(16):8421-8427. DOI: 10.1021/acs.jpcc.6b00019

[48] Jin H, Wang L, Searles DJ, Sun C. Comparison of the effect of hydrogen incorporation and oxygen vacancies on the properties of anatase TiO_2: Electronics, optical absorption, and interaction with water. Chinese Science Bulletin. 2014 Jun 1;**59**(18):2175-2180. DOI: 10.1007/s11434-014-0229-2

[49] Wang S, Pan L, Song JJ, Mi W, Zou JJ, Wang L, Zhang X. Titanium-defected undoped anatase TiO_2 with p-type conductivity, room-temperature ferromagnetism, and remarkable photocatalytic performance. Journal of the American Chemical Society. 2015 Feb 18;**137**(8):2975-2983. DOI: 10.1021/ja512047k

[50] Furukawa H, Cordova KE, O'Keeffe M, Yaghi OM. The chemistry and applications of metal-organic frameworks. Science. 2013 Aug 30;**341**(6149):1230444. DOI: 10.1126/science.1230444

[51] Paulsen H, Schünemann V, Wolny JA. Progress in electronic structure calculations on spin-crossover complexes. European Journal of Inorganic Chemistry. 2013 Feb 18;**2013**(5-6):628-641. DOI: 10.1002/ejic.201201289

[52] Cramer CJ, Truhlar DG. Density functional theory for transition metals and transition metal chemistry. Physical Chemistry Chemical Physics. 2009;**11**(46):10757-10816. DOI: 10.1039/B907148B

[53] Zener C. Interaction between the d shells in the transition metals. Physics Review. 1951; **81**:440-444. DOI: 10.1103/PhysRev.81.440

[54] Faraggi MN, Golovach VN, Stepanow S, Tseng TC, Abdurakhmanova N, Kley CS, Langner A, Sessi V, Kern K, Arnau A. Modeling Ferro-and antiferromagnetic interactions in metal–organic coordination networks. The Journal of Physical Chemistry C. 2014 Dec 24;**119**(1):547-555. DOI: 10.1021/jp512019w

[55] Saha-Dasgupta T, Oppeneer PM. Computational design of magnetic metal-organic complexes and coordination polymers with spin-switchable functionalities. MRS Bulletin. 2014 Jul;**39**(7):614-620. DOI: 10.1557/mrs.2014.112

[56] Wang Z, Jain P, Choi KY, van Tol J, Cheetham AK, Kroto HW, Koo HJ, Zhou H, Hwang J, Choi ES, Whangbo MH. Dimethylammonium copper formate $[(CH_3)_2NH_2]$ cu $(HCOO)_3$: A metal-organic framework with quasi-one-dimensional antiferromagnetism and magnetostriction. Physical Review B. 2013 Jun 10;**87**(22):224406. DOI: 10.1103/PhysRevB.87.224406

[57] Mann GW, Lee K, Cococcioni M, Smit B, Neaton JB. First-principles Hubbard U approach for small molecule binding in metal-organic frameworks. The Journal of Chemical Physics. 2016 May 7;**144**(17):174104. DOI: 10.1063/1.4947240

[58] Chui SS, Lo SM, Charmant JP, Orpen AG, Williams ID. A chemically functionalizable nanoporous material $[Cu_3(TMA)_2(H_2O)_3]$ n. Science. 1999 Feb 19;**283**(5405):1148-1150. DOI: 10.1126/science.283.5405.1148

[59] Cockayne E, Nelson EB. Density functional theory meta-GGA+U study of water incorporation in the metal-organic framework material cu-BTC. The Journal of Chemical Physics. 2015 Jul 14;**143**(2):024701. DOI: 10.1063/1.4923461

[60] Gütlich P, Goodwin HA. Spin crossover—an overall perspective. In: Spin Crossover in Transition Metal Compounds I 2004 (pp. 1-47). Springer Berlin Heidelberg. DOI: 10.1007/b13527

[61] Brooker S, Kitchen JA. Nano-magnetic materials: Spin crossover compounds vs. single molecule magnets vs. single chain magnets. Dalton Transactions. 2009;(36):7331-7340. DOI: 10.1039/B907682D

[62] Lebègue S, Pillet S, Ángyán JG. Modeling spin-crossover compounds by periodic DFT+ U approach. Physical Review B. 2008 Jul 25;**78**(2):024433. DOI: 10.1103/PhysRevB.78.024433

[63] Choe YK, Nakajima T, Hirao K, Lindh R. Theoretical study of the electronic ground state of iron (II) porphine. II. The Journal of Chemical Physics. 1999 Sep 1;**111**(9):3837-3845. DOI: 10.1063/1.479687

[64] Jensen KP, Roos BO, Ryde U. O_2-binding to heme: Electronic structure and spectrum of oxyheme, studied by multiconfigurational methods. Journal of Inorganic Biochemistry. 2005 Jan 31;**99**(1):45-54. DOI: 10.1016/j.jinorgbio.2004.11.008

[65] Le HM, Pham TT, Dat VD, Kawazoe Y. First-principles modeling of metal (ii) ferrocyanide: Electronic property, magnetism, bulk moduli, and the role of C≡N⁻ defect. Journal of Physics D: Applied Physics. 2016 Dec 12;**50**(3):035004. DOI: 10.1088/1361-6463/50/3/035004

[66] Niel V, Thompson AL, Muñoz MC, Galet A, Goeta AE, Real JA. Crystalline-state reaction with allosteric effect in spin-crossover, interpenetrated networks with magnetic and optical Bistability. Angewandte Chemie. 2003 Aug 18;**115**(32):3890-3893. DOI: 10.1002/ange.200351853

[67] Sarkar S, Tarafder K, Oppeneer PM, Saha-Dasgupta T. Spin-crossover in cyanide-based bimetallic coordination polymers—Insight from first-principles calculations. Journal of Materials Chemistry. 2011;**21**(36):13832-13840. DOI: 10.1039/C1JM11679G

[68] Collman JP, Hoard JL, Kim N, Lang G, Reed CA. Synthesis, stereochemistry, and struc-
ture-related properties of. Alpha, Beta, Gamma, Delta-tetraphenylporphinatoiron (II).
Journal of the American Chemical Society. 1975 May;**97**(10):2676-2681. DOI: 10.1021/
ja00843a015

[69] Lang G, Spartalian K, Reed CA, Collman JP. Mössbauer effect study of the magnetic
properties of S=1 ferrous tetraphenylporphyrin. The Journal of Chemical Physics. 1978
Dec 15;**69**(12):5424-5427. DOI: 10.1063/1.436532

[70] Hu C, Roth A, Ellison MK, An J, Ellis CM, Schulz CE, Scheidt WR. Electronic configu-
ration assignment and the importance of low-lying excited states in high-spin imidaz-
ole-ligated iron (II) porphyrinates. Journal of the American Chemical Society. 2005 Apr
20;**127**(15):5675-5688. DOI: 10.1021/ja044077p

[71] Boyd PD, Buckingham DA, McMeeking RF, Mitra S. Paramagnetic anisotropy, aver-
age magnetic susceptibility, and electronic structure of intermediate-spin S= 1 (5, 10,
15, 20-tetraphenylporphyrin) iron (II). Inorganic Chemistry. 1979 Dec;**18**(12):3585-3591.
DOI: 10.1021/ic50202a059

[72] Goff H, La Mar GN, Reed CA. Nuclear magnetic resonance investigation of mag-
netic and electronic properties of" intermediate spin" ferrous porphyrin complexes.
Journal of the American Chemical Society. 1977 Mar;**99**(11):3641-3646. DOI: 10.1021/
ja00453a022

[73] Mispelter J, Momenteau M, Lhoste JM. Proton magnetic resonance characterization of
the intermediate (S= 1) spin state of ferrous porphyrins. The Journal of Chemical Physics.
1980 Jan 15;**72**(2):1003-1012. DOI: 10.1063/1.439266

[74] Kitagawa T, Teraoka J. The resonance Raman spectra of intermediate-spin ferrous porphy-
rin. Chemical Physics Letters. 1979 Jun 1;**63**(3):443-446. DOI: 10.1016/0009-2614(79)80685-5

[75] Steiner MM, Albers RC, Sham LJ. Quasiparticle properties of Fe, co, and Ni. Physical
Review B. 1992 Jun 15;**45**(23):13272. DOI: 10.1103/PhysRevB.45.13272

[76] Panchmatia PM, Sanyal B, Oppeneer PM. GGA+U modeling of structural, electronic,
and magnetic properties of iron porphyrin-type molecules. Chemical Physics. 2008 Jan
22;**343**(1):47-60. DOI: 10.1016/j.chemphys.2007.10.030

[77] Scherlis DA, Cococcioni M, Sit P, Marzari N. Simulation of heme using DFT+U: A step
toward accurate spin-state energetics. The Journal of Physical Chemistry B. 2007 Jun
28;**111**(25):7384-7391. DOI: 10.1021/jp070549l

[78] Wang Y, Wu G, Yang M, Wang J. Competition between Eley–Rideal and Langmuir–
Hinshelwood pathways of CO oxidation on Cu_n and Cu_nO (n = 6, 7) clusters. Journal of
Physical Chemistry C. 2013;**117**(17):8767-8773. DOI: 10.1021/jp3122775

[79] a Akhade S, Luo W, Nie X, Bernstein NJ, Asthagiri A, Janik MJ. Poisoning effect of
adsorbed CO during CO2 electroreduction on late transition metals. Physical Chemistry
Chemical Physics. 2014;**16**(38):20429-20435. DOI: 10.1039/c4cp03340j

[80] Abbas A, Ullah M, Ali Q, Zahid I, Abbas S, Wang X. An overview of CO_2 electrore-duction into hydrocarbons and liquid fuels on nanostructured copper catalysts. Green Chemistry Letters and Reviews. 2016;**9**(3):166-178. DOI: 10.1080/17518253.2016.1188162

[81] Chen MS, Cai Y, Yan Z, Gath KK, Axnanda S, Goodman DW. Highly active surfaces for CO oxidation on Rh, Pd, and Pt. Surface Science. 2007;**601**(23):5326-5331. DOI: 10.1016/j.susc.2007.08.019

[82] Kortlever R, Shen J, Schouten KJP, Calle-Vallejo F, Koper MTM. Catalysts and reac-tion pathways for the electrochemical reduction of carbon dioxide. Journal of Physical Chemistry Letters. 2015;**6**(20):4073-4082. DOI: 10.1021/acs.jpclett.5b01559

[83] Nakao K, Watanabe O, Sasaki T, ichi Ito S, Tomishige K, Kunimori K. CO oxidation on Pd(1 1 1), Pt(1 1 1), and Rh (1 1 1) surfaces studied by infrared chemiluminescence spec-troscopy. Surface Science. 2007;**601**(18):3796-3800. DOI: 10.1016/j.susc.2007.04.015

[84] Sung S, Hoffmann R. How Carbon Monoxide Bonds to Metal Surfaces. 1985:pp. 578-584. DOI: 10.1021/ja00289a009

[85] Froitzheim H, Hopster H, Ibach H, Lehwald S. Applied Physics Adsorption Sites of CO on Pt (1 1 l). Applied Physics A.1977;**13**(2):147-151. DOI: 10.1007/BF00882473

[86] Aizawa H, Tsuneyuki S. First-principles study of CO bonding to Pt(111): validity of the Blyholder model. Surface Science. 1998;**399**:0-6. DOI: 10.1016/S0039-6028(98)00042-9

[87] Pendry JB. Structure of CO Adsorbed on Cu (l00) and Ni (l00). Physical Review Letters. 1979;**43**(5):363-366. DOI: 10.1103/PhysRevLett.43.363

[88] Föhlisch A, Nyberg M, Bennich P, Triguero L, Hasselström J, Karis O, Pettersson LGM, Nilsson A. The bonding of CO to metal surfaces. The Journal of Chemical Physics. 2000;**112**(4):1946. DOI: 10.1063/1.480773

[89] Föhlisch A, Nyberg M, Hasselström J, Karis O, Pettersson LGM, Nilsson A. How CO adsorbs in different sites. Physical Review Letters. 2000;**85**:3309. DOI: 10.1103/PhysRevLett. 85.3309

[90] Gajdos M, Eichler A, Hafner J. CO adsorption on close-packed transition and noble metal surfaces: Trends from ab initio calculations. Journal of Physics. Condensed Matter. 2004;**16**(8):1141-1164. DOI: 10.1088/0953-8984/16/8/001

[91] Wasileski SA, Koper MTM, Weaver MJ. Field-dependent chemisorption of carbon mon-oxide on platinum-group (111) surfaces: Relationships between binding energetics, geometries, and vibrational properties as assessed by density functional theory. The Journal of Physical Chemistry. B. 2001;**105**(111):3518-3530. DOI: 10.1021/jp003263o

[92] Feibelman PJ, Hammer B, Wagner F, Scheffler M, Stumpf R, Watwe R, Dumesic J. The CO / Pt (111) Puzzle. 2001;**111**:pp. 4018-4025. DOI: 10.1021/jp002302t

[93] Hammer B, Morikawa Y. CO chemisorption at metal surfaces and Overlayers. Physical Review Letters. 1996:2141-2144. DOI: 10.1103/PhysRevLett.76.2141

[94] Andersson MP. CO adsorption energies on metals with correction for high coordination adsorption sites – A density functional study. Surface Science. 2007;**601**:1747-1753. DOI: 10.1016/j.susc.2007.01.052

[95] Schimka L, Harl J, Stroppa A, Grüneis A, Marsman M, Mittendorfer F, Kresse G. Accurate surface and adsorption energies from many-body perturbation theory. Nature Materials. 2010;**9**(9):741-744. DOI: 10.1038/nmat2806

[96] Stroppa A, Termentzidis K, Paier J, Kresse G, Hafner J. CO adsorption on metal surfaces : A hybrid functional study with plane-wave basis set. 2007. no. November:pp. 1-12. DOI: 10.1103/PhysRevB.76.195440

[97] Mason SE, Grinberg I, Rappe AM. First-principles extrapolation method for accurate CO adsorption energies on metal surfaces. Physical Review B. 2004;**69**(16):1-4. DOI: 10.1103/PhysRevB.69.161401

[98] Gajdos M. CO adsorption on Cu (111) and Cu (001) surfaces : Improving site preference in DFT calculations. 2005;**590**:pp. 117-126. DOI: 10.1016/j.susc.2005.04.047

[99] Kresse G, Gil A, Sautet P. Significance of single-electron energies for the description of CO on Pt (111). Physical Review B. 2003;**68**(7):3-6. DOI: 10.1103/PhysRevB.68.073401

Constricted Variational Density Functional Theory Approach to the Description of Excited States

Florian Senn, Issaka Seidu and Young Choon Park

Additional information is available at the end of the chapter

Abstract

The aim of this chapter is to present constricted variational density functional theory (CV-DFT), a DFT-based method for calculating excited-state energies. This method involves constructing from the ground-state orbitals, a new set of 'occupied' excited-state orbitals. Consequently, a constraint is applied to ensure that exactly one electron is fully transferred from the occupied to the virtual space. This constraint also prevents a collapse to a lower state. With this set of orbitals, one obtains an electron density for the excited-state and therewith the CV-DFT excitation energy. This excitation energy can now be variationally optimized. With our successful applications to systems differing in the type of excitation, namely, charge-transfer, charge-transfer in disguise, and Rydberg excitations, as well as in size, we demonstrate the strengths of the CV-DFT method. Therewith, CV-DFT provides a valid alternative to calculate excited-state properties, especially in cases where TD-DFT has difficulties. Finally, our studies have shown that the difficulties arising in the TD-DFT excited states are not necessarily stemming from the functional used, but from the application of these standard functionals in combination with the linear response theory.

Keywords: CV-DFT, excited state, charge-transfer, Rydberg excitations, ZnBC-BC

1. Introduction

The behavior of atoms and polyatomic systems in the excited-state are of immense importance in the studies of several photophysical phenomena. Thus, the search for methods to study systems in their electronically excited state is the subject of ongoing research [1–13]. Resultantly, there are several methods to choose from within certain consideration such as system size, expected level of accuracy and nature of initial and final electronic state of the system under study. Therefore, some background knowledge is necessary for the accurate treatment of excited states with the available methods. These methods fall under different families, and

the *ab initio* wave function family of methods includes multi-reference configuration interaction (MRCI) [14], multi-configurational self-consistent field (MCSCF) [15, 16], complete active space self-consistent field (CASSCF) [17], time-dependent Hartree-Fock (TD-HF) [18–21], restricted active space self-consistent field (RASSCF) [22], RASPT2 [23], complete active space second-order perturbation theory (CASPT2) [24], equation-of-motion coupled cluster (EOMCC) [25], *n*-electron valence state perturbation theory (NEVPT) [26], spectroscopically oriented configuration interaction (SORCI) [27] and coupled cluster (CC) theory [28, 29].

However, the focus of this book is the Kohn-Sham density functional theory (DFT) [30] and methods based on it. In this chapter, our attention is on the calculation of excited states. Excited-state studies within DFT gained considerable attention owing to the increasing success of DFT in ground-state studies. Significant research effort toward the development of excited-state methods has resulted in a variety of approaches varying in both major and minor details, each method having its own advantages and disadvantages. The result of this endeavor includes self-consistent-field DFT (ΔSCF-DFT) [31–33] with extensions [34–36], time-dependent DFT [40–44], ensemble DFT [37–39, 45–47], constrained orthogonality method (COM) [48–50], restricted open-shell Kohn-Sham (ROKS) [47, 51, 52], constrained DFT (CDFT) [53], 'taking orthogonality constraints into account' (TOCIA) [54, 55], maximum overlap method (MOM) [56, 57], constricted variational density functional theory (CV-DFT) [58] and extensions [59–62], orthogonality constrained DFT (OCDFT) [63] and guided SCF [64] among others. However, the most widely used by both expert and nonexpert is TD-DFT in the form of linear response adiabatic time-dependent DFT [40, 41, 65–69] (which we will refer to as TD-DFT) due to its successes.

The strengths and weaknesses of TD-DFT are well known and understood through extensive benchmark studies carried out over the years. The strengths explain its wide usage by delivering 'an excellent compromise between computational efficiency and accuracy' [70]. The weaknesses explain the ongoing fundamental studies searching for solutions in the cases where TD-DFT is found lacking. These include its deficiency in describing Rydberg transitions [71–74], charge-transfer (CT) transitions [75–84] and electronic transition with significant double contribution [42, 43, 83–87]. TD-DFT is a formally exact theory; however, its practical application relies on the adiabatic formalism where use is made of the available ground-state exchange-correlation (*XC*) functionals [71, 82, 88–90]. As a result, one can necessarily trace all the problems encountered in the application of TD-DFT to this approximation. The numerous research attempts to remedy the pitfalls in TD-DFT are classified as follows:

1. Finding the *XC* functionals with the correct short- and long-range behavior or going beyond the adiabatic approximation.

2. Developing new DFT-based excited-state methods.

An often-encountered problem with the development of specialized functionals is that it usually performs very well for the purpose for which it was originally developed but unimaginably erratic for any other situation [71–74, 77, 79, 82, 88, 91–98].

Our contribution to this area of research is in the development of the constricted variational DFT (CV-DFT) [58–62], which combines the strengths of ΔSCF-DFT and TD-DFT methods without the need for 'specialized' functionals.

In this chapter, we will explain the idea and theory of CV-DFT, before we have a look at different examples, where CV-DFT has been applied for transitions of Rydberg and charge-transfer type following the publications [99–103].

2. Theory

In this chapter, we review the theoretical framework of CV-DFT in a nutshell. We refer to the original publications [58–62, 104] for a more in-depth description.

2.1. The CV-DFT scheme

Here, we only consider the excitation from the closed-shell ground state described with single Slater determinant, $\Psi^0 = \left| \phi_1 \phi_2 \ldots \phi_i \ldots \phi_{n_{occ}} \right|$, where n_{occ} is the number of occupied orbitals. CV-DFT starts from the ansatz which describes the excitation as an admixture of occupied $\left\{ \phi_i; i = 1, \cdots, n_{occ} \right\}$ and virtual $\left\{ \phi_a; a = 1, \cdots, n_{vir} \right\}$ ground-state orbitals [105]:

$$\phi'_i = \sum_a^{n_{vir}} U_{ai} \phi_a \tag{1}$$

where ϕ'_i is the excited-state orbital and n_{vir} the number of virtual orbitals. The transition matrix, $\mathbf{U}$, only mixes between occupied and virtual orbitals ($U_{ij} = U_{ab} = 0$) and is skew symmetric ($U_{ai} = -U_{ia}$). In CV-DFT, we use the exponential expansion of $\mathbf{U}$ which leads to the unitary transformation $\mathbf{Y}$:

$$\mathbf{Y} = \exp(\mathbf{U}) = \sum_{k=0}^{\infty} \frac{\mathbf{U}^k}{k!}. \tag{2}$$

Thus, once the transition matrix, $\mathbf{U}$, is determined, a new set of orbitals is obtained over the unitary transformation

$$\begin{pmatrix} \phi'_{occ} \\ \phi'_{vir} \end{pmatrix} = \left(\sum_{k=0}^{\infty} \frac{\mathbf{U}^k}{k!} \right) \begin{pmatrix} \phi_{occ} \\ \phi_{vir} \end{pmatrix}. \tag{3}$$

Due to the properties of the transition matrix, $\mathbf{U}$, the 'occupied' excited-state orbitals can be written as

$$\phi_i^{'} = \sum_j^{n_{occ}} Y_{ji} \phi_j + \sum_a^{n_{vir}} Y_{ai} \phi_a. \tag{4}$$

The corresponding excited-state density becomes

$$\rho'(1, 1') = \sum_{i}^{n_{\text{occ}}} \phi_i'(1)\phi_i'(1')$$

$$= \sum_{i}^{n_{\text{occ}}} \phi_i(1)\phi_i(1') + \sum_{a}^{n_{\text{vir}}}\sum_{i}^{n_{\text{occ}}} \Delta P_{ai}\left[\phi_i(1)\phi_a(1') + \phi_a(1)\phi_i(1')\right] \tag{5}$$

$$+ \sum_{i}^{n_{\text{occ}}}\sum_{j}^{n_{\text{occ}}} \Delta P_{ij}\phi_i(1)\phi_j(1') + \sum_{a}^{n_{\text{vir}}}\sum_{b}^{n_{\text{vir}}} \Delta P_{ab}\phi_a(1)\phi_b(1')$$

with the change in density matrix (ΔP). Later, one is given by

$$\Delta P_{aj} = \sum_{i}^{n_{\text{occ}}} Y_{ai}Y_{ji} \tag{6}$$

$$\Delta P_{jk} = \sum_{i}^{n_{\text{occ}}} \left(Y_{ji}Y_{ki} - \delta_{jk}\right) \tag{7}$$

$$\Delta P_{ab} = \sum_{i}^{n_{\text{occ}}} Y_{ai}Y_{bi}. \tag{8}$$

In CV-DFT, we apply the important condition that one electron is fully transferred from occupied into virtual spaces. This condition can be written as the following equation:

$$\sum_{a}^{n_{\text{vir}}} \Delta P_{aa} = 1 \quad \text{and} \quad \sum_{i}^{n_{\text{occ}}} \Delta P_{ii} = -1. \tag{9}$$

It should be noted that in CV-DFT we describe the excited state with a single Slater determinant. Thus, we obtain the mixed and triplet states. While this is uncritical for triplet excitations, for the singlet transition energy, we have to account for this by using the relation (which is also referred to as sum rule) [61]

$$\Delta E_S = 2\Delta E_M - \Delta E_T. \tag{10}$$

2.2. CV(n)-DFT

The nth-order CV-DFT, CV(n)-DFT, is determined from the maximum order of $\mathbf{U}$ in the CV-DFT energy description. To understand how the order of the applied transition matrix, $\mathbf{U}$, affects the excited-state energies, it is beneficial to discuss two extreme cases—second ($n = 2$)-order and infinite ($n = \infty$)-order CV-DFT.

The second-order CV-DFT (CV(2)-DFT) limits the $\mathbf{U}$ up to the second order in the Kohn-Sham energy description. For simplicity, the occupied excited-state orbitals in Eq. (4) are approximated to the second order in $\mathbf{U}$:

$$\phi_i' = \phi_i + \sum_a^{n_{vir}} U_{ai}\phi_a - \frac{1}{2}\sum_j^{n_{occ}}\sum_a^{n_{vir}} U_{ai}U_{aj}\phi_j + O\left[U^{(3)}\right] . \tag{11}$$

With these orbitals, some higher order contributions in **U** can arise in the density and therewith also in the energy, but we only keep up to the second order in **U**, as the contribution of higher order terms is negligible [60]. The second-order CV-DFT energy expression becomes

$$\begin{aligned} E_{KS}[\rho'(1,1')] &= E_{KS}\left[\rho^0\right] + \sum_{ai} U_{ai}U_{ai}^*\left(\varepsilon_a^0 - \varepsilon_i^0\right) + \sum_{ai} U_{ai}U_{bj}^* K_{ai,bj} \\ &+ \frac{1}{2}\sum_{ai}\sum_{bj} U_{ai}U_{bj}K_{ai,jb} + \frac{1}{2}\sum_{ai}\sum_{bj} U_{ai}^* U_{bj}^* K_{ai,jb} + O\left[U^{(3)}\right] \end{aligned} \tag{12}$$

where the two-electron integral is composed of a Coulomb and an exchange-correlation part:

$$K_{pq,st} = K_{pq,st}^C + K_{pq,st}^{XC} \tag{13}$$

with

$$K_{pq,st}^C = \int\int \psi_p(1)\psi_q(1)\frac{1}{r_{12}}\psi_s(2)\psi_t(2)dv_1 dv_2. \tag{14}$$

The exchange-correlation integral is further decomposed into the local (KS) and nonlocal (HF):

$$K_{pq,st}^{XC(KS)} = \int \psi_p(r_1)\psi_q(r_1)f(r_1)\psi_s(r_1)\psi_t(r_1)dr_1 \tag{15}$$

and

$$K_{pq,st}^{XC(HF)} = -\int\int \psi_p(1)\psi_q(1)\frac{1}{r_{12}}\psi_s(2)\psi_t(2)dv_1 dv_2 \tag{16}$$

where $f(r_1)$ represents the regular energy kernel. We have shown that CV(2)-DFT is equivalent to TD-DFT [59, 106] within the Tamm-Dancoff approximation (TDA) [107].

In the infinite-order theory (CV(∞)-DFT), the new set of excited-state orbitals is obtained taking the sum in Eq. (3) to infinite order. These excited-state orbitals can be written in the convenient form of natural transition orbitals (NTO) [108]. For this, we decompose the transition matrix, **U**, into its singular values. Here, we also used a spin-adapted form for further description of the different spin states in the excited-state calculation:

$$\mathbf{U}^{\sigma\alpha} = \mathbf{V}^{\sigma\sigma}\Sigma(\mathbf{W}^{\alpha\alpha})^T \tag{17}$$

where $\Sigma_{ii} = \gamma_i$ and $\sigma \in \{\alpha,\beta\}$ depend on spin state (mixed and triplet states, respectively). This leads to the occupied and virtual NTOs as

$$\phi_i^{o_\alpha} = \sum_{j}^{n_{\mathrm{occ}}} (\mathbf{W}^{\alpha\alpha})_{ji}\phi_j^\alpha \tag{18}$$

$$\phi_i^{v_\sigma} = \sum_{a}^{n_{\mathrm{vir}}} (\mathbf{V}^{\sigma\sigma})_{ai}\phi_a^\sigma. \tag{19}$$

The resulting matrix $\mathbf{W}$ rotates ground-state KS orbitals as j runs over the occupied ground-state orbitals to give the corresponding ith 'occupied' NTO orbital ($\phi_i^{o_\alpha}$). For its virtual counterpart ($\phi_i^{v_\sigma}$), $\mathbf{V}$ does the similar role as $\mathbf{W}$ with a running over the virtual ground-state orbitals. With these NTOs, we can rewrite Eq. (4) for the 'occupied' excited-state orbitals as

$$\phi_i^{'} = \cos[\gamma_i]\phi_i^{o_\alpha} + \sin[\gamma_i]\phi_i^{v_\sigma}. \tag{20}$$

Also, the condition of exciting exactly one electron (Eq. (9)) is now written as

$$\sum_{i}^{n_{\mathrm{occ}}} \sin(\eta\gamma_i)^2 = 1. \tag{21}$$

With the sum rule in Eq. (10), the excited-state CV(∞)-DFT energy of the mixed state becomes

$$\Delta E_M = \sum_{i}^{n_{\mathrm{occ}}} \sin^2[\eta\gamma_i]\left(\varepsilon_i^{v_\alpha} - \varepsilon_i^{o_\alpha}\right)$$

$$+ \frac{1}{2}\sum_{i}^{n_{\mathrm{occ}}}\sum_{j}^{n_{\mathrm{occ}}} \sin^2[\eta\gamma_i]\sin^2[\eta\gamma_j]\left(K_{i^{o_\alpha} i^{o_\alpha} j^{o_\alpha} j^{o_\alpha}} K_{i^{v_\alpha} i^{o_\alpha} j^{o_\alpha} j^{v_\alpha}} - 2K_{i^{o_\alpha} i^{o_\alpha} j^{o_\alpha} j^{v_\alpha}}\right)$$

$$+ \frac{1}{2}\sum_{i}^{n_{\mathrm{occ}}}\sum_{j}^{n_{\mathrm{occ}}} \sin[\eta\gamma_i]\cos[\eta\gamma_i]\sin[\eta\gamma_j]\cos[\eta\gamma_j]\left(K_{i^{o_\alpha} i^{v_\alpha} j^{o_\alpha} j^{v_\alpha}} + K_{i^{o_\alpha} i^{v_\alpha} j^{v_\alpha} j^{o_\alpha}}\right)$$

$$+ 2\sum_{i}^{n_{\mathrm{occ}}}\sum_{j}^{n_{\mathrm{occ}}} \sin[\eta\gamma_i]\sin[\eta\gamma_i]\sin[\eta\gamma_j]\cos[\eta\gamma_j]\left(K_{i^{v_\alpha} i^{v_\alpha} j^{o_\alpha} j^{v_\alpha}} - K_{i^{o_\alpha} i^{o_\alpha} j^{o_\alpha} j^{v_\alpha}}\right) \tag{22}$$

whereas the triplet exited-state energy has a simpler form:

$$\Delta E_T = \sum_{i}^{n_{\mathrm{occ}}} \sin^2[\eta\gamma_i]\left(\varepsilon_i^{v_\beta} - \varepsilon_i^{o_\alpha}\right)$$

$$+ \frac{1}{2}\sum_{i}^{n_{\mathrm{occ}}}\sum_{j}^{n_{\mathrm{occ}}} \sin^2[\eta\gamma_i]\sin^2[\eta\gamma_j]\left(K_{i^{o_\alpha} i^{o_\alpha} j^{o_\alpha} j^{o_\alpha}} K_{i^{v_\beta} i^{v_\beta} j^{v_\beta} j^{v_\beta}} - 2K_{i^{o_\alpha} i^{o_\alpha} j^{v_\beta} j^{v_\beta}}\right) \tag{23}$$

The γ values out of Eq. (21) give information about the excitation character [60]. Keeping only the largest γ value in the excitation will give the most general form of single orbital

replacement [104], which is used as the ΔSCF-DFT-like scheme within the RSCF-CV(∞)-DFT formulation. This will be briefly mentioned in the next section.

2.3. SCF-CV(∞)-DFT, R-CV(∞)-DFT and RSCF-CV(∞)-DFT

In Eqs. (22, 23), we obtain the excited-state energy of the mixed and triplet state. The transition matrix, $\mathbf{U}$, is the same as one obtains within TD-DFT (and thus the TD-DFT excitation vector is implemented in CV-DFT). In SCF-CV(∞)-DFT, $\mathbf{U}$ is optimized with the variational procedure [60]. For this step, we derived the gradient of the mixed and triplet excited state. The detailed procedures can be found in the [59–61, 104]. Further, also the orbitals which do not participate in the excitation can be changed after the excitation. We refer to this change as the relaxation of orbitals. This leads to R-CV(∞)-DFT. To account for this orbital relaxation effect, we introduced $\mathbf{R}$, which is orthogonal to $\mathbf{U}$, and apply it on the orbitals from Eq. (4). Therewith, the 'occupied' and 'virtual' orbitals become

$$\psi_i(1) = \phi_i(1) + \sum_c^{n_{\mathrm{vir}}} R_{ci}\phi_c(1) - \frac{1}{2}\sum_c^{n_{\mathrm{vir}}}\sum_k^{n_{\mathrm{occ}}} R_{ci}R_{ck}\phi_k(1) \tag{24}$$

$$\psi_a(1) = \phi_a(1) - \sum_k^{n_{\mathrm{occ}}} R_{ak}\phi_k(1) - \frac{1}{2}\sum_c^{n_{\mathrm{vir}}}\sum_k^{n_{\mathrm{occ}}} R_{ak}R_{ck}\phi_c(1). \tag{25}$$

It is possible to combine the approach of the variational optimization of the transition matrix and orbital relaxation, meaning the variational optimization of $\mathbf{U}$ and $\mathbf{R}$, resulting in the most general form of CV-DFT (RSCF-CV(∞)-DFT). The excitation energy expression of RSCF-CV(∞)-DFT can be written for the mixed and triplet state, respectively:

$$\Delta E_M = E_M^{\mathbf{U},\mathbf{R}}\left[\rho_0^\alpha + \frac{1}{2}\Delta\rho_M^{\mathbf{U},\mathbf{R}}, \rho_0^\beta + \frac{1}{2}\Delta\rho_M^{\mathbf{U},\mathbf{R}}\right] - E\left[\rho_0^\alpha, \rho_0^\beta\right]$$

$$= \int F_{KS}\left[\rho_0^\alpha + \frac{1}{2}\Delta\rho_M^{\mathbf{U},\mathbf{R}}, \rho_0^\beta + \frac{1}{2}\Delta\rho_M^{\mathbf{U},\mathbf{R}}\right]\Delta\rho_M^{\mathbf{U},\mathbf{R}}dv_1 \tag{26}$$

$$\Delta E_T = E_T^{\mathbf{U},\mathbf{R}}\left[\rho_0^\alpha + \frac{1}{2}\Delta\rho_T^{\mathbf{U},\mathbf{R}}, \rho_0^\beta + \frac{1}{2}\Delta\rho_T^{\mathbf{U},\mathbf{R}}\right] - E\left[\rho_0^\alpha, \rho_0^\beta\right]$$

$$= \int F_{KS}\left[\rho_0^\alpha + \frac{1}{2}\Delta\rho_T^{\mathbf{U},\mathbf{R}}, \rho_0^\beta + \frac{1}{2}\Delta\rho_T^{\mathbf{U},\mathbf{R}}\right]\Delta\rho_T^{\mathbf{U},\mathbf{R}}dv_1 \tag{27}$$

where ρ_0^α and ρ_0^β are the ground-state density and $\Delta\rho^{\mathbf{U},\mathbf{R}}$ indicates the excited-state density changes including relaxation effect. The F_{KS} is the Kohn-Sham Fock operator.

Another idea is to restrict the transition matrix, $\mathbf{U}$, in CV-DFT to the case of single NTO excitations, that is, Eq. (17) is approximated to include only one major excitation in the transition matrix. Three different forms of such restrictions on $\mathbf{U}$ were shown and discussed in the previous work [104], which referred to as SOR-R-CV(∞)-DFT, COL-RSCF-CV(∞)-DFT

	Transition U			Relaxation R		Introduced	
	Order n	Optimization	Restrictions	Order	Optimization	Singlets	Triplets
CV(2)-DFT	Second	No	No	N/A	No	T [58], I [109]	T [60], I [110]
CV(4)-DFT	Fourth	No	No	N/A	No	T [93], I [109]	T [109], I [109]
CV(∞)-DFT	∞	No	No	N/A	No	T [59], I [111]	T [60], I [60]
SCF-CV(∞)-DFT	∞	Yes	No	N/A	No	T [59], I [60]	T [60], I [104]
RSCF-CV(∞)-DFT	∞	Yes	No	Second	Yes	T [61], I [61]	T [61], I [104]
SOR-R-CV(∞)-DFT	∞	No	$U_{ai} = \delta_{ab}\delta_{ij}$	Second	Yes	T [62]	T [62], I [62]
COL-RSCF-CV(∞)-DFT	∞	Yes	$U_{ai} = \delta_{ij}$	Second	Yes	T [104]	T [104], I [104]
SVD-RSCF-CV(∞)-DFT	∞	Yes	$\gamma_1 = 1$	Second	Yes	T [104]	T [104], I [104]

'T' indicates that it is introduced theoretically.
'I' indicates that it is implemented into the code.

Table 1. Variation of CV-DFT applied.

and SVD-RSCF-CV(∞)-DFT. Among the three methods, we have shown that SVD-RSCF-CV (∞)-DFT as rank 1 approximation is the most general form for such a single NTO excitation:

$$\mathbf{U} = v_1^{\sigma\sigma}\left(w_1^{\alpha\alpha}\right)^{\mathrm{T}} \qquad (28)$$

where the $v_1^{\sigma\sigma}$ and $w_1^{\alpha\alpha}$ are the vector of the largest singular value $\mathbf{V}^{\sigma\sigma}$ and $\mathbf{W}^{\alpha\alpha}$ out of Eq. (17). The SVD-RSCF-CV(∞)-DFT was also shown to give the same excitation energies as ΔSCF-DFT within 0.1 eV [104].

As a roundup we list the current different versions of CV-DFT in **Table 1**.

3. Applications

In this section, we will show examples of excitations where different versions of CV-DFT have been applied successfully. These excitations are of Rydberg type or possess a dominant charge-transfer character; the work has been published in [99–103]. We would like to note that all CV-DFT-calculations presented here were carried out with developers versions of ADF [112, 113] and we refer to the original publications for the technical details.

3.1. Rydberg excitations

It is well understood that the success of TD-DFT directly depends on how well the approximate exchange-correlation density functional used describes the potential ($\widehat{V}_{XC}^{\mathrm{KS}}(\vec{r})$). Further, it is evident that functionals based on the local density approximation (LDA) or the generalized gradient approximation (GGA) result in the potential, $\tilde{V}_{XC}^{\mathrm{KS}}(\vec{r})$, that is insufficiently stabilizing

when compared to $\widehat{V}_{XC}^{\text{KS}}(\vec{r})$ from an exact functional derived from high-level wave function theory [71–74]. This results in higher occupied orbital ($\tilde{\varepsilon}_i$) and virtual orbital ($\tilde{\varepsilon}_a$) energies obtained with $\tilde{V}_{XC}^{\text{KS}}(\vec{r})$ as opposed to those (($\widehat{\varepsilon}_i$),($\widehat{\varepsilon}_a$)) derived from $\widehat{V}_{XC}^{\text{KS}}(\vec{r})$. Additionally, the weakness of $\tilde{V}_{XC}^{\text{KS}}(\vec{r})$ becomes apparent at medium and large separations r from the polyatomic center of mass where it decays exponentially with r, while $\widehat{V}_{XC}^{\text{KS}}(\vec{r})$ decays as $\sim -1/r$.

Excitation energies in TD-DFT are not necessarily affected by the instability of $\tilde{V}_{XC}^{\text{KS}}(\vec{r})$ for medium to large values of r in the valence region and in the density tail. This is primarily due to the dependence of the excitation energies in TD-DFT to the difference $\tilde{\varepsilon}_a - \tilde{\varepsilon}_i$. As can be noted, the large errors in the individual orbital energies might be canceled after the energy difference is calculated provided that the average potential experienced by ψ_i and ψ_a shows similar deviations from $\widehat{V}_{XC}^{\text{KS}}(\vec{r})$. Resultantly, the success of TD-DFT for valence excitations is attributable to this phenomenon for transitions $\psi_i \rightarrow \psi_a$ where the overlap S_{ia} between the two densities ρ^i and ρ^a is large [92, 114]. However, for cases such as Rydberg transitions [71–74] as well as charge-transfer excitations [77, 79, 82, 90, 96, 97, 115] where S_{ia} is small, the error in $\tilde{V}_{XC}^{\text{KS}}(\vec{r})$ gets more pronounced. It is a common practice in the case of small S_{ia} to construct specialized potentials [71–74, 77, 79, 82, 90–98] in which the proper $-1/r$ decay is enforced yielding acceptable results. The disadvantage here is that these parameterized potentials might yield inaccurate results for transitions in which $S_{ia} >> 0$.

Since Rydberg transitions are characterized by a single orbital replacement $\psi_v \rightarrow \psi_r$, RSCF-CV($\infty$)-DFT will give results very similar to ΔSCF-DFT; this similarity in case of a single NTO transition has been demonstrated in [104]. Although for ΔSCF-DFT, states of the same symmetry as the ground-state almost always decompose to the ground-state, this weakness is absent in RSCF-CV(∞)-DFT. The RSCF-CV(∞)-DFT triplet and singlet transition energies for these single orbital replacement-type excitations are obtained as special case of Eqs. (26) and (27), with the singlet excitation energy given as $2\Delta E_M - \Delta E_T$. In the analysis of Rydberg excitations based on RSCF-CV(∞)-DFT, the excitation energy is considered as a sum of the ionization potential (IP) of a neutral species, A, and the electron affinity (EA) of the resulting cation, A^+, after ionization: $\Delta E(\phi_v \rightarrow \phi_r) = \text{EA}(A^+, \phi_v, \phi_r) + \text{IP}(A, \phi_v)$. Thus, errors in the excitation energies are due to error in the calculated EAs and IPs. Consequently, a method or 'specialized' *XC* functional that provide accurate EAs and IPs would in turn afford accurate Rydberg excitation energies [100].

Shown in **Table 2** for comparison with the experimental data are the IPs (N_2) and EAs (N_2^+) calculated by RSCF-CV(∞)-DFT (or ΔSCF-DFT). The near-perfect agreement (RMSDs between 0.1 and 0.3 eV) with the experimental data is transferred to the excitation energies afforded by the RSCF-CV(∞)-DFT method. As noted previously by Verma and Bartlett for functionals used within TD-DFT [118–120] and the authors of the work discussed here [100]. A test set including 73 excitations (32 singlet, 41 triplet) from nine different species (N_2, 5; CO, 7; CH_2O, 8; C_2H_2, 8; H_2O, 10; C_2H_4, 13; Be, 6; Mg, 6; Zn, 10) has been used. Broken down into the different species, the results are given in **Table 3** in terms of mean absolute error (MAE) and root-mean-square deviation (RMSD).

Energy term	LDA	BP86	B3LYP	LCBP86*[c]	LCBP86[d]	Expt.
IP(N_2, σ_g)	15.63	15.50	15.74	15.96	16.38	15.58[e,f]
IP(N_2, π_u)	17.46	17.07	16.87	17.22	17.18	17.07[f]
EA(N_2^+, σ_g, $3s\sigma_g$, S)	−3.64	−3.61	−3.49	−3.55	−3.44	−3.38[g]
EA(N_2^+, σ_g, $3p\pi_u$, S)	−2.92	−3.01	−2.87	−2.81	−2.77	−2.68[g]
EA(N_2^+, σ_g, $3p\sigma_u$, S)	−2.84	−2.95	−2.79	−2.71	−2.66	−2.60[g]
EA(N_2^+, π_u, $3s\sigma_g$, S)	−3.77	−3.77	−3.71	−3.73	−3.67	−3.83[g]
EA(N_2^+, σ_g, $3s\sigma_g$, T)	−3.82	−3.81	−3.73	−3.79	−3.72	−3.58[h]

[a]Energies in eV.
[b][72].
[c]Refers to LC functional combined with BP86 and $\omega = 0.40$.
[d]Represents LC functional combined with BP86 and $\omega = 0.75$.
[e][116].
[f][117].
[g]Evaluated as EA(A^+, ϕ_v, ϕ_r, S) = $\Delta E_S(\phi_v \rightarrow \phi_r) -$ IP(A, ϕ_v).
[h]Evaluated as EA(A^+, ϕ_v, ϕ_r, T) = $\Delta E_T(\phi_v \rightarrow \phi_r) -$ IP(A, ϕ_v).
Data represented in this table was first published in [100].

Table 2. IP[a] of N_2 and EA[a] of N_2^+ calculated with ΔSCF using an extended basis set[b] and five different functionals.

Species	No. of states	LDA	BP86	B3LYP	LCBP86*[c]	LCBP86[d]
N_2	5	0.27	0.34	0.05	0.23	0.62
CO	7	0.22	0.43	0.13	0.12	0.37
CH_2O	8	0.21	0.28	0.12	0.20	0.34
C_2H_2	8	0.31	0.50	0.52	0.25	0.24
H_2O	10	0.27	0.17	0.14	0.21	0.24
C_2H_4	13	0.15	0.20	0.28[e]	0.28	0.29
Be	6	0.45	0.60	0.47	0.31	0.23
Mg	6	0.18	0.35	0.19	0.13	0.12
Zn	10	0.18	0.25	0.27	0.34	0.46
RMSD	—	0.24	0.32	0.24	0.23	0.32

[a]Energies in eV.
[b][72].
[c]Refers to LC functional combined with BP86 and $\omega = 0.40$.
[d]Represents LC functional combined with BP86 and $\omega = 0.75$.
[e]Comprising 12 states.
Data represented in this table was first published in [100].

Table 3. Summary of RMSDs of Rydberg excitation energies[a] calculated with ΔSCF using an extended basis set[b] and five different functionals.

The results in **Table 3** for RSCF-CV(∞)-DFT (or ΔSCF-DFT) are in general better than TD-DFT with the same functionals but at par with TD-DFT results with 'specialized' functionals [71–74].

With this benchmark the suitability of RSCF-CV(∞)-DFT without the need for sophisticated (or 'specialized') functionals for Rydberg excitations has been demonstrated. The origin of this good performance is attributable to the ability of RSCF-CV(∞)-DFT to afford good estimates of IPs and EAs for all functionals [100, 121, 122]. Admittedly, fortuitous error cancelation in IPs and EAs obtained for both RSCF-CV(∞)-DFT and TD-DFT plays a role in the accuracy of the resultant excitation energies.

3.2. Charge-transfer excitations

In this subsection we will have a look at excitations with charge-transfer character.

It is well known that TD-DFT applied with standard local exchange and correlation functionals has difficulties for transitions with charge-transfer character between two spatially separated regions [82, 91, 109], a finding nicely explained by Drew, Weisman and Head-Gordon [114]. According to several authors, the reason lies in the exchange and correlation functional [79, 82, 91, 123, 124]. Indeed, a functional like CAM-B3LYP [125] includes a certain Hartree-Fock exchange and results in a clear improvement of TD-DFT excitation energies for transitions involving a charge-transfer character [79, 124, 126]. To further improve the asymptote of the exchange-correlation potential, long-range corrected hybrid scheme like the ones proposed in [76, 95, 98, 127] and asymptotically corrected model potential scheme like in [128, 129] have been designed. Of course modifying the functional is not the only approach, and it is not surprising also that other DFT-based approaches have been suggested, all having their own assets and drawbacks. Several of them have been applied for excitations involving charge-transfer character, for example, constrained orthogonality method (COM) [49, 50], maximum overlap method (MOM) [56], constricted variational density functional theory (CV-DFT) [58] and its extensions [104, 105], constrained density functional theory [130], self-consistent field DFT (ΔSCF-DFT) [131], orthogonality constrained DFT (OCDFT) [63], ensemble DFT [132, 133] and subsystem DFT (FDE-ET) [134].

Ziegler *et al.* showed in [115] how the theoretical framework of CV-DFT is able to cope with excitations including a charge-transfer character and demonstrated this capability with different applications [102, 109, 121]. Here, we will have a look at examples out of three of these mentioned types.

3.2.1. $C_2H_4xC_2F_4$: long-range charge-transfer excitations

Ethylene tetrafluoroethylene, $C_2H_4xC_2F_4$, is a system well studied in literature [76, 91, 93, 114, 126, 134]. It allows for the study of the dependence of excitation energies on the separation of the donor and acceptor and test for the expected $-1/R$ behavior.

For the system $C_2H_4xC_2F_4$, two transitions are of particular interest, the excitations HOMO → LUMO and HOMO-1 → LUMO + 1, both resulting in an excited state of b_1 symmetry. With these transitions, a charge is transferred between the two molecules C_2H_4 and C_2F_4. Although the concrete orbital localization is highly functional dependent, the orbitals HOMO-1, HOMO,
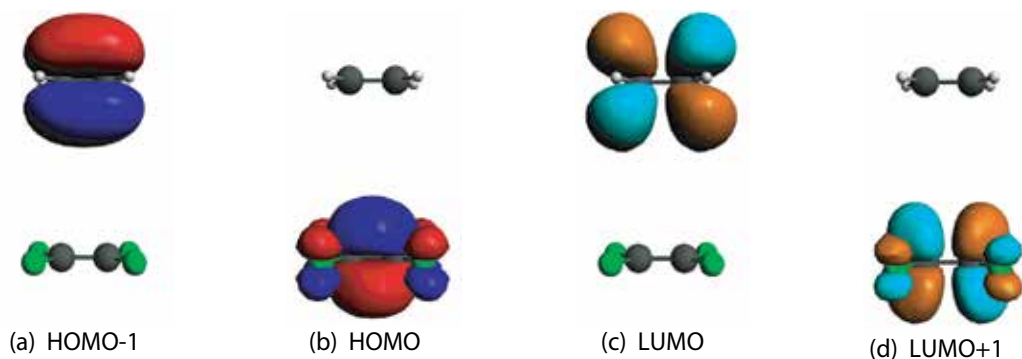
(a) HOMO-1   (b) HOMO   (c) LUMO   (d) LUMO+1

Figure 1. $C_2H_4xC_2F_4$: Representation of ground-state KS orbitals (LDA) ($R = 5.0$ Å) (reprinted from [102], with the permission of AIP Publishing).

LUMO and LUMO + 1 are from certain separation distance, dominantly located on one of the fragments, as visible in **Figure 1** (see, e.g., [77, 102]). It should be noted that for a classification to one of the aforementioned types, it is sufficient when the mentioned ground-state orbitals contribute the most, not necessarily uniquely.

The results obtained with CV-DFT and selected reference values for comparison are shown in **Figure 2**.

First, consideration will be given to the singlet and triplet excitation results with different versions of CV-DFT, where the transition matrix, **U**, is not optimized, before turning to the most general form RSCF-CV(∞)-DFT.

CV(∞)-DFT results in a $-1/R$-like behavior, or when assuming a $\Delta E(R) = -c_1/R + c_0$ function, fitting coefficients c_1 for the results presented in **Figure 2** of 1.1 and 0.9 $E_h a_0$ are obtained. For

(a) HOMO $\rightarrow$ LUMO   (b) HOMO-1 $\rightarrow$ LUMO+1
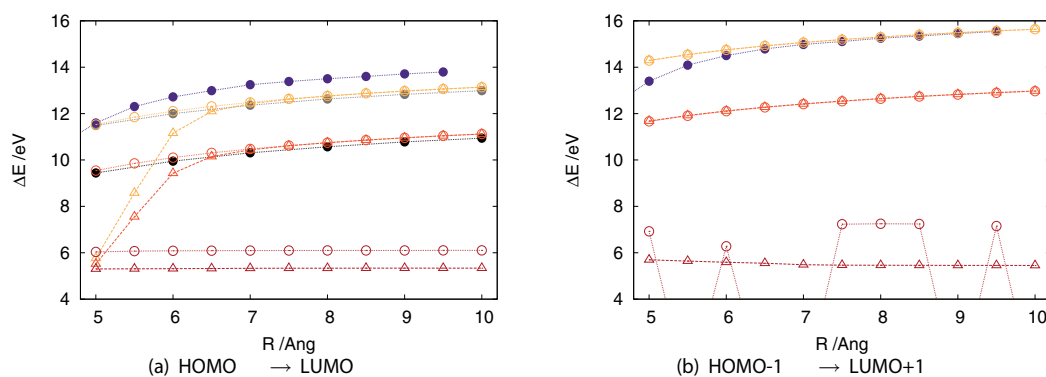
Figure 2. $C_2H_4xC_2F_4$ vertical excitation energies for singlets (circles) and triplets (triangles) using CV(∞)-DFT (orange), R-CV(∞)-DFT (red) and RSCF-CV(∞)-DFT (dark red). The values for the revised hessian out of [96] (purple-filled circles), LC-BLYP out of [76] (black-filled circles) and SAC-CI out of [76] (gray-filled circles) are given as reference. The lines serve as a guide for the eyes, and when the excitation is not dominated by one of the charge-transfer excitations, we set its value to zero (and are therewith not visible in the figure). (reprinted from Senn F, Park YC. The Journal of Chemical Physics. 2016;**145**(24):244108-1 – 10). DOI: 10.1063/1.4972231. with the permission of AIP Publishing. Color specifications refer to the original figure).

these excitations, similar energies are reported using the revised Hessian in [93]. In R-CV(∞)-DFT [61], relaxation of orbitals not directly participating is allowed (see Section 2.3), and it is of no surprise that excitation energies decrease. These results still correspond to a $-1/R$ behavior (resulting in fitting coefficients c_1 for the values presented in **Figure 2** of 1.1 and 0.9 $E_h a_0$). For the HOMO $\rightarrow$ LUMO transition, the values agree with those reported in [76] using LC-BLYP (MAD = 0.2 eV, RMSD = 0.2 eV). Thus, the extrapolated infinite separation value, $\Delta E_{R\rightarrow\infty} = 12.7$ eV, is close to the $\Delta E_{R\rightarrow\infty} = 12.5$ eV reported in [76].

Turning next to the triplet excitations for both CV(∞)-DFT and R-CV(∞)-DFT, similar findings are obtained. At longer distances, no spin interaction is expected; as envisioned the triplet excitation energies match values obtained for the corresponding singlet excitation. Excluding the HOMO $\rightarrow$ LUMO triplet excitations with $R < 6$ Å, a nice $-1/R$ behavior is obtained.

Until now all the applied methods have one thing in common: the transition matrix **U** has not been optimized. This means the character of the transition itself has not been changed. With CV-DFT being a variational method, the transition matrix **U** can be optimized with the aim of minimizing the energy (see Section 2.3). In this case the RSCF-CV(∞)-DFT method [59–61] is applied, whose strength and merits have been demonstrated several times [100, 104, 121]. From **Figure 2**, it can clearly be seen that RSCF-CV(∞)-DFT minimizes the excitation energy at the expense of nearly distance-independent excitation energies and the loss of the $-1/R$ long-range dependence. This energy gain stems from the optimization of the transition matrix **U**; a thorough explanation is given in [102]. In summary, the charge-transfer transitions, HOMO $\rightarrow$ LUMO and HOMO-1 $\rightarrow$ LUMO + 1, are dominated by single NTO transitions. Optimizing the transition matrix results in a mix of (mainly) two NTO transitions with (at least one) different participating fragments, meaning that the two charge-transfer excitations, clearly separated before, do mix now. This mixing of the two different excitations leads to a smaller destabilization and a larger stabilization, resulting in a clear reduction of the excitation energy [102]. An additional issue comes now from having a partial charge $c_A \in (0, 1)$ located on fragment A and a partial charge $1 - c_A$ on fragment B, even when these two fragments are further apart. Therefore, from a certain distance on this mixing should be suppressed. To block the optimization algorithm from mixing such unwanted excitations in RSCF-CV(∞)-DFT calculations, two different strategies have been proposed in [102]. But while working, they both depend highly on an arbitrarily chosen value for a threshold parameter. It remains to be seen, if a strategy without the need of such a parameter can be found for RSCF-CV(∞)-DFT.

3.2.2. Polyacenes: excitations with hidden charge-transfer character

The focus of this subchapter is on polyacenes, a system with an intramolecular charge-transfer-like character, also referred to as charge-transfer in disguise [135]. The polyacenes are understood as a number n_r of linearly fused benzene rings. Such linear polyacenes possess $\pi \rightarrow \pi^\star$ excitations L_a (or B_{2u} when the x-axis corresponds to the long molecular axis) and L_b (or B_{3u}) with distinct properties, described, for instance, in [136]. Additionally, these polyacenes have a singlet-triplet gap for which a function of n_r has been proposed. An extrapolation of this function gave rise to a discussion: if polyacenes with a certain size would have a triplet ground state [137–143].

Polyacenes and their derivatives have been used in a plethora of applications; an overview of some of these applications can be found in [144, 145]. Thus, it is not surprising that polyacenes and their excitation energies have been studied extensively. While high-level calculations exist, see, for example, the work presented in [140, 141, 143], considering the size of larger polyacenes TD-DFT calculations is more common. But the latter ones applied with standard functionals have several difficulties. This is why different methods and strategies have been used, each one having its advantages, and we refer to [101] and references therein for more details. Before moving on to the results obtained with CV-DFT, it must be noted that the polyradical character in the ground-state builds up with increasing number of fused acenes, which was deduced by Ibeji *et al.* [143] and was confirmed by Plasser *et al.* [146]. This polyradical character gets bigger and for polyacenes larger than hexacene even big enough to lead to a 'breakdown of single reference approximation used to describe the ground-state of polyacenes in conventional DFT' [132]. Within CV-DFT we rely on a DFT ground-state description. The awareness of this limitation is the reason why only polyacenes as large as hexacene have been studied with CV-DFT.

We will now have a look at the singlet excitation energies. As these energies are not directly measurable, we will use the modified experimental values from Grimme and Parac [136] as reference, for simplicity referred to as experimental results.

As visible from **Table 4** and **Figure 3**, CV(∞)-DFT with LDA results in vertical singlet excitation energies in a very good agreement with the experimental values [147], while for R-CV(∞)-DFT [101], the values deviate more from the experimental ones, although still in an acceptable agreement (a discussion of the difference is given in [101]). As can be seen from **Table 4** and **Figure 3**, both versions of CV-DFT obtain a crossover between 1^1B_{2u} and 1^1B_{3u} for Anthracene onwards, which is in agreement with experimental findings.

No. acene units	Exp.[a]			CV(∞)-DFT[b]			R-CV(∞)-DFT[c]		
	1^1B_{2u}	1^1B_{3u}	ΔE[d]	1^1B_{2u}	1^1B_{3u}	ΔE[d]	1^1B_{2u}	1^1B_{3u}	ΔE[d]
2	4.66	4.13	0.53	4.73	4.39	0.34	4.58	4.42	0.16
3	3.60	3.64	−0.04	3.68	3.73	−0.05	3.46	3.75	−0.29
4	2.88	3.39	−0.51	2.91	3.32	−0.41	2.69	3.33	−0.63
5	2.37	3.12	−0.75	2.35	3.03	−0.68	2.15	3.04	−0.89
6	2.02	2.87	−0.85	1.93	2.82	−0.89	1.74	2.83	−1.09
MAD	—	—	—	0.06	0.11	—	0.18	0.12	
RMSD	—	—	—	0.06	0.13	—	0.19	0.15	

a Out of [136].
b Out of [147].
c Out of [101].
d $\Delta E = \Delta E(1^1B_{2u}) - \Delta E(1^1B_{3u})$.

Table 4. Vertical singlet excitation energies (in eV) for linear polyacenes.
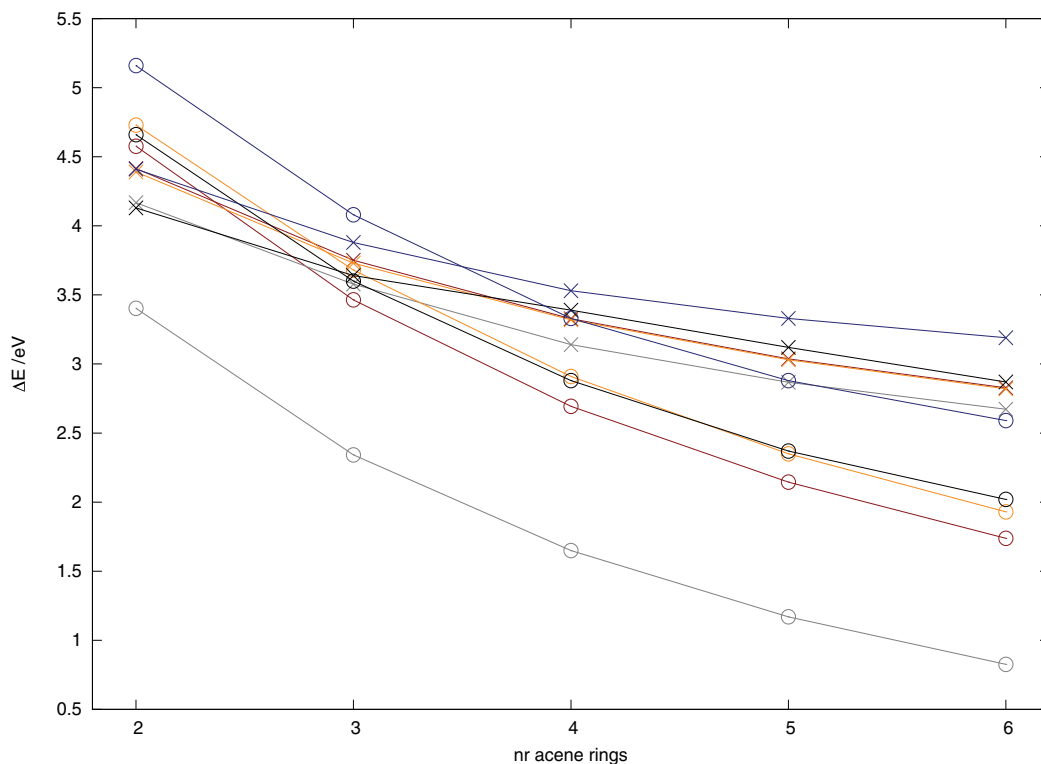
Figure 3. Vertical singlet excitation energies for the states 1^1B_{2u} (circles) and 1^1B_{3u} (crosses) of linear polyacenes: R-CV(∞)-DFT (maroon), ΔSCF-DFT (gray), CV-DFT (orange, out of [147]), [143] (dark blue), experimental values (black, out of [136]). The solid lines serve as guides for the eyes. (reprinted with permission from Senn F, Krykunov M. The Journal of Physical Chemistry. A. 2015;**119**(42):10575-10581. DOI: 10.1021/acs.jpca.5b07075. Copyright 2015 American Chemical Society. Color specifications refer to the original figure).

Next, take a look at the obtained triplet excitation energies for the studied polyacenes, shown in **Table 5**. The equivalency of CV(2)-DFT and TD-DFT with the TDA stated in theory section (Section 2.2) is once again confirmed by the numbers in **Table 5**. It can also be seen that in the triplet case, the energies obtained with R-CV(∞)-DFT change only slightly in comparison with the values obtained with CV(2)-DFT, on average by 0.05 eV (for comparison, singlet excitations have a MAD of 0.30 eV for 1^1B_{2u} and 0.13 eV for 1^1B_{3u}, values out of [101, 147]). This surprisingly small difference is due to the nature of the excitation, and for a further discussion of the contributions, we refer to [101].

As previously pointed out in [104], R-CV(∞)-DFT results in triplet states of excitation energies being lower than the ones obtained by coupled cluster methods. Nevertheless, with a RMSD of 0.31 and 0.29 eV, respectively, when compared to the values given in [140 and 143], the results are in reasonable agreement (we note that coordinates were optimized slightly differently). The nature of the triplet excited states is in agreements with the findings of [148], namely, a 1^3B_{2u} state for the first triplet excitation, T_1; for the second triplet excitation, T_2; $^3B_{3u}$ for Naphthalene; and $^3B_{1g}$ for Anthracene to Hexacene.

No. acene units	Vertical					Adiabatic		
	R-CV(∞)-DFT[a]	CV(2)-DFT[a]	TDDFT[b]	Ref. [143]	Ref. [140]	R-CV(∞)-DFT[a]	Exp.[c]	Ref. [143]
2	3.16	3.08	3.08	3.34	3.31	2.89	2.64	2.70
3	2.15	2.09	2.09	2.47	2.47	1.94	1.86	2.06
4	1.49	1.44	1.44	1.82	1.76	1.31	1.27	1.48
5	1.02	0.99	0.99	1.37	1.37	0.88	0.86	1.11
6	0.69	0.66	0.66	1.07	1.00	0.57	0.54	0.83
MAD[d]	—	0.05	0.05	0.31	0.28	—	0.09	0.19
RMSD[d]	—	0.06	0.06	0.32	0.29	—	0.12	0.20

a Out of [101].
b With LDA as functional.
c Out of [143] and references therein.
d To be understood as the deviation of the values obtained with R-CV(∞)-DFT in comparison to the values of this column as reference values.

Table 5. Vertical and adiabatic triplet excitation energies (in eV) for linear polyacenes.

From **Figure 4** one can see the singlet-triplet gap (ST) decreasing, resembling an exponential function. In order to estimate the ST gap for infinitely large polyacenes, giving an indication if there would be a ST crossover, several authors fitted the excitation energies to the function $f(n_r) = a\exp(-bn_r) + c$ (see [140, 142, 143]). With the results of R-CV(∞)-DFT for the vertical transition, the limes of an infinitely long polyacene $E_{vert}^{ST}(n_r \rightarrow \infty) = (0.3 \pm 4.5)$ kcal mol^{-1} have been obtained and for the 'adiabatic' transition $E_{ad}^{ST}(n_r \rightarrow \infty) = (-1.6 \pm 4.0)$ kcal mol^{-1} [101]. For the 'adiabatic' or well-to-well excitations, results from different methods in literature are controversial about a possible ST gap crossover ([140, 142] versus [143, 149, 150]); for TD-DFT it even depends on the functional used [142]. Therefore, necessarily the findings presented here will agree with some findings, while disagree with others. It should be noted that these energies are very small, actually smaller than the estimated accuracy of the CV-DFT method, and with its error it must be regarded as giving only a tendency for no ST crossover. Two additional points of precaution which puts the value of the extrapolated results into question: (a) it has been shown in [142] how a small change of a single excitation energy can influence the obtained polymeric limit, and (b) one should have in mind the change of the ground-state character with the polyacene length and, thus, the number of fused acenes.

3.2.3. Charge-transfer excitations in transition metals

The complicated electronic structure of transition metal (TM) complexes [151] makes them ideal for testing the performance of newly developed methods. This section deals with charge-transfer (and hidden charge-transfer) excitations in these complexes, more precisely the 3d complexes MnO_4^-, CrO_4^{2-} and VO_4^{3-}, as well as their 4d congeners RuO_4, TcO_4^-, MoO_4^{2-} and 5d homologues OsO_4, ReO_4^- and WO_4^{2-} [99]. For these systems, the three lowest valence excitations involving transitions from $1t_1$, $2t_2$ to $2e$ and $3t_2$ are considered [99]. The comparison is
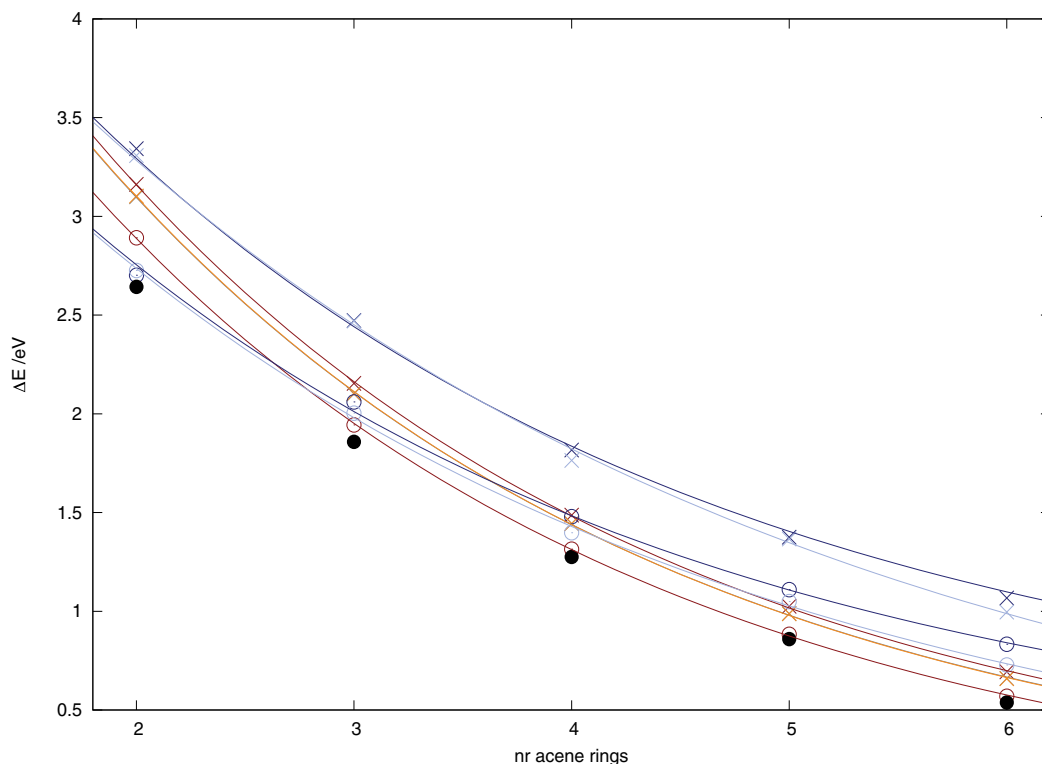
Figure 4. Triplet excitation energies for the 1^3B_{2u} states of linear polyacenes: R-CV(∞)-DFT (maroon), ΔSCF-DFT (gray), SVD-R-CV(∞)-DFT (orange), [143] (dark blue), [140] (light blue), experimental values (black, out of [143] and references therein). The symbols are used to distinguish between vertical transitions (crosses) and adiabatic as well as 'imitated adiabatic' transitions (circles). The lines are the curves fitted to the function $f(n_r) = a \exp(-b\,n_r) + c$ and serve as guides for the eyes. (reprinted with permission from Senn F, Krykunov M. The Journal of Physical Chemistry. A. 2015;**119**(42):10575-10581. DOI: 10.1021/acs.jpca.5b07075. Copyright 2015 American Chemical Society. Color specifications refer to the original figure).

made with available experimental data [152, 153] and high-level *ab initio* calculations [154–160]. There are several adjustable parameters that can influence the excitation energies. These include the size of the basis set used, functionals used, geometry (optimized structures or experimental geometries), medium (since the complexes are anions), etc. Use was made of experimental structures which lead to higher excitation energies (0.1–0.3 eV) compared to optimized structures. Marginal influence of solvation was found for the three valence excitations; the calculated COSMO [161, 162] excitation energies lower the energies by 0.01–0.02 eV [163, 164].

Table 6 displays the RMSD between the first three experimental dipole-allowed transitions and the corresponding values calculated by RSCF-CV(∞)-DFT.

On average, the three functionals B3LYP, PBE0 with an intermediate fraction of HF exchange and LCBP86* have the lowest RMSD of 0.2 eV, whereas the local functionals (LDA, BP86, BPE) and BHLYP with the highest HF fraction and LCBP86 have a somewhat larger RMSD of 0.3 eV for both 3d and 4d + 5d averages. TD-DFT with the same functionals performs poorly for the 3d complexes but shows good agreement with experiment for the heavier tetraoxo complexes.

Complex	LDA	BP86	PBE	B3LYP	BHLYP	PBE0	LCBP86*	LCBP86
MnO_4^-	0.41	0.32	0.33	0.15	0.62	0.19	0.24	0.37
CrO_4^{2-}	0.40	0.31	0.34	0.09	0.55	0.04	0.22	0.32
VO_4^{3-}	0.25	0.14	0.16	0.07	0.18	0.14	0.27	0.37
RuO_4	0.32	0.28	0.28	0.21	0.44	0.22	0.19	0.31
TcO_4^-	0.10	0.13	0.13	0.25	0.13	0.29	0.27	0.17
MoO_4^{2-}	0.14	0.23	0.23	0.06	0.22	0.18	0.13	0.34
OsO_4	0.53	0.51	0.50	0.27	0.39	0.31	0.21	0.26
ReO_4^-	0.36	0.43	0.43	0.14	0.25	0.16	0.14	0.16
WO_4^{2-}	0.43	0.51	0.51	0.14	0.11	0.07	0.11	0.16
Average 3d[f]	0.35	0.26	0.28	0.10	0.45	0.12	0.24	0.35
Average 4d + 5d[g]	0.31	0.34	0.34	0.19	0.27	0.22	0.19	0.24
Total average 3d[h]	0.33	0.31	0.32	0.16	0.34	0.18	0.21	0.28

[a]Root-mean-square deviation.
[b]The reference is the observed vertical excitation energies for the three first dipole-allowed transitions.
[c]For MoO_4^{2-} and WO_4^{2-} only, the first two experimental transitions are available.
[d]Deviations are in eV.
[e]No TDA was applied.
[f]Average of the three 3d complexes.
[g]Average of the six 4d and 5d complexes.
[h]Average over all complexes.
Data represented in this table was first published in [99].

Table 6. RMSDs for tetraoxo excitation energies based on RSCF-CV(∞)-DFT and a TZ2P basis set[a, b, c, d, e].

This shows a clear lack of consistency. However, RSCF-CV(∞)-DFT shows good and consistent performance for all complexes studied here.

Next, the excitation energies of the octahedral TM complexes [103] are presented. The analyses will be primarily focused on $Cr(CO)_6$ and $[Fe(CN)_6]^{4-}$ where experimental excitation energies are available. The first system to be considered is $Cr(CO)_6$; the RSCF-CV(∞)-DFT results are displayed in **Table 7**. The results afforded by RSCF-CV(∞)-DFT are in good agreement with the experimental data even at the RSCF-CV(∞)-DFT/LDA level of theory. The RSCF-CV(∞)-DFT/LDA results show performance identical to the TD-DFT/B3LYP [151] and better performance than TD-DFT with LDA and GGAs.

Considered next is the $[Fe(CN)_6]^{4-}$ complex; the results are shown in **Table 8**. The RMSDs here were calculated with the lower limit of the experimental [153] excitation energies where ranges are applicable. There are some theoretical calculations carried with TD-DFT [151] and other DFT-based approaches [151] as well as some high-level *ab initio* methods [156]. Again, there are good performances even for the LDA and GGA functionals. The accurate excitation energies afforded by the RSCF-CV(∞)-DFT method when compared to the experimental data are as a result of, to some extent, fortuitous error cancelation.

STATE	RASPT2[b]	LDA	BP86	PBE	B3LYP	PBE0	BHLYP	LCBP86*[c]	LCBP86[d]	Expt.[e]
Singlet										
$^1T_{1g}$(MC)	4.98	5.33	5.14	5.17	4.85	5.25	4.52	4.78	4.97	—
$^1T_{1u}$(MLCT)	4.50	4.45	4.39	4.40	4.48	4.62	4.68	4.61	4.37	4.44
2^1T_{1u}(MLCT)	5.42	5.46	5.47	5.47	5.73	5.93	6.20	6.23	5.85	5.48
Triplet										
1^3T_{1g}(MC)	4.28[f]	4.72	4.88	4.91	4.54	4.62	4.15	4.18	4.49	—
1^3T_{2g}(MC)	4.64[f]	4.63	4.59	4.60	4.39	4.45	4.17	4.45	4.59	—
RMSD	0.06	0.02	0.04	0.03	0.18	0.34	0.54	0.54	0.27	

[a]Energies in eV.
[b][154].
[c]Represents LC functional combined with BP86 with $\omega = 0.75$.
[d]Refers to LC functional combined with BP86 using $\omega = 0.4$.
[e][152].
[f][155].
Data represented in this table was first published in [103].

Table 7. Calculated excitation energies[a] for $Cr(CO)_6$ based on the RSCF-CV(∞)-DFT method.

STATE	CASPT2[b]	LDA	BP86	PBE	B3LYP	PBE0	BHLYP	LCBP86*[c]	LCBP86[d]	Expt.[e]
Singlet										
$^1T_{1g}$(MC)	3.60	4.17	3.72	3.75	3.42	3.35	3.04	3.35	3.64	3.80–3.94
3^1T_{1u}(MLCT)	—	5.57	5.57	5.64	6.10	6.44	—	—	6.34	5.69–5.89
4^1T_{1u}(MLCT)	—	5.83	5.80	5.72	6.25	6.63	—	—	6.93	6.20
1^1T_{2g}(MC)	4.33	4.05	3.74	4.12	4.47	4.46	4.47	4.14	4.37	4.43–4.77
Triplet										
1^3T_{1g}(MC)	2.67	3.60	3.39	3.41	2.98	2.90	2.49	2.56	2.93	2.94
RMSD	0.20[f]	0.42	0.41	0.33	0.25	0.44	0.40[f]	0.29[f]	0.44	

[a]Energies in eV.
[b][156].
[c]Represents LC functional combined with BP86 with $\omega = 0.75$.
[d]Refers to LC functional combined with BP86 using $\omega = 0.4$.
[e][153].
[f]Calculated with three excitation energies.
Data represented in this table was first published in [103].

Table 8. Calculated excitation energies[a] for $[Fe(CN)_6]^{4-}$ based on the RSCF-CV(∞)-DFT method.

A look now at the electronic density change that accompanies the electronic excitation. **Figure 5** (**a** and **b**) shows the plot of the density changes associated with the electronic transitions in Cr (CO)$_6$. The charge redistribution can be seen from the figure, where the density depletion (ρ_{occ}), the accumulation (ρ_{vir}) as well as the density change ($\Delta\rho_{ex} = \rho_{vir} - \rho_{occ}$) occurs, resulting from the total change in density associated with the electronic transition. For the MLCT transition, the ρ_{occ} (**Figure 5a**) is situated on the Cr metal center, the area or space spun by the density that is reminiscent of the d_{yz} and the ρ_{vir} is mostly situated on the equatorial CO ligands. The depletion density is in the yz plane, the accumulation density is situated on the CO ligand, and there is little interaction between them as can be seen from the difference (**Figure 5b**). The movement of density is from the metal center to the ligands corresponding to an intramolecular charge-transfer transition. It is clear from **Figure 5c** that this transition has a significant $d \rightarrow d$ character. In the density plots that follow, there is a depletion in the density situated on
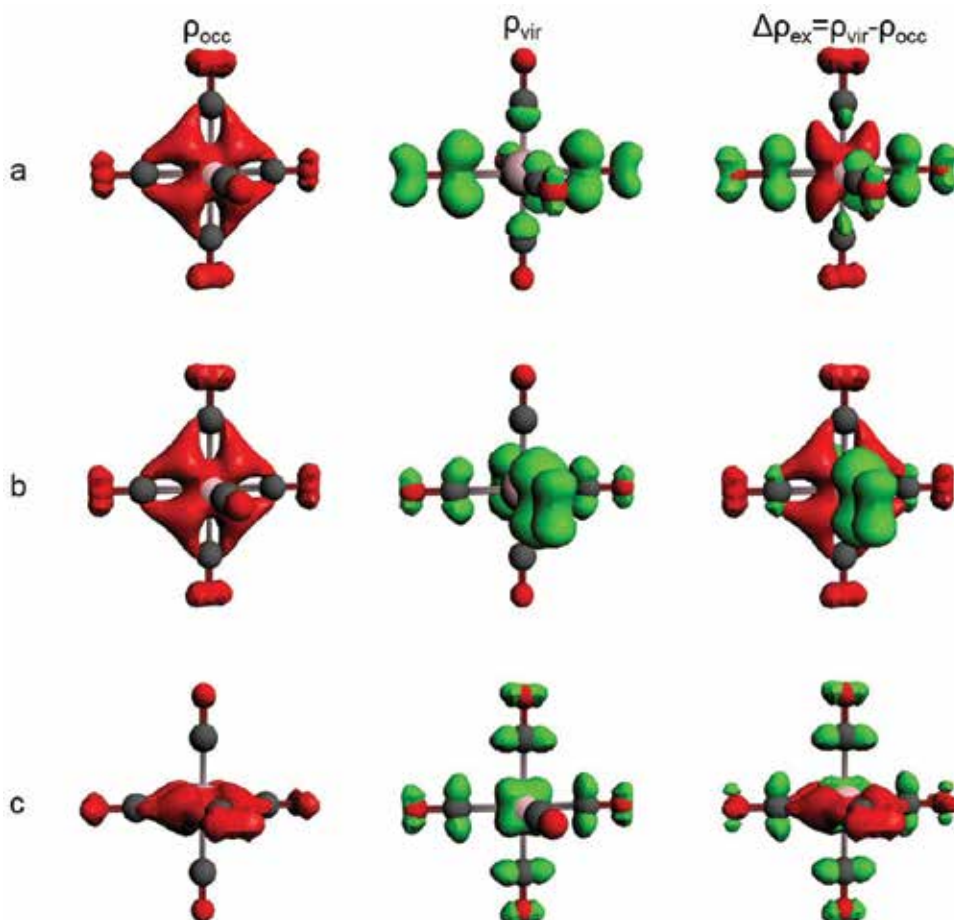

Figure 5. $\Delta\rho$ associated with the CrCO$_6$, red signifies depletion and green shows accumulation of density. (a) The density change associated with the 1^1T_{1u} state. (b) Exemplifies the density redistribution associated with the 2^1T_{1u} state. (c) Densities accompanying the calculated 1^1T_{1g} state. (a) and (b) are MLCT-type transitions, and (c) is an example of MC-type transition. See Seidu I. Excited-State Studies with the Constricted Variational Density Functional Theory (CV-DFT) Method. PhD dissertation. University of Calgary; 2016 for coloured pictures.

the metal with some contribution from the CO in the *xy*-plane and accumulation of density largely on the central Cr metal along the *yz*-plane with some accumulation on the CO ligands in the same plane.

Displayed in **Figure 6** are the density plots for $[Fe(CN)_6]^{4-}$. Similar features are seen here as seen for $Cr(CO)_6$. The differences in the density plots representing the MC transition; there is more significant accumulation on the CN^- ligands, and the density accumulation is in the same plane (*xy*-plane) as the depletion density ($d_{x^2-y^2}-d_{xy}$). As for the MLCT, the associated density movement is identical to that of $Cr(CO)_6$ (see **Figure 6(b** and **c)**).

The benchmark studies on the tetrahedral and octahedral TM complexes probed the ability of RSCF-CV(∞)-DFT to describe CT and hidden CT excitations. Use was made of the tetrahedral d^0 metal oxides as the first benchmark series since the tetra oxides have a long history as a
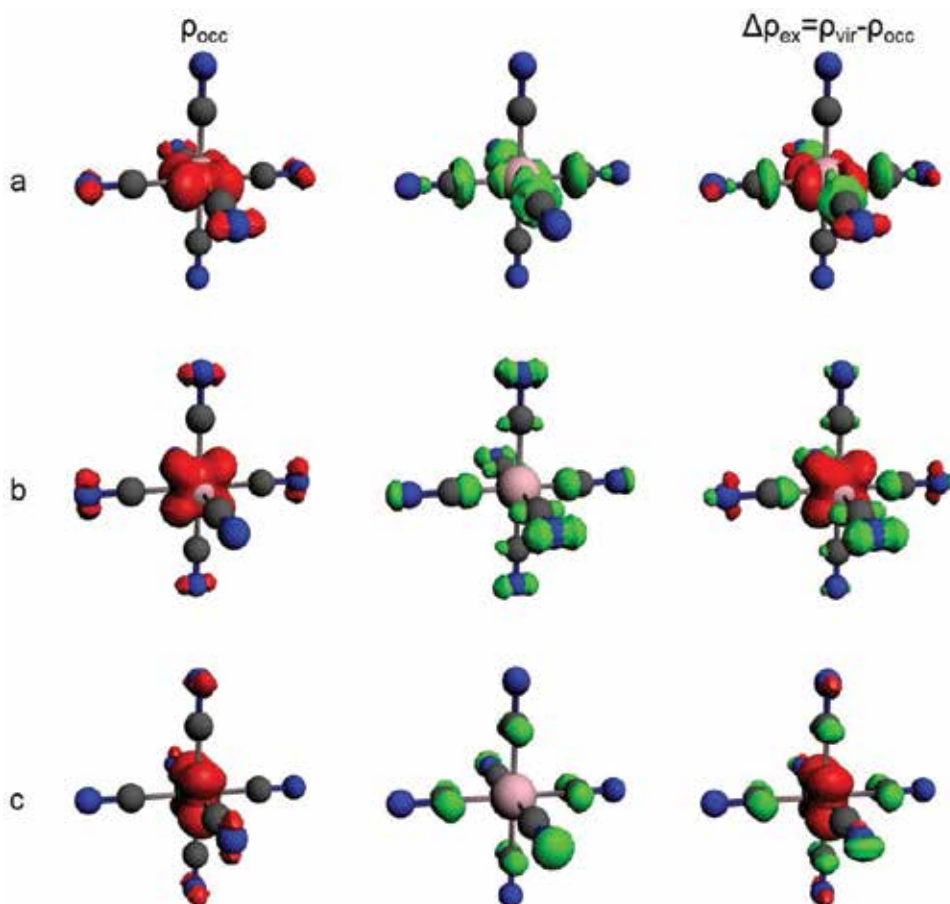

Figure 6. $\Delta\rho$ associated with the $Fe(CN)_6^{4-}$. (a) the density change associated with the 1^1T_{1g} state. (b) Exemplifies the density redistribution associated with the 3^1T_{1u} state. (c) Densities accompanying the calculated 3^1T_{1u} state. (a) Is an example of MC-type transition, and (b) and (c) are MLCT-type transitions. Red signifies loss and green shows gain in density. See Seidu I. Excited-State Studies with the Constricted Variational Density Functional Theory (CV-DFT) Method. PhD dissertation. University of Calgary; 2016 for coloured pictures.

challenging testing ground for new methods due to their complex electronic structure. In general there is either a comparable performance for RSCF-CV(∞)-DFT and TD-DFT in cases where TD-DFT shows good performances or RSCF-CV(∞)-DFT outperforms TD-DFT.

A trend that manifests itself at larger r for the TM complexes is the excitation energies which become more functional dependent and less accurate. Further, the accuracy of RSCF-CV(∞)-DFT for smaller r is not attributable to the ability of our method to afford accurate values of the IP of the complex and the EA of the cation formed alone; some error cancelation occurs when the IPs and EAs are combined to obtain the excitation energy. Finally, it is possible to plot the density change associated with the electronic transitions afforded by our method with regions of density depletion and accumulation supporting a qualitative classification of excitations as MLCT or MC.

4. Conclusion

In this chapter we presented the CV-DFT method and its different variants. While CV(2)-DFT is consistent with (adiabatic) TD-DFT within the TDA approximation, CV-DFT allows to go to higher order. Indeed, its strength lies in going beyond linear response and therewith obtaining distance-dependent contributions to the excitation energy naturally. Additionally, the theory allows for the calculation of excitation energies for singlet and triplet states on the same footing. Of course as a variational method, CV-DFT relies on an accurate ground-state description. The theoretical framework allows us to apply special restrictions as done in [104] and therewith obtain a numerically stable method being numerically equivalent to ΔSCF-DFT.

How CV-DFT performs has been shown in Section 3 with the aid of selected examples of charge-transfer or Rydberg excitation type. With these examples, we could demonstrate how CV(∞)-DFT is able to reproduce the expected $-1/R$ long-range behavior for charge-transfer excitations. When orbital relaxation is allowed, the excitation energies obtained by R-CV(∞)-DFT with LDA agree nicely with the findings of long-range corrected functionals. For short distance, the optimization of the transition matrix $\mathbf{U}$ is clearly beneficial [100, 104, 121]. But for medium- and long-range distances, a notion of care is to be taken as the optimization may lead to an unwanted mixing of transitions as shown in the case of $C_2H_4xC_2F_4$. Also, for excitations with hidden charge-transfer character, meaningful results are obtained with CV-DFT, for example, accurate results for the first singlet excitation energies of polyacenes [101, 147] for polyacenes as large as hexacene. Not only is CV-DFT able to deliver meaningful results, even for the LDA functional, it has an incredible ability to provide a qualitative picture of the nature or type of excitation under consideration. This is seen in the case of the TM complexes, a complicated yet excellent test set for assessing the range of applicability of every newly developed method. In the case of Rydberg excitations, RSCF-CV(∞)-DFT produces meaningful results without the need for sophisticated (or 'specialized') functionals. This good performance is attributable to the ability of our method affords good estimates of IPs and EAs for all functionals [100, 121, 122]. Admittedly, fortuitous error cancelation in IPs and EAs obtained for both RSCF-CV(∞)-DFT and TD-DFT plays a role in the accuracy of the resultant excitation energies.

Acknowledgements

Author details

Florian Senn[1]*, Issaka Seidu[2] and Young Choon Park[3]

*Address all correspondence to: florian.senn@ucalgary.ca

1 Department of Chemistry, University of Calgary, Calgary, Alberta, Canada

2 Department of Chemistry, Carleton University, Ottawa, Ontario, Canada

3 Quantum Theory Project, University of Florida, Gainesville, FL, United States

References

[1] Wolfsberg M, Helmholz L. The Journal of Chemical Physics. 1952;**20**(5):837-843. DOI: http://dx.doi.org/10.1063/1.1700580

[2] Hoffmann R. The Journal of Chemical Physics. 1963;**39**(6):1397-1412. DOI: http://dx.doi.org/10.1063/1.1734456

[3] Pople JA, Santry DP, Segal GA. The Journal of Chemical Physics. 1965;**43**(10):S129-S135. DOI: http://dx.doi.org/10.1063/1.1701475

[4] Holt S, Ballhausen C. Theoretica Chimica Acta. 1967;**7**(4):313-320. DOI: 10.1007/BF00537508

[5] Hillier H, Saunders VR. Proceedings of the Royal Society of London, Series A. 1970;**320**(1541):161-173. DOI: 10.1098/rspa.1970.0203

[6] Slater JC. In: Löwdin PO, editor. Advances in Quantum Chemistry, Vol. 6 of *Advances in Quantum Chemistry*: 1-92. Academic Press; 1972. DOI: http://dx.doi.org/10.1016/S0065-3276(08)60541-9

[7] Hall MB, Fenske RF. Inorganic Chemistry. 1972;**11**(4):768-775. DOI: 10.1021/ic50110a022

[8] Truax DR, Geer JA, Ziegler T. The Journal of Chemical Physics. 1973;**59**(12):6662-6666. DOI: http://dx.doi.org/10.1063/1.1680049

[9] Ziegler T, Rauk A, Baerends E. Theoretica Chimica Acta. 1977;**43**(3):261-271. DOI: 10.1007/BF00551551

[10] Dewar MJS, Thiel W. Journal of the American Chemical Society. 1977;**99**(15):4899-4907. DOI: 10.1021/ja00457a004

[11] Hall MB. Journal of the American Chemical Society. 1978;**100**(20):6333-6338. DOI: 10.1021/ja00488a007

[12] Stewart JJP. Journal of Computational Chemistry. 1989;**10**(2):221-264. DOI: 10.1002/jcc.540100209

[13] Bursten BE, Drummond ML, Li J. Faraday Discussions. 2003;**124**:1-24. DOI: 10.1039/B305317M

[14] Buenker RJ, Peyerimhoff SD. Theoretica Chimica Acta. 1968;**12**(3):183-199. DOI: 10.1007/BF00528266

[15] Levy B, Berthier G. International Journal of Quantum Chemistry. 1969;**3**(2):247-247. DOI: 10.1002/qua.560030213

[16] Godefroid M, Lievin J, Metz JY. International Journal of Quantum Chemistry. 1991; **40**(2):243-264. DOI: 10.1002/qua.560400207

[17] Hegarty D, Robb MA. Molecular Physics. 1979;**38**(6):1795-1812. DOI: 10.1080/00268977900102871

[18] Maruhn-Rezwani V, Grün N, Scheid W. Physical Review Letters. 1979;**43**:512-515. DOI: 10.1103/PhysRevLett.43.512

[19] Kulander KC, Devi KRS, Koonin SE. Physical Review A. 1982;**25**:2968-2975. DOI: 10.1103/PhysRevA.25.2968

[20] Devi KRS, Garcia JD. Physical Review A. 1984;**30**:600-603. DOI: 10.1103/PhysRevA.30.600

[21] Kulander KC. Physical Review A. 1987;**36**:2726-2738. DOI: 10.1103/PhysRevA.36.2726

[22] Olsen J, Roos BO, Jørgensen P, Jensen HJA. The Journal of Chemical Physics. 1988; **89**(4):2185-2192. DOI: http://dx.doi.org/10.1063/1.455063

[23] Malmqvist PÅ, Pierloot K, Shahi ARM, Cramer CJ, Gagliardi L. The Journal of Chemical Physics. 2008;**128**(20):204109. DOI: http://dx.doi.org/10.1063/1.2920188

[24] Andersson K, Malmqvist PÅ, Roos BO. The Journal of Chemical Physics. 1992;**96**(2):1218-1226. DOI: http://dx.doi.org/10.1063/1.462209

[25] Stanton JF, Bartlett RJ. The Journal of Chemical Physics. 1993;**98**(9):7029-7039. DOI: http://dx.doi.org/10.1063/1.464746

[26] Angeli C, Cimiraglia R, Evangelisti S, Leininger T, Malrieu JP. The Journal of Chemical Physics. 2001;**114**(23):10252-10264. DOI: http://dx.doi.org/10.1063/1.1361246

[27] Neese F. The Journal of Chemical Physics. 2003;**119**(18):9428-9443. DOI: http://dx.doi.org/10.1063/1.1615956

[28] Crawford TD, Schaefer HF. An Introduction to Coupled Cluster Theory for Computational Chemists. John Wiley & Sons, Inc.; 2007. pp. 33-136. DOI: 10.1002/9780470125915.ch2

[29] Bartlett RJ, Stanton JF. Applications of Post-Hartree-Fock Methods: A Tutorial. John Wiley & Sons, Inc.; 2007. pp. 65-169. DOI: 10.1002/9780470125823.ch2

[30] Kohn W, Sham LJ. Physics Review. 1965;**140**:A1133-A1138. DOI: 10.1103/PhysRev.140.A1133

[31] Slater JC. Physics Review. 1951;**81**(3):385-390. DOI: 10.1103/PhysRev.81.385

[32] Slater JC, Wood JH. International Journal of Quantum Chemistry. 1970;**5**(S4):3-34. DOI: 10.1002/qua.560050703

[33] Slater JC. Advances in Quantum Chemistry, 1972;**6**:1-92. Academic Press; DOI: http://dx.doi.org/10.1016/S0065-3276(08)60541-9

[34] Nagy Á. Physical Review A. 1996;**53**(5):3660-3663. DOI: 10.1103/PhysRevA.53.3660

[35] Liu T, Han WG, Himo F, Ullmann GM, Bashford D, et al. The Journal of Physical Chemistry. A. 2004;**108**(16):3545-3555. DOI: 10.1021/jp031062p

[36] Gavnholt J, Olsen T, Engelund M, Schiotz J. Physical Review B: Condensed Matter and Materials Physics. 2008;**78**(7):075441–1 – 10. DOI: 10.1103/PhysRevB.78.075441

[37] Theophilou AK. Journal of Physics C: Solid State Physics. 1979;**12**(24):5419-5430

[38] Gross EKU, Oliveira LN, Kohn W. Physical Review A. 1988;**37**:2821-2833. DOI: 10.1103/PhysRevA.37.2809

[39] Gidopoulos N, Papaconstantinou P, Gross EKU. Physical Review Letters. 2002;**88**(3):033003–1 – 4. DOI: 10.1103/PhysRevLett.88.033003

[40] Casida ME. Time-Dependent Density Functional Response Theory for Molecules, Chap. 5. World Scientific; 1995. pp. 155-192. DOI: 10.1142/9789812830586_0005

[41] Runge E, Gross EKU. Physical Review Letters. 1984;**52**(12):997-1000. DOI: 10.1103/PhysRevLett.52.997

[42] Casida ME. The Journal of Chemical Physics. 2005;**122**(5):054111. DOI: http://dx.doi.org/10.1063/1.1836757

[43] Casida M, Huix-Rotllant M. In: Ferré N, Filatov M, Huix-Rotllant M, editors. Density-Functional Methods for Excited States, vol. 368 of Top. Curr. Chem., 1-60. Springer International Publishing, 2016; DOI: 10.1007/128_2015_632

[44] Casida ME, Jamorski C, Casida KC, Salahub DR. The Journal of Chemical Physics. 1998;**108**(11):4439-4449. DOI: http://dx.doi.org/10.1063/1.475855

[45] Oliveira L, Gross EKU, Kohn W. Physical Review A. 1988;**37**(8):2821-2833. DOI: 10.1103/PhysRevA.37.2821

[46] Filatov M, Shaik S. Chemical Physics Letters. 1998;**288**(5–6):689-697

[47] Filatov M, Shaik S. Chemical Physics Letters, 1999;**304**(5–6):429-437. DOI: http://dx.doi. org/10.1016/S0009-2614(99)00336-X

[48] Pederson MR, Klein BM. Physical Review B. 1988;**37**:10319-10331. DOI: 10.1103/Phys RevB.37.10319

[49] Baruah T, Pederson MR. The Journal of Chemical Physics. 2006;**125**(16):164706. DOI: http://dx.doi.org/10.1063/1.2360265

[50] Baruah T, Pederson MR. Journal of Chemical Theory and Computation. 2009;**5**(4):834-843. DOI: 10.1021/ct900024f

[51] Frank I, Hutter J, Marx D, Parrinello M. The Journal of Chemical Physics. 1998;**108**(10): 4060-4069. DOI: http://dx.doi.org/10.1063/1.475804

[52] Okazaki I, Sato F, Yoshihiro T, Ueno T, Kashiwagi H. THEOCHEM Journal of Molecular Structure. 1998;**451**(1–2):109-119. DOI: http://dx.doi.org/10.1016/S0166-1280(98)00164-X

[53] Wu Q, Van Voorhis T. Physical Review A. 2005;**72**:024502–1–4. DOI: 10.1103/Phys RevA.72.024502

[54] Glushkov VN, Levy M. The Journal of Chemical Physics. 2007;**126**(17):174106. DOI: http://dx.doi.org/10.1063/1.2733657

[55] Glushkov VN, Assfeld X. The Journal of Chemical Physics. 2010;**132**(20):204106. DOI: http://dx.doi.org/10.1063/1.3443777

[56] Gilbert ATB, Besley NA, Gill PMW. The Journal of Physical Chemistry. A. 2008;**112**(50): 13164-13171. DOI: 10.1021/jp801738f

[57] Besley NA, Gilbert ATB, Gill PMW. The Journal of Chemical Physics. 2009;**130**(12) 124308–1 – 7. DOI: http://dx.doi.org/10.1063/1.3092928

[58] Ziegler T, Seth M, Krykunov M, Autschbach J, Wang F. The Journal of Chemical Physics. 2009;**130**(15):154102. DOI: http://dx.doi.org/10.1063/1.3114988

[59] Cullen J, Krykunov M, Ziegler T. Chemical Physics. 2011;**391**(1):11-18. DOI: http://dx. doi.org/10.1016/j.chemphys.2011.05.021

[60] Ziegler T, Krykunov M, Cullen J. The Journal of Chemical Physics. 2012;**136**(12):124107. DOI: http://dx.doi.org/10.1063/1.3696967

[61] Krykunov M, Ziegler T. Journal of Chemical Theory and Computation. 2013;**9**(6):2761-2773. DOI: 10.1021/ct300891k

[62] Park YC, Krykunov M, Ziegler T. Molecular Physics. 2015;**113**(13–14):1636-1647. DOI: 10.1080/00268976.2014.1003260

[63] Evangelista FA, Shushkov P, Tully JC. The Journal of Physical Chemistry. A. 2013; **117**(32):7378-7392. DOI: 10.1021/jp401323d

[64] Peng B, Van Kuiken BE, Ding F, Li X. Journal of Chemical Theory and Computation. 2013;**9**(9):3933-3938. DOI: 10.1021/ct400547n

[65] van Gisbergen SJA, Snijders JG, Baerends EJ. The Journal of Chemical Physics. 1995; **103**(21):9347-9354. DOI: http://dx.doi.org/10.1063/1.469994

[66] Petersilka M, Gossmann U, Gross EKU. Physical Review Letters. 1996;**76**(8):1212-1215. DOI: 10.1103/PhysRevLett.76.1212

[67] Bauernschmitt R, Ahlrichs R. Chemical Physics Letters. 1996;**256**(4):454-464. DOI: http://dx.doi.org/10.1016/0009-2614(96)00440-X

[68] Furche F. The Journal of Chemical Physics. 2001;**114**(14):5982-5992. DOI: http://dx.doi.org/10.1063/1.1353585

[69] Furche F, Ahlrichs R. The Journal of Chemical Physics. 2002;**117**(16):7433-7447. DOI: http://dx.doi.org/10.1063/1.1508368

[70] Ullrich CA. Time-Dependent Density-Functional Theory. Oxford Graduate Texts, 2012

[71] Tozer DJ, Handy NC. The Journal of Chemical Physics. 1998;**109**(23):10180-10189. DOI: http://dx.doi.org/10.1063/1.477711

[72] Schipper PRT, Gritsenko OV, van Gisbergen SJA, Baerends EJ. The Journal of Chemical Physics, 2000;**112**(3):1344-1352. DOI: http://dx.doi.org/10.1063/1.480688

[73] Wasserman A, Burke K. Physical Review Letters. 2005;**95**:163006–1 – 4. DOI: 10.1103/PhysRevLett.95.163006

[74] Gaiduk AP, Firaha DS, Staroverov VN. Physical Review Letters. 2012;**108**:253005–1 – 5. DOI: 10.1103/PhysRevLett.108.253005

[75] Jaramillo J, Scuseria GE, Ernzerhof M. The Journal of Chemical Physics. 2003; **118**(3):1068-1073. DOI: http://dx.doi.org/10.1063/1.1528936

[76] Tawada Y, Tsuneda T, Yanagisawa S, Yanai T, Hirao K. The Journal of Chemical Physics. 2004;**120**(18):8425-8433. DOI: http://dx.doi.org/10.1063/1.1688752

[77] Neugebauer J, Gritsenko O, Baerends EJ. The Journal of Chemical Physics. 2006; **124**(21):214102. DOI: http://dx.doi.org/10.1063/1.2197829

[78] Livshits E, Baer R. Physical Chemistry Chemical Physics. 2007;**9**:2932-2941. DOI: 10.1039/B617919C

[79] Peach MJG, Benfield P, Helgaker T, Tozer DJ. The Journal of Chemical Physics. 2008; **128**(4):044118–1 – 8. DOI: http://dx.doi.org/10.1063/1.2831900

[80] Zhao Y, Truhlar DG. Accounts of Chemical Research. 2008;**41**(2):157-167. DOI: 10.1021/ar700111a PMID: 18186612

[81] Stein T, Kronik L, Baer R. The Journal of Chemical Physics. 2009;**131**(24):244119. DOI: http://dx.doi.org/10.1063/1.3269029

[82] Autschbach J. Chemphyschem. 2009;**10**(11):1757-1760. DOI: 10.1002/cphc.200900268

[83] Gritsenko O, Baerends EJ. Physical Chemistry Chemical Physics. 2009;**11**:4640-4646. DOI: 10.1039/B903123E

[84] Elliott P, Goldson S, Canahui C, Maitra NT. Chemical Physics. 2011;**391**(1):110-119. DOI: http://dx.doi.org/10.1016/j.chemphys.2011.03.020

[85] Cave RJ, Zhang F, Maitra NT, Burke K. Chemical Physics Letters. 2004;**389**(1–3):39-42. DOI: http://dx.doi.org/10.1016/j.cplett.2004.03.051

[86] Mazur G, Włodarczyk R. Journal of Computational Chemistry. 2009;**30**(5):811-817. DOI: 10.1002/jcc.21102

[87] Romaniello P, Sangalli D, Berger JA, Sottile F, Molinari LG, et al. The Journal of Chemical Physics. 2009;**130**(4):044108. DOI: http://dx.doi.org/10.1063/1.3065669

[88] Dreuw A, Fleming GR, Head-Gordon M. The Journal of Physical Chemistry. B. 2003;**107**(27):6500-6503. DOI: 10.1021/jp034562r

[89] Dreuw A, Fleming GR, Head-Gordon M. Phys. Chemis. Chemical Physics. 2003;**5**:3247-3256. DOI: 10.1039/B304944B

[90] Dreuw A, Head-Gordon M. Journal of the American Chemical Society. 2004;**126**(12):4007-4016. DOI: 10.1021/ja039556n

[91] Tozer DJ. The Journal of Chemical Physics. 2003;**119**(24):12697-12699. DOI: http://dx.doi.org/10.1063/1.1633756

[92] Stein T, Kronik L, Baer R. Journal of the American Chemical Society. 2009;**131**(8):2818-2820. DOI: 10.1021/ja8087482

[93] Ziegler T, Seth M, Krykunov M, Autschbach J. The Journal of Chemical Physics. 2008;**129**(18):184114. DOI: http://dx.doi.org/10.1063/1.3009622

[94] Iikura H, Tsuneda T, Tanai T, Hirao K. The Journal of Chemical Physics. 2001;**115**(8):3540–3544. DOI: http://dx.doi.org/10.1063/1.1383587

[95] Song JW, Watson MA, Hirao K. The Journal of Chemical Physics. 2009;**131**(14):144108. DOI: http://dx.doi.org/10.1063/1.3243819

[96] Heyd J, Scuseria GE, Ernzerhof M. The Journal of Chemical Physics. 2003;**118**(18):8207-8216. DOI: http://dx.doi.org/10.1063/1.1564060

[97] Baer R, Neuhauser D: Physical Review Letters. 2005;**94**:043002–1–4. DOI: 10.1103/PhysRevLett.94.043002

[98] Zhao Y, Truhlar DG. The Journal of Physical Chemistry. A. 2006;**110**(49):13126-13130. DOI: 10.1021/jp066479k

[99] Seidu I, Krykunov M, Ziegler T. Journal of Chemical Theory and Computation. 2015;**11**(9):4041-4053. DOI: 10.1021/acs.jctc.5b00298

[100] Seidu I, Krykunov M, Ziegler T. The Journal of Physical Chemistry. A. 2015;**119**(21): 5107-5116. DOI: 10.1021/jp5082802

[101] Senn F, Krykunov M. The Journal of Physical Chemistry. A. 2015;**119**(42):10575-10581. DOI: 10.1021/acs.jpca.5b07075

[102] Senn F, Park YC. The Journal of Chemical Physics. 2016;**145**(24):244108–1 – 10. DOI: 10.1063/1.4972231

[103] Seidu I. Excited-State Studies with the Constricted Variational Density Functional Theory (CV-DFT) Method. PhD dissertation. University of Calgary; 2016

[104] Park YC, Senn F, Krykunov M, Ziegler T. Journal of Chemical Theory and Computation. 2016;**12**(11):5438-5452. DOI: 10.1021/acs.jctc.6b00333

[105] Ziegler T, Krykunov M, Seidu I, Park YC. In: Ferré N, Filatov M, Huix-Rotllant M, editors. Density-Functional Methods for Excited States, Vol. 368 of Top. Curr. Chem. Springer International Publishing; 2016. pp. 61-95. DOI: 10.1007/128_2014_611

[106] Ziegler T, Krykunov M, Autschbach J. Journal of Chemical Theory and Computation. 2014;**10**(9):3980-3986. DOI: 10.1021/ct500385a

[107] Hirata S, Head-Gordon M. Chemical Physics Letters. 1999;**314**(3–4):291-299. DOI: http://dx.doi.org/10.1016/S0009-2614(99)01149-5

[108] Martin RL. The Journal of Chemical Physics. 2003;**118**(11):4775-4777. DOI: http://dx.doi.org/10.1063/1.1558471

[109] Ziegler T, Krykunov M. The Journal of Chemical Physics. 2010;**133**(7):074104. DOI: http://dx.doi.org/10.1063/1.3471449

[110] Seidu I, Zhekova HR, Seth M, Ziegler T. The Journal of Physical Chemistry. A. 2012; **116**(9):2268-2277. DOI: 10.1021/jp209507n

[111] Ziegler T, Krykunov M, Cullen J. Journal of Chemical Theory and Computation. 2011; **7**(8):2485-2491. DOI: 10.1021/ct200261a

[112] Baerends E, Ziegler T, Autschbach J, Bashford D, Bérces A, et al. ADF. Theoretical chemistry, Vrije Universiteit, Amsterdam. In: The Netherlands. 2012

[113] Baerends E, T Z, Atkins A, Autschbach J, Bashford D, et al.: ADF Developers Version. Theoretical Chemistry, Vrije Universiteit, Amsterdam, The Netherlands, 2016

[114] Dreuw A, Weisman JL, Head-Gordon M. The Journal of Chemical Physics. 2003;**119**(6): 2943-2946. DOI: http://dx.doi.org/10.1063/1.1590951

[115] Ziegler T, Seth M, Krykunov M, Autschbach J, Wang F. THEOCHEM Journal of Molecular Structure. 2009;**914**(1–3):106-109. DOI: http://dx.doi.org/10.1016/j.theochem.2009.04.021

[116] Trickl T, Cronwell EF, Lee YT, Kung AH. The Journal of Chemical Physics. 1989; **91**(10):6006-6012. DOI: http://dx.doi.org/10.1063/1.457417

[117] Ben-Shlomo SB, Kaldor U. The Journal of Chemical Physics. 1990;**92**(6):3680-3683. DOI: http://dx.doi.org/10.1063/1.457824

[118] Verma P, Bartlett RJ. The Journal of Chemical Physics 2014;**140**(18):18A534. DOI: http://dx.doi.org/10.1063/1.4871409

[119] Gruening M, Gritsenko OV, van Gisbergen SJA, Baerends EJ. Chemical Physics. 2002;**116**(22):9591-9601. DOI: http://dx.doi.org/10.1063/1.1476007

[120] Autschbach J, Srebro M. Accounts of Chemical Research. 2014;**47**(8):2592-2602. DOI: 10.1021/ar500171t

[121] Krykunov M, Seth M, Ziegler T. The Journal of Chemical Physics. 2014;**140**(18):18A502. DOI: http://dx.doi.org/10.1063/1.4849397

[122] Zhekova H, Krykunov M, Autschbach J, Ziegler T. Journal of Chemical Theory and Computation. 2014;**10**(8):3299-3307. DOI: 10.1021/ct500292c

[123] Hieringer W, Görling A. Chemical Physics Letters. 2006;**419**(4–6):557-562. DOI: http://dx.doi.org/10.1016/j.cplett.2005.11.112

[124] Kobayashi R, Amos RD. Chemical Physics Letters. 2006;**420**(1–3):106-109. DOI: http://dx.doi.org/10.1016/j.cplett.2005.12.040

[125] Yanai T, Tew DP, Handy NC. Chemical Physics Letters. 2004;**393**(1–3):51-57. DOI: http://dx.doi.org/10.1016/j.cplett.2004.06.011

[126] Rudberg E, Sałek P, Helgaker T, Ågren H. The Journal of Chemical Physics. 2005;**123**(18):184108-184101-7. DOI: http://dx.doi.org/10.1063/1.2104367

[127] Tsai CW, YC S, Li GD, Chai JD. Physical Chemistry Chemical Physics. 2013;**15**:8352-8361. DOI: 10.1039/C3CP50441G

[128] Gritsenko O, Baerends EJ. The Journal of Chemical Physics. 2004;**121**(2):655-660. DOI: http://dx.doi.org/10.1063/1.1759320

[129] Maitra NT, Tempel DG. The Journal of Chemical Physics. 2006;**125**(18):184111. DOI: http://dx.doi.org/10.1063/1.2387951

[130] Kaduk B, Kowalczyk T, Voorhis TV. Chemical Reviews. 2012;**112**(1):321-370. DOI: 10.1021/cr200148b

[131] Baruah T, Olguin M, Zope RR. The Journal of Chemical Physics. 2012;**137**(8):084316. DOI: http://dx.doi.org/10.1063/1.4739269

[132] Filatov M, Huix-Rotllant M. The Journal of Chemical Physics. 2014;**141**(2):024112. DOI: http://dx.doi.org/10.1063/1.4887087

[133] Filatov M. Ensemble DFT Approach to Excited States of Strongly Correlated Molecular Systems. Cham: Springer International Publishing; 2016. pp. 97-124. DOI: 10.1007/128_2015_630

[134] Solovyeva A, Pavanello M, Neugebauer J. The Journal of Chemical Physics. 2014;**140** (16):164103. DOI: http://dx.doi.org/10.1063/1.4871301

[135] Richard RM, Herbert JM. Journal of Chemical Theory and Computation. 2011;**7**(5):1296-1306. DOI: 10.1021/ct100607w

[136] Grimme S, Parac M. Chemphyschem. 2003;**4**(3):292-295. DOI: 10.1002/cphc.200390047

[137] Angliker H, Rommel E, Wirz J. Chemical Physics Letters. 1982;**87**(2):208-212. DOI: http://dx.doi.org/10.1016/0009-2614(82)83589-6

[138] Houk KN, Lee PS, Nendel M. The Journal of Organic Chemistry. 2001;**66**(16):5517-5521. DOI: 10.1021/jo010391f

[139] Bendikov M, Duong HM, Starkey K, Houk KN, Carter EA, et al. Journal of the American Chemical Society. 2004;**126**(24):7416-7417. DOI: 10.1021/ja048919w

[140] Hajgató B, Szieberth D, Geerlings P, De Proft F, Deleuze MS. The Journal of Chemical Physics. 2009;**131**(22):224321. DOI: http://dx.doi.org/10.1063/1.3270190

[141] Hajgató B, Huzak M, Deleuze MS. The Journal of Physical Chemistry. A. 2011;**115**(33): 9282-9293. DOI: 10.1021/jp2043043

[142] Rayne S, Forest K. Computational & Theoretical Chemistry. 2011;**976**(1–3):105-112. DOI: http://dx.doi.org/10.1016/j.comptc.2011.08.010

[143] Ibeji CU, Ghosh D. Physical Chemistry Chemical Physics. 2015;**17**:9849-9856. DOI: 10.1039/C5CP00214A

[144] Anthony JE. Chemical Reviews. 2006;**106**(12):5028-5048. DOI: 10.1021/cr050966z

[145] Anthony J. Angewandte Chemie, International Edition. 2008;**47**(3):452-483. DOI: 10.1002/anie.200604045

[146] Plasser F, Pašalić H, Gerzabek MH, Libisch F, Reiter R, et al. Angewandte Chemie, International Edition. 2013;**52**(9):2581-2584. DOI: 10.1002/anie.201207671

[147] Krykunov M, Grimme S, Ziegler T. Journal of Chemical Theory and Computation. 2012;**8**(11):4434-4440. DOI: 10.1021/ct300372x

[148] Heinze HH, Görling A, Rösch N. The Journal of Chemical Physics. 2000;**113**(6):2088-2099. DOI: http://dx.doi.org/10.1063/1.482020

[149] Raghu C, Anusooya Pati Y, Ramasesha S. Physical Review B. 2002;**66**:035116–1 – 11. DOI: 10.1103/PhysRevB.66.035116

[150] Hachmann J, Dorando JJ, Avilés M, Chan GKL. The Journal of Chemical Physics. 2007;**127**(13):134309. DOI: http://dx.doi.org/10.1063/1.2768362

[151] Escudero D, Thiel W. The Journal of Chemical Physics. 2014;**140**(19):194105. DOI: http://dx.doi.org/10.1063/1.4875810

[152] Beach NA, Gray HB. Journal of the American Chemical Society. 1968;**90**(21):5713-5721. DOI: 10.1021/ja01023a011

[153] Ayers JB, Waggoner WH. Journal of Inorganic and Nuclear Chemistry. 1971;**33**(3):721-733. DOI: http://dx.doi.org/10.1016/0022-1902(71)80470-0

[154] Vancoillie S, Zhao H, Tran VT, Hendrickx MFA, Pierloot K. Journal of Chemical Theory and Computation. 2011;**7**(12):3961-3977. DOI: 10.1021/ct200597h

[155] Pierloot K, Tsokos E, Vanquickenborne LG. The Journal of Physical Chemistry. 1996;**100**(41):16545-16550. DOI: 10.1021/jp9614355

[156] Pierloot K, Praet EV, Vanquickenborne LG, Roos BO. The Journal of Physical Chemistry. 1993;**97**(47):12220-12228. DOI: 10.1021/j100149a021

[157] Formiga ALB, Vancoillie S, Pierloot K. Inorganic Chemistry. 2013;**52**(18):10653-10663. DOI: 10.1021/ic401704r. PMID: 23992205

[158] Coe BJ, Avramopoulos A, Papadopoulos MG, Pierloot K, Vancoillie S, et al. Chemistry - A European Journal. 2013;**19**(47):15955-15963. DOI: 10.1002/chem.201301380

[159] Escudero D, González L. Journal of Chemical Theory and Computation. 2012;**8**(1):203-213. DOI: 10.1021/ct200640q

[160] de Graaf C, Sousa C: Chemistry - A European Journal, 2010;**16**(15):4550-4556. DOI: 10.1002/chem.200903423

[161] Klamt A, Schüürmann G. Journal of the Chemical Society, Perkin Transactions. 1993;**2**:799-805. DOI: 10.1039/P29930000799

[162] Pye CC, Ziegler T. Theoretical Chemistry Accounts. 1999;**101**(6):396-408. DOI: 10.1007/s002140050457

[163] Su J, WH X, CF X, Schwarz WHE, Li J. Inorganic Chemistry. 2013;**52**(17):9867-9874. DOI: 10.1021/ic4009625 PMID: 23957772

[164] Dierksen M, Grimme S. The Journal of Physical Chemistry. A. 2004;**108**(46):10225-10237. DOI: 10.1021/jp047289h

Assessment of the Validity of Some Minnesota Density Functionals for the Prediction of the Chemical Reactivity of the SYBR Green I and Ethidium Bromide Nucleic Acid Stains

Norma Flores-Holguín, Juan Frau and
Daniel Glossman-Mitnik

Additional information is available at the end of the chapter

Abstract

This research work has assessed many Minnesota density functionals to find their molecular structure and electronic properties possessed by SYBR green I (SYBRGI) and ethidium bromide (EtBr) nucleic acid stains. In the determination of the global descriptors that come up from conceptual density functional theory (CDFT), the processes include: Self-Consistent Field Energy Differences (ΔSCF) and higher occupied molecular orbital (HOMO) and lower unoccupied molecular orbital (LUMO) frontier orbitals energies. Regarding the deduced outcomes for the conceptual DFT indices, many of the descriptors have been adjusted to achieve the "Koopmans in DFT (KID)" process. It has also been shown that the only density functionals that confirm this approximation are the range-separated hybrids (RSH).

Keywords: computational chemistry, SYBR green I, chemical reactivity theory, molecular modeling, conceptual DFT, ethidium bromide

1. Introduction

The chemical reactivity theory [also known as the conceptual density functional theory (CDFT)] is a vital technique that is used to predict, evaluate, and interpret the results from chemical processes [1–4].

Research done by Parr and his associates [1] reveals that several theories and models have been discovered after the evaluation of the molecular system with the use of DFT. Almost all the discovered theories are helpful in research because they enable scholars to achieve quantitative forecasts of a chemical reactivity system. In addition to this, the theories can further be quantified and are generally termed as conceptual DFT descriptors.

To obtain the quantitative figures of conceptual descriptors, it may be necessary to analyze the Kohn-Sham theory by calculating the energy system, molecular density, and the orbital energies associated with frontier orbitals [i.e., higher occupied molecular orbital (HOMO) and lower unoccupied molecular orbital (LUMO)] [5–10].

For research on a molecular system, the first activity before proceeding is selection of the model chemistry. Model chemistry is the collection of basic set, density function, together with an implied solvent model that is known to be consistent for the problem under research. Several studies provide insights on the way to choose the model chemistry. A researcher may also decide to preview past studies when choosing the model.

Even though the fundamentals of DFT reveal that universal functional density is present and that computations using this function can be used to obtain all the features of the system, it is always necessary in practical cases that one refers to the estimated density functionals that have been established for the past 3 decades. For the approximate functionals, almost all of them are perfectly fit to be used in estimating some features, while some can be used for estimating other features. In separate scenarios, you can encounter density functionals that are perfectly fit for estimating the features of a given molecular system and a functional group. It is also important to assess separate density functionals for a separate functional group which can be added to the molecular system under research.

When researching on chemical reactivity (which is a process that entails the transfer of electrons), a person performs computations for both ground and open systems, i.e., cation and anion. It is not easy to obtain consistent outcomes using these computations (when diffuse functions should be a part of the basis set) [5–10]. This necessitates adoption of a more consistent technique that provides all the data that a person will require directly from the outcomes of the computations at ground state in the molecular system under research. In addition to this, a person may also want to find the deionization ability together with the electron affinity of any system being researched without having to calculate the radical cation and anion. This can be determined by the Koopmans' theorem [7–10] that relies on Hartree-Fock Theory, which states that the energy of the HOMO (i.e., $I = -\varepsilon H$) can be used to estimate the ionization potential. Alternatively, the electron affinity can be estimated using the minus the energy of the LUMO (i.e., $A = -\varepsilon L$).

The legitimacy of the Koopmans' theorem is yet again a contentious issue because of the existing difference between the fundamental band gap and the HOMO and the LUMO gaps. This can be termed as derivative discontinuity. It has again been discovered that an exact physical description may be assigned to Kohn-Sham HOMO using "the Kohn-Sham analogue of Koopmans' theorem in Hartree-Fock theory" (this theory explains that in the exact theory, the KS HOMO is opposite and same as the ionization potential) [11–14]. The effects brought about by the difference between the fundamental band gap and the HOMO and the LUMO gaps have ensured that no Koopmans' theorem creates a direct relationship between the LUMO energy and the electron affinity. To eliminate these effects, a suggestion has been made by scholars to conceive that the ionization potential of the N + 1 electron system (anion) is almost equal to the electron affinity of N electron system [15]. Regarding the range-separated hybrids (RSH) density functionals [16–18], e.g., that the repulsive coulomb potential has to be separated in the long-range (LR) and short-range (SR) terms, e.g., via $r^{-1} = r^{-1} \text{erf}(\gamma r) + r^{-1} \text{erfc}(\gamma r)$, with γ representing the range-separation parameter, it was highlighted by Kronik et al.

[15] that the legitimacy of the Koopmans' theorem may be approximately approved with a well-informed choice of this final parameter.

Use of the γ-tuning technique can be useful in upgrading the features projected by the density functionals. This is due to better utilization of the of Koopmans' theorem, leading to a superior understanding of frontier orbitals energies with I and A. An example can be cited from Lima et al. [19], who just demonstrated a better explanation of the optical features of carotenoids through tuning of some LR density functionals that are linked.

This therefore illustrates that conformity of any given density functional can be determined by assessing how it has adopted the "Koopmans' in DFT" (KID) process, which guides its behavior to be almost equal to the ideal density functional. This is essential for any precise computation of the conceptual DFT descriptors that help in forecasting and analysis of chemical reactivity in molecular systems. Still, the γ-tuning technique for range-separated hybrids density functional is system dependent. This implies that separate density functionals are to be used in the computations of the descriptors for separate molecular features. We are then going to concentrate on part of the density functionals that have displayed the required precision in physics and chemistry [20].

The main aim of this study is to do a comparative research relating to the performance of the just identified Minnesota family of density functionals for the account of the chemical reactivity of two nucleic acids intercalating stains, SYBR green I (SYBRGI) [21] and ethidium bromide (EtBr) [22]. The molecular structures of the two are shown in **Figure 1**.
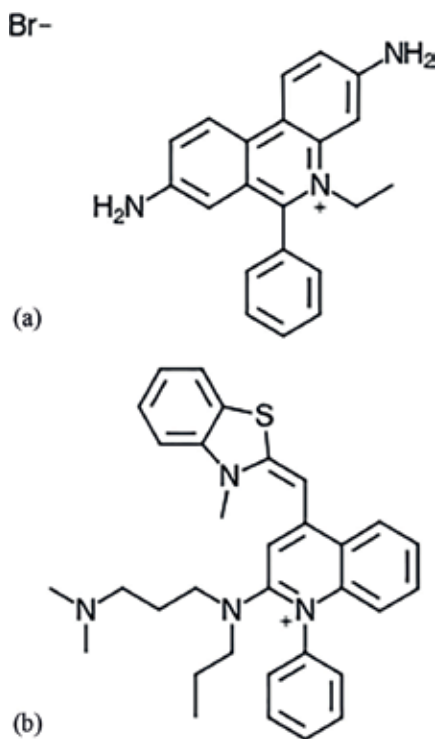

Figure 1. Molecular structures of (a) ethidium bromide (EtBr) and (b) SYBR green I (SYBRGI).

2. Theoretical background

Within the context of DFT [2, 23], the chemical potential μ, which estimates the escaping tendency of the electron from the equilibrium point is stated as follows:

$$\mu = \left(\frac{\partial E}{\partial N}\right)_{v(r)} \tag{1}$$

where χ represents the electronegativity.

Chemical hardness is represented by η, which is the opposition to charge transfer:

$$\eta = \left(\frac{\partial^2 E}{\partial N^2}\right)_{v(r)} \tag{2}$$

Employing a finite difference approximation and the Koopmans's theorem [7–10], we can write the above equation as:

$$\mu = -\frac{1}{2}(I + A) \approx \frac{1}{2}(\varepsilon_L + \varepsilon_H) = -\chi_K \tag{3}$$

$$\eta = (I - A) \approx (\varepsilon_L - \varepsilon_H) = \eta_K \tag{4}$$

where ε_H is the HOMO energy and ε_L is the LUMO energy.

An expression for the electrophilicity index ω is as below:

$$\omega = \frac{\mu^2}{2\eta} = \frac{(I + A)^2}{4(I - A)} \approx \frac{(\varepsilon_L + \varepsilon_H)^2}{4(\varepsilon_L - \varepsilon_H)} = \omega_K \tag{5}$$

Expressions for electrodonating ω^- and electroaccepting ω^+ powers are as below [24]:

$$\omega^- = \frac{(3I + A)^2}{4(I - A)} \approx \frac{(3\varepsilon_H + \varepsilon_L)^2}{16\eta_K} = \omega_K^- \tag{6}$$

and

$$\omega^+ = \frac{(I + 3A)^2}{4(I - A)} \approx \frac{(\varepsilon_H + 3\varepsilon_L)^2}{16\eta_K} = \omega_K^+ \tag{7}$$

To obtain a comparison for ω^+ and $-\omega^-$, the explanation below for net electrophilicity has been suggested [25]:

$$\Delta\omega^\pm = \omega^+ - (-\omega^-) = \omega^+ + \omega^- \approx \omega_K^+ - (-\omega_K^-) = \omega_K^+ + \omega_K^- = \Delta\omega_K^\pm \tag{8}$$

3. Settings and computational details

In this research project, each of the computations was done using Gaussian 09 programs [26] and the density functional methods as compelled in the computational package. The gradient method was used to obtain the equilibrium geometries of molecules in this research. Additionally, vibration frequencies and the force parameters were estimated through computation of analytical frequencies on still areas after optimization to check whether they were the actual minima. Def2SVP was used in this research project as the basic set for optimization of geometry and frequencies. Computation of the electronic features was achieved using Def2TZVP basic set [27, 28].

We chose a group of Minnesota density functionals, which give consistent outcomes when computing the molecular structures and systems during the research activities. The group below were selected: M11, which falls under RSH meta-generalized gradient approximation (GGA) [29]; M11L, which falls under double-range local meta-GGA [30]; MN12L, which falls under nonseparable meta-nonseparable gradient approximation (NGA) [31]; MN12SX, which falls under nonseparable hybrid nonseparable meta-NGA [32]; N12, which falls under nonseparable gradient estimation [33]; N12SX, which falls under RSH nonseparable gradient estimation [32]; SOGGA11, which falls under generalized gradient approximation (GGA) density functional [34]; and SOGGA11X, which falls under generalized gradient approximation density functional [35]. GGA can be explained as a functional whereby the functional relies on the both the up down spin densities and the minimized gradient. Nonseparable gradient approximation (NGA) can be explained as a functional that relies on up down spin densities and minimized gradient and falls under nonseparable. In the current research, each of the computations was done where the solvent used was water and by doing the calculations in conformity to the Solvation Model based on Density (SMD) solvation standard [36].

4. Results and discussion

Firstly, the molecular structures of SYBRGI and EtBr were first optimized by MOL structures, then by finding the most stable conformers through Avogadro program [37, 38]. This was done through random sampling with molecular mechanic techniques. After the optimization, the resulting conformers were then re-optimized with MN12SX, M11L, M11, N12, SOGGA11X, and SOGGA11 density functionals. In addition, Def2SVP basic set and SMD solvation model were used, water being used as a solvent.

The HOMO and LUMO energies (in eV), the ionization potential I and electron affinity A (in eV), electronegativity χ, chemical hardness η, global electrophilicity ω, electrodonating ω^-, and electroaccepting ω^+ powers, and the net electrophilicity $\Delta\omega^{\pm}$ of the EtBr and SYBRGI molecules calculated with the same density functionals and solvation model are presented in **Tables 1** and **2**, respectively. The upper part of the tables shows the results derived assuming the validity of the Kid procedure (hence the subscript K), and the lower part of the tables shows the results derived from the calculated vertical I and A through a ΔSCF technique.

Property	M11	M11L	MN12L	MN12SX	N12	N12SX	SOGGA11	SOGGA11X
HOMO	−7.535	−4.956	−4.684	−5.187	−4.164	−4.951	−4.151	−6.108
LUMO	−0.535	−3.028	−2.613	−2.576	−2.674	−2.511	−3.121	−1.808
χ_K	4.035	3.992	3.649	3.882	3.419	3.731	3.636	3.958
η_K	7.000	1.928	2.071	2.611	1.490	2.440	1.030	4.300
ω_K	1.163	4.133	3.213	2.886	3.924	2.852	6.420	1.822
ω^-_K	4.781	10.383	8.380	7.876	9.651	7.723	14.722	5.891
ω^+_K	0.746	6.391	4.732	3.994	6.232	3.992	11.086	1.933
$\Delta\omega^\pm_K$	5.527	16.774	13.112	11.869	15.883	11.714	25.808	7.824
I	5.585	5.183	4.883	5.216	4.520	4.970	4.819	5.385
A	2.711	2.782	2.408	2.624	2.344	2.579	2.788	2.663
χ	4.148	3.983	3.646	3.920	3.432	3.775	3.804	4.024
η	2.874	2.401	2.475	2.592	2.177	2.392	2.031	2.721
ω	2.994	3.303	2.685	2.965	2.706	2.978	3.562	2.975
ω^-	8.241	8.748	7.348	8.051	7.263	7.993	9.152	8.132
ω^+	4.093	4.786	3.702	4.131	3.831	4.219	5.348	4.108
$\Delta\omega^\pm$	12.335	13.514	11.050	12.182	11.094	12.212	14.500	12.241

Table 1. HOMO and LUMO energies (in eV), the ionization potential I and electron affinity A (in eV), electronegativity χ, chemical hardness η, global electrophilicity ω, electrodonating ω^- and electroaccepting ω^+ powers, and the net electrophilicity $\Delta\omega^\pm$ of the EtBr molecule.

For examining the outcomes to determine if the KID process is fulfilled, and the drive from past works [15, 19], we have come up with descriptors having the ability to compare the outcomes from HOMO and LUMO computations with those attained using vertical I and A and a ΔSCF technique. It should again be known that we have no plans to form a gap fitting by reducing the descriptor. We plan to determine if the density functionals employed in this research contain the fixed range parameter γ that helps in effective execution of the KID process. It is somehow astonishing that our research at present lacks the parameter γ. We also included a minus of the energy of the LUMO of the neutral system instead of using A as minus of HOMO of the electron system [15, 19].

The initial three descriptors are associated with the basic accomplishment of "Koopmans in DFT" estimation by associating ε_H with $-I$, ε_L with $-A$, and their responses in explaining the HOMO-LUMO gap:

$$J_I = \left| \varepsilon_H + E_{gs}(N-1) - E_{gs}(N) \right| \tag{9}$$

$$J_A = \left| \varepsilon_L + E_{gs}(N1) - E_{gs}(N+1) \right| \tag{10}$$

$$J_{HL} = \sqrt{J_I^2 + J_A^2} \tag{11}$$

Property	M11	M11L	MN12L	MN12SX	N12	N12SX	SOGGA11	SOGGA11X
HOMO	−7.593	−5.132	−4.924	−5.325	−4.587	−5.160	−4.779	−6.099
LUMO	−0.558	−2.933	−2.569	−2.545	−2.618	−2.460	−2.959	−1.768
χ_K	4.075	4.033	3.747	3.935	3.603	3.810	3.869	3.933
η_K	7.034	2.199	2.355	2.780	1.970	2.700	1.820	4.331
ω_K	1.181	3.698	2.980	2.785	3.295	2.688	4.112	1.786
ω^-_K	4.839	9.550	7.981	7.711	8.514	7.449	10.273	5.809
ω^+_K	0.763	5.517	4.234	3.776	4.911	3.639	6.404	1.876
$\Delta\omega^\pm_K$	5.602	15.067	12.214	11.486	13.425	11.088	16.677	7.685
I	5.407	5.302	5.062	5.263	4.767	5.074	4.980	5.252
A	2.643	2.747	2.400	2.589	2.358	2.521	2.690	2.564
χ	4.025	4.024	3.731	3.926	3.563	3.797	3.835	3.908
η	2.764	2.555	2.661	2.674	2.409	2.553	2.290	2.688
ω	2.931	3.169	2.615	2.882	2.635	2.824	3.210	2.841
ω^-	8.048	8.509	7.262	7.894	7.202	7.706	8.481	7.803
ω^+	4.023	4.485	3.531	3.968	3.639	3.909	4.646	3.895
$\Delta\omega^\pm$	12.071	12.994	10.972	11.862	10.841	11.615	13.128	11.699

Table 2. HOMO and LUMO energies (in eV), the ionization potential I and electron affinity A (in eV), electronegativity χ, chemical hardness η, global electrophilicity ω, electrodonating ω^- and electroaccepting ω^+ powers, and the net electrophilicity $\Delta\omega^\pm$ of the SYBRGI molecule.

Four separate descriptors will then be used to examine how the density functionals under research will help in forecasting the electronegativity χ, the chemical hardness η, the global electrophilicity ω, and the collection of conceptual DFT descriptors through deliberation of the energies of the HOMO and LUMO or the vertical I and A:

$$J_\chi = |\chi - \chi_K| \tag{12}$$

$$J_\eta = |\eta - \eta_K| \tag{13}$$

$$J_\omega = |\omega - \omega_K| \tag{14}$$

$$J_{D1} = \sqrt{J_\chi^2 + J_\eta^2 + J_\omega^2} \tag{15}$$

D1 represents the initial collection of conceptual DFT descriptors.

Finally, we came up with four extra descriptors to determine the success of the density functionals under research in forecasting of electrodonating power $\omega-$, the electroaccepting power ω^+, the net electrophilicity $\Delta\omega^\pm$, together with the four descriptors combined and considering the HOMO and LUMO energies or the vertical I and A:

$$J_{\omega^-} = \left| \omega^- - \omega_K^- \right| \tag{16}$$

$$J_{\omega^+} = \left| \omega^+ - \omega_K^+ \right| \tag{17}$$

$$J_{\Delta\omega\pm} = \left| \Delta\omega \pm -\Delta\omega\pm_K \right| \tag{18}$$

$$J_{D2} = \sqrt{J_{\omega^-}^2 + J_{\omega^+}^2 + J_{\Delta\omega\pm}^2} \tag{19}$$

D2 represents the second collection of conceptual DFT descriptors.

The results of the calculations of $J_I, J_A, J_{HL}, J_\chi, J_\eta, J_\omega, J_{D1}, J_{\omega\ -}, J_{\omega\ +}, J_{\Delta\omega\pm}$, and J_{D2} for the EtBr and SYBRGI are displayed in **Tables 3** and **4**, respectively.

As shown in **Tables 1** and **2**, and the outcomes from **Tables 3** and **4**, the precision provided by the KID process is outstanding for the MN12SX, which falls under RSH meta-NGA, and N12SX, which falls under RSH NGA density functionals. In reality, values for J_I, J_A and J_{HL} is not zero. However, the values found can satisfactorily be likened to the past studies of Lima et al. [19], whereby the minima were found by selecting a parameter that imposes such a trend.

The outcomes are necessary because they reveal that we should not depend on $\boldsymbol{J_I, J_A}$, and $\boldsymbol{J_{HL}}$ alone, i.e., if we depend on outcomes from J_χ, alone, almost all the values will near zero. For the remaining descriptors, only MN12SX and N12SX reveal such trends. This shows that outcomes for J_χ can be due to elimination of errors.

Authentication of the KID process is not done correctly by the GGA (SOGGA11) and hybrid-GGA (SOGGA11X). Local density functionals like M11L, MN12L, and N12 are also inappropriate.

Descriptor	M11	M11L	MN12L	MN12SX	N12	N12SX	SOGGA11	SOGGA11X
J_I	1.950	0.228	0.199	0.028	0.356	0.020	0.668	0.724
J_A	2.176	0.246	0.205	0.048	0.331	0.068	0.333	0.855
J_{HL}	2.922	0.335	0.285	0.055	0.486	0.071	0.747	1.120
J_χ	0.113	0.009	0.003	0.038	0.013	0.044	0.168	0.066
J_η	4.127	0.473	0.403	0.019	0.687	0.048	1.001	1.579
J_ω	1.831	0.830	0.528	0.079	1.219	0.126	2.858	1.154
J_{D1}	4.516	0.955	0.665	0.090	1.399	0.142	3.033	1.957
$J_{\omega-}$	3.460	1.635	1.033	0.175	2.388	0.271	5.570	2.242
$J_{\omega+}$	3.347	1.626	1.030	0.137	2.401	0.227	5.738	2.176
$J_{\Delta\omega+}$	6.808	3.260	2.062	0.313	4.788	0.498	11.307	4.417
J_{D2}	8.338	3.993	2.526	0.384	5.864	0.611	13.849	5.410

Table 3. Descriptors $J_I, J_A, J_{HL}, J_\chi, J_\eta, J_\omega, J_{D1}, J_{\omega\ -}, J_{\omega+}, J_{\Delta\omega\pm}$, and J_{D2} for the ethidium bromide (EtBr) molecule calculated from the results of **Table 1**.

Descriptor	M11	M11L	MN12L	MN12SX	N12	N12SX	SOGGA11	SOGGA11X
J_1	2.185	0.170	0.137	0.062	0.180	0.086	0.201	0.847
J_A	2.085	0.187	0.169	0.044	0.259	0.061	0.269	0.796
J_{HL}	3.020	0.252	0.218	0.076	0.316	0.105	0.336	1.162
J_χ	0.050	0.009	0.016	0.009	0.040	0.012	0.034	0.025
J_η	4.270	0.356	0.306	0.106	0.439	0.147	0.470	1.643
J_ω	1.751	0.529	0.365	0.097	0.660	0.136	0.902	1.055
J_{D1}	4.615	0.638	0.477	0.144	0.794	0.201	1.018	1.952
$J_{\omega-}$	3.209	1.041	0.719	0.183	1.312	0.257	1.792	1.994
$J_{\omega+}$	3.259	1.032	0.703	0.192	1.272	0.270	1.758	2.019
$J_{\Delta\omega+}$	6.469	2.073	1.422	0.376	2.584	0.527	3.550	4.013
J_{D2}	7.923	2.539	1.742	0.460	3.165	0.646	4.348	4.915

Table 4. Descriptors J_1, J_A, J_{HL}, J_χ, J_η, J_ω, J_{D1}, $J_{\omega-}$, $J_{\omega+}$, $J_{\Delta\omega\pm}$ and J_{D2} for the SYBR green I (SYBRGI) molecule calculated from the results of **Table 2**.

It is vital to know that even though the RSH hybrid NGA and RSH meta-NGA density functionalities are necessary when computing the conceptual DFT descriptors, it is a different case for RSH GGA (M11) density functional. According to **Tables 1** and **2**, this functional doesnot provide enough explanation concerning LUMO energy, and this can be due to an inaccurate figure of γ in the functional. A fine tuning of γ can handle the issue.

5. Conclusions

Weighing on the outcomes from this research work, DFT-based reactivity descriptors like electronegativity, chemical hardness, global electrophilicity, electrodonating, and electro-accepting powers, and net electrophilicity can be used to forecast EtBr's chemical reactivity.

It has also been illustrated that the KID process can effectively be implemented by the RSH meta-NGA (MN12SX) and the RSH NGA (N12SX) density functionalities. They can then be used in place of the tuned density functionals using a gap-fitting process, and we believe that such a trend can be helpful when analyzing the chemical reactivity of bigger molecular systems.

Acknowledgements

Author details

Norma Flores-Holguín[1], Juan Frau[2] and Daniel Glossman-Mitnik[1]*

*Address all correspondence to: dglossman@gmail.com

1 Laboratorio Virtual NANOCOSMOS, Departamento de Medio Ambiente y Energía, Centro de Investigación en Materiales Avanzados, Chihuahua, Mexico

2 Departament de Química, Universitat de les Illes Balears, Palma de Mallorca, Spain

References

[1] Parr RG, Yang W. Density Functional Theory of Atoms and Molecules. New York: Oxford University Press; 1989

[2] Geerlings P, De Proft F, Langenaeker W. Conceptual density functional theory. Chemical Reviews. 2003;**103**:1793-1873

[3] Toro-Labbé A, editor. Theoretical Aspects of Chemical Reactivity. Vol. 19. Amsterdam: Elsevier Science; 2007

[4] Chattaraj PK, editor. Chemical Reactivity Theory – A Density Functional View. Boca Raton: CRC Press, Taylor & Francis Group; 2009

[5] Huzinaga S, Andzelm J, Klobukowski M, Radzio-Audzelm E, Sakai Y, Tatewaki H, Gaussian Basis Sets for Molecular Calculations. Amsterdam: Elsevier; 1984

[6] Easton R, Giesen D, Welch A, Cramer C, Truhlar D. The MIDI! basis set for quantum mechanical calculations of molecular geometries and partial charges. Theoretical Chemistry Accounts. 1996;**93**:281-301

[7] Lewars E. Computational Chemistry – Introduction to the Theory and Applications of Molecular and Quantum Mechanics. Dordrecht: Kluwer Academic Publishers; 2003

[8] Young D. Computational Chemistry – A Practical Guide for Applying Techniques to Real-World Problems. New York: John Wiley & Sons; 2001

[9] Jensen F. Introduction to Computational Chemistry. 2nd ed. Chichester, England: John Wiley & Sons; 2007

[10] Cramer C. Essentials of Computational Chemistry – Theories and Models. 2nd ed. Chichester, England: John Wiley & Sons; 2004

[11] Perdew JP, Parr RG, Levy M, Balduz JLJ. Density-functional theory for fractional particle number: Derivative discontinuities of the energy. Physical Review Letters. 1982;**49**: 1691-1694

[12] Almbladh CO, von Barth U. Exact results for the charge and spin densities, exchange-correlation potentials, and density-functional eigenvalues. Physical Review B. 1985;**31**: 3231-3244

[13] Perdew JP, Burke K, Ersernhof M. Erratum: Generalized gradient approximation made simple. Physical Review Letters. 1997;**78**:1396

[14] Levy M, Perdew JP, Sahni V. Exact differential equation for the density and ionization energy of a many-particle system. Physical Review A. 1984;**30**:2745-2748

[15] Kronik L, Stein T, Refaely-Abramson S, Baer R. Excitation gaps of finite-sized systems from optimally tuned range-separated hybrid functionals. Journal of Chemical Theory and Computation. 2012;**8**(5):1515-1531

[16] Savin A. Beyond the Kohn-Sham determinant. In: Recent Advances in Density Functional Methods. Singapore: World Scientific; 2011. Ch. 4. pp. 129-153

[17] Leininger T, Stoll H, Werner HJ, Savin A. Combining long-range configuration interaction with short-range density functionals. Chemical Physics Letters. 1997;**275**(3):151-160

[18] Savin A, Flad HJ. Density functionals for the Yukawa electron-electron interaction. International Journal of Quantum Chemistry. 1995;**56**(4):327-332

[19] Lima IT, Prado ADS, Martins JBL, de Oliveira Neto PH, Ceschin AM, da Cunha WF, da Silva Filho DA. Improving the description of the optical properties of carotenoids by tuning the long-range corrected functionals. The Journal of Physical Chemistry A. 2016;**120**(27):4944-4950

[20] Peverati R, Truhlar DG. Quest for a universal density functional: The accuracy of density functionals across a broad spectrum of databases in chemistry and physics. Philosophical Transactions. Series A, Mathematical, Physical, and Engineering Sciences. 2014;**372**(2011): 20120476

[21] Green F, editor. The Sigma-Aldrich Handbook of Stains, Dyes, and Indicators. Milwaukee, Wis: Aldrich Chemical Co.; 1990

[22] Sabnis R, editor. Handbook of Biological Dyes and Stains. New Jersey, Hoboken: John Wiley & Sons; 2010

[23] Parr RG, Yang W. Density functional approach to the frontier-electron theory of chemical reactivity. Journal of the American Chemical Society. 1984;**106**:4049-4050

[24] Gázquez JL, Cedillo A, Vela A. Electrodonating and electroaccepting powers. Journal of Physical Chemistry A. 2007;**111**(10):1966-1970

[25] Chattaraj PK, Chakraborty A, Giri S. Net electrophilicity. Journal of Physical Chemistry A. 2009;**113**(37):10068-10074

[26] Frisch MJ, Trucks GW, Schlegel HB, Scuseria GE, Robb MA, Cheeseman JR, Scalmani G, Barone V, Mennucci B, Petersson GA, Nakatsuji H, Caricato M, Li X, Hratchian HP, Izmaylov AF, Bloino J, Zheng G, Sonnenberg JL, Hada M, Ehara M, Toyota K, Fukuda R, Hasegawa J, Ishida M, Nakajima T, Honda Y, Kitao O, Nakai H, Vreven T, Montgomery Jr JA, Peralta JE, Ogliaro F, Bearpark M, Heyd JJ, Brothers E, Kudin KN, Staroverov VN, Kobayashi R, Normand J, Raghavachari K, Rendell A, Burant JC, Iyengar SS, Tomasi J, Cossi M, Rega N, Millam JM, Klene M, Knox JE, Cross JB, Bakken V, Adamo C, Jaramillo J, Gomperts R, Stratmann RE, Yazyev O, Austin AJ, Cammi R, Pomelli C, Ochterski JW, Martin RL, Morokuma K, Zakrzewski VG, Voth GA, Salvador P, Dannenberg JJ, Dapprich S, Daniels AD, Farkas O, Foresman JB, Ortiz JV, Cioslowski J, Fox DJ. Gaussian 09 Revision D.01. Wallingford CT: Gaussian Inc.; 2016

[27] Weigend F, Ahlrichs R. Balanced basis sets of split valence, triple zeta valence and quadruple zeta valence quality for H to Rn: Design and assessment of accuracy. Physical Chemistry Chemical Physics. 2005;**7**:3297-3305

[28] Weigend F. Accurate coulomb-fitting basis sets for H to R. Physical Chemistry Chemical Physics. 2006;**8**:1057-1065

[29] Peverati R, Truhlar DG. Improving the accuracy of hybrid meta-GGA density functionals by range separation. The Journal of Physical Chemistry Letters. 2011;**2**(21):2810-2817

[30] Peverati R, Truhlar DG. M11-L: A local density functional that provides improved accuracy for electronic structure calculations in chemistry and physics. The Journal of Physical Chemistry Letters. 2012;**3**(1):117-124

[31] Peverati R, Truhlar DG. An improved and broadly accurate local approximation to the exchange-correlation density functional: The MN12-L functional for electronic structure calculations in chemistry and physics. Physical Chemistry Chemical Physics. 2012;**14**(38):13171-13174

[32] Peverati R, Truhlar DG. Screened-exchange density functionals with broad accuracy for chemistry and solid-state physics. Physical Chemistry Chemical Physics. 2012;**14**(47):16187-16191

[33] Peverati R, Truhlar DG. Exchange-correlation functional with good accuracy for both structural and energetic properties while depending only on the density and its gradient. Journal of Chemical Theory and Computation. 2012;**8**(7):2310-2319

[34] Peverati R, Zhao Y, Truhlar DG. Generalized gradient approximation that recovers the second-order density-gradient expansion with optimized across-the-board performance. The Journal of Physical Chemistry Letters. 2011;**2**(16):1991-1997

[35] Peverati R, Truhlar DG. Communication: A global hybrid generalized gradient approximation to the exchange-correlation functional that satisfies the second-order density-gradient constraint and has broad applicability in chemistry. The Journal of Chemical Physics. 2011;**135**(19):191102

[36] Marenich A, Cramer C, Truhlar DG. Universal solvation model based on solute electron density and a continuum model of the solvent defined by the bulk dielectric constant and atomic surface tensions. Journal of Physical Chemistry B. 2009;**113**:6378-6396

[37] Avogadro: An Open-Source Molecular Builder and Visualization Tool – Version 1.2.0. 2016. Available from: http://avogadro.openmolecules.net

[38] Hanweel M, Curtis DE, Lonie D, Vandermeersch T, Zurek E, Hutchison G. Avogadro: An advanced semantic chemical editor, visualization, and analysis platform. Journal of Cheminformatics. 2012;**4**:17

Spectra and Thermodynamics

Spectroscopy, Substituent Effects, and Reaction Mechanisms

Burkhard Kirste

Additional information is available at the end of the chapter

Abstract

Applications of density functional theory (DFT) calculations to organic chemistry are shown, beginning with geometry optimization and the calculation of vibrational frequencies, infrared (IR) intensities, and thermodynamic properties. The isotropic chemical shielding values and anisotropies relevant to nuclear magnetic resonance (NMR) can be calculated using gauge-invariant atomic orbitals (GIAOs); the calculation of spin-spin couplings is possible but time-consuming. For free radicals, hyperfine couplings and g tensors pertaining to EPR can be obtained. Regarding UV/vis spectra, wavelengths and oscillator strengths can be calculated by using a time-dependent Hamiltonian. In addition to gas-phase acidities, approximate pK_a values can be obtained, provided that solvation is taken into account. Several sets of substituent parameters have been calculated: Hammett σ and σ^+ parameters and inductive and mesomeric effects. Regarding reaction mechanisms, geometries and energies of intermediates and transition structures have been calculated for pericyclic reactions, nucleophilic aliphatic substitutions, electrophilic aromatic substitutions, additions, and eliminations.

Keywords: density functional theory, spectroscopy, magnetic resonance, Hammett parameters, reaction mechanisms, pericyclic reactions

1. Introduction

Focusing on density functional theory (DFT) calculations with Gaussian 09 [1] and the B3LYP/6-311G(d,p) method, several applications to organic chemistry will be shown. After geometry optimization, which yields the total energy, a frequency calculation can be done, yielding the infrared spectrum (wave numbers and intensities) and, if requested, the Raman intensities and the thermodynamic properties (enthalpy, entropy, and Gibbs free energy).

Using a time-dependent Hamiltonian, UV/vis spectra can be calculated (wave lengths and oscillator strengths). Nuclear magnetic resonance (NMR) spectra can be calculated, providing

isotropic shielding values as well as tensor data (anisotropies) of all magnetic nuclei, using gauge-invariant atomic orbitals (GIAOs). The calculation of spin-spin coupling constants is also possible but requires much more computational time. For free radicals, EPR data can be calculated: isotropic hyperfine coupling constants, hyperfine tensors, and g tensors; in this case, the restricted B3LYP method has to be replaced by the unrestricted UB3LYP method.

Substituent effects such as the σ parameters in the Hammett equation can also be estimated. Although a calculation of changes in the charge distribution might seem to be a promising method for that purpose, it was found that calculated ^{19}F shielding values ("virtual NMR experiments") yielded much more convincing results. The calculation of gas-phase acidities or basicities is straightforward, and the calculated data show a good correlation with experimental data. However, the correlation with pK_a values, which refer to aqueous solutions, is very poor. A reasonable correlation was obtained by taking a few water molecules explicitly into account, in addition to the bulk solvent properties of water.

Regarding organic reaction mechanisms, pericyclic reactions are particularly well amenable to DFT calculations. Usually, the transition structure can be obtained which is characterized by a single imaginary frequency, which belongs to the reaction coordinate. For many other reaction types (substitutions, additions, eliminations, and rearrangements), at least an approximation to the transition structure can be calculated. Moreover, starting with such a structure and performing an optimization, the approximate dynamics of the reaction can be followed.

2. Geometries, energies, and thermodynamic data

2.1. Geometry optimization

As a starting point, a reasonable approximation to the geometry of the target molecule is required. Preferably, the coordinate file should be given as Z matrix, and standard bond lengths and angles may be used. A convenient tool for the generation of Z matrices is molden [2]: in the Z-mat editor, start with methane, substitute by phenyl and finally by vinyl, and save as Z matrix (GAMESS). Next, the input file for the quantum-chemical calculation has to be created by supplementing the Z matrix file with the necessary parameters (see Appendix A).

After a successful calculation, the log file contains the energy (in Hartree) and the coordinates of the optimized structure. Again, it is advantageous to use a tool such as molden for analyzing the log file.

2.2. Calculation of thermodynamic properties

For a determination of the thermodynamic properties, it is necessary to calculate the (vibrational) frequencies. In the Gaussian input file, the preliminary coordinates have to be replaced by the optimized ones and the task "Opt" by "Freq". (Actually, the request for "Freq Prop Pop = Full" additionally provides useful information such as charges and dipole moment. By default, the calculation is done for 298 K and 1.000 atm, but a different temperature or pressure may be specified.)

For the example molecule (*p*-methylstyrene), the salient results are as follows:

SCF Done: E(RB3LYP)	−349.054882687 AU
Zero-point correction	0.159885 (Hartree/particle)
Thermal correction to energy	0.167687
Thermal correction to enthalpy	0.168631
Thermal correction to Gibbs free energy	0.127033
Sum of electronic and zero-point energies	−348.894997
Sum of electronic and thermal energies	−348.887196
Sum of electronic and thermal enthalpies	−348.886252
Sum of electronic and thermal free energies	−348.927850
Total E (thermal)	105.225 kcal/mol
Total CV	30.240 cal/mol-K
Total S (entropy)	87.551 cal/mol-K

Most data are given in Hartree (see Appendix A), they refer to the formation from atomic nuclei and electrons. It is fairly easy to calculate the energy of formation from the atoms by subtracting the energies obtained for respective calculations of free atoms. In order to obtain approximate values for standard enthalpies of formation, bond energies and possibly enthalpies of phase changes (to the gas phase) have to be taken into account. It should be mentioned that the accuracy of these data, i.e., the agreement with experimental data, is not very good. It is advisable to restrain to energy (or enthalpy) differences of similar structures. Alternatively, approximate enthalpies of formation can be obtained more easily from semiempirical calculations (such as MNDO, AM1, or PM3).

Energies of some important free atoms (UB3LYP/6-311G(d,p) in Hartree): H, −0.502155930031; C, −37.8559889346; N, −54.5985431427; O, −75.0853856058; F, −99.7538096003; P, −341.280503655; S, −398.132082447; and Cl, −460.166160487.

Hence, the following energy of formation from the atoms is obtained for *p*-methylstyrene, C_9H_{10}, $\Delta E_{f\ atomic}$ = −348.887196−9 × (−37.8559889346)−10 × (−0.502155930031) = −3.161736288290 Hartree = −8301.139 kJ/mol.

Enthalpies required to generate free atoms from the elements in the standard state (kJ/mol) [3]: H, 218.00; C, 716.67; N, 472.68; O, 249.17; F, 78.4; P, 314.55; S, 276.98; and Cl, 121.29.

These values have to be added to the above-given atomic energy of formation (ignoring somewhat the difference between energy and enthalpy), yielding the following energy of formation for our example: −8301.14 + 9 × 716.67 + 10 × 218.00 = 328.89 kJ/mol.

The energy can be converted to the enthalpy by means of Eq. (1), assuming the validity of the ideal gas law; Δn is the change in the number of moles of gases:

$$\Delta H = \Delta E + \Delta nRT \qquad (1)$$

$$\Delta H = \Delta E + \Delta n \times 2.479 \frac{kJ}{mol} \ (T = 298.15 \ K) \qquad (2)$$

In the example, 1 mole of product molecules (in the gas phase) is formed from 19 moles of atoms; therefore, Δn is -18 and the correction is -44.62 kJ/mol. Hence, the calculated enthalpy of formation of p-methylstyrene in the gas phase is $\Delta H_f^\circ = 284.27$ kJ/mol.

The following experimental value for the enthalpy of formation of liquid p-methylstyrene is given in the literature: $\Delta H_f^\circ(l) = 114.6$ kJ/mol [3]; adding the heat of vaporization of 47.6 kJ/mol [4], $\Delta H_f^\circ(g) = 162.2$ kJ/mol for the gas phase. Thus, the calculated value deviates by about 120 kJ/mol.

By comparison, a semiempirical AM1 calculation yields an enthalpy of formation of $\Delta H_f^\circ = 140.3$ kJ/mol, in better agreement with experiment.

3. Spectroscopy

3.1. Vibrational spectroscopy: infrared and Raman

Vibrational frequencies and hence infrared (IR) and Raman spectra can be calculated (Gaussian keyword "Freq"). In Gaussian 09, the infrared intensities are calculated by default, but the Raman intensities can also be obtained (keyword "Freq = Raman"). The calculated frequencies can be assigned to the respective molecular motions. The visualization of vibrations is easily achieved by tools such as molden.

As an example, p-cyanobenzaldehyde will be considered (**Figure 1**). The experimental IR data have been taken from the SDBS database [5]. The two most prominent features are the C=O valence vibration at 1788 (exp. 1708) and the CN valence vibration at 2340 (2230) cm^{-1}.
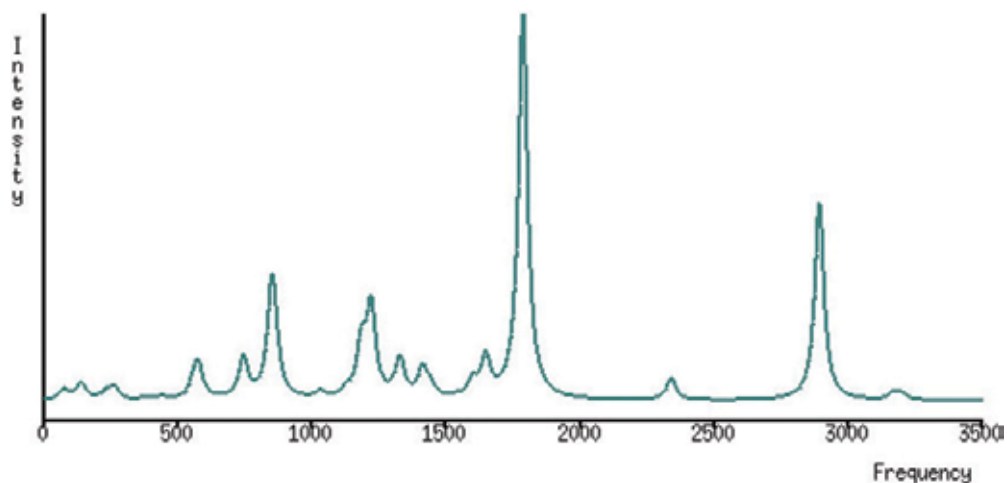

Figure 1. Calculated IR spectrum of p-cyanobenzaldehyde.

3.2. Nuclear magnetic resonance (NMR)

The calculation of isotropic chemical shielding values *(σ)* or shielding tensors requires some kind of "scaling" of the orbitals, for instance, the use of gauge-invariant atomic orbitals (GIAOs) [6]. In Gaussian 09, the keyword "NMR" automatically invokes the use of GIAOs, and isotropic shielding values, anisotropies, and shielding tensors are calculated. In NMR experiments, however, not the shielding values are measured, but chemical shifts, which refer to some standard. For ^{1}H, ^{13}C, and ^{29}Si NMR, tetramethylsilane (TMS) is used as a standard, and the respective chemical shifts of the three kinds of magnetic nuclei are set to zero (δ_{H-1}(TMS) = 0 ppm, δ_{C-13}(TMS) = 0 ppm, and δ_{Si-29}(TMS) = 0 ppm). Using the hybrid method B3LYP/6-311(d,p), the following average shielding values are obtained for protons and for ^{13}C nuclei: $\sigma(^1H)$ = 31.3919 ppm and $\sigma(^{13}C)$ = 179.7024 ppm. The chemical shifts are then simply obtained by subtraction:

$$\delta_i = \sigma_{ref} - \sigma_i \tag{3}$$

Using the abovementioned reference value for protons, the calculated chemical shifts are generally too small by about 0.5 ppm. In a survey of 21 natural products, a better fit for ^{13}C nuclei, on the average, was obtained by using a reference value of 177.0 ppm instead [7].

For the example molecule *p*-methylstyrene, the following ^{1}H and ^{13}C chemical shifts (δ in ppm) were calculated (using the above-given calculated shielding values for TMS as reference); experimental ^{13}C chemical shifts were taken from the NMRSHIFTDB database (**Figure 2** and **Table 1**) [8].

It is also possible to calculate NMR spin-spin coupling constants, i.e., J [Hz] (Gaussian keyword "NMR = SpinSpin"), but at the expense of computational time. The results obtained with the B3LYP hybrid functional are much better than those of HF ab initio calculations.

For *p*-methylstyrene, the following proton-proton spin-spin coupling constants J [Hz] were calculated: $J_{13,14}$ = 6.86, $J_{15,16}$ = 7.09 (*o*), $J_{14,15}$ = 1.29, $J_{13,16}$ = 1.26 (*m*), $J_{13,15}$ = 0.41, $J_{14,16}$ = 0.28 (*p*),
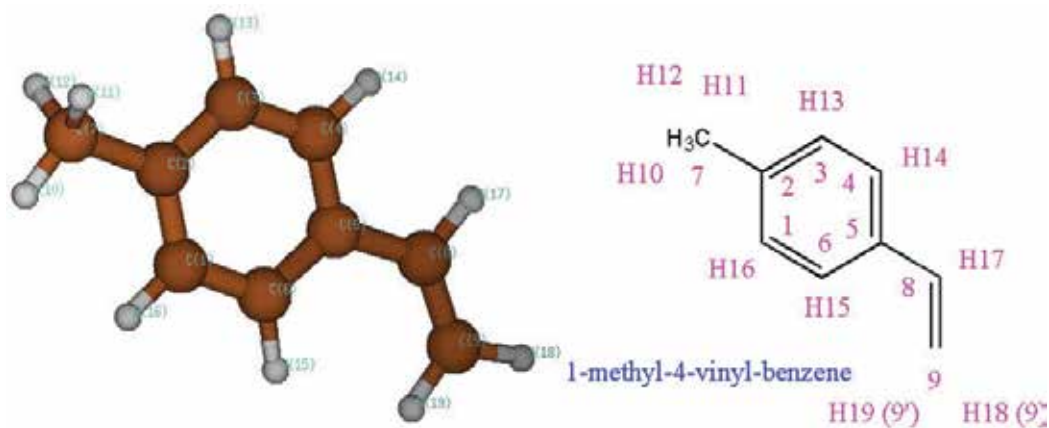

Figure 2. 3D model and numbering scheme of 1-methyl-4-vinylbenzene.

Pos.	C calc	C exp	H calc	H pred
1	129.7	128.6	6.67	7.39
2	140.2	136.5	–	–
3	129.7	128.6	6.73	7.39
4	131.0	127.7	6.54	7.59
5	136.1	136.0	–	–
6	122.8	127.7	7.24	7.59
7	18.7	20.0	1.71	2.41
8	139.7	136.3	6.07	6.72
9	109.8	112.8	4.70	5.25
9'			5.42	5.76

Table 1. Chemical shifts of *p*-methylstyrene (δ in ppm) (cf. **Figure 2**).

$J_{17,19}$ = 14.72 (*trans*), $J_{17,18}$ = 10.11 (*cis*), and $J_{18,19}$ = −0.53 (*gem*). These values are in accordance with those found in similar systems.

It should be mentioned that NMR data provide an excellent and sensitive test for the accuracy of quantum-chemical calculations.

3.3. Electron paramagnetic resonance (EPR)

In the case of free radicals, unrestricted calculations have to be performed in which different orbitals are assigned to α and β spins. Whereas unrestricted Hartree-Fock (UHF) calculations yield poor results for hyperfine couplings (HFC) because of serious problems due to spin contamination, calculations with the UB3LYP hybrid functional yield fairly acceptable results [9]. The calculations yield Mulliken spin densities (better designated as spin populations), isotropic HFC (Fermi contact coupling constants), and anisotropic hyperfine tensors. *g* values and *g* tensors can also be calculated (in the Gaussian system, this requires the "NMR" keyword). The *g* value is a dimensionless proportionality factor which relates the magnetic moment to the angular momentum; the value for the free electron is g_e = 2.00232, and only the electron spin is involved. In molecules, contributions from orbital momentum have to be taken into account, and the phenomenon becomes anisotropic. The calculated HFC and *g* values may be compared with experimental data from EPR spectroscopy (electron spin resonance, also called electron paramagnetic resonance) [10].

The method will be illustrated using the ubisemiquinone-Q1 radical anion as example, which serves as a model compound for coenzyme Q10.

Figure 3 shows the calculated Mulliken spin densities and the calculated proton HFC of this radical anion. The rotation of the long side chain is hindered; therefore, the two methylene
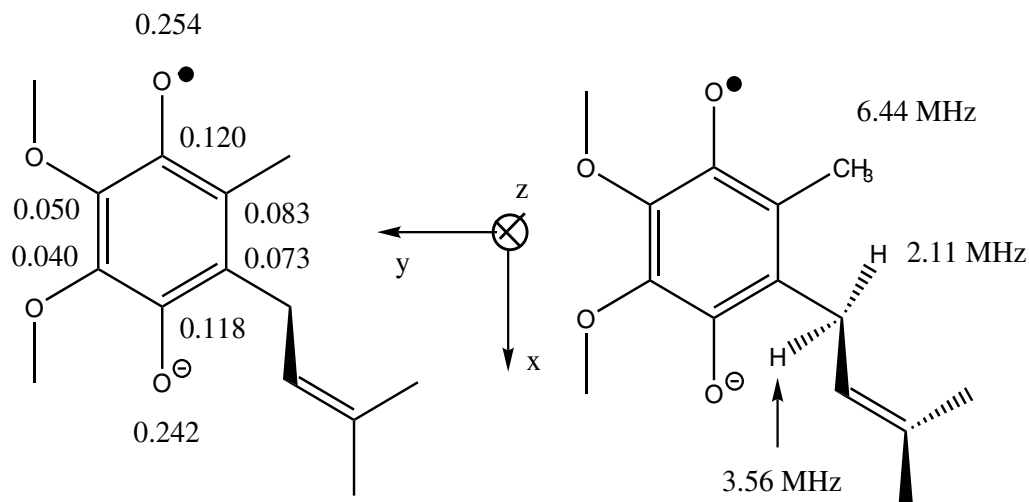
Figure 3. Ubisemiquinone-Q1 radical anion. Left: Mulliken spin densities. Right: calculated HFC.

protons are inequivalent. Comparison with experimental data (ethanol, 230 K, in parentheses) [11]: 6.44 (5.84), methyl protons, and 3.56 (3.68) and 2.11 (2.17) MHz, methylene protons. The g tensor has been measured by high-field EPR experiments [12]; again, the experimental values are given in parentheses: g_{xx} = 2.00826 (2.00646), g_{yy} = 2.00601 (2.00542), g_{zz} = 2.00207 (2.00222), and g_{iso} = 2.00545 (2.00470).

3.4. Electron spectroscopy (UV/vis)

In Hückel molecular orbital (HMO) theory, electronic excitation may be viewed as excitation of an electron from an occupied to an unoccupied orbital. The transition with the lowest energy, i.e., the longest wavelength, involves the excitation from the highest occupied molecular orbital (HOMO) to the lowest unoccupied molecular orbital (LUMO), although this transition might be forbidden.

In DFT, however, the Kohn-Sham orbitals are not suitable for this procedure, and a time-dependent Hamiltonian has to be used in the calculation (Gaussian keyword "TD"). The calculation gives the energies and the wavelengths of the excitations, the oscillator strengths f, and reports the orbitals which are involved. The vibrational fine structure and the consequences of the Franck-Condon principle are not taken into account.

In the case of the symmetrical crystal violet cation, the HOMO is represented by two degenerate orbitals, and two excitations have the same wavelength, calculated as 504.7 nm (f = 0.806); experimental data for the absorption maxima: 591.0 and 540.5 nm.

For further examples, see [13].

4. Substituent effects

4.1. Hammett σ parameters

The Hammett σ parameters refer to the acidities of substituted benzoic acids which will be considered in Section 4.3. Regarding electrophilic aromatic substitution (see Section 5.3), a modified set has to be used, at least for the *para* positions (σ^+ parameters). The Hammett equation is

$$\log \frac{k_i}{k_0} = \sigma\rho \qquad (4)$$

where ρ is the reaction parameter and k_0 and k_i are the rate constants for the unsubstituted and substituted compounds, respectively. The σ/σ^+ parameters for electrophilic aromatic substitution have been determined from the relative stabilities of the σ complexes as averages for the following four reactions: protonation, bromination, nitration, and alkylation (by ethyl groups). A linear fit of σ/σ^+ (literature data [14]) versus calculated σ (DFT) was determined for 17 substituents both in *meta* and in *para* positions, yielding a squared correlation coefficient of $r^2 = 0.932$ (see **Figure 4** and **Table 2**).
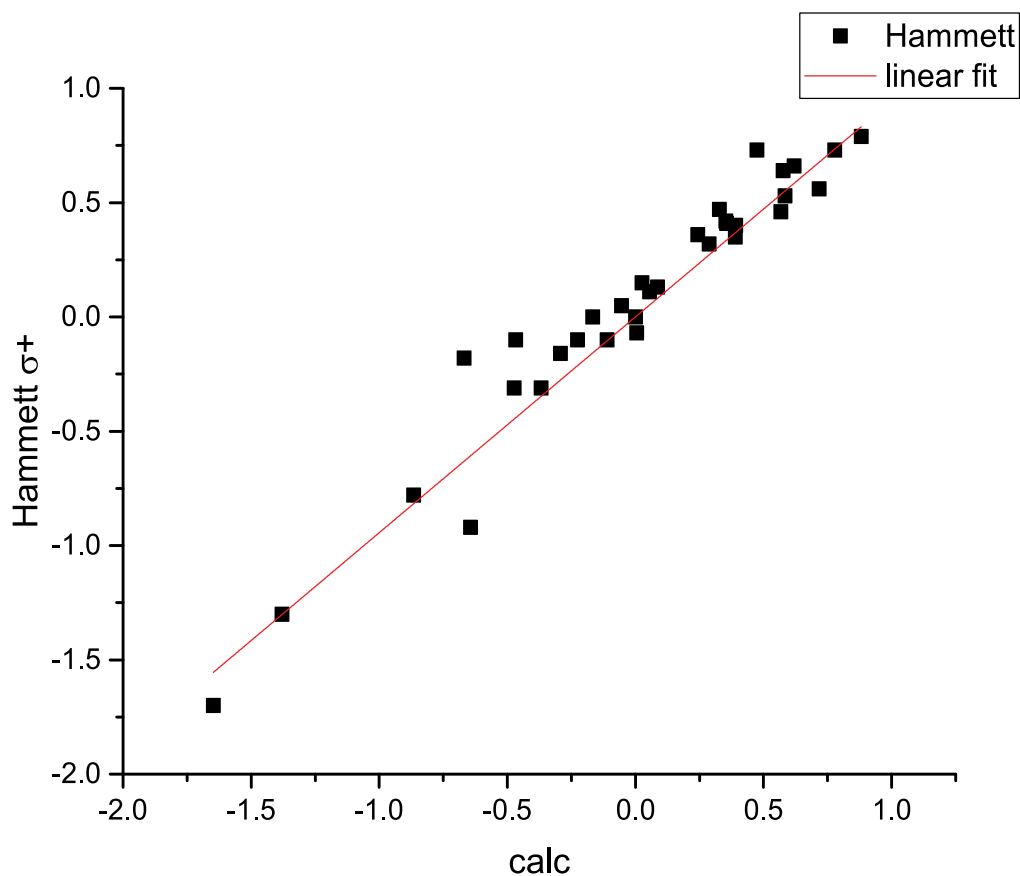
Figure 4. Plot of literature data for Hammett σ/σ^+ parameters versus calculated values (DFT).

Substituent	σ meta DFT	σ meta lit.	σ^+ para DFT	σ^+ para lit.
H	0.00	0.00	0.00	0.00
Methyl	−0.11	−0.10	−0.37	−0.31
t-Butyl	−0.23	−0.10	−0.47	−0.31
Phenyl	−0.17	0.00	−0.67	−0.18
Hydroxy	0.09	0.13	−0.64	−0.92
Methoxy	−0.06	0.05	−0.87	−0.78
Amino	−0.29	−0.16	−1.38	−1.30
Dimethylamino	−0.47	−0.10	−1.65	−1.70
Fluoro	0.39	0.35	0.00	−0.07
Chloro	0.39	0.40	0.06	0.11
Bromo	0.36	0.41	0.03	0.15
Nitro	0.78	0.73	0.88	0.79
Cyano	0.72	0.56	0.62	0.66
Trifluoromethyl	0.57	0.46	0.58	0.53
Acetyl	0.24	0.36	0.33	0.47
Carboxy	0.29	0.32	0.35	0.42
Sulfonyl	0.58	0.64	0.47	0.73

Table 2. Calculated (DFT) and literature data [14] for Hammett σ/σ^+ parameters.

4.2. Estimating inductive and mesomeric effects by virtual ^{19}F NMR

The relative contributions of inductive *(I)* and mesomeric *(M)* effects might be inferred from a comparison of the Hammett σ/σ^+ parameters (see Section 4.1) for the *para (I + M)* and *meta (I + M/3)* positions. Yet, a different approach is taken here. Using DFT, the obvious target to look for should be the charge density distribution. However, it turned out that the Mulliken charges, at least, did not yield satisfying results. Therefore, calculated isotropic ^{19}F shielding values were used as a probe of local charge density. As a suitable system, 4-substituted (*E,E*)-1-fluoro-1,3-butadienes were chosen, in two conformations (**Figure 5**).

The geometries were optimized for the planar conformation, and the shielding values were calculated for this conformation (0°) and for the orthogonal conformation with a dihedral angle of 90° for the central single bond (see **Figure 5**). The relative shielding values $\sigma_{rel}(^{19}F)$ at 90° should be proportional to the inductive *(I)* effect, and the differences of the relative shielding values at 0° and at 90°, $\sigma_{rel}(^{19}F)_{0°} - \sigma_{rel}(^{19}F)_{90°}$, should be proportional to the mesomeric *(M)* effect. The reference compound is, of course, the unsubstituted compound (R = H). These data were calibrated against the Hammett σ/σ^+ parameters, yielding a slope of −20.447, i.e., the data have to be divided by this factor. According to the sign convention of the Hammett σ/σ^+ parameters, electron-withdrawing groups (EWG, $-I$, $-M$) have a positive sign (e.g., nitro and cyano), whereas electron-releasing groups (ERG, $+I$, $+M$) have a negative sign (e.g., alkyl groups) (see **Table 3**).
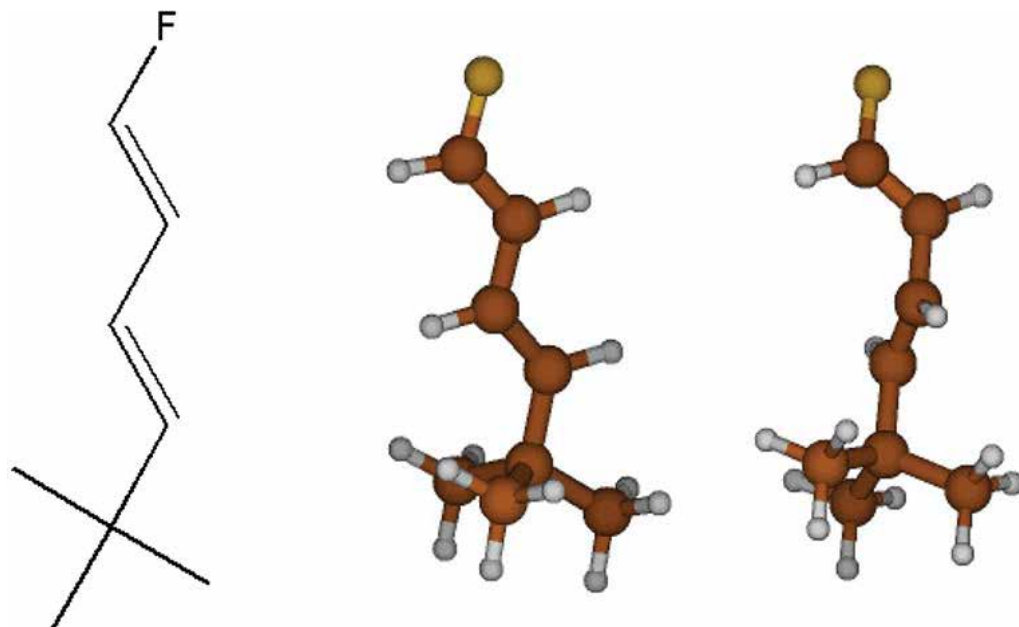
Figure 5. 3D models of two conformations of 1-fluoro-5,5-dimethyl-1,3-hexadiene.

Substituent	σ_I	σ_M
H	0.00	0.00
Nitro	0.47	0.99
Cyano	0.35	0.57
Acetyl	0.16	0.69
Carboxy	0.16	0.75
Methoxycarbonyl	0.12	0.69
Trifluoromethyl	1.02	−0.29
Fluoro	0.39	−0.43
Chloro	0.33	−0.23
Bromo	0.30	−0.21
Methyl	−0.04	−0.25
Hydroxy	0.18	−0.74
Methoxy	0.16	−0.74
Amino	0.01	−1.21
Dimethylamino	−0.02	−1.17

Table 3. Calculated inductive (σ_I) and mesomeric (σ_M) effects (DFT) (see text).

4.3. Acids and bases: pK_a values

The calculation of gas-phase acidities is straightforward, but they do not correlate well with experimental pK_a values [13]. This situation is only partially improved by taking the bulk properties of the solvent (water) into account (Gaussian keyword "SCRF = (Solvent = Water)"). A much better approximation is obtained when additionally a few water molecules are taken into account explicitly, e.g., two water molecules in the case of carboxylic acids (see **Figure 6**).

Thus, Gibbs free energies for benzoic acid and a series of substituted benzoic acids (15 substituents both in *meta* and in *para* positions) as well as the respective anions were calculated. $\Delta G^{\circ} = G^{\circ}(\text{anion}) - G^{\circ}(\text{acid})$ was converted from Hartree to kJ/mol (see Appendix A), and log K_a was calculated according to

$$\Delta G^{\circ} = -2.3026 \, RT \log K_a \tag{5}$$

$$pK_a = -\log K_a \tag{6}$$

The *relative* pK_a values were found to be quite reasonable but have to be scaled. Since the difference log K_a (substituted benzoic acid)-log K_a (benzoic acid) should be equal to the Hammett σ parameter, a linear fit of σ (literature data [14]) versus calculated $\Delta(\log K_a)$ (DFT) was determined, yielding a slope of 0.3437 and a squared correlation coefficient of $r^2 = 0.967$
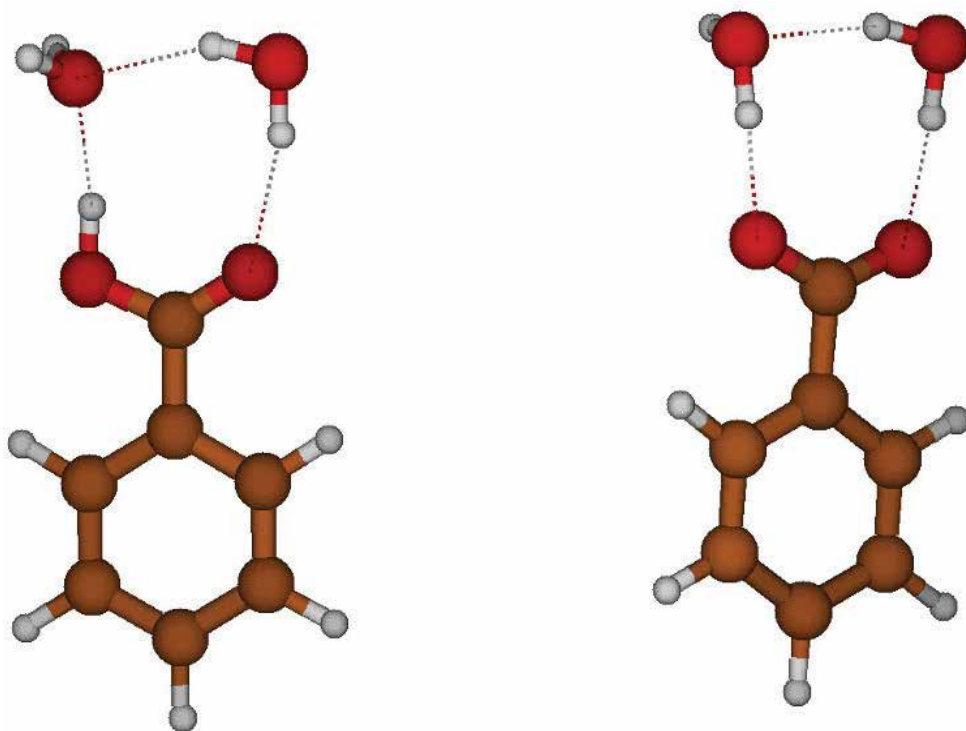
Figure 6. 3D models of dihydrates of benzoic acid and benzoate anion.
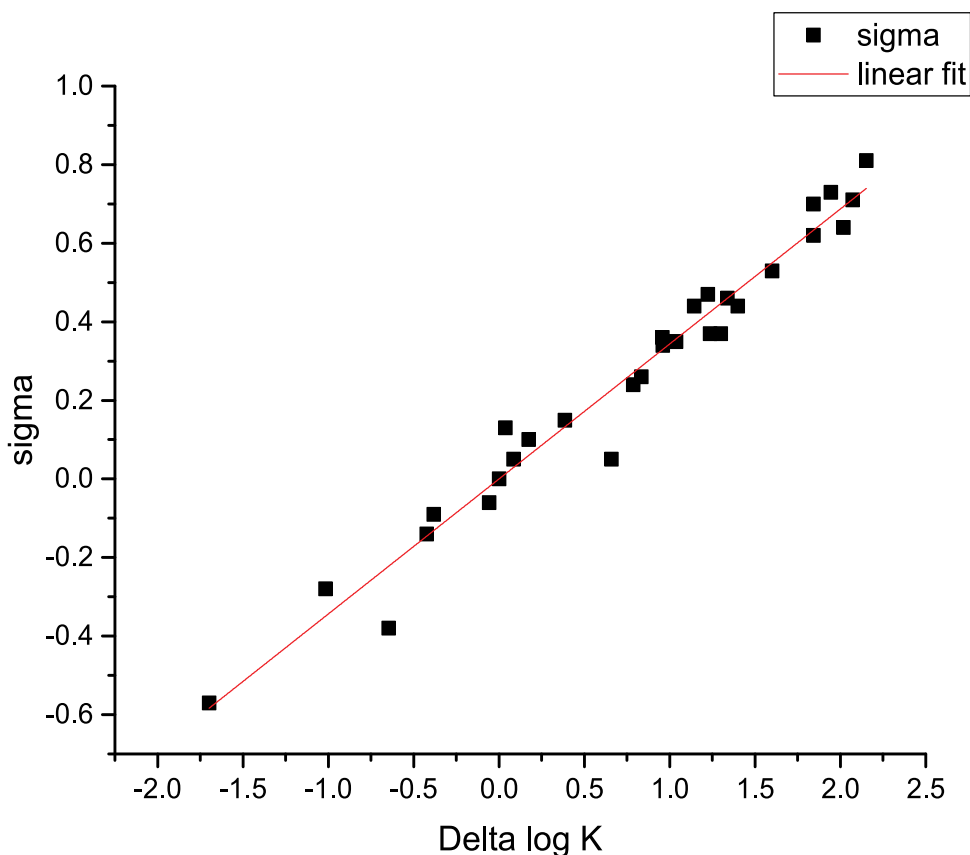
Figure 7. Plot of Hammett σ parameters versus calculated relative log K_a values (DFT).

(**Figure 7**). That means, the substituent effect on the calculated pK_a value is overestimated by about a factor of 3.

For the calculation of *absolute* pK_a values, the considerable Gibbs free solvation energy of the proton has to be taken into account ($\Delta G° = -1120.39$ kJ/mol). The calculated Gibbs free energy of the dissociation of benzoic acid in the gas phase is $\Delta G° = 1446.04$ kJ/mol. For the hydration (dihydrate model, vide supra), $\Delta G° = -47.35$ kJ/mol and $\Delta G° = -302.76$ kJ/mol are obtained for benzoic acid and benzoate anion, respectively; in total, $\Delta G° = 1375.80$ kJ/mol. Hence, the estimate for the Gibbs free energy of the dissociation of benzoic acid in aqueous solution is $\Delta G° = 1446.04 - 1375.80 = 70.24$ kJ/mol corresponding to a pK_a value of 12.31 (exp. 4.19). To put it differently, the model applied here accounts for about 96.7% of the true Gibbs free energy of solvation.

5. Reaction mechanisms

5.1. Pericyclic reactions

In a pericyclic reaction, σ or π bonds change concertedly ("simultaneously") along a perimeter, i.e., a cycle. They have first been studied theoretically by Woodward and Hoffmann ("the

conservation of orbital symmetry") [15]. Typical examples are sigmatropic reactions such as the Cope rearrangement, cycloadditions such as the Diels-Alder addition, or electrocyclic reactions (ring closures or openings).

Pericyclic reactions are particularly well amenable to DFT calculations; the transition structure can usually be obtained. The transition structure is a saddle point in the energy hyperspace, i.e., the energy has a maximum along the reaction path (the reaction coordinate), but is minimized with respect to all other coordinates. This can be checked by a frequency calculation. Exactly one frequency should be imaginary, namely, the one pertaining to the reaction coordinate. Thus, the reaction dynamics can be visualized by looking at that vibration.

5.1.1. Cope rearrangement

The Cope rearrangement is a [3,3] sigmatropic reaction. As an example, the degenerate Cope reaction of 1,5-hexadiene is shown (see **Figures 8** and **9**). The calculated activation energy is 129 kJ/mol (DFT).
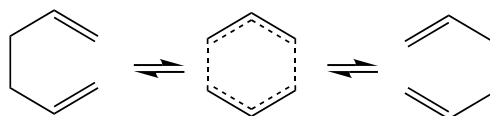
Figure 8. Scheme of the degenerate cope reaction of 1,5-hexadiene.

Figure 9. Cope reaction: 3D models of reactant, transition structure, and product.

5.1.2. Diels-Alder addition

The Diels-Alder addition is a [4 + 2] cycloaddition, a diene reacts with a dienophile to form a (substituted) cyclohexene. As an example, the Diels-Alder addition of acrylonitrile to cyclopentadiene leading to the *endo*-product is shown (see **Figures 10** and **11**). The calculated activation energy is 40 kJ/mol, and the calculated reaction energy is −132 kJ/mol (DFT).
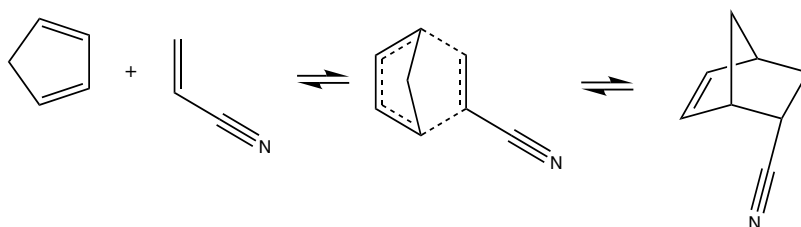

Figure 10. Scheme of the Diels-Alder reaction between cyclopentadiene and acrylonitrile.

Figure 11. Diels-Alder reaction: 3D models of reactants, transition structure, and product.

5.1.3. Electrocyclic reactions

In an electrocyclic reaction, an unsaturated cycloalkane is formed from a conjugated polyene, or the reverse reaction occurs. Here, only thermally allowed electrocyclic reactions will be considered. For instance, cyclobutene is opened in a conrotatory manner to form 1,3-butadiene. (The calculated activation energy is 149 kJ/mol, and the calculated reaction energy is −39 kJ/mol, assuming that the most stable conformation of 1,3-butadiene is formed.) The example shown here is the disrotatory ring closure of 1,3,5-hexatriene to form 1,3-cyclohexadiene (see **Figures 12** and **13**). Starting with the most stable conformer of 1,3,5-hexatriene, the calculated activation energy is 252 kJ/mol, and the calculated reaction energy is −64 kJ/mol (DFT).
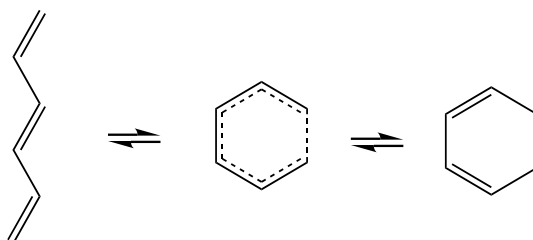
Figure 12. Scheme of the electrocyclic ring closure of 1,3,5-hexatriene.
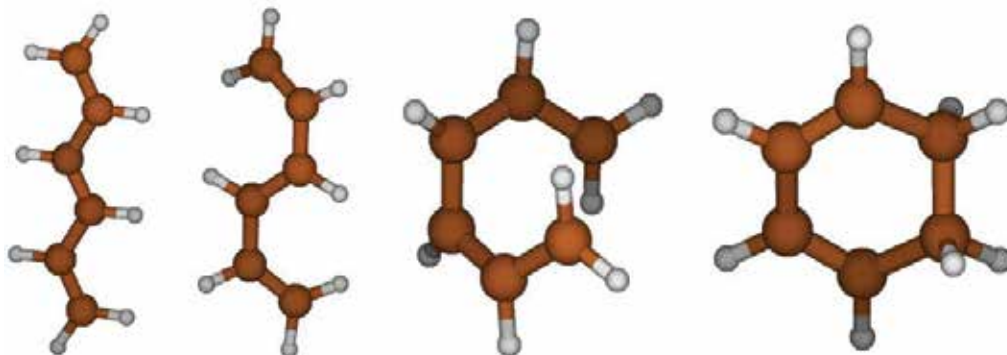
Figure 13. Electrocyclic ring closure of 1,3,5-hexatriene: 3D models of reactant (two conformations), transition structure, and product.

5.2. Nucleophilic aliphatic substitutions

The most important mechanisms for nucleophilic aliphatic substitutions are the single-step S_N2 mechanism with backside attack of the nucleophile and a trigonal-bipyramidal transition state (for primary or secondary substrates) and the two-step S_N1 mechanism with a carbenium ion intermediate (for secondary or tertiary substrates). Since these are ionic reactions, the progress in the gas phase may differ considerably from that in a polar solvent.

Considering first the degenerate S_N2 reaction of fluoromethane with fluoride anion in the gas phase, the most stable species is a cluster of these two particles, which is formed in an exothermic reaction and calculated reaction energy −106 kJ/mol. The formation of the symmetric trigonal-bipyramidal transition state from this cluster requires an activation energy of 29 kJ/mol.

In the gas-phase reaction of chloromethane with fluoride anion (see **Figures 14** and **15**), the calculated reaction energy for the formation of fluoromethane and chloride anion at infinite distance is −198 kJ/mol. There is no activation energy for the forward reaction; the energy of the trigonal-bipyramidal transition state is lower by 19 kJ/mol than that of the cluster of chloromethane with fluoride. The most stable species is the cluster of fluoromethane with chloride anion, and the activation energy of the reverse reaction, starting with this cluster, would be 132 kJ/mol.
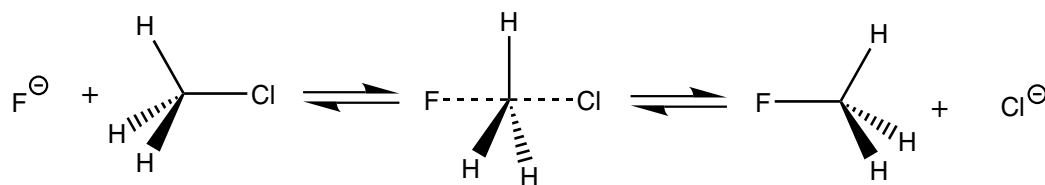

Figure 14. Scheme of an S_N2 reaction.

Figure 15. S_N2 reaction: 3D models of reactants, transition structure, and products.

A typical example for an S_N1 reaction is the reaction between *tert*-butanol and hydrogen chloride, yielding *tert*-butyl chloride and water (or the reverse reaction; see **Figures 16** and **17**). In the gas phase, this reaction is slightly exothermic with a calculated reaction energy of −8 kJ/mol (DFT). The concurrent elimination reaction (E1), yielding isobutene, water, and hydrogen chloride, is endothermic with a calculated reaction energy of 47 kJ/mol. For the reaction to proceed, it is necessary to form the protonated alcohol. Only the formation of an ion pair of chloride and protonated *tert*-butanol is conceivable, requiring an estimated activation energy of about 165 kJ/mol. The formation of a free *tert*-butyl carbenium ion is not feasible, because the energy required would be about 682 kJ/mol. The reaction should rather proceed by a backside attack similar to
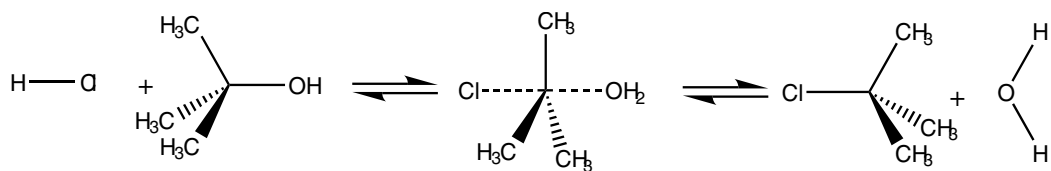
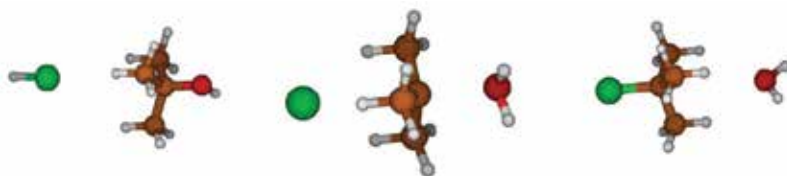**Figure 16.** Scheme of an S_N1 reaction.

Figure 17. S_N1 reaction: 3D models of reactants, intermediate, and products.

the S_N2 reaction and stop at a cluster of *tert*-butyl chloride and water (reaction energy −19 kJ/mol).

A true S_N1 mechanism requires an efficient solvation of the intermediate carbenium ion by polar solvent molecules.

5.3. Electrophilic aromatic substitutions

In gas-phase reactions of benzene with a reactive cationic electrophile such as H^+, Br^+, NO_2^+, or $CH_3CH_2^+$ (cf. Section 4.1), the reaction proceeds without any energy barrier to the σ complex and stops there. Some kind of π complex is formed on the reaction path, but it is not a true intermediate because it is not characterized by a local energy minimum.

In a more realistic scenario, the electrophile is a less reactive complex, e.g., of a halogen, an alkyl, or an acyl chloride, with a Lewis acid such as aluminum chloride or iron(III) bromide. Now, the reaction will usually stop at the π complex stage. In order to force the reaction to proceed to the σ complex, a strongly activating substituent such as oxido (i.e., phenolate anion) was introduced. After removal or replacement of this substituent, the optimization procedure allowed the study of either the backward reaction or the forward reaction to the products, possibly after a modification of the arrangement of the reaction partners.

As an example, the chlorination of benzene catalyzed by aluminum chloride will be considered in detail (see **Figures 18** and **19**). The overall reaction in the gas phase, yielding chlorobenzene and hydrogen chloride, is exothermic with a calculated reaction energy of −131 kJ/mol and a Gibbs free reaction energy of $\Delta_r G^\circ$ = −143 kJ/mol (DFT). The reaction involves three intermediates, π complex 1, σ complex, and π complex 2, which were calculated as local minima and two transition structures, which could not yet be identified unambiguously. The crucial energy barrier is most likely the transition state leading to the σ complex. Taking the energies of the separated reactants as reference, the relative energies are as follows: −45 kJ/mol for π complex 1, approximately 208 kJ/mol for transition state 1, −80 kJ/mol for the σ complex, approximately
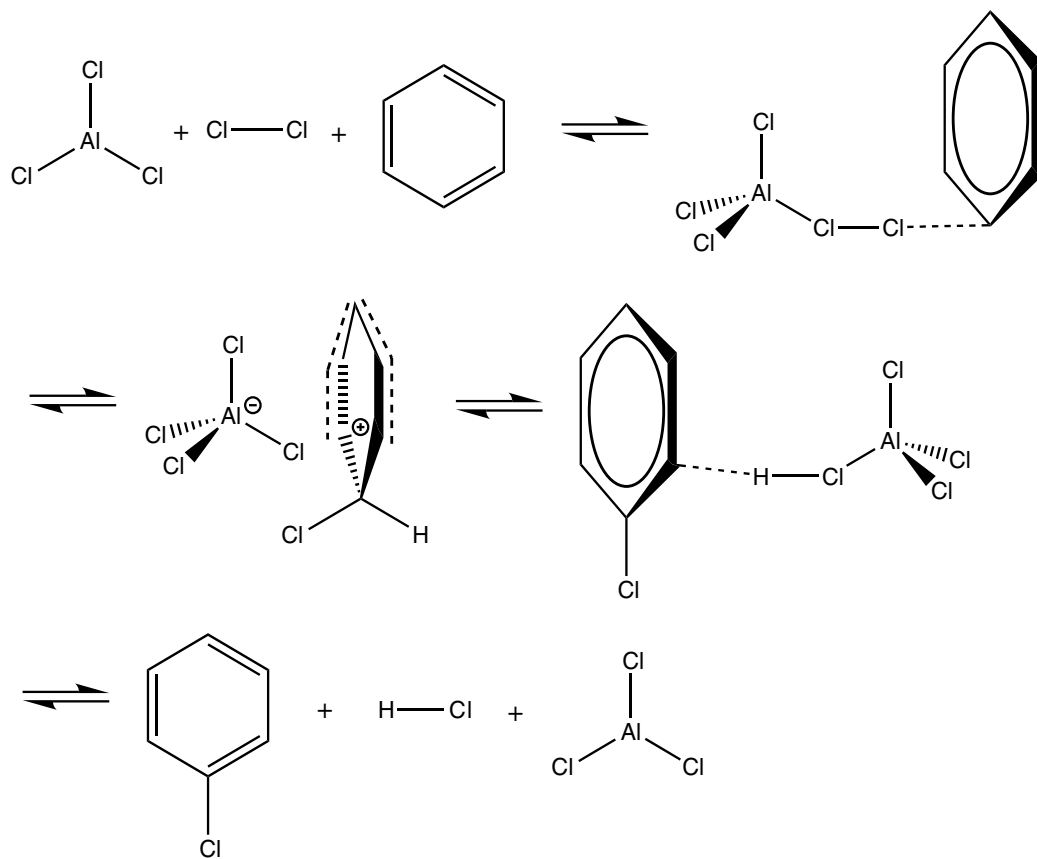
Figure 18. Scheme of the AlCl$_3$-catalyzed electrophilic substitution of benzene by chlorine.
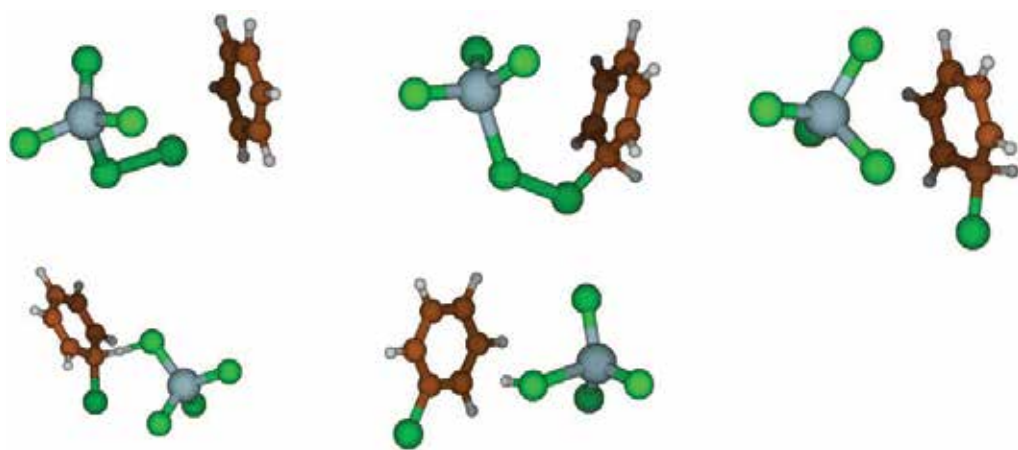

Figure 19. Electrophilic chlorination of benzene. Top row: first π complex, approximate first transition structure, and σ complex. Bottom row: approximate second transition structure and second π complex (of products).

27 kJ/mol for transition state 2, −169 kJ/mol for π complex 2 (global minimum), and −131 kJ/mol for the separated products.

5.4. Additions and eliminations

5.4.1. Electrophilic addition

As an example, the addition of bromine to cyclohexene will be considered, yielding *trans*-1,2-dibromocyclohexane (see **Figures 20** and **21**). First, a π complex is formed (relative energy −22 kJ/mol with respect to the separated reactants) and, next, a bicyclic bromonium ion, which is more stable than the respective carbenium ion (by roughly 100 kJ/mol). Finally, the diaxial conformer of *trans*-1,2-dibromocyclohexane is formed, which is actually more stable than the diequatorial conformer by 7 kJ/mol. This finding is somewhat surprising and stands in contrast to previous assumptions. Apparently, electrostatic repulsion favors the diaxial form, whereas in monosubstituted cyclohexanes, the substituent prefers the equatorial position. The reaction energy is −108 kJ/mol, and the Gibbs free reaction energy is −50 kJ/mol; this is due to the unfavorable reaction entropy.
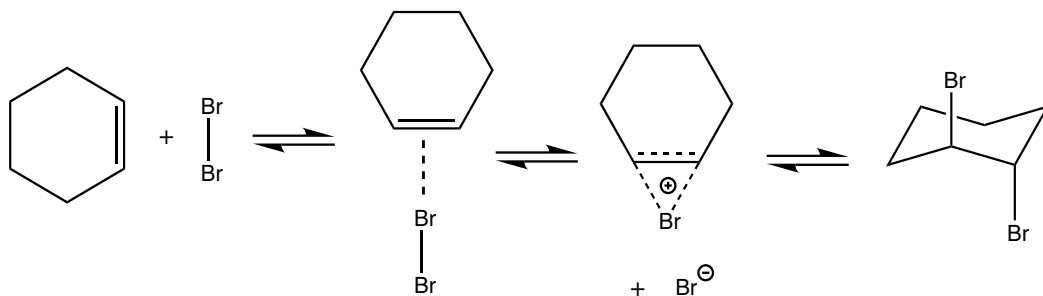

Figure 20. Scheme for the electrophilic addition of bromine to cyclohexene.

Figure 21. Electrophilic addition of bromine to cyclohexene: 3D models of reactants, π complex, bromonium ion, and product.

5.4.2. Elimination

In Section 5.2, it was already briefly mentioned that the reaction between *tert*-butanol and hydrogen chloride might proceed as an elimination instead of a substitution. The mechanism is E1, and isobutene (2-methylpropene) is formed as product (see **Figures 22** and **23**).
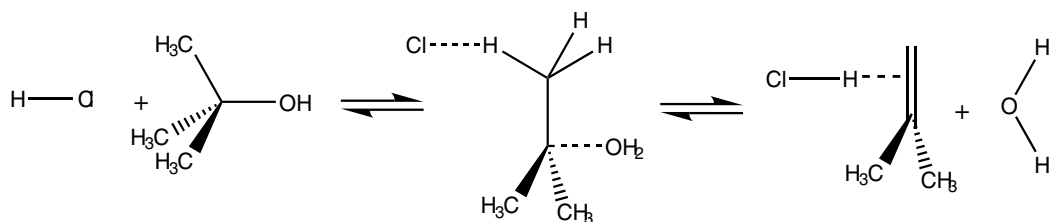
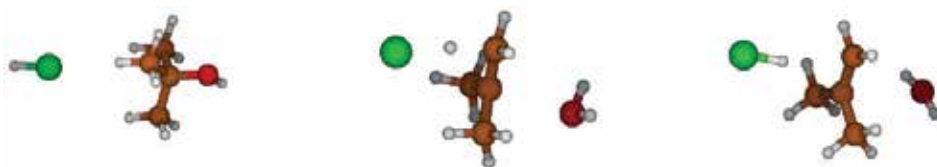**Figure 22.** Scheme for the E1 elimination of water from *tert*-butanol.

Figure 23. Elimination of water from *tert*-butanol: 3D models of reactants, approximate transition state, and π complex of products.

6. Conclusions and outlook

In the field of molecular chemistry, the use of DFT in combination with efficient software and modern computer equipment allows the development of "virtual chemistry," i.e., the prediction of essentially all molecular properties and of reaction paths. To a certain extent, supramolecular chemistry is also accessible to this method; molecular clusters and microdroplets of solvents can be simulated. It stands to a reason, however, that computational time increases heavily with molecular size (or cluster size). In the case of ab initio calculations, the proportionality is to the fourth power of the size of the basis set; in DFT, the situation might be somewhat better; computational time is proportional to roughly the third power of the number of orbitals involved, judging from NMR calculations.

It should be pointed out that present-day DFT is only an *approximate* theory. Therefore, it is necessary to check the quality of the computational results against experimental data.

A. Appendix

The following conversion factors have been used in this study: 1 Hartree (a.u.) = 2625.50 kJ/mol, 1 cal = 4.184 J, and $pK = \Delta G°$ [kJ/mol] /5.708008 (at T = 298.15 K).

Computational details. For all computations in Chapters 2 to 4, Gaussian 09 was used B3LYP/6–311(d,p) [1]. For most computations in Chapter 5, deMon2k was used [16]. For the

preparation of input files, i.e., the generation of Z matrices, and the visualization of the results, molden [2] was of great help.

Sample Gaussian input file: methane

```
%Chk = methane
#B3LYP/6–311G(d,p) Opt

Methane

0          1
c
h          1 hc2
h          1 hc2        2 hch3
h          1 hc2        3 hch3      2 dih4
h          1 hc2        4 hch3      3 dih5

hc2        1.089
hch3       109.47
dih4       −120.0
dih5       120.0
```

(The first line specifies the checkpoint file; the second the method and the task, in this case the geometry optimization; the fourth the title, the sixth the total charge, here 0; and the multiplicity, usually 1. Then, the Z matrix follows immediately.)

Author details

Burkhard Kirste

Address all correspondence to: kirste@chemie.fu-berlin.de

Institute of Chemistry and Biochemistry, Freie Universität Berlin, Germany

References

[1] Frisch MJ, Trucks GW, Schlegel HB, Scuseria GE, Robb MA, et al. Gaussian 09. Wallingford CT: Gaussian Inc.; 2013 http://www.gaussian.com/

[2] Schaftenaar G. CMBI. The Netherlands: Molden http://www.cmbi.ru.nl/molden/

[3]   Weast RC, editor. Handbook of Chemistry and Physics. 57th ed. Cleveland, Ohio: CRC Press; 1976

[4]   NIST Chemistry WebBook. http://webbook.nist.gov/chemistry/

[5]   Spectral Database for Organic Compounds, SDBS. http://sdbs.db.aist.go.jp/

[6]   Kaupp M, Bühl M, Malkin VG, editors. Calculation of NMR and EPR Parameters. Weinheim: Wiley-VCH; 2004

[7]   Kirste B. 3D Structure Determination of Natural Products by ^{13}C–NMR-Controlled DFT Calculations [Internet]. 2016. Available from: http://kirste.userpage.fu-berlin.de/chemistry/nmr/nmrdft/index.html [Accessed: 2017-07-03]

[8]   NMRShiftDB. https://nmrshiftdb.nmr.uni-koeln.de/

[9]   Kirste B. DFT calculations of hyperfine coupling constants of organic π radicals and comparison with empirical equations and experiment. Magnetic Resonance in Chemistry. 2016;**54**:835-841. DOI: 10.1002/mrc.4467

[10] Gerson F, Huber W. Electron Spin Resonance Spectroscopy of Organic Radicals. Weinheim: Wiley-VCH; 2003

[11] Kirste B. Untersuchung paramagnetischer organischer Verbindungen in flüssigen Kristallen und in Festkörpern mit der magnetischen Resonanz (EPR/ENDOR) [habilitation thesis]. Berlin; 1985. Available from: http://kirste.userpage.fu-berlin.de/ag/kirste/pdf/bkihabil.pdf Accessed: 2017–07-03

[12] Möbius K, Savitsky A. High-Field EPR Spectroscopy on Proteins and their Model Systems. Cambridge: RSC Publishing; 2009

[13] Kirste B. Applications of density functional theory to theoretical organic chemistry. Chemical Sciences Journal. 2016;**7**:127. DOI: 10.4172/2150-3494.1000127

[14] Smith MB, March J. March's Advanced Organic Chemistry. 6th ed. Hoboken, New Jersey: Wiley; 2007

[15] Woodward RB, Hoffmann R. The conservation of orbital symmetry. Angewandte Chemie (International Ed. in English). 1969;**8**:781-853. DOI: 10.1002/anie.196907811

[16] Koster AM, Calaminici P, Casida ME, Dominguez VD, Flores-Moreno, et al. deMon2k, Version 2. Cinvestav, Mexico City: The deMon Developers; 2006 http://www.demon-software.com/

Spectral Calculations with DFT

Ataf Ali Altaf, Samia Kausar and Amin Badshah

Additional information is available at the end of the chapter

Abstract

Spectra calculations are an important branch of theoretical modeling, and due to the significant improvements of high-level computational methods, the calculated spectra can be used directly and sometimes help to correct the errors of experimental observations. On the other hand, theoretical computations assist the experimental assignments. The authors discuss three spectral calculations (UV-Vis, IR and NMR) that are the most widely used. UV-Visible spectrum can be carried out employing time-dependent density functional theory (TDDFT) with B3LYP/631G(d,p) and CAM-B3LYP functional method to illustrate the characteristics of vertical electronic excitations. The vibrational spectra can be generated from a list of frequencies and intensities using a Gaussian broadening function method. NMR chemical shifts can be calculated by density functional theory individual gauge for localized orbitals (DFTIGLO) method and by gauge including atomic orbitals (GIAO) approach.

Keywords: spectral calculation, vibrational spectra, DFT NMR calculation, TDDFT for UV-visible spectra

1. Introduction

Early days of quantum chemistry go back to Thomas-Fermi and Thomas-Fermi-Dirac models of the electronic structure of atoms, which gave the concept of articulating some parts or all of the molecular energy as a functional of the electron density, and then comes the traditional Hartree-Fock (HF) theory [1]. HF theory was a simplest ab initio technique and among the first principles of quantum-chemical theories, being attained directly from the Schrodinger-wave equation that did not incorporate any pragmatic contemplations. Although such theories and techniques proved beneficial, it was density functional theory (DFT) that laid a demanding theoretical foundation in 1964 by an outstanding result established by Hohenberg and Kohn [2].

The Hohenberg-Kohn theorems state that the exact ground state energy of the system is produced by a unique functional of the electron density ρ. The first theorem demonstrates a many-particle system n(x,y,z) for which one-to-one plotting happens between the ground state electric density and the ground state wave function. The second theorem verifies that total electric energy of the system E[n(x,y,z)] is minimized by the ground state density [3]. The work of Kohn and Sham instantly surveyed and paved the way for hands-on computational applicability of DFT to physical systems, by linking a reference-state comprising of a set of noninteracting one-particle orbitals with a particular functional. The reference orbitals determined by a set of operative one-particle Schrodinger-wave equations are called Kohn-Sham (KS) equations [4]; one of them is depicted in Eq. (1).

$$\left(-\frac{1}{2}\nabla^2\left(\vec{r}\right) + V_{KS} \right)\Psi_i = \varepsilon_i\Psi_i \tag{1}$$

where V_{KS} is a local one-body potential defined as total density of the noninteracting system and is the same as the density of a real system.

2. Spectral implementations of DFT

The density functional theory (DFT) has become a powerful tool in computational chemistry owing to its usefulness. Spectroscopic analysis of chemical entities by this technique emerged as commanding implementation. Prediction of frequencies and spectral intensities by DFT calculations are indispensable nowadays for interpreting the experimental spectra of complex molecules. Much advancement has been made in the past decade to design new DFT approaches that can be employed into available quantum-chemical computational programs. For calculation of the molecular and electronic structures of ground-state systems and various spectral parameters related to NMR, ESR, UV-Vis and IR, various density functional practices are available now. Functionals available today can strive with best previous ab initio methods [5].

For experimental spectroscopists, theoretical computation of vibrational frequencies has become practically essential these days as specifically in problematic and uncertain cases it assists to assign and interpret experimental infrared/Raman spectra. Previously, the HF method was used in many studies to calculate vibrational frequencies, but it has long been identified that this approach miscalculates these frequencies even occasionally to a disturbing degree. Inadequate handling of electron correlation and anharmonicity of the vibrations are found to be the main contributions to error [6]. DFT largely overcome the errors as theoretical computations helped to interpret experimental conclusions depicting that using DFT these theoretical data can nearly be attained at the harmonic level. Calculation of optimized geometry, IR intensities, vibrational frequencies and Raman scattering activities can be done by employing different density functional approaches [7].

Taking NMR spectroscopy into consideration, DFT-based new methods are developed that are appropriate for the satisfactory hypothetical interpretation of NMR spectra of various chemical

and biochemical systems. It is obvious that local geometrical and electronic structures influence magnetic resonance parameters, i.e., shielding tensors, nuclear spin-spin coupling parameters, hyperfine tensors and g-tensors. For speculations of NMR parameters, a practical approximation of the real system is depicted by a model system in which 50–100 atoms are treated with ab initio techniques. Over the last years, DFT advanced by the capability to include effects of electron correlation in a very effectual means to the forefront of field of calculating NMR parameters [8, 9].

Competent calculations of excited states properties are emerging field of interest for quantum chemists; hence, they are developing interesting solutions for these properties. Because of advancement of computations based on the time-dependent density functional theory (TD-DFT) [10] in recent years, calculations of electronic structures in the excited states have become a motivation of interest. A commanding method of carrying out exact quantum mechanical calculations of the intervalence absorption spectrum is provided by the time-dependent concept of electronic spectroscopy. A corporeal picture of the effects of the coupling of electronic and nuclear motions became available by employing calculations in the time realm due to reason that the time development of the wave-packet can be tracked and inferred as well [11]. Plentiful successes of this technique have been recently revised as electronic spectra are often calculated with TD-DFT. Vertical excitation energies, absorption wavelength and oscillator strength calculations can be performed by this technique [12].

2.1. Theoretical vibrational spectra analysis

The influence of vibrational spectroscopy as an analytical tool in several fields is obvious. Qualitative association of bands and specific structures or chemical groups is basic interpretation of vibrational spectra. In contrast to nuclear magnetic resonance where nuclear spin is associated with one peak or multiplet is proved advantageous, united motion of all of the nuclei in sample is reason for observed bands in vibrational spectra. For N nuclei, there are at most 3 N-6 experiential fundamental bands and so far the matrix of internuclear force interactions, i.e., the second derivative matrix in harmonic approximation, has (3 N-6)(3 N -5)/2 exclusive terms. The extraction of force constants from vibrational frequencies is yet an undetermined mathematical problem as many bands are not actually observed; e.g., there are overtones, combination bands and nonconformities from the harmonic approximation; hence, the problem seems obstinate [13].

For the ground state's potential energy surface computation, discovery of effectual codes delivers a possible answer to the problem. A technique that will precisely determine the bonding, as well as intermolecular interactions, will be helpful for calculating vibrational spectra. The ground state properties and potential energies are accurately calculated by DFT approaches; therefore, DFT excellently and proficiently calculates the vibrational spectra from first principles [7]. The absolute values of the frequencies are high in contrast to experimental values while using DFT models as they seem to characterize the bonding pretty well and comparison with experimental trends is possible. DFT methods give sufficiently high accuracy of normal mode calculations as the restrictions of the harmonic approximation are often a foremost cause of divergence between theory and experiment.

It is reasonable to outspread the approach by including molecular interactions after given achievement of the method employed to small molecules. There are two aspects that can be reasons for inconsistency, i.e., anharmonicity and hydrogen bonding, both result in a lower frequency for a specific normal mode than projected by harmonic approximation [14].

2.1.1. Spectral generation via Gaussian broadening function

Computation of vibrational spectra of molecules in their ground and excited states can be done by using the Gaussian program. The program can also designate the dislocations of the molecule as it undergoes normal modes of vibrations along with prediction of spectral frequencies and intensities. The spectra can be produced from a list of frequencies and intensities employing a Gaussian broadening function as depicted in Eq. (2) [13]:

$$I(v) = \sum_k^N \frac{A_k}{\sqrt{2\pi\sigma}} \, exp \left\{ -\frac{(v - v_0)^2}{2\sigma^2} \right\}$$

(2)

For each of the N vibrational modes calculated, intensity of each band is A_k in km/mol.

2.1.2. Calculating the vibrational frequencies

Study of a molecular system behind calculating the vibrational frequencies [7]. If springs are considered Hookean, for example, equations of motion can readily be solved when force is proportional to the displacement and we can find that vibrational frequencies are associated with force constants and masses of atoms. For instance, in a simple molecule like CO where there is only one spring, the frequency is calculated as in Eq. (3).

$$v = \frac{1}{2\pi} \sqrt{k/\mu}$$

(3)

where $\frac{1}{\mu} = \frac{1}{m_c} + \frac{1}{m_a}$ and k is the spring constant. The value of k can be computed from DFT calculations at equilibrium state, bond length $k = \frac{\partial^2 E}{\partial x^2}$. It is essential to perform geometry optimization prior to frequency calculations as these calculations are effective only at fixed points on the potential energy surface.

2.1.2.1. Calculating second derivative of energy

Before calculating the second derivative of energy, the first step in quantum chemical calculations is optimization of molecular geometry. Vibrational frequency calculations are done after optimizing geometry by using the same method and basis set as used for calculating vibrational frequency. Model's development is constructed on spontaneously rational values for interbond angles, bond distances and dihedral angles in the absence of experimental data. It is usually done by solving the following Schrodinger wave equation [15]:

$$\left(\widehat{H}_{el} + V_{NN}\right)\Psi_{el} = U\Psi_{el} \tag{4}$$

where $\widehat{H}_{el}$ is the one-electron Hamiltonian and V_{NN} is the operator of potential energy between the nuclei of molecular system intended for numerous molecular geometries to discover equilibrium geometry of the molecule, i.e., geometry optimization.

The second derivative of energy regarding the position of nuclei is factor on which molecular frequencies hinge on. Hartree-Fock theory, DFT-B3LYP and other approaches make available the analytic second derivative of energy. Input for frequency calculation is given by the optimized energy [16]. These derivatives are estimated at the equilibrium geometry with origin at the middle of mass by manipulating a set of second derivatives of molecular energy U respecting the 3 N nuclear Cartesian coordinates of a coordinate system as in Eq. (5) [15].

$$\left(\frac{\partial^2 U}{\partial X_i \partial X_j}\right)_{eq} \quad i, j = 1, 2, \dots 3N \tag{5}$$

Mass-weighted force constant matrix elements give:

$$F_y = \frac{1}{\left(m_i m_j\right)^{1/2}}\left(\frac{\partial^2 U}{\partial X_i \partial X_j}\right)_{eq} \tag{6}$$

where m_i is mass of the nucleus in correspondence to coordinate X_i.

Then, set of 3 N linear equations in 3 N unknowns in Eq. (7) are being solved.

$$\sum_{j=1}^{3N} \left(F_{ij} - \delta_{ij}\lambda_k\right)I_{jk} = 0 \quad i, j = 1, 2, \dots 3N \tag{7}$$

If coefficient of determinant vanishes, this set of consistent equations has a nontrivial explanation as follows:

$$\det\left(F_{ij} - \delta_{ij}\lambda_k\right) = 0 \tag{8}$$

This determinant is of order 3 N and on extension gives a polynomial whose highest power of λ_k is λ_k^{3N}, so the determinantal equation will yield 3 N roots (some of which may be the same) for λ_k.

2.1.2.2. Calculating vibrational frequencies

Calculation of molecular harmonic vibrational frequencies is now done as follows [15]:

$$v_k = \frac{\lambda_k^{1/2}}{2\pi} \tag{9}$$

By solving Eq. (9), six of the λ_k values originated will be zero giving six frequencies with zero value, in correspondence to the three translational and three rotational degrees of freedom of

molecule. In practice, one may find six vibrational frequencies with values almost zero because equilibrium geometry never originates with infinite precision. The remaining 36-N vibrational frequencies depict molecular-harmonic vibrational frequencies.

2.1.2.3. Zero-point energy calculations for maximum vibrations

Zero-point energy is defined as the sum over all the vibrational modes for a molecule with maximum number of vibrational modes and calculated as:

$$E_{ZPE} = \sum_i \frac{1}{2} h v_i \tag{10}$$

2.1.3. Normal coordinate analysis

Normal coordinate analysis gives comprehensive explanation of vibrational modes. It is termed a practice that calculates the vibrational frequencies involving observed frequencies of more preferably infrared and Raman harmonic frequencies to equilibrium geometry, force constants and atomic masses of an oscillating system. In assigning vibrational spectra, normal coordinate analysis proved beneficial, but reliable intramolecular force constants influence its predictive ability [17].

2.1.4. B3LYP density functional method

DFT syndicates accuracy with computational rapidity and user-friendliness for investigating the ground state characteristics in sturdily bound systems. Consistent highly reliable hybrid DFT methods (discussed in Section 3.1) make them more proficient and endearing. B3LYP functional [18] (discussed in hybrid methods of Section 3.1) is the most extensively used among all hybrid density functional methods as it is considered to give most exact vibrational frequencies of compounds only if calculated frequencies are scaled by a uniform scaling factor. Scaling is done to compensate for all probable causes of inaccuracy produced owing to electronic structure method–related inaccuracies, e.g., basis set insufficiencies and estimated handling of electron-correlation and nuclear motion treatment inaccuracies [19].

2.1.5. IR calculations in Gaussian software

Gaussian is a most employed computational chemistry software program, whereas Gauss View is an inexpensive full featured graphical user interface for Gaussian. One can submit inputs to Gaussian and can observe output graphically, which is usually produced by Gaussian software via using Gauss View. For IR spectrum calculations in Gaussian, the following are the steps:

i. After predicting the number of vibrational modes and expected regions for frequencies for molecule by theoretical calculations, build molecule in Gauss View. Go to Calculate from Gauss View toolbar and select Gaussian. In the Job Type dialog box, select Opt + Freq and optimize to a 'Minimum' Calculate Force Constants-'Never,' Compute Raman- 'Default,' deselect any other option.

ii. In Method section, select ground state (HF, Restricted or DFT Restricted and B3LYP according to required calculation) and select a basis set, Charge-0 and Spin-Singlet. Insert SCF = Tight in the Additional Keywords section and if your calculation is in vacuo, select 'None' in the Solvation dialog box. Submit the calculation.

iii. Open the output file of the optimized structure in Gauss View. Verify that the optimization calculation has converged by checking that the maximum force, RMS force, maximum displacement and RMS displacement parameters are all converged.

iv. Go to Results and select the 'Vibrations' option. View the IR spectrum by pressing the 'Spectrum' button and check out whether the number of modes are in accordance with theoretical calculations or not. Each vibrational mode can be visualized by highlighting it in the 'Display Vibrations' table and pressing the 'Start' button.

3. DFT methods for nuclear magnetic resonance (NMR)

NMR is based on the principle that the energy of a system containing nuclear or electron magnetic moments arising from the spin of a particle, in the existence of an external stationary magnetic field, depends upon the direction of the magnetic moment with respect to the external field. One can thus measure the energy difference for different directions of the electronic magnetic moment (electronic Zeeman effect) or of nuclear magnetic moment (nuclear Zeeman effect) by employing a suitable oscillating external magnetic field as a probe [20].

NMR parameters are considered as quantities which are determined shifts, indirect spin-spin coupling constant and direct dipole-dipole coupling constants. This electronic structure in turn confidentially interrelated to local and global geometry and hence internal flexibility and intramolecular interactions influences NMR parameters. Chemical shifts along with spin-spin coupling constants found an average experimentally in comparison to those values belonging to all geometrical arrangements arising throughout the sequence of NMR experiment. Unfortunately, chemical shifts are generally found to be dependent on the internal dynamics or on the intermolecular interactions in various descriptions. Consequently, for obtaining structural information, most experimental NMR techniques imply coupling constants or the nuclear Overhauser effect instead of chemical shifts. However, ab initio calculations provide the understanding to structure-chemical shifts or spin-spin coupling constant associations, which can make the experimental data interpretation much easier in this sense. That is the reason that highly capable and steadfast computational calculations are in high demand [21].

As commonly noted that, when results of sufficient quality are attainable by employing various strategies based on wave function properties. These procedures are restricted to small- and medium-sized systems unfortunately. With the advancements of density functional methods, it is possible to acquire pertinent results even for larger molecules, such as fragments of proteins and nucleic acids [22] where the electron correlation effects are

indirectly accounted through the exchange-correlation functional. DFT-based NMR calculations have seen a rapid expansion during the last 10 years—that is perhaps best designated with the word explosion. Since the publication of these calculations, methods have already entered the standard repertoire of quantum chemistry in short time length. More comprehensive and technical as well as more general reviews are available as theoretical portrayal of NMR chemical shifts based on the more traditional ab initio procedures has seen a marvelous progress as well [23]. For NMR calculations, density functional theory (DFT) is recently proved to substitute the traditional Hartree-Fock (HF) and post-HF methods [24]. Inclusion of electron correlation effects in a very efficient way to calculate NMR parameters is a rather new field of application in DFT over the last years.

3.1. Calculations of NMR parameters

Total energy E of an n-electron system is expressed exactly on the basis of DFT approach as in Eq. (11) [2].

$$E = \sum_i^n \int d\vec{r} \Psi_i^* \left(\frac{p^2}{2} + V_N \right) \Psi_i \frac{1}{2} \int d\vec{r^1} \vec{r^2} \ \frac{\rho\left(\vec{r^1}\right)\rho\left(\vec{r^2}\right)}{|\vec{r^1} - \vec{r^2}|} + E_{XC} \tag{11}$$

In Eq. (11), the $\{\Psi_i\}$ is a set of n orthonormal one-electron functions, $\rho = \sum_i^n \Psi_i^* \Psi_i$ is electronic density of the system, V_N is the external (nuclear) potential, and $\vec{p}$ is momentum operator. Hence, the kinetic and potential energy of a model system with the same density is signified by the first integral but without incorporating electron-electron communication. The second term represents itself as coulomb interaction of electron density. The XC energy and E proper (E_{XC}) are functionals of the density although exact functional arrangement for E_{XC} is not known (defined through Eq. (11)). Any application of DFT is mainly concerned with the assessment of numerous approximations; hence, Kohn-Sham (KS) equations are typically derived from Eq. (11) [4, 25].

$$h_{KS}\Psi_i = \varepsilon_i \Psi_i \tag{12}$$

$$h_{KS} = \frac{p^2}{2} + V_{KS} = \frac{p^2}{2} + V_N + \int d\vec{r} \ \frac{\rho\left(\vec{r^2}\right)}{|\vec{r^1} - \vec{r^2}|} + V_{XC} \tag{13}$$

The XC potential V_{XC} is the functional derivative of the XC energy E_{XC} with respect to the density, ρ. The inclusion of magnetic fields is another extension, which can be introduced. Obviously, this is essential to all the properties to be introduced. The magnetic field $\vec{B}$ is most accessibly acquaint with supposed minimal coupling as in Eq. (13) [26].

$$\vec{p} = \vec{p} + \vec{A}/c \tag{14}$$

where $\vec{A}$ is the vector potential of the field. Though this is not the entire division in DFT. Rather, the XC energy (E_{XC}) becomes a relativistic for current density functional, which interprets in nonrelativistic system to the electron density ρ and the current density $\vec{j}$ depicted in Eq. (14) [27].

$$E_{XC}[p] \xrightarrow{substitute} E_{XC}\left[p, \vec{j}\,\right] \tag{15}$$

3.1.1. Exchange-correlation functional

Quality of the description centers exclusively on precision of the approximation to Exc as mentioned earlier that obvious form of the exchange-correlation functional (Exc) is not identified yet. Unfortunately, there is no systematic mode of improving exchange-correlation functionals although the pursuit for improved and better functionals is at the very core of DFT. Prevailing XC functionals can be roughly categorized into three distinct groups [28] as several approximations used for Exc are as follows:

3.1.1.1. The local density approximation (LDA)

The idea of a nonvariating electron gas laid the foundation of this model, which approximates Exc in turn written as:

$$E_{XC}^{LDA}[\rho] = \int \rho(r)\epsilon_{xc}[\rho]dr \tag{16}$$

$\epsilon_{xc}[\rho]$ is the exchange-correlation energy per particle of a uniform electron gas of density ρ(r) in Eq. (15). The $E_{XC}^{LDA}[\rho]$ can be correctly split into exchange and correlation parts as:

$$E_{XC}^{LDA}[\rho] = E_X^{LDA} + E_C^{LDA} \tag{17}$$

3.1.1.2. The generalized gradient approximations (GGA)

The generalized gradient approximations (GGA) for Exc are not lone functions of local density ρ(r) but also functions of the gradient of charge density ∇ρ(r) in comparison to LDA. They can be generically inscribed as:

$$E_{XC}^{GGA}\left[\rho_\alpha, \rho_\beta\right] = \int f\left(\rho_\alpha, \rho_\beta, \Delta\rho_\alpha, \Delta\rho_\beta\right)dr \tag{18}$$

α and β denote to "up" and "down" spin, respectively, in Eq. (17). Now, E_{XC}^{GGA} is also typically split into its exchange and correlation parts as:

$$E_{XC}^{GGA}[\rho] = E_X^{GGA} + E_C^{GGA} \tag{19}$$

The GGA exchange functional's representatives are functionals by Becke, 1988 (B or B88) [18] and by Perdew and Wang, 1986 (P or PW86) [29] and are the most familiar ones. Perdew and Wang also established the PW91 exchange-correlation functional [30] comprising exchange

and correlation contributions; if used separately, both functionals are symbolized by PW91. The exchange fragment of PW91 is analogous to B88 and the correlation part is a modified form of P86. Currently, possibly the most prevalent correlation functional accounts to contributions of Lee et al. (LYP) [31]. Because of presence of some indigenous components, it differs from the other GGA functionals.

3.1.1.3. The hybrid methods

Exchange-correlation functionals in which exchange part is composed of particular Hartree-Fock exchange and pure density functionals for exchange are called hybrid functionals. These functionals consist of a mixture of Hartree-Fock exchange with DFT exchange and correlation in other words as depicted in Eq. (19).

$$E_{XC}^{hybrid} = c^{HF}E_X^{HF} + c^{DFT}E_C^{DFT} \tag{20}$$

3.1.1.4. Becke's three-parameter hybrid functional (B_3LYP) method

An illustrative example of the above-mentioned hybrid representations is Becke's three-parameter hybrid functional (B3), depicted in Eq. (20). [18], and exchange energy is being calculated by using this (B3) functional. If correlation functional LYP or PW91 is assumed for E_C^{GGA}, B3LYP or B3PW91 will be obtained, respectively. The earlier mentioned is most widely used exchange-correlation functional nowadays, and in many research domains throughout, it was also rigorously active. Since GGAs are better in comparison to LSDA, they could also employ a functional form like this (B3) as follows:

$$E_{XC}^{B3} = (1-a)E_X^{LSDA} + aE_X^{HF} + b\Delta E_X^{B88} + (1-c)E_C^{LSDA} + cE_c^{GGA} \tag{21}$$

B_3LYP uses this formulation, with LYP for ΔE_c^{GGA}.

3.2. Shielding tensor calculations

The most basic DFT calculations of NMR chemical shifts were done years ago in which very small basis sets were employed and inappropriate approximation to the exchange-correlation (XC) functional was done due to which point of practical applicability was lost. Also in any handling of magnetic fields, another central exertion that surfaces is the so-called gauge problem [28] be it in DFT or otherwise.

3.2.1. Solving gauge problem

The gauge requirement should disappear just as any anticipation value together with NMR possessions that can only hinge on the values of observable quantities. Certainly, this is the case for particular solutions of, for example, the KS equations, Eq. (12a, b) where large (immeasurable) basis sets are employed. A strong dependence on the choice of gauge is of main concern for approximate solutions with smaller (infinite) basis sets. Current applications of DFT for calculating NMR chemical shifts have used density functional theory individual gauge

for localized orbitals (DFTIGLO) method [9] and gauge including atomic orbitals (GIAO) approach [32].

3.2.2. The GIAO method

One appraises matrix fundamentals of the Hamiltonian in terms of a basis of field-dependent atomic orbitals (AO) in the GIAO method. By insertion of an intricate phase factor denoting the position of basis function, which is usually nucleus, the basic functions are made obviously dependent on the magnetic field. Such orbitals are termed as London atomic orbitals (LAO) or the gauge including atomic orbitals (GIAO). Matrix elements involved in GIAOs only differentiate in the vector potentials is the essence of idea, in that way entirely eradicating the reference to a complete gauge origin. Employment of field-dependent GIAOs as basic functions [33] is possibly the best solution to the gauge problem.

$$\chi_a\left(\vec{B},\vec{r}\right) = exp\left[\frac{i}{2c}\left(\vec{B}x\vec{R}_a\right).\vec{r}\right]\chi_a\left(\vec{r}\right) \tag{22}$$

where $\vec{R}_a$ and $\chi_a\left(\vec{B},\vec{r}\right)$ are the conforming GIAO and $\chi_a\left(\vec{r}\right)$ is customary field-free basis function that is adjusted at position. The field-dependent prefactor Eq. (21) guarantees that only differences of position vectors give the impression in expectation values. This eradicates any origin dependence, even for estimated MOs and finite basis sets. For showing the complete basis set limit, correspondence of the GIAO and the simpler common gauge methods to the NMR shielding are depicted. Nucleus-attached basis functions in geometry optimization processes have been equated with specific AOs (Eq. (21)) by assigning a field-dependent phase factor to them.

Working equations for the NMR shielding tensor ($\vec{\sigma}$) can be derived from the GIAO formulation of Eq. (21). The absolute shielding σ is interrelated to the more acquainted chemical shift δ as follows [33]:

$$\delta = \sigma_{ref} - \sigma \tag{23}$$

where σ_{ref} is the absolute shielding of reference compound (e.g., tetramethylsilane [TMS] for ^{1}H, ^{13}C and ^{29}Si NMR). Opposite sign between δ and σ can be noted, whereas GIAO shielding tensor is specified in DFT as [34]:

$$\vec{\sigma} = \vec{\sigma^p} + \vec{\sigma^p} \tag{24}$$

where $\vec{\sigma}$ has been divided into its paramagnetic and diamagnetic fragments. Generally, this division is not exceptional as only the total shielding is an apparent quantity, but for the GIAO method, it has been defined exclusively.

3.2.3. The IGLO method

The use of disseminated gauge origins was depicted by the individual gauge for localized orbitals method (IGLO) [9], which was the first to empower the organized learning of nuclear shielding in larger systems. Evaluation of shielding tensor in terms of localized molecular orbitals (MO) is the idea of approach. To minimalize the absolute value of paramagnetic involvement, individual gauge origins of shielding tensor are selected. In the IGLO method, local phase factors are involved to molecular orbital in comparison to the GIAO approach where a phase factor is associated to each atomic orbital. In computational analysis point of view, IGLO approach is less challenging in contrast to the GIAO method since the use of distinct approximations of derivative two-electron integrals by this approach is most probable. By using localized orbitals, previously mentioned approximations are empowered; hence, it is important to select an appropriate basis set in an IGLO calculation [35]. According to IGLO approach, it is possible to allot comparable exponential prefactors to other objects, e.g., to localized MOs as a replacement for GIAO method. In IGLO method, specific integrals are easier to estimate analytically. Gauge difficulty has been resolute recently by retaining numerical integration or by techniques that were used in geometry optimization measures.

3.3. Nuclear spin-spin coupling constant calculations

Highly appropriate ab initio calculations of spin-spin coupling constants are still very infrequent and usually deal with the simplest molecules only in comparison to excessive advancement in concept and computer codes for shielding tensor scheming. Shielding tensors are the reasons behind sensitivity of nuclear spin spin coupling constants to the correlation effects and basis set quality [36]. There are four significant contributions which causes other problems to the nuclear spin-spin coupling constants, are enlisted as follows:

a. Fermi contact (FC),

b. Paramagnetic spin orbit (PSO)

c. Spin dipolar (SD)

d. Diamagnetic spin orbit (DSO)

HF calculations of the spin-spin coupling constants of large molecules lead to deprived contract with experimental numbers and further empirical scaling has to be done. On the other hand, the use of post–Hartree-Fock methods and prolonged basis sets for demanding handlings of all the four contributions is very inefficient and time-consuming.

In DFT, only a single paper by Fukui [23] published years ago was worthy initially, where the blend of finite perturbation theory (FPT) and the LCAO-Xa method was employed and only calculations of the FC contribution to the spin-spin coupling constant were carried out, which gave somewhat poor results likely as too poor basis set in combination with the Xa potential was used. As in Ref. [37], a new method to calculate the nuclear spin-spin coupling tensor using DFT procedure is developed sideways to the shielding tensor calculations in accordance.

The portrayal of calculations follows Ref. [37]. By meaning, the nuclear spin-spin coupling tensor $J_{MN_{uv}}$ is the second derivative of the total energy of the system with respect to the spins of the nuclei M and N as depicted in Eq. (24).

$$J_{MN_{uv}} = \left[\frac{\partial^2 E(I_{Mu}.I_{Nv})}{(\delta I_{Mu}.\delta I_{Nv})}\right]_{I_{Mu}=I_{Nv}=0} \quad u, v = \{x, y, z\} \tag{25}$$

The orientationally averaged value of the nuclear spin-spin coupling tensor ($J_{MN_{uv}}$) of nuclear spin-spin coupling constant (J_{MN}) is the focus of interest in many cases.

$$J_{MN} = \frac{1}{3}\left(J_{MN_{xx}} + J_{MN_{yy}} + J_{MN_{zz}}\right) \tag{26}$$

3.4. Chemical shift calculation from DFT-B$_3$LYP-GIAO method

Since calculations for TMS are encompassed in many software, DFT-B$_3$LYP-GIAO is the 6-311 + G(2d.p) [38], a suitable basis set, which easily determines the chemical shifts relative to TMS. The use of smaller 6-31 + G(d,p) basis set for calculations is most suitable for students compared to larger basis sets such as the 6-311 + G(2d,p) or even the very large 6-311++G (3df,3pd) basis sets that are employed for research purposes on small molecules. Many of the movements necessitate much less than 3 hours fixed for a standard research laboratory session even while using the larger basic sets. First of all, in this method, the structure is optimized in all the cases, and then to establish that either optimized structure is at least a local minimal or not, vibrational frequencies are determined. After the complete optimization of the structure, shielding constants are calculated using the GIAO method. Calculations for chemical shifts are carried out by subtracting the value of the screening constant (σ), which is calculated from the value of the screening constant calculated for TMS using the same level of theory [38].

$$\delta = \sigma_{TMS\_}\sigma_{Calculated} \tag{27}$$

3.5. NMR calculation steps using Gaussian software

Basic considerations in NMR calculations are as follows: first, how many types of protons are there in molecule and which are they and second, how many NMR signals are expected to see and in which regions. In the case of an NMR spectrum calculation, geometry optimization calculation is needed first of all and then optimized structure is used to perform NMR spectrum calculation using the same method and basis set.

i.   Follow the calculations in Section 2.1.5 till step i for geometry optimization calculations and then follow steps used to perform an HNMR spectrum calculation of the optimized structure with the same method and basis set.

ii.   Press the Calculate button in the Gauss View toolbar and select Gaussian. In the Job Type dialog box, select 'NMR' and 'GIAO method. Submit the calculation after checking all parameters. Open the output file and select the NMR option from Results.

iii. In the 'SCF GIAO magnetic shielding dialog box, select 'H' option in Element drop-down list, and in the Reference list, select the calculation method earlier used. The number of peaks of magnetic shielding observed is noted. Infer calculated spectrum and compare it with theoretical calculations. With this, multiplicity of the peaks, temperature at which NMR experiment is simulated and width of the NMR peaks can be discussed.

iv. Open the log file and search for or scroll to the line "SCF GIAO Magnetic Shielding tensor (ppm)." For simple NMR experiments, the signals are found at the chemical shifts, which appear after the heading "isotropic." All other numbers relate to the directionality of the NMR signals.

4. Time-dependent density functional theory (TD-DFT) for UV-vis spectra

As classic DFT is concerned with ground stationary state and applications, i.e., UV-vis spectroscopy, photochemistry, NLO and others, comprise either electronic excited states or time-dependent electronic characteristics, which are in agreement with time-dependent density functional theory (TD-DFT). From classic paper of Runge and Gross [39], formal TD-DFT is traced back, which strained to firm up former efforts on the same topic. Therefore, Runge-Gross TD-DFT is two decades younger than Hohenberg Kohn-Sham theory [2], which is about stationary ground state as mentioned earlier. Four theorems proposed in the Runge-Gross paper. First, Runge-Gross theorem states that external potential up to an additive function of time is regulated by time-dependent charge density, $\rho(r,t)$, in cooperation with preliminary wave function (Ψ_0).

Various chemical and physical molecular properties provide basis for electronic spectra. Different chemical and physical effects can easily be computationally investigated by modifying the spectral characteristics of molecules as many stimulating chemical problems are included in both ground and excited states of molecules. As for ground state properties of atoms, molecules and solids, DFT gave an effective explanation; hence, in order to designate photochemical and photophysical procedures, DFT formalism has to be expanded to excited states. So, for excited state calculations, time-dependent DFT (TD-DFT) is established as an operative tool [40] as it provides first principle technique for calculating excitation energies and various response-related characteristics in density functional outline.

There are classically one or more low energy excited states for a molecule that can be designated as valence-MO-valence-MO single electronic excitations and replicated in spectra. Energies of excited determinants are essential for multiplet energy calculation such as employing spin-orbital number (i) to the empty spin-orbital number (j). Accordingly, specific states are denoted as $\pi \rightarrow \pi^*$, $n \rightarrow \pi^*$ transitions. Relative easiness of character sometimes smoothes the process of concluding wave functions for these states. The calculation of the dynamic answer of charge density proposes a rigorous direction to time-dependent simplification of DFT formalism. The poles of dynamic polarizability regulate excitation energies permitting the

determination of electronic excitation spectrum in typical dipole approximation [41]. The poles' strengths are provided by oscillator strengths (f_i) or by transition dipole moment (μ_i) consistently also termed as intensity of the optical transitions.

4.1. Absorption spectra calculation

Electronic absorption spectra calculation is foremost applicability of TD-DFT after the geometry got optimized by using linear response theory. First, the Hohenberg-Kohn theorem statement that dynamic linear response of a system of N-electrons is determined by the ground-state charge density was discussed earlier but no applied mean was found to build this response. A productive procedure was provided by TD-DFT from which absorption spectra can be calculated by following steps [42]:

Step 1: The calculations comprised of promulgating Kohn-Sham orbital incidence of a trivial dynamic perturbation, e.g., considering system being perturbed by Eq. (27).

Step 2: Then induced dipole moment, $\mu_{induced}(t)$, is calculated by Eq. (28), which depicts the difference among time-dependent and permanent dipole moments of a system.

Step 3: Dynamic polarizability, α, is expressed by linear term, $\mu_{induced}(t) = \int \alpha(t - t')\varepsilon(t)$. Final calculations of dynamic polarizability in Eq. (29) are carried out after applying Fourier transform convolution theorem.

Step 4: Sum-over-states (SOS) form of dynamic polarizability has the form:

$$v_{applied}(r, t) = \varepsilon(t).\boldsymbol{r} \tag{28}$$

$$\mu_{induced}(t) = -e \int \boldsymbol{r}n(r.t)\boldsymbol{r}d \tag{29}$$

$$\alpha(\omega) = \mu(\omega)/E(\omega) \tag{30}$$

$$\alpha(\omega) = \sum_{I \neq 0} \frac{f_I}{\omega_I^2 - \omega^2} \tag{31}$$

where ω_I and f_I are corresponding vertical excitation energies and conforming oscillator strength.

Finally, spectrum was obtained employing Eq. (31) also termed as Lorentzian broadened stick spectrum:

$$S(\omega) = \frac{2\omega}{\pi} Im\alpha(\omega + i\eta) \tag{32}$$

Such a procedure has been executed in many computer codes, e.g., in Octopus code [43], and has benefited that absorption spectrum of a very huge molecule over a wide range of energies can be calculated even though using only reasonable spectral resolution. This function parallels to optical absorption spectrum, e.g., calculating spectra of benzene [44] by TD-DFT approach depicted in **Figure 1**.
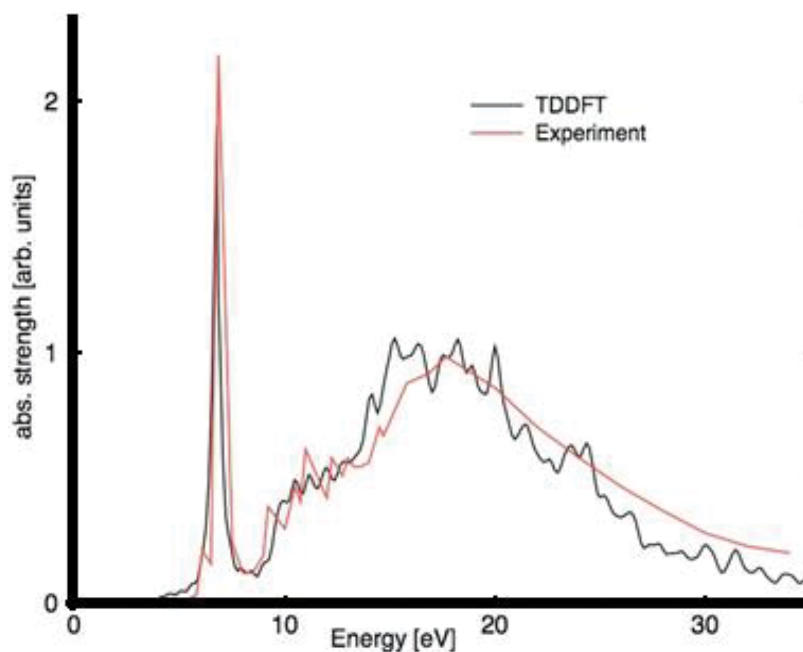
Figure 1. Absorption spectra of benzene.

4.1.1. Calculating the oscillator strength

It is an important point to note that TD-DFT calculations not only give excitation energies (ω) but also provide respective oscillator strengths. Oscillator strengths are actually pure numbers in a complete basis set [42].

$$f_I = \frac{2m_e}{3h}\omega_I|\langle 0|r|I\rangle|2 \tag{33}$$

Obviously, $\omega = E_I - E_0$ is an excitation energy in the case of $|I\rangle\langle 0|$ and $\omega = E_0 - E_I$ is a de-excitation in the case of $|0\rangle\langle I|$. To more simply relate the molar extinction coefficient (ε) in an absorption experimentation, Eq. (32) has been consciously expressed in Gaussian instead of atomic units. In SI units, frequency spectrum is assumed to first approximation [42] by:

$$\epsilon(v) = \sum_I \frac{N_A e^2}{4m_e c \, \ln(10)\epsilon_0} S(v - v_I) = \left(6.94 \times 10^{+18}\frac{L}{cm}.s\right)\sum_I S(v - v_I) \tag{34}$$

where $S(v)$ is a spectral shape function usually a Gaussian whose full width at half maximal is determined through experiment with area normalized to unity, whereas N_A depicts the Avogadro's number.

Absorption spectrum frequently results by excitations having larger oscillator strength because absorption peaks are often scaled with oscillator strength (f_I) of the excitation. Excitations with small oscillator strength (f_I) are also omitted from final spectrum while fundamentally working

on oscillator strength carrying subspace so that absorption spectrum is possibly calculated with less excitations in a fixed energy space. A common problem considered is that a large number of excitations have to be estimated with the purpose of covering energy space of concentration, while figure of absorption spectrum is determined by only some of them because of their greater oscillator strength (f_I) [45].

4.1.2. Calculating the intensity of absorption

Another detailed DFT method is presented, proposed in ref. [46], to calculate UV absorption spectra. The integration is completed over real $\vec{r}$ space. Intensity of absorption is in direct proportion to transition dipole moment $\vec{\mu_{jk}}$ from ground jth to kth excited state; hence, it can be estimated by formula [47]:

$$I_{jk} \approx \omega_{jk} \frac{\left(\mu_{jk}\right)2}{\hbar\omega_{jk} - \hbar\omega \pm i\Gamma_{jk}} \tag{35}$$

where $\hbar\omega$ is the input running radiation energy and $\hbar\omega_{jk}$ is energy difference between ground (j) and excited (k) state. Γ_{jk} is termed as line broadening, which is characterized by electron vibration broadening and inversely proportional to the period of k state.

4.1.3. Emission spectra calculation

As high harmonic generation is possible with TD-DFT methods, emission spectra [48] are calculated by:

$$\sigma_{emision}(\omega) = \left| \int dt e^{i\omega t} \frac{d^2}{dt^2} d(t) \right|^2 \tag{36}$$

4.2. Linear response TD-DFT(LR-TD-DFT) and absorption spectrum

Absorption spectrum is the fundamental property of a system. One working on absorption spectra calculations is mainly concerned with the lowest excited states commonly. Though, excitations over a broader energy range may be essential, consequentially requiring very challenging calculations while working for large molecular complexes and high density of states (DOS) materials [49]. Hence, for large systems approximate, precise and efficient computational methods have to be looked for. LR-TD-DFT is extensively employed to compute absorption spectra of larger systems as well [50]. To estimate the absorption spectrum in full LR-TD-DFT context, a two-sided Lanczos process is proposed in Ref. [51]. To acquire an accurate estimation of absorption spectrum, a more standard Lanczos algorithm with an appropriately selected inner product was employed.

4.2.1. LR-TD-DFT formulation

Density response of a system by applying an external time-dependent perturbation in linear response formulation of TD-DFT (LR-TD-DFT) is usually studied as [52]:

$$\rho(\boldsymbol{r}, t) = \rho_0(\boldsymbol{r}) + \boldsymbol{\delta}(\boldsymbol{r}, t) \tag{37}$$

In chemistry, LR-TD-DFT equations are articulated in matrix arrangement using the Kohn-Sham basic formulation. First-order density response $\delta\rho(\boldsymbol{r}, t)$ can be extended on the basis of unperturbed orbitals. Linear response of the electronic density articulated in matrix form is depicted as:

$$\delta\rho_{ij}(t) = \int_{t0}^{t} dt' \sum_{kl} \delta v_{kl}(t') \chi_{ij,\;kl}(\boldsymbol{r}, t, \boldsymbol{r}', \boldsymbol{t}') \tag{38}$$

In Fourier space, it is represented as:

$$\delta\rho_{ij}(\omega) = \sum_{kl} \delta v_{kl}(\omega) \chi_{ij,\;kl}(\omega) \tag{39}$$

The connection between Kohn-Sham response function and particular density response function is efficiently stated in terms of the inverse of their conforming Fourier transform time, $t_2 - t_1$ as follows:

$$\chi^{-1}(\boldsymbol{r}, \boldsymbol{r}', \omega) = \chi_s^{-1}(\boldsymbol{r}, \boldsymbol{r}', \omega) - \frac{1}{|\boldsymbol{r}_1 - \boldsymbol{r}_2|} - f_{xc}(\boldsymbol{r}_1, \boldsymbol{r}_2\omega) \tag{40}$$

In summary, locating excitation energies of the interacting system is problematic, and poles of the response function give the way to calculate excitation energies.

$$\{f_I, \omega_I\} \Rightarrow poles\ of\ \chi(\omega)$$

Actually, $\chi(\omega)$ has poles at correct excitation energies ω_I. From this point, calculations for absorption spectra follow the route as explained in Section 4.1. Computation of the dynamic dipole polarizability [$\alpha(\omega)$] is a noninteracting response of specific interest in calculating absorption spectra, which is a response function that relays external potential to the change in dipole as depicted in Section 4.1. The Fourier transform of the dynamic dipole polarizability can be written as in Eq. (29). Excitation energies (ω_I) are calculated by poles of the dynamic polarizability [53], while the oscillator strengths are determined by residual (f_I) [52].

Calculating the absorption spectrum with LR-TD-DFT method also includes resolving a non-Hermitian eigenvalue problem; therefore, the absorption spectrum is attained as [50]:

$$\sigma(\omega) = \frac{1}{3} \sum_{i} f_i^2 |\delta(\omega - \lambda_i) - \delta(\omega + \lambda_i)| \tag{41}$$

4.3. Electronic calculations using Gaussian software

TD-DFT method in Gaussian makes it practical to study excited state systems since it produces results that are comparable in accuracy to ground-state DFT calculations. Natural transition orbitals (NTOs) can be a helpful way of obtaining a qualitative description of electronic

excitations. They do so by transforming the ordinary orbital representation into a more compact particle (occupied) to empty hole (unoccupied) [54].

i.   First step follows the calculations presented in Section 2.1.5 till step i for geometry optimization calculations and then follow steps used to perform TD-DFT calculation of the optimized structure for UV-Visible spectral calculations. Solvent can be added using TD (singlets, nstates).

ii.   Calculate the absorption spectrum. Compare the calculated absorption spectra (lambda max) with the experiment taking f > 0.0. Basis set/methods can be changed to generate spectrum in good agreement with theoretical assumption.

Generating NTOs:

i.   Run an excited state calculation, saving the checkpoint file.

ii.   Examine the calculation results to determine the excited state of interest.

iii. Run a single point calculation to generate the NTOs for the desired excited state. This step can be repeated to view focusing excited state.

5. Examples illustrating vibrational calculations

In our work [55], we have synthesized 1,3-diisobutyl thiourea ($C_9H_{20}N_2S$) and its vibrational analysis was carried out using DFT methods. Theoretical calculations for vibrational spectra
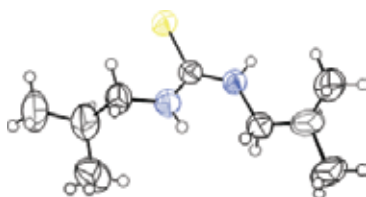
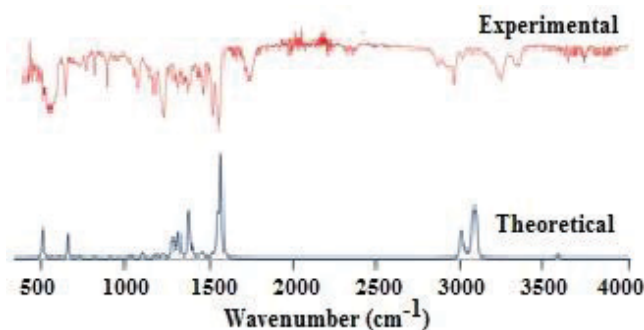**Figure 2.** Crystal structure (ORTEP plot) of 1,3-diisobutyl thiourea compound.

Figure 3. Comparative vibrational spectra of compound in gaseous state (theoretical, calculated using B3LYP/6–311G method) and in the solid state (experimental).
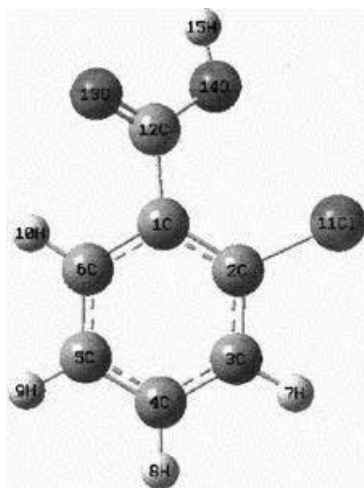
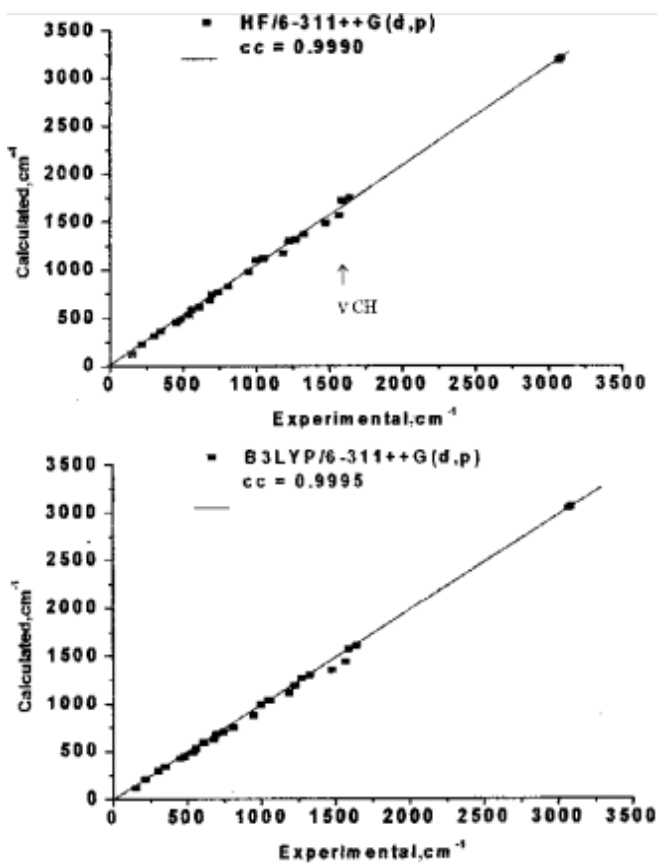**Figure 4.** Numbering system implemented for 2-chlorobenzoic acid.

Figure 5. Graphic correlation between the experimental and calculated wavenumber obtained by the *ab initio* HF and DFT/B3LYP/6–311++G(d,p) methods for 2-chlorobenzoic acid.

analysis using DFT B3LYP/6–311G method were done in gaseous state, while experimental calculations were done in solid state. Geometry of compound was optimized using Gaussian employing DFT/B3LYP method with the 6–311G basis set. Optimized geometry of compound was compared with crystal structure of compound that depicted the support for the crystal structure (**Figure 2**). DFT results for vibrational analysis were compared with experimental analysis, which were found in good agreement with each other (**Figure 3**) [55].

Sundaraganesun et al., calculated structure, harmonic frequencies and vibrational mode assignments for 2-chlorobenzoic acid using HF and DFT methods employing the 6-311++G(d,p) basis set. The results of the molecular structure and vibrational frequencies obtained on the basis of calculations in Gaussian are critically equated with experimental IR data recorded in gas phase (**Figures 4** and **5**) [56].

6. Example illustrating calculation of NMR parameters

Alver et al. carried out NMR spectroscopic study, and DFT calculations of GIAO NMR shieldings and ^{1}J spin-spin coupling constants of 1,9-diaminononane (danon, $C_9H_{22}N_2$) were done. ^{1}H, ^{13}C NMR chemical shifts and $^1J_{CH}$ coupling constants of danon are calculated by means of B3LYP method, and 6-311++G(d,p) basis set is used. Comparison between the experimental and the theoretical results illustrates that density functional B3LYP method is able to deliver suitable results for expecting NMR properties (**Table 1**, **Figures 6** and **7**) [57].

Nuclei	Experimental (ppm)	B3LYP (ppm)
C_3, C_7	28.2	31.1
C_4, C_6	30.5	34.6
C_5	30.6	34.9
C_2, C_8	33.2	37.9
C_1, C_9	42.4	48.9
$H_{16, 17}$, $H_{24, 25}$	1.3	1.2
$H_{18, 19}$, $H_{22, 23}$, $H_{20, 21}$	1.3	1.3
$H_{30, 31}$, $H_{32, 33}$	1.5	1.2
$H_{14, 15}$, $H_{26, 27}$	1.5	1.3
$H_{12, 13}$, $H_{28, 29}$	2.6	2.5
^{1}J(C_nH_n)	Experimental (Hz)	B3LYP (Hz)
$C_2H_{14}H_{15}$, $C_8H_{26}H_{27}$	122.4	118.2
$C_3H_{16}H_{17}$, $C_7H_{24}H_{25}$	122.9	119.1
$C_4H_{18}H_{19}$, $C_6H_{22}H_{23}$	123.8	119.7
$C_5H_{20}H_{21}$, $C_1H_{12}H_{13}$, $C_9H_{28}H_{29}$	135.2	132.1

Table 1. Experimental and calculated ^{13}C, ^{1}H NMR chemical shifts (ppm) and $^1J_{CH}$ NMR coupling constants (Hz) of danon.
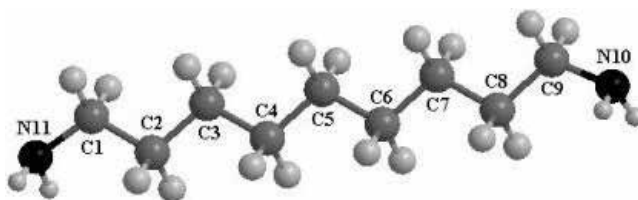
Figure 6. Optimized molecular structure of danon.
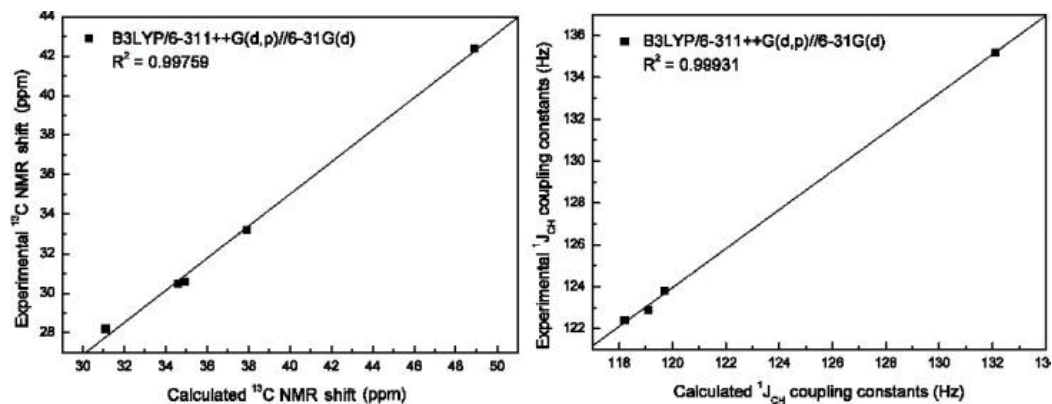

Figure 7. Plot of the calculated vs. the experimental ^{13}C NMR chemical shifts (ppm) and ^{1}J coupling constants (Hz) of danon.

6.1. Different software for DFT calculations

Gaussian is most extensively used software as graphical demonstration of variability of results, e.g., simulation of normal modes, molecular orbital, atomic charges, electrostatic potential, NMR shielding density and potential energy surface scans, can be displayed. Besides this, **Octopus** is a scientific program aimed at the ab initio virtual experimentation. Electrons are described quantum-mechanically within DFT and TDDFT when doing simulations in time. **Spartan** is a potent software tool that applies the power of molecular mechanics and quantum chemical calculations on chemistry research with sophisticated computational algorithms. **Dalton** is a powerful molecular electronic structure program, with an extensive functional for the calculation of molecular properties at the HF, DFT, MCSCF and CC levels of theory. **DMol3** is a unique, accurate and reliable DFT quantum mechanical code for research in the chemical and pharmaceutical industries. **CASTEP** is a software package that uses DFT to provide a good atomic level description of all manner of materials and molecules. It can give information about total energies, forces and stresses on an atomic system, as well as calculate optimum geometries, band structures, optical spectra, phonon spectra and much more. Dynamic simulations can be performed also. **HyperChem** software includes molecular mechanics, molecular dynamics, and semi-empirical and ab initio molecular orbital methods. HyperChemData and HyperNMR have been migrated into HyperChem and new features have been added.

7. Conclusion

This chapter focused on the use of DFT-based methods for spectral calculations, i.e., of vibrational, NMR and electronic calculations. Vibrational spectral generation depends upon Gaussian broadening function, while vibrational frequencies are calculated by determining the second derivative of energy after geometry optimization. Vibrational frequencies and zero-point energy for maximum vibration can be calculated theoretically as well. B3LYP density functional hybrid method is proposed to give more exact values of vibrational frequencies. The calculation of NMR parameters on DFT grounds depends upon exchange correlation functional, i.e., LDA, GGA and mostly employed hybrid functional B_3LYP. The GIAO and IGLO methods are used to solving gauge problems in NMR shielding tensor calculations. Nuclear spin-spin coupling constants can be calculated on theoretical grounds, whereas DFT-B3LYP-GIAO method is employed for chemical shift calculations. For electronic spectral calculations, TD-DFT is employed for excited state measurements. Vertical excitations, oscillator strength and intensity of absorption are calculated using TD-DFT theoretical methods. Linear response function incorporation to TD-DFT approach has proved helpful to study electronic density and absorption spectrum calculations of larger systems. Gaussian software is most employed for IR, NMR and UV spectral calculations.

Author details

Ataf Ali Altaf[1]*, Samia Kausar[1] and Amin Badshah[2]

*Address all correspondence to: atafali.altaf@uog.edu.pk

1 Department of Chemistry, University of Gujrat, Gujrat, Pakistan

2 Department of Chemistry, Quaid-i-Azam University, Islamabad, Pakistan

References

[1] Becke AD. A new mixing of Hartree-Fock and local density-functional theories. The Journal of Chemical Physics. 1993;**98**:1372-1377. DOI: 10.1063/1.464304

[2] Hohenberg P, Kohn W. Inhomogeneous electron gas. Physical Review. 1964;**136**:B864. DOI: 10.1103/PhysRev.136.B864

[3] Johnson BG. Development, implementation and applications of efficient methodologies for density functional calculations. Theoretical and Computational Chemistry. 1995;**2**: 169-219. DOI: 10.1016/S1380-7323(05)80036-6

[4] Kohn W, Sham LJ. Self-consistent equations including exchange and correlation effects. Physical Review. 1965;**140**:A1133. DOI: 10.1103/PhysRev.140.A1133

[5] Seminario JM. An introduction to density functional theory in chemistry. Theoretical and Computational Chemistry. 1995;**2**:1-27. DOI: 10.1016/S1380-7323(05)80031-7

[6] Watson TM, Hirst JD. Density functional theory vibrational frequencies of amides and amide dimers. The Journal of Physical Chemistry A. 2002;**106**:7858-7867. DOI: 10.1021/jp025551l

[7] Wong MW. Vibrational frequency prediction using density functional theory. Chemical Physics Letters. 1996;**256**:391-399. DOI: 10.1016/0009-2614(96)00483-6

[8] Malkin VG. Nuclear magnetic resonance shielding tensors calculated with a sum-over-states density functional perturbation theory. Journal of the American Chemical Society. 1994;**116**:5898-5908. DOI: 10.1021/ja00092a046

[9] Kutzelnigg W, Fleischer U, Schindler M. The IGLO-method: Ab-initio calculation and interpretation of NMR chemical shifts and magnetic susceptibilities. In: Deuterium and Shift Calculation. Verlag, Heidelberg: Springer; 1990. pp. 165-262

[10] Stratmann RE, Scuseria GE, Frisch MJ. An efficient implementation of time-dependent density-functional theory for the calculation of excitation energies of large molecules. The Journal of Chemical Physics. 1998;**109**:8218-8224. DOI: 10.1063/1.477483

[11] Alvarellos J, Metiu H. The evolution of the wave function in a curve crossing problem computed by a fast Fourier transform method. The Journal of Chemical Physics. 1988;**88**:4957-4966. DOI: 10.1063/1.454707

[12] Simoni E. Time-dependent theoretical treatment of intervalance absorption spectra. Exact calculations in a one-dimensional model. The Journal of Physical Chemistry. 1993;**97**:12678-12684. DOI: 10.1021/j100151a009

[13] Franzen S. Use of periodic boundary conditions to calculate accurate β-sheet frequencies using density functional theory. The Journal of Physical Chemistry A. 2003;**107**:9898-9902. DOI: 10.1021/jp035215k

[14] Scott AP, Radom L. Harmonic vibrational frequencies: An evaluation of Hartree-Fock, Møller-Plesset, quadratic configuration interaction, density functional theory, and semi-empirical scale factors. The Journal of Physical Chemistry. 1996;**100**:16502-16513. DOI: 10.1021/jp960976r

[15] Levine IN, Busch DH, Shull H. Quantum Chemistry. 5th ed. Upper Saddle River NJ: Pearson Prentice Hall; 2009. p. 6

[16] Foresman JB. Ab initio techniques in chemistry: Interpretation and visualization. In: Swift ML, Zielinski TJ, editors. Ch. 14 in Using Computers in Chemistry and Chemical Education. Washington, DC: ACS Books; 1997

[17] Nagabalasubramanian P. FTIR and FT Raman spectra, vibrational assignments, ab initio, DFT and normal coordinate analysis of α,α dichlorotoluene. Spectrochimica Acta Part A: Molecular and Biomolecular Spectroscopy. 2009;**73**:277-280. DOI: 10.1016/j.saa.2009.02.044

[18] Becke AD. Density-functional exchange-energy approximation with correct asymptotic behavior. Physical Review A. 1988;**38**:3098. DOI: 10.1103/PhysRevA.38.3098

[19] Andersson MP, Uvdal P. New scale factors for harmonic vibrational frequencies using the B3LYP density functional method with the triple-ζ basis set 6-311+ G (d, p). The Journal of Physical Chemistry A. 2005;**109**:2937-2941. DOI: 10.1021/jp045733a

[20] Ernst RR, Bodenhausen G, Wokaun A. Principles of Nuclear Magnetic Resonance in one and two Dimensions. 2nd ed. Clarendon Press Oxford. 1987;**14**:640 p. ISBN: 0-19-855647-0

[21] Tossell JA. Nuclear Magnetic Shieldings and Molecular Structure. 2nd ed. Springer Netherlands: Springer Science & Business Media. 2012;**386**:584 p. DOI: 10.1007/978-94-011-1652-7

[22] Jensen F. Introduction to Computational Chemistry. United States: John Wiley & Sons; 2017

[23] Fukui H. Methods of calculating NMR chemical shifts. Magnetic Resonance Review. 1987;**11**:205-274

[24] Schreckenbach G, Ziegler T. The calculation of NMR shielding tensors based on density functional theory and the frozen-core approximation. International Journal of Quantum Chemistry. 1996;**60**:753-766. DOI: 10.1002/(SICI)1097-461X

[25] Parr RG, Weitao Y. Density-Functional Theory of Atoms and Molecules. Oxford University Press; 1994. p. 16

[26] McWeeny R. Methods of Molecular Quantum Mechanics. Academic Press; 1992

[27] Becke AD. Current-density dependent exchange-correlation functionals. Canadian Journal of Chemistry. 1996;**74**:995-997. DOI: 10.1139/V09-102

[28] Bru K, DFT Study of NMR Chemical Shifts and Spin-Spin Scalar Interactions in Nucleic Acids. National Centre for Biomolecular Research. 2003;9-81

[29] Perdew JP. Density-functional approximation for the correlation energy of the inhomogeneous electron gas. Physical Review B. 1986;**33**:8822. DOI: 10.1103/PhysRevB.33.8822

[30] Perdew JP, Pederson MR, Singh DJ, Fiolhais C, et al. Atoms, molecules, solids, and surfaces: Applications of the generalized gradient approximation for exchange and correlation. Physical Review B. 1992;**46**(6671):9

[31] Lee C, Yang W, Parr RG. Development of the Colle-Salvetti correlation-energy formula into a functional of the electron density. Physical Review B. 1988;**37**:785. DOI: 10.1103/PhysRevB.37.785

[32] Kutzelnigg W. Ab initio calculation of molecular properties. Journal of Molecular Structure: Theochem. 1989;**202**:11-61. DOI: 10.1016/0166-1280(89)87003-4

[33] Schreckenbach G, Ziegler T. Density functional calculations of NMR chemical shifts and ESR g-tensors. Theoretical Chemistry Accounts: Theory, Computation, and Modeling (Theoretica Chimica Acta). 1998;**99**:71-82. DOI: 10.1007/s002140050

[34] Schreckenbach G, Ziegler T. Calculation of NMR shielding tensors using gauge-including atomic orbitals and modern density functional theory. The Journal of Physical Chemistry. 1995;**99**:606-611. DOI: 10.1021/j100002a024

[35] Kutzelnigg W. Theory of magnetic susceptibilities and NMR chemical shifts in terms of localized quantities. Israel Journal of Chemistry. 1980;**19**:193-200. DOI: 10.1002/ijch.198000020

[36] Malkin VG. The calculation of NMR and ESR spectroscopy parameters using density functional theory. Theoretical and Computational Chemistry. 1995;**2**:273-347. DOI: 10.1016/S1380-7323(05)80039-1

[37] Malkin VG, Malkina OL, Salahub DR. Calculation of spin—Spin coupling constants using density functional theory. Chemical Physics Letters. 1994;**221**:91-99. DOI: 10.1016/0009-2614(94)87023-3

[38] Bagley AC. Investigations of NMR chemical shifts using DFT-B3LYP-GIAO calculations. In: NMR Spectroscopy in the Undergraduate Curriculum: Upper-Level Courses and across the Curriculum. Vol. 32016. ACS Publications. pp. 67-77. DOI: 10.1021/bk-2016-1225.ch005

[39] Runge E, Gross EK. Density-functional theory for time-dependent systems. Physical Review Letters. 1984;**52**:997. DOI: 10.1103/PhysRevLett.52.997

[40] Gross E, Kohn W. Time-dependent density-functional theory. Advances in Quantum Chemistry. 1990;**21**:255-291. DOI: 10.1016/S0065-3276(08)60600-0

[41] Gross E, Dobson J, Petersilka M. Density functional theory of time-dependent phenomena. Density Functional Theory II. 1996:81-172

[42] Casida ME, Huix-Rotllant M. Progress in time-dependent density-functional theory. Annual Review of Physical Chemistry. 2012;**63**:287-323. DOI: 10.1146/annurev-physchem-032511-143803

[43] Castro A. Octopus: A tool for the application of time-dependent density functional theory. 2006;**243**:2465-2488. DOI: 10.1002/pssb.200642067

[44] Jacquemin D. Absorption and emission spectra in gas-phase and solution using TD-DFT: Formaldehyde and benzene as case studies. Chemical Physics Letters. 2006;**421**:272-276. DOI: 10.1016/j.cplett.2006.01.068

[45] Rüger R. Efficient calculation of electronic absorption spectra by means of intensity-selected time-dependent density functional tight binding. Journal of Chemical Theory and Computation. 2014;**11**:157-167. DOI: 10.1021/ct500838h

[46] Makowska-Janusik M. Absorption spectra of poly-N-vinylcarbazole derivatives by experiment and simulation. European Polymer Journal. 2004;**40**:799-804. DOI: 10.1016/j.eurpolymj.2003.11.019

[47] Kityk I. Time-dependent DFT simulation of UV-spectra and molecular structure of several bis-pyrazolopyridines derivatives

[48] Adamo C, Jacquemin D. The calculations of excited-state properties with time-dependent density functional theory. Chemical Society Reviews. 2013;**42**:845-856. DOI: 10.1039/C2CS35394F

[49] Tussupbayev S. Comparison of real-time and linear-response time-dependent density functional theories for molecular chromophores ranging from sparse to high densities of states. Journal of Chemical Theory and Computation. 2015;**11**:1102-1109. DOI: 10.1021/ct500763y

[50] Brabec J et al. Fast algorithms for estimating the absorption spectrum within the linear response time-dependent density functional theory. 2015;1-19

[51] Rocca D. Turbo Charging time-dependent density-functional theory with Lanczos chains. The Journal of Chemical Physics. 2008;**128**:154105. DOI: 10.1063/1.2899649

[52] Chong DP. Recent Advances in Density Functional Methods: (Part I). Singapore: World Scientific; 1995. p. 1

[53] Petersilka M, Gossmann U, Gross E. Excitation energies from time-dependent density functional theory. Physical Review Letters. 1996;**76**:1212. DOI: 10.1103/PhysRevLett.76.1212

[54] Martin RL. Natural transition orbitals. The Journal of Chemical Physics. 2003;**118**:4775-4777. DOI: 10.1063/1.1558471

[55] Altaf AA. Synthesis, crystal structure, and DFT calculations of 1,3-diisobutyl thiourea. Journal of Chemistry. 2015;**2015**:1-5. DOI: 10.1155/2015/913435

[56] Sundaraganesan N, Joshua BD, Radjakoumar T. Molecular structure and vibrational spectra of 2-chlorobenzoic acid by density functional theory and ab-initio Hartree-Fock calculations. Indian Journal of Pure and Applied Physics. 2009;**47**:248-258

[57] Alver Ö, Parlak C, Senyel M. NMR spectroscopic study and DFT calculations of GIAO NMR shieldings and 1JCH spin-spin coupling constants of 1,9-diaminononane. Bulletin of the Chemical Society of Ethiopia. 2009;**23**:437-444. DOI: 10.4314/bcse.v23i3.47668

DFT Calculations and Statistical Mechanics Applied to Isomerization of Pseudosaccharins

Zuriel Natanael Cisneros-García,
David Alejandro Hernández-Velázquez,
Francisco J. Tenorio and
Jaime Gustavo Rodríguez-Zavala

Abstract

In the present work, molar fractions were obtained as a function of temperature with different levels of theory for the most representative isomers of three systems belonging to the family of pseudosaccharins. The choice of those three systems was due to the fact that it is known in the scientific literature that these systems present very small differences in their relative energies which make a complicated experimental characterization, in addition these compounds are of interest in the biological area. These systems represent challenges not only from an experimental point of view but also from a theoretical point of view. From the theoretical perspective, this study is also complicated since several possible isomers with very similar energies are presented. The diagrams of species distribution (molar fractions) provide information that cannot be accessed through the electronic structure calculations at T = 0. Here, this tool was useful to identify the most probable isomer from several quasi-degenerate isomers and to discern if thermal effects favor any of them, as well as to find trends despite the different results of each level of theory. Additionally, an analysis was performed on vibrational, rotational and electronic data in order to know the reason of the behavior of molar fractions as function of temperature.

Keywords: molar fractions, pseudosaccharin, isomerism, DFT calculations, statistical mechanics

1. Introduction

Having the same chemical composition, a molecule can present different geometrical arrangements of atoms, leading to distinct chemical and physical properties. Here lies the importance

of knowing the arrangement of the atoms inside molecules. The different atomic arrangements in a molecule are known as isomers and their study gives rise to isomerization or isomerism. Computational chemistry is one of the most used tools in this branch of research. Through the analysis of stabilities by means of the electronic energy, the isomers that could be found in an experiment can be known. However, when the energetic differences between isomers are very small, it is difficult to assure that the lower energy isomer is the only one present in the experiment. Existing models, both in the framework of methods of electronic structure or molecular dynamics, have contributed greatly to the study of the different types of isomerization, and have been improved taking into account, for example, the inclusion of solvents. Despite advances in theory and technology, no current theoretical methodology is 100% accurate. This leads to the fact that it is not sufficient to consider only the results yielded by these methods, mainly in molecules whose isomers have very similar energies, which could be considered as part of the error associated to the level of theory.

For this reason, given the importance of elucidating the isomerism of a molecular system with very small energy differences, it is important to make use of other tools. In this chapter, we will obtain diagrams of species predominance (molar fractions) as a function of the temperature (assuming that the equilibrium has been reached) for some systems of the pseudosaccharin family that have isomeric structures with small energy differences and are of great importance in various fields of applied sciences.

Pseudosaccharins, also known as benzisothiazoles, are molecular systems with a wide variety of properties. Their structures are derived from saccharin, which is the first synthetic sweetener that is still used with that aim, but also has many industrial applications. Its photosensitive properties have aroused interest in the derivatives of this system for applications of synthesis of coordination compounds and bioorganic synthesis [1]. Its general structure can be seen in **Figure 1**, where **R** can be any other functional group or molecule. Additionally, these structures may present a tautomerism known as Chapman rearrangement [2]; this internal reaction of the structure consists in the movement of the **R** group to the oxygen of the carbonyl group as the temperature increases. Depending on the degrees of freedom that the **R** group possesses, different structures can be formed with different properties, reason
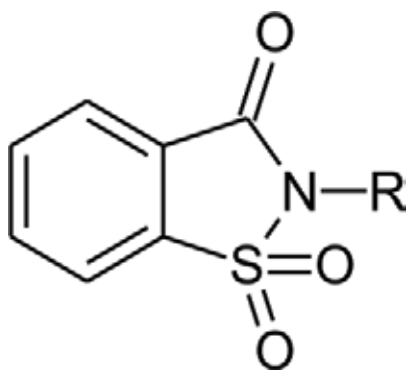

Figure 1. General structure for the family of pseudosaccharins.

why such rearrangement has awakened the interest to elucidate the mechanism of isomerization [3]. Moreover, pseudosaccharins are receptors of a quite potent electronic density that has called attention in research areas of synthesis of organic compounds.

Pseudosaccharins are compounds of interest in several fields of research, specifically in biologically active systems [4]. Their usage has been reported in the treatment of cardiac and hepatic diseases [5, 6], and even for the treatment of breast cancer, as antibiotic agents and herbicides [7–9]. Adding to these applications, Hlasta et al. [10] proposed a series of compounds of the pseudosaccharins family as inhibitors of the human leukocyte elastase protein, which causes the destruction of the connective tissue of the lungs in people with pulmonary emphysema. They also found how this series of compounds have therapeutic usage in people with this condition [10, 11].

Due to the importance of this type of compounds, studies have been carried out to characterize experimentally and theoretically both their structure and properties. A high reactivity can be found mainly in the junction of the heterocyclic ring and **R**, due to an electron-withdrawing effect of the pseudosaccharyl ring system, which is the reason of the Chapman-like rearrangement. The properties of the pseudosaccharins can be modified depending on which structures are combined with saccharin. In the case of tetrazole-saccharin, the properties of tetrazole, which can be very reactive, have been combined with saccharin, resulting in a greater stability of the tetrazole [12]. Furthermore, the combination of an allyl group with saccharin can also form compounds with the properties mentioned in previous paragraphs.

In previous studies [4, 13, 14], the importance of isomerization in these systems has been demonstrated. As the **R** group can be very flexible, it gives rise to several possible isomers. This can lead to challenges in the characterization of these compounds, since there could be a mixture of isomers whose population can become significant during the synthesis. As a result, there are signals in spectrophotometry [4, 12, 13] that cannot be associated with a precise isomer. Theoretical analysis can ease to obtain the different spectra of the possible isomers and the spectra could be weighted by a number or parameter, for example, a calculated molar fraction. However, when there are small energy differences, it is important to consider the methodology used to obtain the most probable isomers to study; that is, having the challenge of solving structures whose differences in energy are small, methodology becomes very important, because a different functional and basis set (BS) could give rise to different relative stabilities between the isomers.

Due to all the previously mentioned, in the present chapter a systematic study of the isomerization of three pseudosaccharins, which have very small energy differences between them and that have also been previously studied experimentally and theoretically, is performed. For this study, a variation of functional and BS is carried out, however, considering that a better comparison can be made between experimental and theoretical results if thermal effects are taken into account, molar fractions are obtained for the different isomers of pseudosaccharins. It is important to mention that, unlike previous studies on these compounds, populations are obtained as a function of temperature, taking into account different contributions through the vibrational, rotational and electronic partition functions. From this, it is possible to observe the effects of methodology in the molar fractions, as well as to find the reason of behavior of molar fractions plots.

2. Theoretical background

All calculations were performed with Gaussian09 suite of programs [15], while the construction of graphics of molar fractions as a function of temperature was made with a program designed by Professor Slanina et al. [16]. Relaxation of molecular structures, vibrational frequencies, rotational constants and excited states were obtained through B3LYP [17, 18], M06-2X [19] and PBE [20] exchange-correlation (XC) functionals, along with 6-311++G(3df,3pd), 6-31++G(3df,3pd), 6-311+G(d,p) and 6-31+G(d,p) [21, 22] basis. The choice of the methodology was made taking as a starting point the level of theory used in previous studies [4, 13, 14]. Additionally, the other functionals and BSs were used in order to be able to compare the results and analyze the importance of the methodology. It is important to mention that, for selected cases, total electronic energies were refined through the second-order Møller-Plesset perturbation theory, MP2, along with 6-311++G(3df,3pd) and 6-31+G(d,p) level of calculation.

In this work, calculations of molar fractions (x_i) including thermal effects for n isomers have been obtained through their partition functions q_i and the enthalpies at the absolute zero temperature or ground-state energies $\Delta H^0_{0,i}$ (i.e. the relative potential energies corrected for the vibrational zero-point energies) by the formula:

$$x_i = \frac{q_i \, exp\left(-\Delta H^0_{0,i}/RT\right)}{\sum_{j=1}^n q_j \, exp\left(-\Delta H^0_{0,j}/RT\right)} \tag{1}$$

where R is the gas constant and T the absolute temperature. It is worth to mention that, as it is expected, single point calculations (MP2 results) are not corrected by the vibrational zero-point energies. Eq. (1) is an exact formula of the isomers, supposing the conditions of the inter-isomeric thermodynamic equilibrium. Rotational-vibrational partition functions were constructed from the calculated structural and vibrational data using the rigid rotator and harmonic oscillator (RRHO) approximation. The electronic partition function was constructed by 10 time-dependent electronic excitation energies. All calculations were performed taking into account a tight convergence in the self-consistent field calculation, and an ultrafine mesh in the integration.

3. Results and discussion

From previous studies on pseudosaccharins, three isomers were reported for 2-allyl-1,2-benzisothiazol-3(2*H*)-one 1,1-dioxide (ABIOD) [4], five isomers for allyl ether 3-(allyloxy)-1,2-benzisothiazole1,1-dioxide (ABID) [13] and six isomers for tetrazole-saccharyl [14]. The isomers for each pseudosaccharyl molecule were obtained through the rotation of two dihedral angles as will be explained in the next subsections. It is shown in **Figure 2(a)** the ABIOD pseudosaccharyl, in **Figure 2(b)** the ABID pseudosaccharyl and in **Figure 2(c)** and **(d)** tetrazole saccharine. The numbers are needed to understand the formation of the different isomers through dihedral angles.
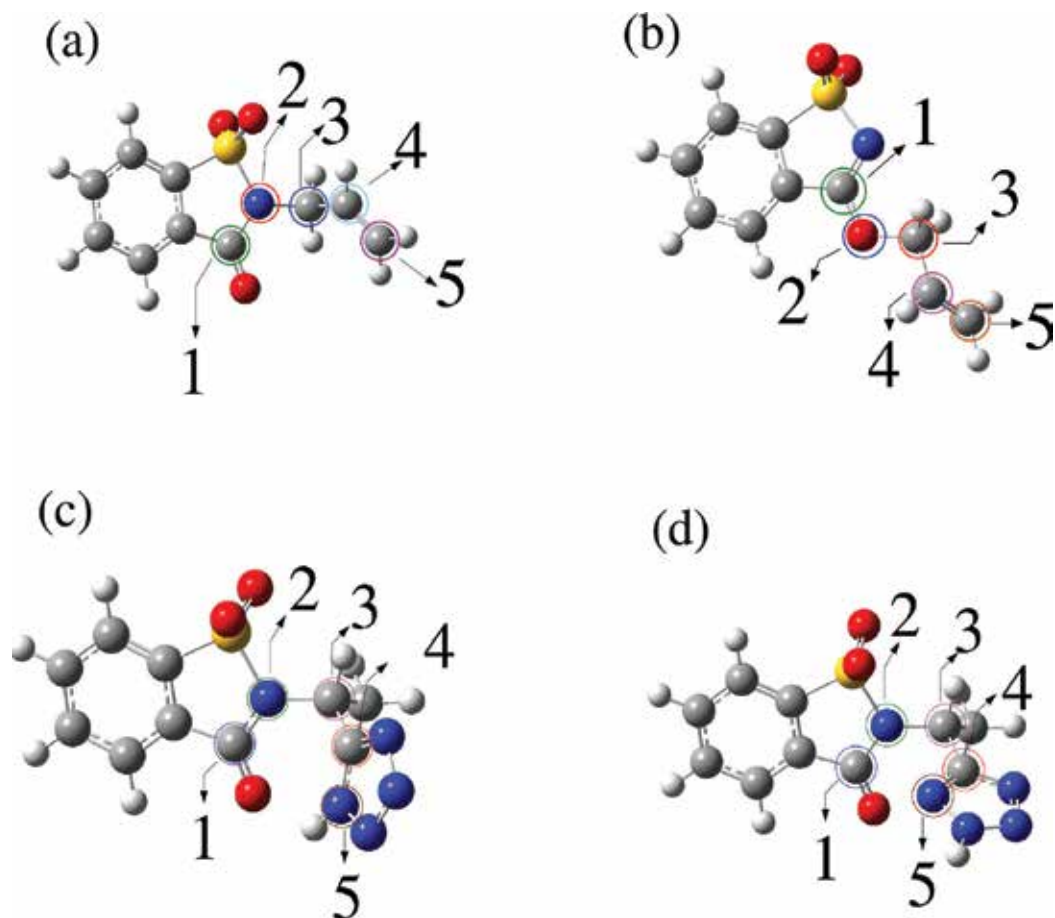
Figure 2. Pseudosaccharins studied in the present work. (a) ABIOD, (b) ABID, (c) and (d) tetrazole-saccharyl.

3.1. 2-allyl-1,2-benzisothiazol-3(2*H*)-one 1,1-dioxide

The molecular structure of the ABIOD pseudosaccharin can be considered to be mainly formed by two components; a heterocyclic ring and a flexible allyl substituent. In ABIOD, the molecule can be rotated two dihedral angles and they give rise to different isomers (see **Figure 2(a)**), nevertheless, according to Ref. [4], the dihedral angle formed by atoms 1, 2, 3 and 4 is irrelevant in the formation of isomers because of the sterical hindrance between the allyl group and the rest of the molecule. Consequently, only the dihedral angle formed by atoms 2, 3, 4 and 5 originate different isomers. In the same study, there were found a total of three isomers of ABIOD in a minimum of the potential-energy surface (PES) and they were represented using the abbreviations $C = cis \approx 0°$, $Sk = skew \approx 120°$, $Sk' = skew' \approx -120°$.

In a first step, molecular optimization was performed through B3LYP functional; after that, reoptimizations were performed with M06-2X and PBE functionals.

The corrected zero-point relative energies of the three ABIOD isomers are presented in **Table 1**. For B3LYP XC-functional, it can be observed that the most stable isomer is *Sk*, however, it is important to note that energy differences with *Sk'* and *C* isomers are less than 1 kcal/mol, no matter the BS used. According to M06-2X XC-functional results, the BS that takes into account more polarization and diffuse functions located the *C* isomer as the most stable and the two BSs that do not possess the maximum increases in diffuse functions and polarization found the *Sk* structure as the most stable in a similar way as the B3LYP functional. Again, note that the energies between these isomers are small since they do not reach 1 kcal/mol. Unlike B3LYP and M06-2X, it was noticed that PBE outcame the *Sk'* isomer as the most stable at T = 0, nonetheless the energetic differences are very small since these do not reach 1 kcal/mol.

As can be observed from DFT calculations at T = 0, the analysis of isomerism is complicated, especially when small energy differences are presented between isomers. Since none of the three functionals (B3LYP, M06-2X and PBE) obtain the same most stable isomer, this quest appears to be quite dependent on the method used. However, it is also worth commenting that the energy difference between the three isomers is very small, regardless of the XC-functional used. Then, it could be considered that the energy differences are within the anticipated error of calculation and therefore, it would be expected that molar fractions as a function of temperature can provide relevant information.

Considering the previous discussion, **Figure 3** shows the molar fractions as a function of temperature for the three isomers of ABIOD pseudosaccharine.

For B3LYP XC-functional it can be observed that the molar fractions do not vary significantly as the temperature increases, in fact, the line corresponding to the *Sk'* isomer is maintained

Isomer	6-311++G(3df,3pd)	6-31++G(3df,3pd)	6-311+G(d,p)	6-31+G(d,p)
B3LYP				
C	0.65	0.73	0.71	0.76
Sk	0	0	0	0
Sk'	0.15	0.16	0.09	0.04
M06-2X				
C	0	0	0.04	0.03
Sk	0.09	0.1	0	0
Sk'	0.59	0.58	0.05	0.43
PBE				
C	0.33	0.33	0.5	0.59
Sk	0.06	0.06	0.18	0.26
Sk'	0	0	0	0

Table 1. Corrected zero-point relative energies (kcal/mol) of ABIOD isomers.
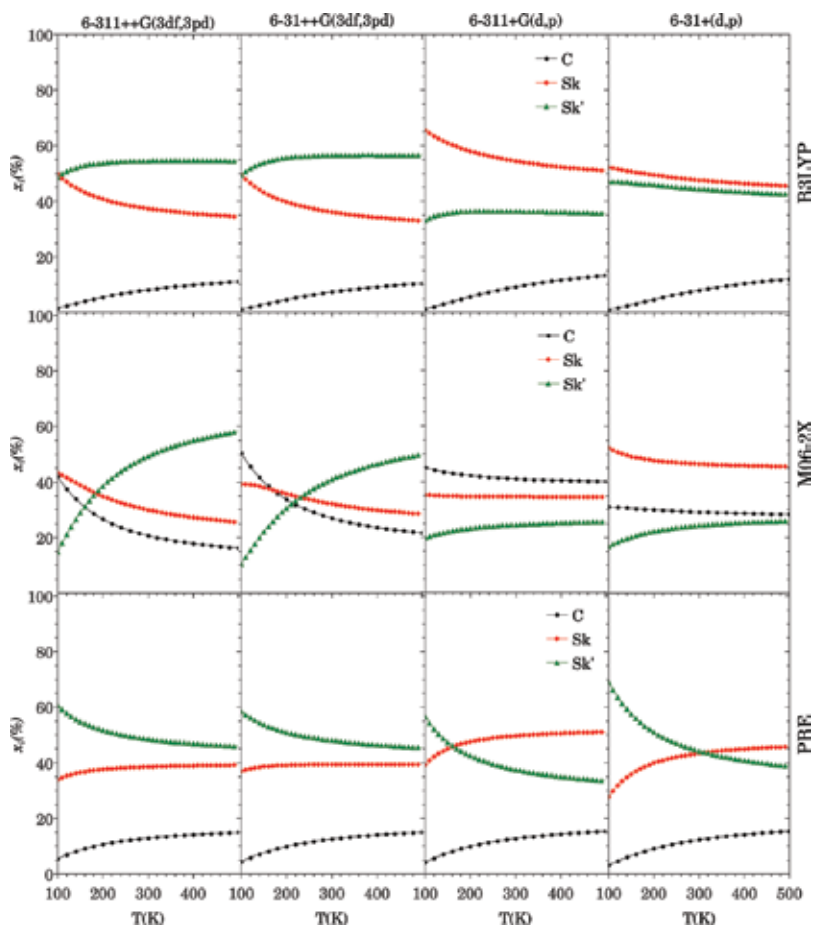
Figure 3. Molar fractions for ABIOD isomers taking into account three XC-functionals with a combination of four BSs.

almost at the same value in all the range of temperature studied. The same trends can be seen for the *Sk* isomer since beyond 200 K there is no significant change. The *C* isomer shows the same trend with a small population increase in the four graphs of B3LYP; that is, at the beginning of the studied range, its population is zero but it slowly grows while temperature increases.

For M06-2X functional, results show that for the first two BSs the graphs are similar and display the same trend in general; however, with 6-31++G(3df,3pd) it is observed that distribution of isomer populations are narrower than in 6-311++G(3df,3pd). Nonetheless, 6-311+G(d,p) and 6-31+G(d,p) present a different trend since the populations change, this behavior could be understood noticing that the energy difference between the three isomers obtained with these methodologies is very close (see **Table 1**), then, the vibrational frequencies, rotational constants and energy levels become important in the construction of the molar fractions. A deeper analysis on vibration frequencies, rotational constants and energy levels is presented below.

As mentioned in a previous paragraph, the relative energies obtained with PBE XC-functional place the *Sk'* isomer as the most stable, therefore, at the beginning of our range of calculation of molar fractions, this was the isomer with the largest population. As observed in (PBE) graphics for the first two BSs in **Figure 3**, the molar fraction plots of each isomer do not cross at any time, which means that the *Sk'* isomer is the most predominant over all the range of temperature studied here, even though the difference in energy with the second most stable isomer is at most 0.06 kcal/mol. For 6-311+G(d,p) and 6-31+G(d,p) a distinct trend can be observed in comparison with 6-311++G(3df,3pd) and 6-31++G(3df,3pd), since in 6-311 G(d,p) there is an exchange (before 200 K) of the most populated isomer which turns now to be *Sk*. Additionally, it can be noticed that the population of both *Sk* and *Sk'* isomers is around 45%. For 6-31+G(d,p), the intersection in the population of *Sk* and *Sk'* isomer is given approximately at 300 K.

From **Figure 3**, it can be observed that B3LYP and PBE XC-functionals obtain the same trends: the less stable structure (*C* isomer) has the lowest population, while the two most stable isomers (*Sk* and *Sk'*) are maintained with the largest population. In fact, it can be seen how for the first two BSs in B3LYP, that even though the *Sk* isomer is the most stable, *Sk'* is the most populated since an exchange in population appears at very low temperatures, which is in agreement with PBE. Additionally, in the last two BSs of the PBE functional, although *Sk'* is the most stable isomer at T = 0, it is not maintained as the isomer with the largest population when the temperature increases. So far, at least it is stated that the two most stable isomers are the ones with the largest population regardless of the methodology (functional and BS) used. On the other hand, M06-2X/6-311++G(3df,3pd) and M06-2X/6-31++G(3df,3pd) are consistent showing that *Sk'* has the largest population at room temperature, however, the last two BSs are not in agreement with these results since 6-311+G(d,p) presents the *C* isomer as the most populated, while 6-31+G(d,p) presents *Sk* isomers as the most populated. Therefore, a deeper analysis must be performed, that is why the peculiar case of M06-2X/6-311+G(d,p) results will be analyzed below.

Due to the complicated comparison between the different results obtained, mainly with M06-2X, both at T = 0 and varying temperature, it was decided to refine the electronic energy through the MP2 method. As a first step, a comparison of energies of the three isomers MP2 optimized and non-optimized was performed.

Firstly, the molecular structures of the three isomers were optimized with MP2/6-311++G(3df,3pd) methodology resulting in the following relative energies: *Sk* = 0, *Sk'* = 0.74 and *C* = 1.09 kcal/mol. The isomer with the lowest energy is taken as 0 kcal/mol. After that, a single point calculation with MP2/6-311++G(3df,3pd) methodology on the previously optimized structure through B3LYP/6-311++G(3df,3pd) methodology was performed, getting the following relative energies: *Sk* = 0, *Sk'* = 0.7 and *C* = 1.2 kcal/mol. These outcomes clarify that optimization of the three isomers, not only result in the same order of stability, but also do not represent a great variation in the relative stability. This can give us confidence in performing only single point calculations with MP2 on structures optimized with different methodologies.

In a second step and according to the results discussed in the previous paragraph, single point calculations were performed with MP2 along with 6-311++G(3df,3pd) and 6-31+G(d,p) BSs on

previously relaxed structures with B3LYP, M06-2X and PBE in order to obtain relative stabilities. For B3LYP optimization and single point calculations through MP2, the relative energies were $Sk = 0$, $Sk' = 0.7$ and $C = 1.2$ kcal/mol using 6-311++G(3df,3pd), on the other hand, $Sk = 0$, $Sk' = 0.68$ and $C = 1.39$ kcal/mol using 6-31+G(d,p). For optimization with M06-2X the results were $Sk = 0$, $Sk' = 0.38$ and $C = 1.21$, additionally, $Sk = 0$, $Sk' = 0.74$ and $C = 1.24$ kcal/mol, when 6-311++G(3df,3pd) and 6-31+G(d,p) were, respectively, used. Finally, for PBE optimization, the results were $Sk = 0$, $Sk' = 0.84$ and $C = 1.31$ with 6-311++G(3df,3pd), and $Sk = 0$, $Sk' = 0.76$ and $C = 1.54$ kcal/mol for 6-31+G(d,p).

As it can be seen, the Sk isomer results as the most stable, as B3LYP functional, however, the energy differences are magnified compared to B3LYP. On the other hand, the narrowest energy difference between the Sk and Sk' isomers is given by MP2/6-311++G(3df,3pd)//M06-2X/6-311++G(3df,3pd) methodology and the largest energy difference is obtained by MP2/6-31G(d,p)//PBE/6-31G(d,p) methodology. It is worth to mention that, regardless of the functional and BS used to relax the molecular structure, the energy obtained through MP2 resulted in the same order of stability ($Sk > Sk' > C$). Therefore, it seems to be that MP2 energy treatment could help to homogenize results at T = 0, additionally, these results are in agreement with the previously reported by Gómez-Zavaglia et al. [4], since they predicted the same most stable isomer with B3LYP functional. In consonance with these results, Sk can be expected to be the isomer with the largest population.

Molar fractions as a function of temperature were re-built using the electronic energy data from MP2 calculations on optimized structures with B3LYP, M06-2X and PBE (see **Figure 4**). As expected, the most populated isomer in all the range of temperature was Sk, however, M06-2X with 6-311++G(3df,3pd) maintained the Sk' isomer as the most populated. From a previous paragraph, it is known that M06-2X got the lowest energy difference between the Sk and Sk' isomers, and it could be the reason of the exchange in population, however, there could be something else inducing that exchange. In order to find a possible reason of this induced exchange, several things were tested, for example, knowing that the Sk' isomer is the one that presents a different behavior in the M06-2X/6-311++G(3df,3pd) methodology (**Figure 4(b)**) in comparison with the other methodologies, rotational constants obtained with M06-2X/6-311++G(d,p) were inserted instead of those obtained with M06-2X/6-311++G(3df,3pd), however, there was no great modification in the graph (see **Figure 5(b)**). Subsequently, the same exchange was made with the electronic transitions, without finding again great modifications in the graph (see **Figure 5(c)**). But, when the same exchange was made with the vibrational frequencies, it was observed that the graphs of the populations changed(see **Figure 5(a)**), obtaining the same trends as the other methodologies of **Figure 4**, where Sk is the most populated isomer followed by Sk' and C.

Having noticed that the vibrational partition function influences in an important way, the vibration frequencies obtained through M06-2X/6-311++G(3df,3pd), were observed for each isomer. Interestingly, it was found that the first frequencies for each isomer are 32, 35 and 14 cm^{-1}, for C, Sk and Sk', respectively. As it can be seen, Sk' has the first frequency of less than half compared to the first frequency of the other two isomers, which could be one reason why the Sk' isomer becomes the one with the highest population at very low temperature
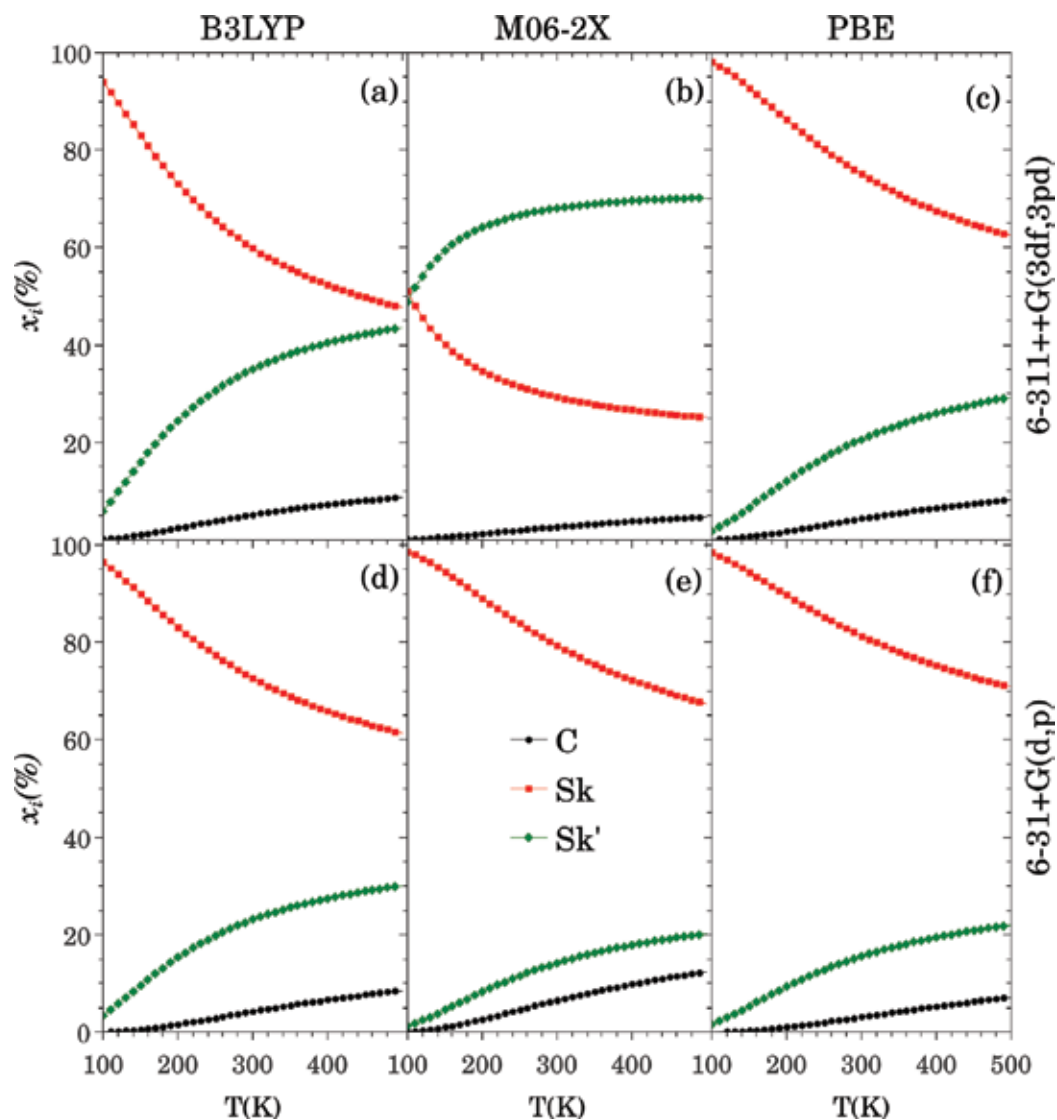
Figure 4. Molar fractions with MP2 energy.

(**Figure 4(b)**), even though the *Sk* isomer had the lowest energy at T = 0. In order to verify if the low value of the first frequency in the isomers result in a larger population when the temperature increases, several variations were made in the vibration frequencies trying to observe an effect. For example, the 66 frequencies of *Sk'*, (with first frequency at 14 cm⁻¹), were changed by the 66 frequencies of *Sk*, (first frequency at 35 cm⁻¹), obtaining the graph of the molar fractions such as those obtained with the other methodologies; that is, when the *Sk'* isomer has similar frequencies to those of the other isomers, this promotes the *Sk* isomer with the largest population due to its lower energy at T = 0. Given this interesting result, a simple test was then proposed by changing only the first frequency of the *Sk'* isomer (14 cm⁻¹), by a
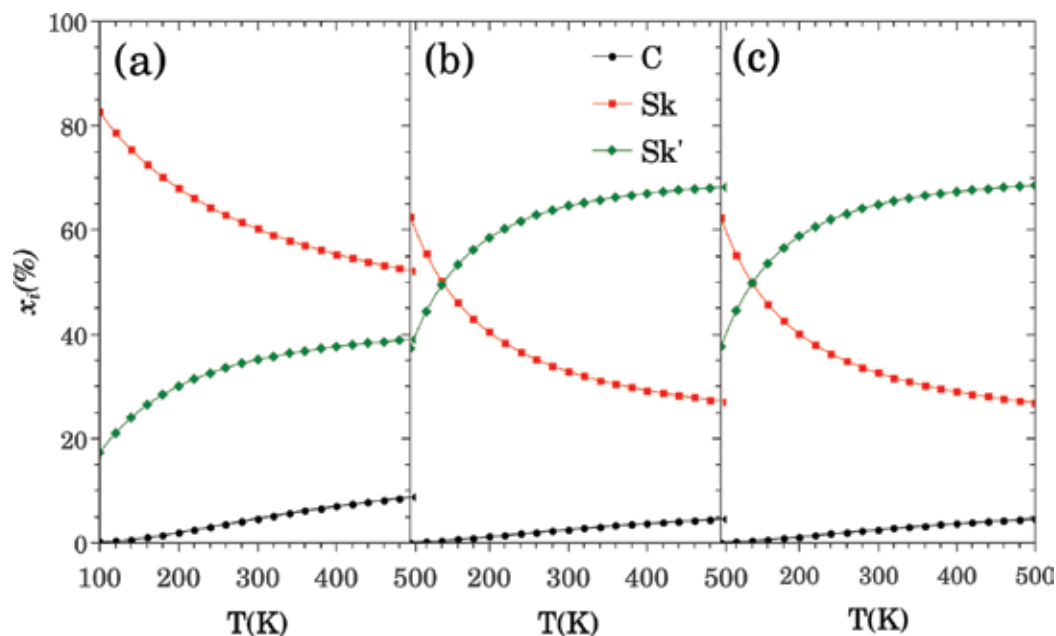
Figure 5. Comparison of molar fractions varying (a) vibrational frequencies, (b) rotational constants and (c) electronic transitions.

value of 34 cm⁻¹, which is a value around the first frequency of the other two isomers. With this modification, it was observed that the molar fractions return to those obtained by the other methodologies; that is, resulting *Sk* as the most populated. According to this analysis, it can be concluded that the vibrational part is very important for the calculation of the molar fractions. In fact, a similar analysis was performed for the molar fractions obtained in **Figure 3** with M06-2X/6-311+G(d,p) results, which showed a different behavior in comparison with the other methodologies. It was observed that the *C* isomer had a frequency of 23 cm⁻¹, whereas the *Sk* and *Sk'* isomers had their first frequencies at 37 and 39 cm⁻¹. A change was then made in the first frequency of the *C* isomer to a value of 38 cm⁻¹, which is close to those of the other two isomers, resulting in a graph of molar fractions where the *Sk* isomer is the most populated for the entire temperature range shown. In summary, when all isomers have very similar first frequency values, enthalpy predicts the isomer with the largest population; however, if one of the isomers presents its first frequency with a very low value in comparison with the correspondent frequency for the other isomers, it is very likely that such isomer presents a larger population when T is increased. From the present analysis, it can be concluded that the choice of a functional that correctly describes the vibration modes of a molecule is of utmost importance for obtaining the predominant zones through molar fractions.

3.2. Pseudosaccharyl allyl ether 3-(allyloxy)-1,2-benzisothiazole1,1-dioxide

The pseudosaccharyl allyl ether 3-(allyloxy)-1,2-benzisothiazole1,1-dioxide (ABID) is a system that has been studied from an experimental and theoretical point of view [13]. In that

study, five structures were found in a minimum in the PES and whose energetic differences are small. The differences between the five isomers are particularly due to the values of two dihedral angles in the structure. In **Figure 2(b)** atoms that conform these angles are shown, the first of them is formed by the atoms numbered as 1, 2, 3, 4 and the second by the atoms 2, 3, 4, 5. From Ref. [13] the five isomers were named according to the values of the dihedral angles in question, the value of the angle formed by the atoms 1, 2, 3, 4 was represented using the abbreviations $T = trans \approx 180°$, $G = gauge \approx 60°$, $G' = gauge' \approx -60°$, for dihedral angle formed by 2, 3, 4, 5 its value was represented by the abbreviations $C = cis \approx 0°$, $Sk = skew \approx 120°$, $Sk' = skew' \approx -120°$. Four of the five isomers belong to the C_1 point group of symmetry with the exception of the TC isomer whose point group is C_S.

Molar fractions as a function of temperature of the five isomers with the XC-functionals and the four BSs used in previous subsection were obtained. For each level of theory, the necessary frequency vibrations were obtained in order to obtain, on one hand, the molar fractions and, on the other hand, to corroborate that molecular structure is in a minimum of PES; rotational constants for building the rotational partition function; and 10 excited states for obtaining the electronic partition function. In **Table 2**, the relative energies obtained with B3LYP, M06-2X

Isomer	6-311++G(3df,3pd)	6-31++G(3df,3pd)	6-311+G(d,p)	6-31+G(d,p)
B3LYP				
GC	1.46	1.51	1.49	1.67
GSk	0.47	0.51	0.38	0.44
GSk'	0.91	0.93	0.8	0.89
TC	0.5	0.59	0.52	0.67
TSk	0	0	0	0
M06-2X				
GC	0.4	0.32	0.41	0.5
GSk	0.18	0.12	0.001	0.004
GSk'	0.39	0.34	0.19	0.24
TC	0	0	0	0
TSk	0.1	0.05	0.05	0.004
PBE				
GC	1.1	1.18	1.18	1.38
GSk	0.13	0.33	0.14	0.27
GSk'	0.64	0.8	0.64	0.77
TC	0.37	0.43	0.36	0.5
TSk	0	0	0	0

Table 2. Corrected zero-point relative energies (kcal/mol) of ABID isomers.

and PBE XC-functional and the proposed BS for the five isomers are shown. It can be observed that B3LYP and PBE got the same order of stability (*TSk* > *GSk* > *TC* > *GSk′* > *GC*) independently of the BS. Although the energy difference between the isomers is not maintained at the same rate, the order of stability is not compromised by varying the BS.

With M06-2X functional a change in order of stability is shown, in contrast to B3LYP and PBE functional, *TC* isomer is the most stable. In spite of the order of stability changes, it is also possible to observe that the energy differences are narrower than B3LYP and PBE, since with this functional the largest difference of energy between the distinct isomers and taking into account the four BSs is at most of 0.5 kcal/mol. From M06-2X, it is difficult to propose an isomer to work in a theoretical study. Then, considering that energy differences are very small, it would be worthwhile to observe the effects of temperature on populations of the five isomers.

The temperature of interest is around 350 K, since these compounds are synthesized at this temperature. Remember that for B3LYP XC-functional and the four BSs, the *TSk* isomer is the most stable and the energy difference with the second and third most stable isomers is small. In **Figure 6**, molar fractions as a function of temperature obtained with B3LYP and the utilized BSs are shown. The results display that all used BSs are consistent, it is observed that the isomer of greatest population for all BSs at the temperature of interest is *TSk*, although it is the predominant isomer, its population at 350 K does not exceed 60%, the second is around 17% and the rest is lower than 12%. As it can be observed in **Figure 6**, populations obtained through PBE functional have the same trends as B3LYP functional, and despite there is only a small difference, it is shown that the second most stable isomer (*GSk*) has a higher population (at around T = 300 K) compared to its population with B3LYP functional.

Regarding M06-2X, there is an interesting event with the lowest potential-energy species, in spite of *TC* isomer having actually the lowest energy at absolute zero (see **Table 2**), the most populated is the second lowest potential-energy isomer. Therefore, the molar fraction calculations showed the *TSk* isomer as the most predominant at the temperature of interest and the rest of them with very similar populations no matter the BS used, in fact, from the theoretical point of view, it is worth mentioning that two well-defined horizontal lines begin to form in **Figure 6**, the first one with the population of the most stable isomer and the other one with the populations of the rest of the isomers. The molar fractions determine that the consideration of statistical physics, in order to introduce thermal effects in the isomerization of molecular structures with small energy differences, becomes important, since, as we can see in **Figure 6**, regardless of the greater stability of the *TC* isomer, *TSk* is obtained as the most abundant, even at very low temperatures as the ones used in the present analysis. Based on these results, the importance of performing an analysis of this nature must be considered.

From these results, it can be concluded that, in one hand, both B3LYP and PBE XC-functional remark the same trends and, on the other hand, in spite than M06-2X obtained a more complicated distribution of relative energies at T = 0, when thermal effects are taken into account, the same trends in populations of the five isomers compared to B3LYP and PBE functionals are obtained.
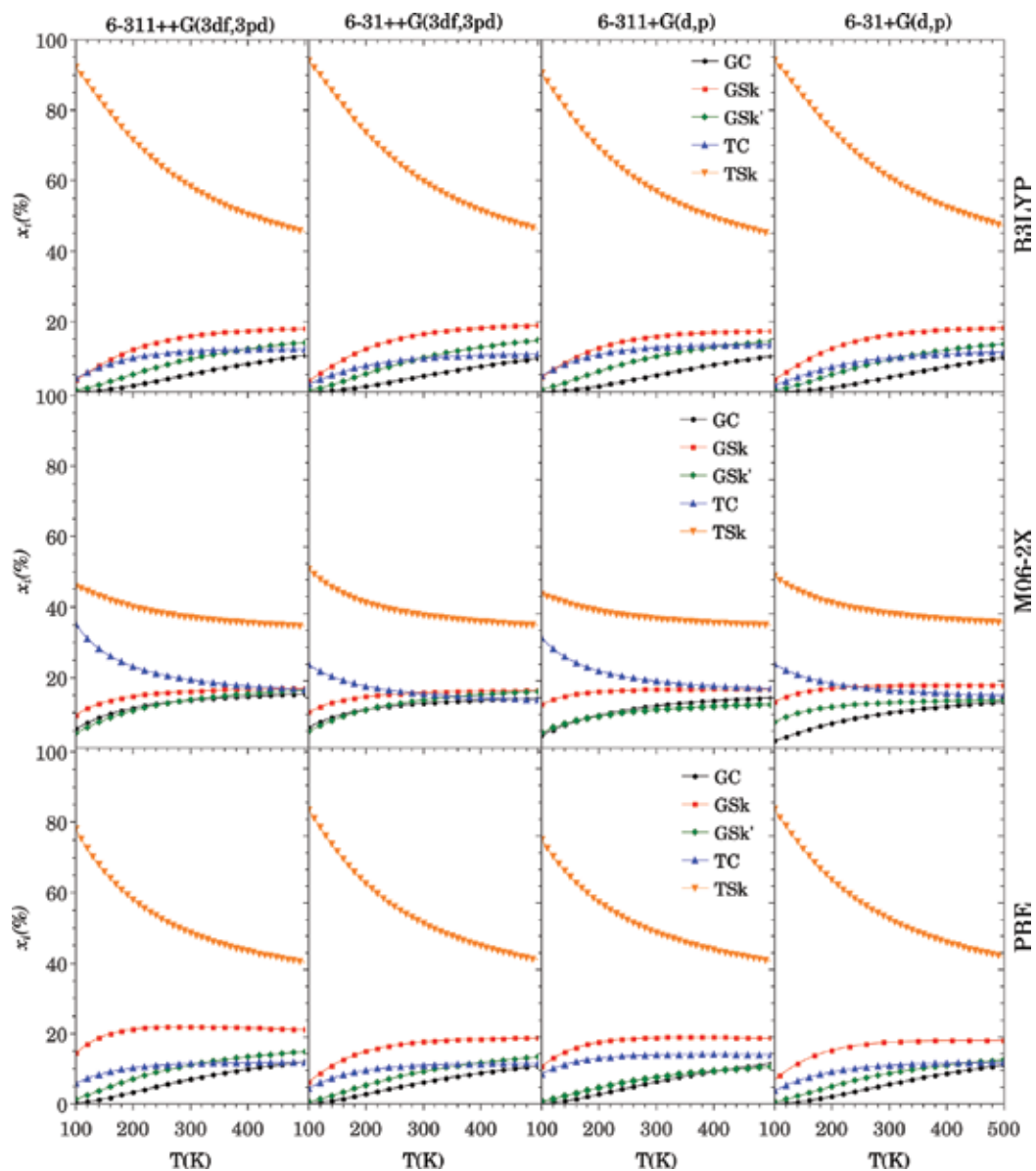
Figure 6. Molar fractions for ABID isomers.

3.3. Tetrazole-saccharyl

The third system of the pseudosaccharine family studied in this work is tetrazole-saccharyl (see **Figure 2(c) and (d)**). This system, as well as the previous ones, has been studied from an experimental and theoretical approach, for this molecule there are two tautomers and for each one of them several isomers can be generated by the rotation of two dihedral angles. In **Figure 2(c) and (d)** the involved atoms in the dihedral angles are shown, again the structures

were named according to the letters *G* = *gauge* ≈ 60°, *Sk* = *Skew* ≈ 120°, *G'* = *gauge'* ≈ −60°, *Sk'* = *Skew'* ≈ −120°, the angle formed by the atoms numbered as 1, 2, 3 and 4 was used to assign the first letter, while the angle formed by the atoms numbered as 2, 3, 4 and 5 were taken as reference for the second letter [14].

Tautomers are called as 1H tautomer and 2H tautomer, the first one is obtained when H is bonded to atom number 5 (**Figure 2(c)**) and the second one is obtained when H is bonded to the nitrogen atom beside to atom number 5 (**Figure 2(d)**) [14]. Relative energies were obtained for the same levels of theory as previous subsections.

In **Table 3**, corrected zero-point relative energies are shown. As it can be seen, B3LYP and PBE are consistent in the sense that they present the *G'Sk'* isomer as the most stable, with the exception of the B3LYP/6-311+G(d,p) methodology, since this gives *GSk'* as the most stable, although it should be noted that, in this case, the energy difference between *G'Sk'* and *GSk'*

Isomer	6-311++G(3df,3pd)	6-31++G(3df,3pd)	6-311+G(d,p)	6-31+G(d,p)
B3LYP				
G'Sk'	0	0	0.06	0
GSk'	0.51	0.55	0	0.25
G'Sk	1	1.12	0.65	0.9
GSk	1.96	2	1.94	1.85
G'G'	1.64	1.8	1.37	1.65
GG'	1.97	2.17	1.49	1.74
M06-2X				
G'Sk'	0.48	0.37	1.2	0.78
GSk'	0	0	0	0
G'Sk	0.47	0.47	0.57	0.46
GSk	1.18	1.22	1.93	1.49
G'G'	1.75	1.81	1.92	1.73
GG'	1.23	1.33	1.09	1.06
PBE				
G'Sk'	0	0	0	0
GSk'	0.64	0.67	0.16	0.44
G'Sk	1.23	1.34	0.89	1.18
GSk	1.75	1.77	1.65	1.62
G'G'	1.63	1.78	1.31	1.64
GG'	1.71	1.91	1.19	1.48

Table 3. Corrected zero-point relative energies (kcal/mol) of the six isomers of tetrazole-saccharyl.

is only 0.06 kcal/mol. On the other hand, M06-2X states the *GSk'* isomer as the most stable for all used BSs. As a summary, all methodologies showed the *G'Sk'* and *GSk'* isomers as the most stables at T = 0 K, with the exceptions of M06-2X/6-311+G(d,p) and M06-2X/6-31+G(d,p).

Here it is worth to mention that in ABIOD and ABID molecules, M06-2X reduced the energy differences, while tetrazole-saccharyl M06-2X does not reduce the energy differences in comparison with the results of B3LYP and PBE. The molar fractions as a function of temperature are analyzed below.

Observing **Figure 7**, it can be seen that the trend of B3LYP and PBE with the four BSs is maintained, there are two predominant isomers in all the graphs at room temperature, with the first two BSs the isomer of greatest abundance is the *G'Sk'* and the second is the *GSk'*, with populations of almost 50 and 20%, respectively. For the last two BSs the difference between the isomers of largest population is reduced, even in the case of B3LYP and the third BS, the *GSk'* isomer has the greatest population, although it is important to note that at room temperature the difference is not very significant, in general the same behavior is kept with PBE, however, in the third BS, *G'Sk'* has the largest population but with a small difference in population with *GSk'*, since it is approximately 33 and 30% for *G'Sk'* and *GSk'*, respectively.

Analyzing the molar fractions as a function of temperature for M06-2X functional, it can be observed that the first two BSs found three isomers with significant populations and the rest remained with a very low population, therefore, it is possible to say that the three isomers whose populations are considered important are the same ones that are predicted as the most stable. For the third and fourth BSs, we can observe that the *GSk'* and *G'Sk* isomers maintained a large population; however, the *G'Sk'* isomer, which had the largest population with B3LYP and PBE, disappears from the isomers of greater population. From this, it can be indicated that M06-2X describes in a different way the most populated isomer in comparison to B3LYP and PBE, however, we can also see that for the two BSs with more diffuse BS and greater freedom in the polarization also obtain *G'Sk'* and *GSk'* as the largest population isomers, indicating then, that M06-2X could be used with a large BS.

An important difference between the results obtained by B3LYP and M06-2X is the change of the order in stability of isomers since M06-2X always brought the *GSk'* isomer as the one with the lowest energy and greatest abundance. On the other hand, it is interesting to observe that in the work of Ismael et al. [14], they compared the experimental infra-red spectrum with the theoretical one at B3LYP/6-311++G(3df,3pd) level of theory and although they found *G'Sk'* isomer is the most favored energetically (as this work showed through B3LYP), they took the infra-red spectrum of *GSk'* as the representative one because its theoretical spectrum agreed better with the experimental spectrum, for this reason, it is important to remark that the M06-2X presents the *GSk'* isomer as the most stable at T = 0 K, even for all BSs.

As it can be observed, M06-2X predicts a different isomer as the most populated compared with B3LYP and PBE, however, it seems to be that the *GSk'* isomer is the one present in the experiment according to the explanation in the previous paragraph, if this is the case, then the question arises as to why M06-2X is the one that better describes this pseudosaccharin. In order to answer the question, let us note that in **Figure 2**, it can be seen that
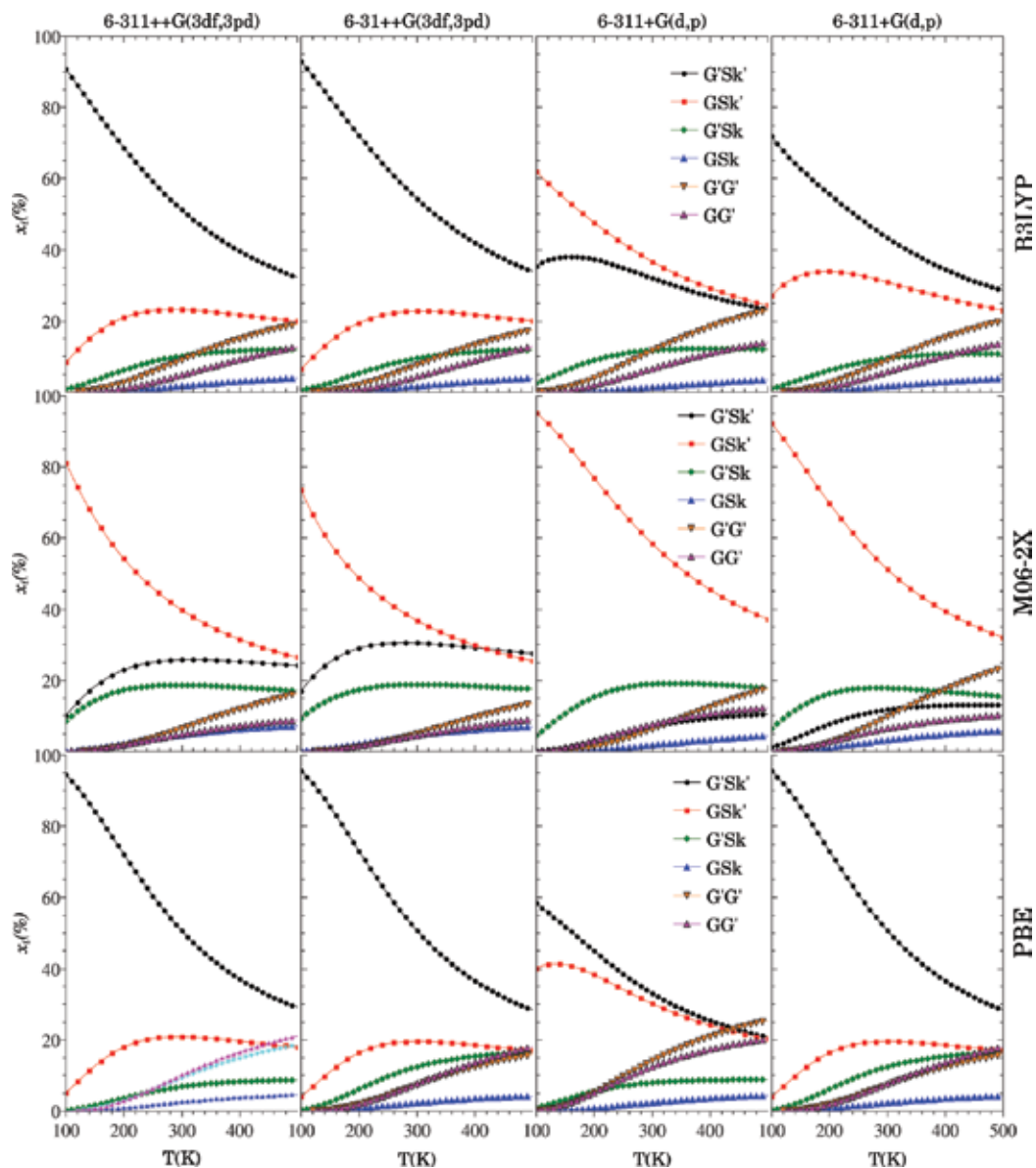
Figure 7. Molar fractions of tetrazole-saccharyl.

tetrazole-saccharyl is bigger (in size) than ABIOD and ABID molecules, in fact, the tetrazole group could interact with the saccharyl group through noncovalent interactions, moreover, it is well-known that the M06-2X functional has shown promising performance for noncovalent interactions [23, 24], thus, it is the reason why M06-2X describes tetrazole-saccharyl molecule in a better way. This once again proves the importance of testing several methodologies.

4. Conclusions

In this work, an analysis of molar fractions as a function of temperature on three pseudosaccharyl systems (ABIOD, ABID and tetrazole-saccharyl) was performed with three XC-functionals and four BSs. In general, for ABIOD and ABID systems, M06-2X functional reduces the energy differences between the isomers, while B3LYP and PBE are in agreement with each other, but different from M06-2X. It is important to observe that in ABID pseudosaccharine, even if the order of stability changes with the M06-2X functional, the molar fractions maintain the same trend, placing the *TSk* isomer as the one with the largest population, in spite of not being the most stable from DFT calculations at T = 0 K. Additionally, considering the results that are shown in **Table 2**, a minimal effect of the BS is evident considering that the same trend is conserved and the results do not vary significantly in ABID. For tetrazole-saccharyl, it seems that M06-2X describes correctly the predominant isomer found experimentally, contrary to B3LYP and PBE results. Although, this could be understood since it is well-known that M06-2X correctly describes systems with noncovalent interactions as can be inferred in the tetrazole-saccharyl system showed in **Figure 2(c)** and **(d)**.

Even though the molar fractions show a dependence on the enthalpies of the isomers, the most stable structure is not necessarily the one with the greatest population. By taking into account the vibrational, rotational and electronic partition functions in the calculation of the molar fractions, several aspects are involved to obtain the most predominant isomers at T ≠ 0. It was found that vibrational contribution is the most important factor in obtaining the predominant isomer. Therefore, the use of methodologies that correctly describe the vibrational spectra in order to obtain molar fractions is recommended. Additionally, when a theoretical-experimental spectra comparison is carried out, calculated spectra could be weighted by molar fractions at the temperature of interest.

One of the main differences between the results obtained with the different methodologies is that herein calculations can predict a different order of stability and modify the relative energies. However, in order to be able to assume that an isomer will predominate, it is important to consider the contributions of the different partition functions instead of only considering the relative potential energies.

Acknowledgements

Author details

Zuriel Natanael Cisneros-García[1], David Alejandro Hernández-Velázquez[1],
Francisco J. Tenorio[1,2] and Jaime Gustavo Rodríguez-Zavala[1]*

*Address all correspondence to: jgrz@culagos.udg.mx

1 Departamento de Ciencias Exactas y Tecnología, Centro Universitario de los Lagos,
Universidad de Guadalajara, Paseos de la Montaña, Lagos de Moreno, Jalisco, México

2 Departamento de Farmacia, Universidad Nacional Autónoma de México,
Ciudad de México, México

References

[1] Wotiz J. The discovery of sacharin. Journal of Chemical Education. 2015;**55**(3):161-162. DOI: 10.1021/ed055p160

[2] Qiao N, Li M, Schilindwen W, Malek W, Davies A, Trappitt G. Pharmaceutical cocrystals. International Journal of Pharmaceutics. 2011;**419**:1-11. DOI: 10.1016/j.ijpharm.2011.07.037

[3] Kaczor A, Proniewicz L, Almeida R, Gómez-Zavaglia A, Cristiano M, Beja A, Silva M, Fausto R. The chapman-type rearrangement in pseudosaccharin: The case of 3-(methoxy)-1,2-benzisothiazole 1,1-dioxide. Journal of molecular Structure. 2008;**892**:343-352. DOI: 10.1016/j.molstruc.2008.05.054

[4] Gómez-Zavaglia A, Kaczor A, Coelho D, Lourdes S, Cristiano M, Fausto R. Conformational and structural analysis of 2-allyl-1,2-benzisothiazol-3(2H)-one 1,1-dioxide as probed by matrix-insolation spectroscopy and quantum chemical calculations. Journal of Molecular Structure. 2009;**919**:271-276. DOI: 10.1016/j.molstruc.2008.09.013

[5] Cabral L, Maria T, Martelo L, Eusebio M, Cristiano M, Fausto R. The thermal sigmatropic isomerization of pseudosaccharylcrotyl ether. Tetrahedron. 2013;**69**:810-815. DOI: 10.1016/j.tet.2012.10.100

[6] Lloyd J, Finlay H, Kover A, Johnson J, Pi Z, Jiang J, Neels J, Cavallaro C, Wexler R, Conder M, Shi H, Li D, Sun H, Chimalakonda A, Huang C, Salvati M, Levesque P. Pseudosaccharin amines as potent and selective Kv 1.5 blockers. Bioorganic & Medicinal Chemistry Letters. 2015;**25**:4983-4986. DOI: 10.1016/j.bmcl.2015.02.066

[7] Eacho P, Foxworthy-Mason P, Lin H, Lopez J, Mosior M, Richett M. Benzisothiazol-3-one-Carboxylic Acid Amides as Phospholipase Inhibitors. 2009. US Patent. Available from: https://www.google.com/patents/US7595403 [Accessed: 2017-07-14]

[8] Wang LH, Yang XY, Zhang X, Mihalic K, Fan X, Xiao W, Howard OMZ, Appella E, Maynard AT, Farrar WL. Suppression of breast cancer by chemical modulation of vulnerable zinc fingers in estrogen receptor. Nature Medicine. 2004;**10**:40-47. DOI: 10.1038/nm969

[9] Wepplo P, Rampulla R, Heffernan G, Cosette M, Langevine C, Kameswaran V, Diehl R, Fiordeliso J, Haley G, Guaciaro M: Herbicidal 3-Heterocyclic Substituted Benzisothiazole and Benzisoxazole Compounds. 2001. WO Patent. Available from: https://www.google.com/patents/WO2001079203A1?cl=en [Accessed: 2017-07-14]

[10] Hlasta DJ, Bell MR, Court JJ, Cundy KC, Desai RC, Ferguson E, Gordon RG, Kumar V, Maycock AL, Subramanyan C. The desing of potent and stable benzisothiazole inhibitors of human leukocyte elastase. Bioorganic & Medicinal Chemistry Letters. 1995;**5**: 331-336. DOI: 10.1016/0960-894X(95)00030-W

[11] Otten M, Von D, Engel S, Hill R, Kardorff U, Vossen M, Plath P, Walter H, Westphalen K, Misslitz U: Isoxazole-4-Yl-Benzoyl Derivatives and the Use There of as Herbicides. 1997. WO Patent App. Available from: https://www.google.com/patents/WO1997019076A1?cl=en [Accessed: 2017-07-14]

[12] Mortazavi ZFA, Islami MR, Khaleghi M. Highly stereoselective synthesis of saccharin-substitued β-lactams via in situ genration of heterosubstituted ketene and a Zwiterionicintermidiate as potential antibacterial agents. Organic Letters. 2015;**17**:3034-3037. DOI: 10.1021/acs.orglett.5b01309

[13] Gómez-Zavaglia A, Kaczor A, Almeida R, Lourdes S, Cristiano M, Fausto R. Conformational space of the pseudosaccharinallyl ether 3-(Allyloxy)-1,2-benzisothiazole 1,1-dioxide in gas phase and rare gas matrices. Journal of Physical Chemistry A. 2008;**112**:1762-1772. DOI: 10.1021/jp0770918

[14] Ismael A, Borba A, Duarte L, Giuliano B, Gómez-Zavaglia A, Cristiano M. Structure and photochemistry of novel tetrazole-saccharyl conjugate isolated in solid argon. Journal of Molecular Structure. 2012;**1025**:105-116. DOI: 10.1016/j.molstruc.2012.04.081

[15] Frisch MJ, Trucks GW, Schlegel HB, Scuseria GE, Robb MA, Cheeseman JR, Scalmani G, Barone V, Mennucci B, Petersson GA, Nakatsuji H, Caricato M, Li X, Hratchian HP, Izmaylov AF, Bloino J, Zheng G, Sonnenberg JL, Hada M, Ehara M, Toyota K, Fukuda R, Hasegawa J, Ishida M, Nakajima T, Honda Y, Kitao O, Nakai H, Vreven T, Montgomery JA, Peralta JE, Ogliaro F, Bearpark M, Heyd JJ, Brothers E, Kudin KN, Staroverov VN, Kobayashi R, Normand J, Raghavachari K, Rendell A, Burant JC, Iyengar SS, Tomasi J, Cossi M, Rega N, Millam JM, Klene M, Knox JE, Cross JB, Bakken V, Adamo C, Jaramillo J, Gomperts R, Stratmann RE, Yazyev O, Austin AJ, Cammi R, Pomelli C, Ochterski JW, Martin RL, Morokuma K, Zakrzewski VG, Voth GA, Salvador P, Dannenberg JJ, Dapprich S, Daniels AD, Farkas 'O, Foresman JB, Ortiz JV, Cioslowski J, Fox DJ. Gaussian 09 Revision C.01. Wallingford CT: Gaussian Inc; 2009

[16] Slanina Z. Multimolecular clusters: Their isomerism and effective characteristics evaluated by quantum chemistry. International Journal of Quantum Chemistry. 1979;**16**:79-86. DOI: 10.1002/qua.560160112

[17] Becke AD. Density-functional exchange-energy approximation with correct asymptotic behavior. Physical Review A. 1988;**38**(6):3098-3100. DOI: 10.1103/PhysRevA.38.3098

[18] Lee C, Yang W, Parr RG. Development of the Colle-Salvetti correlation-energy formula into a functional of the electron density. Physical Review B. 1988;**37**(2):785. DOI: 10.1103/PhysRevB.37.785

[19] Zhao Y, Truhlar DG. The M06 suite of density functionals for main group thermochemistry, thermochemical kinetics, noncovalent interactions, excited states, and transition elements: Two new functionals and systematic testing of four M06-class functionals and 12 other functionals. Theoretical Chemistry Accounts. 2008;**120**(1):215-241. DOI: 10.1007/s00214-007-0310-x

[20] Perdew JP, Burke K, Ernzerhof M. Generalized gradient approximation made simple. Physical Review Letters. 1996;**77**(18):3865. DOI: 10.1103/PhysRevLett.77.3865

[21] McLean A, Chandler G. Contracted Gaussian basis sets for molecular calculations. I. Second row atoms, Z= 11-18. The Journal of Chemical Physics. 1980;**72**(10):5639-5648. DOI: 10.1063/1.438980

[22] Rassolov VA, Ratner MA, Pople JA, Redfern PC, Curtiss LA. 6-31G* basis set for third-row atoms. Journal of Computational Chemistry. 2001;**22**(9):976-984. DOI: 10.1002/jcc.1058

[23] Zhao R, Guo Y, Zhao P, Ehara M, Nagase S, Zhao X. Warning to theoretical structure elucidation of endohedral metallofullerenes. Journal of Physical Chemistry C. 2016;**126**:1275-1283. DOI: 10.1021/acs.jpcc.5b09403

[24] Bryantsen VS, Diallo MS, van Duin ACT, Goddard III WA: Evaluation of B3LYP, and M06-class density functional for predicting the binding energies of neutral, protonated and deprotonated water clusters. Journal of Chemical Theory and Computation. 2009;**5**:1016-1026. DOI: 10.102/ct800549f

Catalysis and Mechanism

Catalytic Activation of PVP-Stabilized Gold/Silver Cluster on p-Nitrophenol Reduction: A DFT

Madhulata Shukla and Indrajit Sinha

Abstract

Systematic DFT calculations on poly(N-vinyl-2-pyrrolidone) (PVP) stabilization of Ag13 cluster have shown that the former acts not only as a stabilizer but also plays an important role in activating the Ag catalyst by supplying extra electrons to it through its oxygen atoms. Natural Bonding Orbital (NBO) calculations show that weak back donation of electrons from M(dπ) orbital of Ag to antibonding σ* of one of the N-O bond, facilitates the formation of the nitroso intermediate. Vibrational frequency calculation of PNP association with Ag13-2PVP cluster carried out to understand the extent and the nature of this interaction better. Red shift in the frequencies is result of strong interaction with that of silver cluster present in Ag13-2PVP-PNP model.

Keywords: nanoparticles, p-nitrophenol, DFT calculation, charge distribution, NBO calculation

1. Introduction

Recently nanoparticle (NP) research is an area of adoring scientific research due to wide variety of potential application in different fields of physics, chemistry, material science, medicine and biology, as a result of their unique electronic, optical, magnetic, mechanical, physical, chemical and catalytic properties. Nanoparticle is a microscopic particle with at least one dimension less than 100 nm. The intrinsic properties of metal nanoparticles are mainly determined by their size, shape, composition, stability, crystallinity, structure, etc. The properties of many conventional materials change when formed from nanoparticles. This is typically because nanoparticles have a greater surface area per weight than larger particles which causes them to be more reactive to some other molecules. It can be silver, gold, iron, iron oxide, platinum, silica, titanium oxide, etc. Nanoparticles are of great scientific interest as they

are effectively a bridge between bulk materials and atomic or molecular structures. Synthesis of M-NPs can proceed by chemical reduction, thermolysis, photochemical decomposition, electro reduction, microwave and sonochemical irradiation. In recent literature there are large number of reports on synthesis, properties and applications of noble metals Au, Ag and Cu NPs [1–3]. This is mainly because all three elements show good localized surface plasmon resonance (LSPR) absorbance in the visible range and also have large number of catalytic applications. However, the high cost of Au and to a lesser extent Ag restrict their applications in many cases. As an alternative of Au and Ag NPs, researchers have investigated Cu nanoparticles. CuNPs are less expensive and exhibit comparably higher electrical conductivity and catalytic activity [4, 5]. The LSPR absorbance of CuNPs in the visible range is comparatively less intense. Another issue is that Cu nanoparticles are easily oxidized [6], yet nanoparticles of copper oxides also have wide applicability as catalysts. Silver NP found to be quite stable and hence chosen for studying the effect of nanostructures on their catalytic activity. In liquid phase nanoparticle synthesis, polymeric molecules are often used for stabilizing nanoparticles against aggregation. The function of the polymers are to avoid the aggregation of the NP in solution and to control the size and shape at the crystallographic level [7–9]. Among various polymeric molecules investigated in literature, polyvinyl pyrrolidone (PVP) has been one of the most frequently used stabilizers since it is non-toxic and soluble in many polar solvents. While such PVP stabilized noble metal nanoparticles have extensively been used as catalysts for various reactions [10, 11], few workers have concentrated in literature on the effect of such stabilizer molecule on the nanoparticle surface on their catalytic properties [12–14]. Nevertheless, only a few research papers have investigated the effect of such stabilization of nanoparticle surfaces on the electronic properties of such nanocomposites. Tsunoyama et al. proposed that electron transfer occurs from the anionic Au cores of Au:PVP into the LUMO (π^*) of O$_2$ which generates superoxo or peroxo like species. Latter plays a key role in the oxidation of alcohol [10]. Similar mechanisms were proposed by some other related experimental studies as well that the adsorption of PVP on to the catalyst surface can also modify the electronic structure of nanoparticles by charge transfer [15, 16]. Yet several aspects remain unclear, such as whether PVP attaches to the metal surface through its O atom or through the N atom [15, 17]. The strength of interaction of PVP with the metal surface is also another aspect that needs to be investigated. Finally, the most important question that in a catalytic reaction how does the interaction between the catalyst surface and the reactant/substrate change in presence of stabilizer. Very few reports are available regarding this topic [18, 19]. The catalytic reduction of nitroarenes to aminoarenes by transfer hydrogenation methodologies is an important class of organic transformations. The reaction does not occur even in the presence of strong reductants like metal hydrides unless catalyzed by a suitable nanocatalyst [12]. Synthesis of silver NP using PVP has been reported in our earlier study [20]. PVP stabilized Ag nanoparticles have often been successfully used as catalysts for such reactions [14, 20]. However, to the best of our knowledge, there is no detailed DFT study on effect of PVP (poly(N-vinyl-2-pyrrolidone)) stabilization of Ag cluster on its catalytic activity with respect to a nitroarene (p-nitrophenol) substrate. In this chapter, we first carry out DFT calculations on Ag/Au cluster along with the monomer of PVP moiety using Gaussian program. Further, the effect of PVP stabilized Ag clusters (catalyst) on p-nitrophenol (PNP) has been investigated in detail. Energy of interaction found by the B3LYP level of calculation elucidates

the stability of the moieties. Mechanism for activation of the nitro group and formation of nitroso intermediate has been proposed from NBO analysis. IR study of the Ag cluster stabilized by PVP and its effect on PNP has been studied in detail using DFT calculation.

2. Computational procedure

A 13 atom silver and gold cluster is carved out of the FCC Ag/Au lattice constructed using the MAPS software (Scienomics). The Gaussian 03 program [21] package employed for the DFT calculations at the Becke's three parameter functional and Lee–Yang–Parr hybrid functional (B3LYP) level [22, 23] of calculation. LaNL2DZ for Ag/Au and 6-31G++(d,p) basis set for C, H, N and O atoms was used while performing DFT calculation. B3LYP functional calculations give the stable cluster and also reproduce the experimental results [17, 18, 24]. Calculations are carried out for ground state geometry optimization in gaseous phase. The Mulliken charges of each atom are calculated by the Mulliken population analysis. NBO analysis and IR frequency calculation performed to find out the strength of interaction of nitro group of PNP with silver cluster.

3. Results and discussion

3.1. Geometry optimization and Mulliken charge distribution

Au13 and Ag13 cluster (magic number) were optimized using B3LYP method and LaNL2DZ basis set using Gaussian program [25, 26]. Optimized structure of Ag13 and Au13 has been shown in **Figure 1(a)** and **(b)** respectively. Mulliken charge present on each atom is shown clearly. Several literature are available explaining the charge distribution on gold and silver cluster by varying number of atoms attached as well as by varying the shape of the clusters [24, 25]. It has been reported by Chen and Johnston [25] that charges on atoms vary with variation in shape of
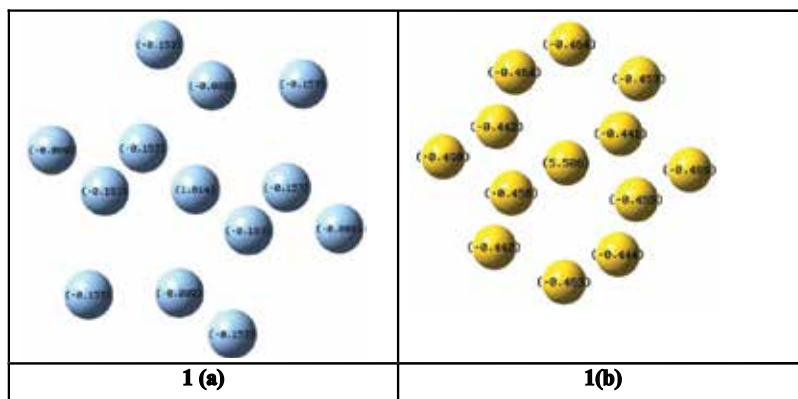

Figure 1. Optimized structure of (a) Ag13 cluster and (b) Au13 cluster with their Mulliken charges present on it.

the cluster. Mulliken charges present in the pure Ag13 Ih (icosahedral) cluster are +0.256 for the central Ag atom and −0.022 for a peripheral Ag atom. The charges in the pure Au13 Oh (cuboctahedral) cluster are +0.379 for the central Au atom and −0.033 for a peripheral Au atom. Hence, the structural order in 13-atom icosahedral (Ih) and cuboctahedral (Oh) clusters also induces charge transfer from the central atom to the peripheral ones. Varying the number of atoms in an alloy changes the property of nanoparticles drastically. It has been shown that with introduction of single Au/Ag atom in Ag13/Au13 cluster, charge present on each atom vary hugely. Stability of nanoalloys comes from a directional charge transfer induced by the structural order, which is added to that induced by the electronegativity difference between unlike atoms. As the Pauling electronegativity of Au (2.4) is greater than that of Ag (1.9), there is a degree of charge transfer from Ag to Au atoms [25]. It is clear from **Figure 1(a)** and **(b)** that charge present on gold is quite higher than that of silver atom. Central atom has huge positive charge as compared to negative charge on the surface. Also one can say that gold is more active catalyst as compared to silver. Okumura et al. [24] had presented the DFT calculation of gold nanoparticle stabilized with PVP at B3LYP level of calculation. Role of PVP on the catalytic activities of gold cluster has been explained very well and in refined way. Presence of PVP not only acts as a stabilizer to prevent aggregation, but also activates the catalyst by supplying charge to it. Calculations have shown that the charge transfer from the adsorbed PVP to Au13 produces negatively charged O_2 on Au13-4PVP. Hence one can conclude that the catalytic activities of Au clusters are affected by the adsorbed PVPs. Varying the number of adsorbed PVP, charge present on the catalyst vary drastically. Similar observation was observed for the silver cluster (Ag13) in our calculation. This is the first report explaining the effect of PVP on the silver cluster.

Optimized structure of Ag13-2PVP with the charge present on each atoms are clearly has been shown in **Figure 2**. Distance between oxygen of PVP and different silver atoms are 2.32 and 2.36 Å. It clearly shows that interaction of PVP with silver cluster is quite strong. Also charge present on bare Ag13 cluster and Ag13 surrounded by 2 PVP moieties are quite different. Higher charge on the surface silver atom of Ag13-2PVP is indicative of the fact that PVP does not just acts as a stabilizer, but activates the catalyst as well, similar as obtained by Okumura et al. for gold cluster [24].
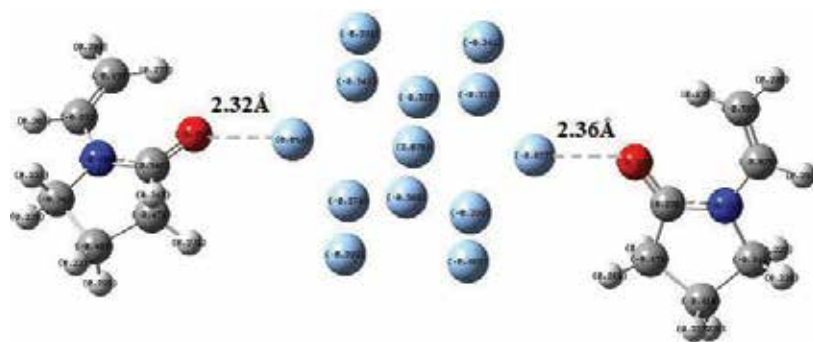

Figure 2. Optimized structure of Ag13-2PVP moiety with charge present on each atom.

3.2. Effect of p-nitrophenol on silver cluster surrounded by PVP

Among the available nitroarenes, the reduction of p-nitrophenol (PNP) using NaBH4 as the reductant has been studied extensively as a model pollutant and catalytic reduction reaction [27]. Several literatures are available for this catalytic reduction reaction. In recent study, it has been investigated that during catalytic reduction of p-nitrophenol to p-aminophenol (AP) glycerol as the reductant also in a mixture of glycerol and water as the reaction medium [20]. Several experimental literatures are available for this reduction reaction [27] but the actual mechanism for this catalytic reduction of p-nitrophenol to p-aminophenol is still unclear. Hence to study the catalytic reduction mechanism DFT proves to be very useful [28].

To study the catalytic reduction mechanism, p-nitrophenol was incorporated in the optimized structure of Ag13-2PVP moiety and reoptimized the whole system at same B3LYP level of calculation. Optimized structure of PNP and Ag13-2PVP-PNP has been shown in **Figure 3(a)** and **(b)** respectively. Important geometrical parameters such as bond length, bond angles have been shown in **Table 1**. It has been observed that N-O bond length increases from 1.28 Å (in PNP) to 1.36 Å in Ag13-2-PVP-PNP moiety. N11-C1 bond length decreases by 0.05 Å when PNP interact with Ag13 cluster. <O12-N11-O13 decrease by ~3° when interact with Ag13 cluster. Ag7----C24=O25, Ag4----C41=O42 distance found to be 2.32 and 2.36 Å. This shows strong interaction with silver cluster and PVP molecules. Ag1-O60 and Ag2-O59 bond length calculated to be 2.28 and 2.27 Å, which clearly shows that PNP is much closer and interacting strongly with silver cluster than that of PVP molecule.

3.3. Electronic effect due to PVP interaction with nanoparticle

Figure 4(a) and **(b)** shows the Mulliken charge distribution of Ag13 and Ag13-2PVP moiety (shown by different colors). Negative charge on Ag13 is symmetrically distributed among the shell Ag atoms of the cluster. This is balanced by the electropositive central Ag atom (shown by green color). Charges on shell silver atoms of the Ag cluster (before interaction) found to be either −0.09 or −0.15. Charge on central silver atom is detected to be +1.61. This result is similar with that as reported by Li and Chen [29] and Chen and Johnston [25]. To balance the negative
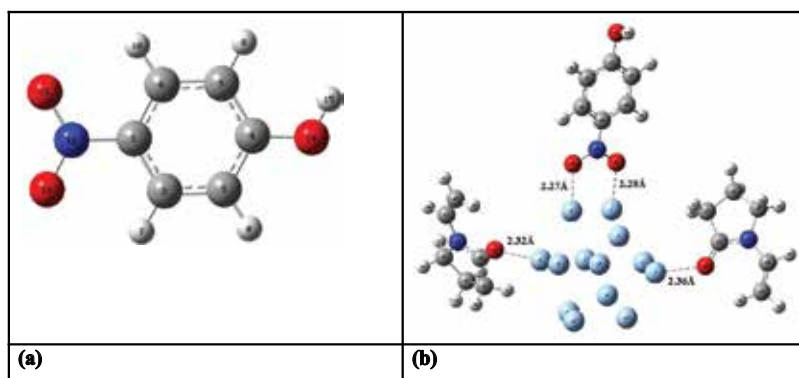

Figure 3. Optimized structure of (a) p-nitrophenol and (b) Ag13-2-PVP-PNP moiety.

Parameters [bond length (Å)/bond angles (°)]	Data obtained from DFT calculation
p-nitrophenol (PNP)	
N11-O12	1.28
N11-C1	1.46
<O12-N11-O13	123.51
<O12-N11-C1	118.23
Ag13-2-PVP-PNP	
N58-O59	1.36
N58-C48	1.41
Ag1-O60	2.28
Ag2-O59	2.27
<O59-N58-O60	120.83
<O59-N58-C48	119.71
Ag7----C24=O25	2.32
Ag4----C41=O42	2.36

Table 1. Selected bond length, bond angles of different system obtained from DFT calculation.

charge present on shell atoms, core becomes positively charged to neutralize and stabilized the whole cluster. As PVP interacts with the Ag13 cluster, charge distribution becomes asymmetrical. The charges present on shell Ag atoms interacting with (PVP) O atoms are −0.07 and −0.05. Rest of the shell Ag atoms have charges more or less around −0.30. The central Ag atom is most electron deficient carrying charge of +3.07. Adsorption of the PVP model molecule onto the surface of Ag13 increases the negative charge density on Ag13 cluster, similar as for Au13 cluster explained by Okumura et al. [24]. With adsorption of PVP on the surface, catalyst becomes more active due to increase of negative charge on the Ag13 surface. To reduce the computational cost, PVP has been removed for further interaction study of PNP with Ag13. Optimized structure of PNP and Ag13-PNP has been shown in **Figure 4(c)** and **(d)** along with their respective charges. Variation in charges on different atoms of PNP before and after interaction has been clearly shown by the different colored atoms of **Figure 4(e)** and **(f)** respectively.

These interactions of PNP with that of Ag13 are better understood from electrostatic potential (ESP) charge distribution shown in **Figure 5**. Orange color represents the negative electron density around the electronegative oxygen atoms.

3.4. Natural bonding orbital (NBO) analysis

Stabilization energy E(2) found to be proportional to the charge transfer energy or charge distribution energy [30]. For each donor NBO(i) and acceptor NBO(j), the stabilization energy E(2) associated with delocalization of electron pair from donor orbital (i) to acceptor orbital (j) and is defined as
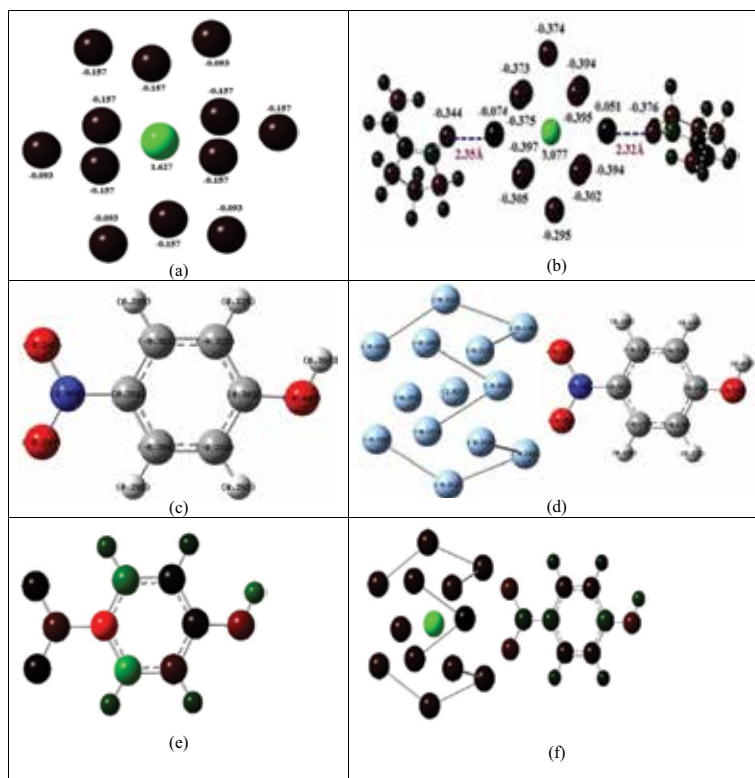
Figure 4. Mulliken charge distribution on different atoms of (a) Ag13 cluster and (b) Ag13-2PVP (c) PNP (d) Ag-PNP. Colour representation of Mulliken charge on different atoms of (e) PNP (f) Ag13-PNP. Red colour represents the most electronegative and green colour represents the most electropositive atom.
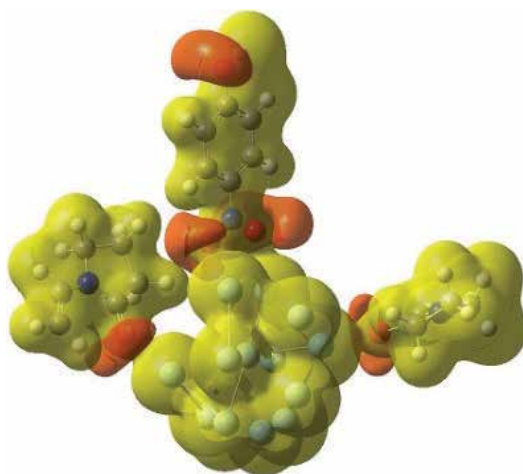

Figure 5. Electrostatic potential charge distribution on Ag13-2PVP-PNP moiety.

$$E(2) \ = \ \Delta E_{ij} \ = \ \frac{q_i\, F\,(i,\,j)^2}{\varepsilon_i - \varepsilon_j} \tag{1}$$

where q_i is the donor orbital occupancy, ε_i and ε_j are the diagonal elements (orbital energies). F(i, j) is the interaction element between donor and acceptor orbitals and is known as diagonal NBO Fock matrix element. The delocalization effects can be identified by means of off-diagonal elements of the Fock matrix. The forces of these delocalization interaction, E(2) (kcal/mol), are estimated by second order perturbation theory [31]. E(2) term corresponding to these interactions can also be the total charge transfer energy in the molecule.

To better understand the interaction between Ag13 cluster and PNP molecules, NBO calculation carried out at same B3LYP level of calculation. **Table 2** presents the major interaction present between silver cluster and PNP through both the oxygen atoms of the latter. It has been observed from **Table 2** that in addition to charge transfer from the oxygen (of the nitro group) to Ag atom, there is also a back donation of electron from M(dπ) orbital of Ag2 to antibonding σ* of N58-O59 [E(2) = 2.06 kcal/mol]. Further, the back donation of electron from M(dπ) orbital of Ag1 to antibonding σ* of N58-O60 is comparatively much weaker [E(2) = 0.71 kcal/mol]. This shows that only one of the two N-O bonds is considerably weakened by this back donation of electron from Ag atoms in comparison to the other N-O bond. Hence, from these obtained NBO results, one can predict the subsequent formation of nitroso compound as an intermediate. This mechanism is in agreement with the one proposed by Liu et al. in an experimental study for reduction of nitrobenzene in presence of Ag catalyst [12] and for reduction of PNP in presence of Ag catalyst by Gu et al. [27].

3.5. Calculated vibrational spectra and analysis of calculated IR spectra of PNP and Ag13-2PVP-PNP

IR frequency calculations prove to be a good tool for predicting the interaction present in a molecule [31]. For better analysis of the interaction of PNP with silver cluster, we perform the

Donor orbital (i)	Acceptor orbital (j)	Second order perturbation stabilization energy E(2)/(kcal/mol)
149. LP*(6)Ag2	564. BD*(1)N58-O59	2.06
262. LP(1)O60	142. LP*(8)Ag1	1.97
264. LP(3)O60	140. LP*(6)Ag1	5.21
264. LP(3)O60	141. LP*(7)Ag1	4.68
264. LP(3)O60	142. LP*(8)Ag1	1.39
261. LP(3)O59	149. LP*(6)Ag2	6.45
261. LP(3)O59	150. LP*(7)Ag2	3.17
260. LP(2)O59	150. LP*(7)Ag2	2.04
259. LP(1)O59	150. LP*(7)Ag2	4.02
55. BD(1)N58-O60	150. LP*(7)Ag2	0.71

Table 2. Significant donor-acceptor NBO interactions in Ag cluster and PNP moiety with calculated second order stabilization energies E(2) (kcal/mol).

IR frequency calculations on the optimized structure of Ag13-2PVP-PNP moiety at same B3LYP level of calculation and same basis set as mention above. To analyze the changes that occurred in the vibrational spectrum due to such association we contrast it with the calculated IR frequencies of the optimized structure of PNP alone. Calculated data has been presented in **Table 3**. For the same vibrational motion, the frequency of the peak present in PNP varies significantly when it is associated with the silver cluster. Scissoring of O-N-O occurs at 621 cm^{-1} in PNP while it is observed at 588 cm^{-1} (red shift of 33 cm^{-1}) when there is interaction with Ag cluster. Similarly, a strong red shift of 131 cm^{-1} is observed when PNP interacts with silver cluster for benzene ring breathing coupled with C-O(H) stretching and O-N-O scissoring motion in PNP. It is due to coupling of NO_2 with that of the silver cluster. Another strong red shift of 103 cm^{-1} is observed for

Wavenumber/(cm^{-1})/ Ag13-2PVP-PNP	Intensity	Wavenumber (cm^{-1})/PNP	Intensity	Difference in wavenumber/(cm^{-1})/ [Ag13-2PVP-PNP-(PNP)]	Assignment of bands
588	85	621	27	33	O-N-O scissoring in PNP
710	65	841	30	131	Benzene ring breathing coupled with C-O(H) stretching and O-N-O scissoring in PNP
864	58	887	68	23	Out of plane bending of C-H in PNP
1113	85	1124	118	11	C-H in plane bending coupled with O-N-O asymmetric stretching in PNP
1167	356	1170	246	3	C-O-H scissoring in PNP coupled with C-H in plane bending
1174	41	1277	341	103	O-N-O symmetric stretching in PNP
1192	32	1204	81	12	H-C=C-H scissoring in PNP
1267	53	1287	55	20	C-O(H) stretching in PNP
1322	42	1277	341	45	C-N stretching in PNP
1520	190	1529	32	9	C-H in plane bending in PNP coupled with C-N stretching
1645	60	1657	120	12	C=C stretching in PNP
3185	34	3210	10	25	C-H asymmetric stretching in PNP coupled with C-O-H scissoring
3708	91	3704	81	4	O-H stretching in PNP

Table 3. DFT calculated IR frequency of NB and Ag13-2PVP-PNP at B3LYP level.

O-N-O symmetric stretching in PNP. For other vibrational motions, difference in wavenumbers has been shown in **Table 3**. Red shifts in most of the frequencies are due to strong interaction of PNP with silver cluster present in Ag13-2PVP-PNP model. Hence IR frequency calculation proves to be a good tool in predicting the strength of interaction present in a molecule [32].

4. Conclusions

DFT calculations on PVP stabilized Ag13 cluster have shown that the PVP acts not only as a stabilizer but also plays an important role in activating the Ag catalyst by supplying extra charge to it, mainly through oxygen atom. Electrostatic potential (ESP) charge distribution demonstrates that nitro group in p-nitrophenol (PNP) interacts strongly through oxygen end with the Ag cluster. Furthermore, Natural Bonding Orbital (NBO) analysis shows that there is weak back donation of electron from $M(d\pi)$ orbital of Ag to antibonding σ^* of one of the N-O bonds while the other N-O bond in PNP is not affected. Therefore, one of the N-O bonds is drastically weakened in comparison to other N-O bond. Hence the formation of the nitroso intermediate will assist its further reduction reaction. Hence stabilization energy calculation can be a good tool in predicting the intermediate in a reaction catalyzed by NPs, which is difficult to predict experimentally. Finally, significant red shifts in calculated IR frequencies are a consequence of strong interaction of PNP with silver cluster present in Ag13-2PVP-PNP model. Hence, IR frequency calculation is a good tool for predicting the strength of interaction present in a molecule.

Acknowledgements

Author details

Madhulata Shukla[1,2]* and Indrajit Sinha[1]

*Address all correspondence to: madhu1.shukla@gmail.com

1 Department of Chemistry, Indian Institute of Technology (Banaras Hindu University), Varanasi, India

2 G.B. College, Ramgarh, Kaimur, Veer Kunwar Singh University, Kaimur, India

References

[1] Iravani S, Korbekandi H, Mirmohammadi SV, Zolfaghari B. Synthesis of silver nanoparticles: chemical, physical and biological methods. Research in Pharmaceutical Sciences. 2014;**9**:385-406

[2]   Stamplecoskie KG, Scaiano J. Optimal size of silver nanoparticles for surface-enhanced Raman spectroscopy. Journal of Physical Chemistry C. 2011;**115**:1403-1409

[3]   Duan XC, Ma JM, Lian JB, Zheng WJ. The art of using ionic liquids in the synthesis of inorganic nanomaterials. CrystEngComm. 2014;**16**:2550-2559

[4]   Choi CS, Jo YH, Kim MG, Lee HM. Control of chemical kinetics for sub-10 nm Cu nanoparticles to fabricate highly conductive ink below 150 °C. Nanotechnology. 2012;**23**:065601 8pp

[5]   Wu T, Huang Q, Li W, Chen G, Ma X, Zeng G. Electroreduction of copper dichloride powder to copper nanoparticles in an ionic liquid. Journal of Nanomaterials. 2014;**399**:6. Article ID 751424

[6]   Muzikansky A, Nanikashvili P, Grinblat J, Zitoun D. Ag dewetting in Cu@Ag mono-disperse core–shell nanoparticles. Journal of Physical Chemistry C. 2013;**117**: 3093-3100

[7]   Bratlie KM, Lee H, Komvopoulos K, Yang P, Somorjai GA. Platinum nanoparticle shape effects on benzene hydrogenation selectivity. Nano Letters. 2007;**7**:3097-3101

[8]   Zhang GH, Guo WL, Wang XK. Sonochemical formation of nanocrystalline gold in aqueous solution. Materials Research Innovations. 2007;**11**:201-206

[9]   Tao AR, Habas S, Yang P. Shape control of colloidal metal nanocrystals. Small. 2008;**4**: 310-325

[10] Tsunoyama H, Ichikuni N, Sakurai H, Tsukuda T. Effect of electronic structures of Au clusters stabilized by poly(N-vinyl-2-pyrrolidone) on aerobic oxidation catalysis. Journal of the American Chemical Society. 2009;**131**:7086-7093

[11] Quintanilla A, Butselaar-Orthlieb VCL, Kwakernaak C, Sloof WG, Kreutzer MT, Kapteijn F. Weakly bound capping agents on gold nanoparticles in catalysis: Surface poison? Journal of Catalysis. 2010;**271**:104-114

[12] Liu X, Cheng H, Cui P. Catalysis by silver nanoparticles/porous silicon for the reduction of nitroaromatics in the presence of sodium borohydride. Applied Surface Science. 2014;**292**:695-701

[13] Vadakkekara R, Chakraborty M, Parikh PA. Reduction of aromatic nitro compounds on colloidal hollow silver nanospheres. Colloids and Surfaces A: Physicochemical and Engineering Aspects. 2012;**2014**:11-17

[14] Tejamaya M, Romer I, Merrified RC, Lead JR. Stability of citrate, PVP, and PEG coated silver nanoparticles in ecotoxicology media. Environmental Science & Technology. 2012; **46**:7011-7017

[15] Xian J, Jiang QHZ, Ma Y, Huang W. Size-dependent interaction of the poly(N-vinyl-2-pyrrolidone) capping ligand with Pd nanocrystals. Langmuir. 2012;**28**:6736-6741

[16] Aguilar JG, Garcia MN, Murcia AB, Mori K, Kuwahara Y, Yamashita H, Amoros DC. Evolution of the PVP–Pd surface interaction in nanoparticles through the case study of formic acid decomposition. Langmuir. 2016;**32**:12110-12118

[17] Abdelghany AM, Mekhail MS, Abdelrazek EM, Aboud MM. Combined DFT/FTIR structural studies of monodispersed PVP/gold and silver nano particles. Journal of Alloys and Compounds. 2015;**646**:326-332

[18] Boekfa B, Pahl E, Gaston N, Sakurai H, Limtrakul J, Ehara M. C–Cl bond activation on Au/Pd bimetallic nanocatalysts studied by density functional theory and genetic algorithm calculations. Journal of Physical Chemistry C. 2014;**118**:22188-22196

[19] Nunzi F, Angelis FD, Selloni A. Ab initio simulation of the absorption spectra of photoexcited carriers in TiO_2 nanoparticles. Journal of Physical Chemistry Letters. 2016;**7**:3597-3602

[20] Verma AD, Mandal RK, Sinha I. Glycerol as green hydrogen source for catalytic reduction over anisotropic silver nanoparticles. RSC Advances. 2016;**6**:103471-103477

[21] Frisch MJ, Trucks GW, Schlegel HB, Scuseria GE, Robb MA, Cheeseman JR, Montgomery JA Jr, Vreven T, Kudin KN, Burant JC, Millam JM, Iyengar SS, Tomasi J, Barone V, Mennucci B, Cossi M, Scalmani G, Rega N, Petersson GA, Nakatsuji H, Hada M, Ehara M, Toyota K, Fukuda R, Hasegawa J, Ishida M, Nakajima T, Honda Y, Kitao O, Nakai H, Klene M, Li X, Knox JE, Hratchian HP, Cross JB, Bakken V, Adamo C, Jaramillo J, Gomperts R, Stratmann RE, Yazyev O, Austin AJ, Cammi R, Pomelli C, Ochterski JW, Ayala PY, Morokuma K, Voth GA, Salvador P, Dannenberg JJ, Zakrzewski VG, Dapprich S, Daniels AD, Strain MC, Farkas O, Malick DK, Rabuck AD, Raghavachari K, Foresman JB, Ortiz JV, Cui Q, Baboul AG, Clifford S, Cioslowski J, Stefanov BB, Liu G, Liashenko A, Piskorz P, Komaromi I, Martin RL, Fox DJ, Keith T, Al-Laham MA, Peng CY, Nanayakkara A, Challacombe M, Gill PMW, Johnson B, Chen W, Wong MW, Gonzalez C, Pople JA. Gaussian, Inc. Wallingford, CT. 2004

[22] Lee C, Yang W, Parr RG. Development of the Colle-Salvetti correlation-energy formula into a functional of the electron density. Physical Review B. 1988;**37**:785-789

[23] Becke AD. Density-functional thermochemistry. III. The role of exact exchange. The Journal of Chemical Physics. 1993;**98**:5648-5652

[24] Okumura M, Kitagawa Y, Kawakami T, Haruta M. Theoretical investigation of the hetero-junction effect in PVP-stabilized Au_{13} clusters. The role of PVP in their catalytic activities. Chemical Physics Letters. 2008;**459**:133-136

[25] Chen F, Johnston RL. Charge transfer driven surface segregation of gold atoms in 13-atom Au–Ag nanoalloys and its relevance to their structural, optical and electronic properties. Acta Materialia. 2008;**56**:2374-2380

[26] Shin K, Kim DH, Yeo SC, Lee HM. Structural stability of AgCu bimetallic nanoparticles and their application as a catalyst: A DFT study. Catalysis Today. 2012;**185**:94-98

[27] Gu S, Wunder S, Lu Y, Ballauff M. Kinetic analysis of the catalytic reduction of 4-nitrophenol by metallic nanoparticles. Journal of Physical Chemistry C. 2014;**118**: 18618-18625

[28] Pozun ZD, Rodenbusch SE, Keller E, Tran K, Tang W, Stevenson KJ, Henkelman G. A systematic investigation of *p*-nitrophenol reduction by bimetallic dendrimer encapsulated nanoparticles. Journal of Physical Chemistry C. 2013;**117**:7598-7604

[29] Li W, Chen F. A density functional theory study of structural, electronic, optical and magnetic properties of small Ag–Cu nanoalloys. Journal of Nanoparticle Research. 2013;**15**:1809-1822

[30] Gineityte V. On the relation between the stabilization energy of a molecular system and the respective charge redistribution. Journal of Molecular Structure (THEOCHEM). 2002;**585**:15-25

[31] Reed AE, Curtiss LA, Weinhold F. Intermolecular interactions from a natural bond orbital, donor-acceptor viewpoint. Chemical Reviews. 1988;**88**:899-926

[32] Shukla M, Srivastava N, Saha S. Theoretical and spectroscopic studies of 1-butyl-3-methylimidazolium iodide room temperature ionic liquid: Its differences with chloride and bromide derivatives. Journal of Molecular Structure. 2010;**975**:349-356

Mechanistic Study on the Formation of Compounds from Thioureas

Warjeet S. Laitonjam and Lokendrajit Nahakpam

Additional information is available at the end of the chapter

Abstract

Formation of 2-(*N*-arylamino)benzothiazole takes place, when *N*,*N'*-diphenylthioureas are treated with polymer-supported tribromide or with iodine-alumina as catalyst under solvent free conditions. However, when *N*-substituted-*N'*-benzoylthioureas are treated with polymer-supported tribromide or with iodine-alumina as catalyst either under various conditions or under solvent free conditions, decomposition takes place to give the respective benzamides and thiobenzamides. Mechanistic study of the formation of these compounds is studied using DFT calculations. It is found that electron donating group at the *para*-position of the aryl group of benzoylthiourea favors the formation of benzamide whereas the presence of electron withdrawing group at *para*-position of the aryl group of benzoylthiourea, formation of thiobenzamide takes place. When the catalyst is changed to diacetoxyiodobenzene (DIB) under similar reaction conditions, benzoxazole amides are formed; expected benzothiazoles or the decomposition products are not obtained. Mechanistic study of the reaction using DFT calculation again shows that the reaction followed through carbodiimide intermediate undergoes the formation of C-O bond in benzoxazole moiety, instead of the expected C-S bond formation of benzothiazole moiety *via* a sequential acylation and deacylation process.

Keywords: mechanism, benzoxazoles, benzothiazoles, decomposition, thioureas, DFT calculations

1. Introduction

Heterocyclic chemistry is the most complex and intriguing branch of organic chemistry, and heterocyclic compounds constitute the largest and most unique family of organic compounds [1–3]. Nitrogen, oxygen, and sulfur are the most common heteroatoms but some other heterocyclic compounds containing selenium, tellurium, phosphorus, arsenic, silicon, boron, etc., are

also widely known. Heterocyclic compounds are present in many natural and non-naturally occurring compounds. Some examples of such compounds are alkaloids, vitamins (vitamin B series and vitamin C), antibiotics, amino acids, hemoglobin, hormones, pigments, and a large number of synthetic drugs and dyes. Several natural drugs such as morphine, codeine, quinine, penicillin, papaverine, atropine, emetine, reserpine, procaine, theophylline, etc., are examples of heterocyclic compounds. Some of the synthetic drugs have shown several therapeutic uses such as antidiabetic, antitubercular, antidepressant, antitumor, anti-HIV, anthelmintic, antibacterial, antifungal, antiviral, antimalarial, antileishmanial, analgesic, anti-inflammatory, anticonvulsant, anticancer, muscle relaxants, lipid peroxidation inhibitor, herbicidal, trypanocidal, fungicidal, and insecticidal activities. Thus, heterocyclic compounds are receiving more and more significance in recent years, particularly owing to their pharmacological as well as synthetic potential.

In recent years, green chemistry has become one of the most important philosophies in chemistry, since it represents a major change in the way we think about practicing chemistry and using chemicals. The emerging area of green chemistry envisages minimum hazard as the performance criteria while designing new chemical processes. The search for new environmentally benign solvents and catalysts that operate efficiently in them and can be easily recycled is of significant academic and industrial interest. There have been several approaches to access to this problem, e.g., the developments of neat reactions that proceed under various conditions such as microwave irradiation, thermal heating, grinding, sonication, etc., or in organic or inorganic solid-media, or in ionic liquid-media under organic solvent-free reactions. Among the proposed solutions, solvent free conditions are becoming more and more popular and it is often claimed that the best solvent from an ecological point of view is, without a doubt, no solvent. The formation of various compounds from thioureas and their derivatives under different catalysts in solvent free condition is highlighted.

The density functional theory (DFT) method has become one of the most prevalent and efficient tools, as compared to the conventional *ab initio* method (HF), for studying the detailed reaction mechanism in chemical systems during the last two decades. With DFT methods, many catalytic reaction mechanisms have been widely studied in addition to the assignment of experimental spectra. It is to be noted that study of reaction mechanism is important not only for understanding the reaction and its stereochemistry but also for designing new reactions and catalysts. The mechanistic pathways for the decomposition of benzoylthioureas into benzamides and thiobenzamides; and also the conversion of benzoylthioureas into benzoxazoles, instead of forming bezothiazoles, using different catalysts have also been highlighted with the help of DFT calculations.

2. 2-Aminobenzothiazoles from thioureas

Benzothiazoles are an important class of heterocycles that possess a broad range of biological activities [4]. They were studied extensively for their anti-allergic, anti-inflammatory, antitumor, antimicrobial, and analgesic activities. Among those 2-substituted benzothiazole derivatives, the

2-aminobenzothiazoles are one of the most important structural motifs in pharmaceutically active compounds and natural products [5]. A large number of 2-aminobenzothiazole derivatives are also found to be anticancer active and the 2-aminobenzothiazole moieties act as a privileged pharmacophores as well as valuable reactive intermediates [6–8]. For example, *N*-aryl substituted 2-aminobenzothiazole (**A**; R116010) is a potential inhibitor of retinoic acid metabolism for cancer treatment [9]; 6-substituted 2-aminobenzothiazole (**B**) is found to exhibit antifungal activity [10]. Riluzole (**C**) is a 2-aminobenzothiazole compound employed in the treatment of amyotrophic lateral sclerosis [11] and *N*-disubstituted 2-aminobenzothiazole (**D**, HM13N) is used as anti-HIV agent [12]. 2-(*N*-acylamino) benzothiazole derivatives, such as trihydroxybenzoyl-2-aminobenzothiazole (**E**) [12] exhibit significant topoisomerase I inhibitory activity. Moreover, derivatives of 2-aminobenzothiazoles such as benzothiazole-triazole-pyridine conjugated analogs (**F**) [13] showed better anti-TB activity compared to rifampicin (RIF) (**Figure 1**).

The main objectives of benzothiazoles synthesis are not only for the development of more diverse and complex bioactive compounds for biological activity and structure-activity relationship (SAR) studies but also for other applications, such as preparation of dyes. There are several methods for the synthesis of 2-aminobenzothiazoles. The most versatile and economical method involves the treatment of various substituted arylthioureas (which are synthesized *via* treatment of an aromatic amine with isothiocyanate) with oxidizing agent or cyclizing agent using different reaction conditions to yield 2-aminobenzothiazoles.

Recently, several methods have been reported which utilize bromine as catalyst. Basically, cyclization with bromine is achieved by oxidation of aniline, substituted aniline, and arylthiourea in acid or chloroform with alkali thiocyanate. Hugerschoff, in early 1900s, synthesized 2-aminobenzothiazole and found that 1, 3-diarylthiourea can be cyclized with liquid bromine in chloroform to form a 2-aminobenzothiazoles (**Scheme 1**) [14, 15].

This reaction worked well for symmetrical thioureas giving exclusively one product. But, when the same reaction is performed using unsymmetrical 1,3-diaryl thioureas, there is always uncertainty as to on which aryl ring the intramolecular electrophilic substitution would take place to give aminobenzothiazole. Kamel *et al.* have reported the synthesis of 6-chloro-4-(trifluoromethyl) 2-aminobenzothiazole by oxidative cyclization of 4-chloro-2-(trifluoromethyl)phenylthiourea with bromine in chloroform to give an intermediate followed by basification with NH_3 (**Scheme 2**) [16].

Jordan *et al*. have reported the use of benzyltrimethylammoniumtribromide ($PhCH_2NMe_3Br_3$) which is an electrophilic bromine source for the conversion of substituted arylthiourea to 2-aminobenzothiazoles under mild conditions in different solvents with good yields (**Scheme 3**) [17].

Liu *et al.* have reported the metal-free synthesis of 2-aminobenzothiazoles from *N'*-substituted *N*-(2-halophenyl) thioureas *via* a base-promoted cyclization in dioxane (**Scheme 4**) [18]. However, this reaction requires drastic conditions, like heating the vial which was sealed in an oil bath.

The palladium-catalyzed intramolecular cyclization of 2-bromophenylthioureas to synthesize 2-substituted benzothiazoles was also reported. Castillon *et al.* reported Pd- catalyzed cyclization of 2-bromophenylthioamides using $Pd_2(dba)_3$/(2-biphenyl)P(*t*-Bu)$_2$ catalytic system (**Scheme 5**) [19].
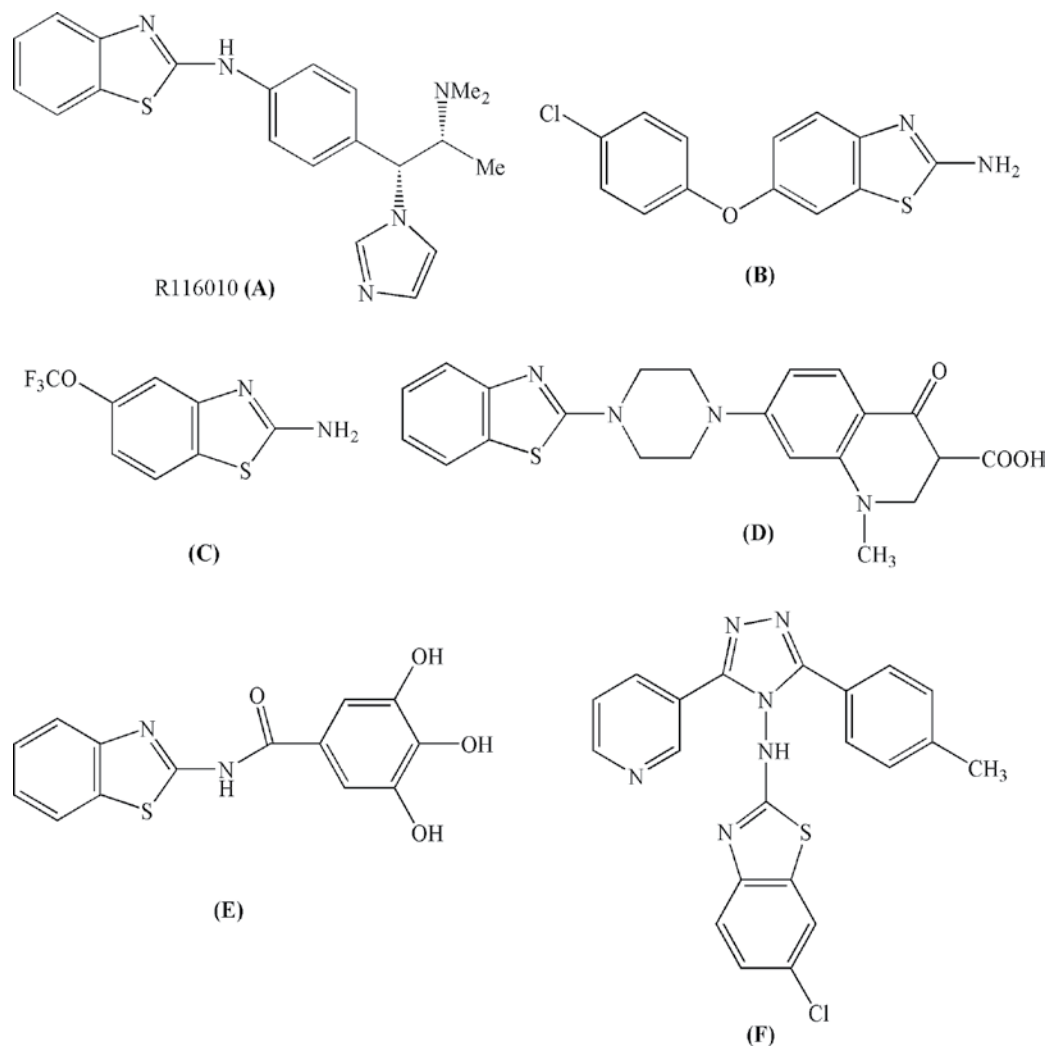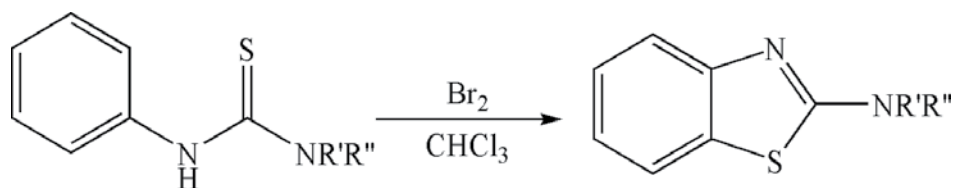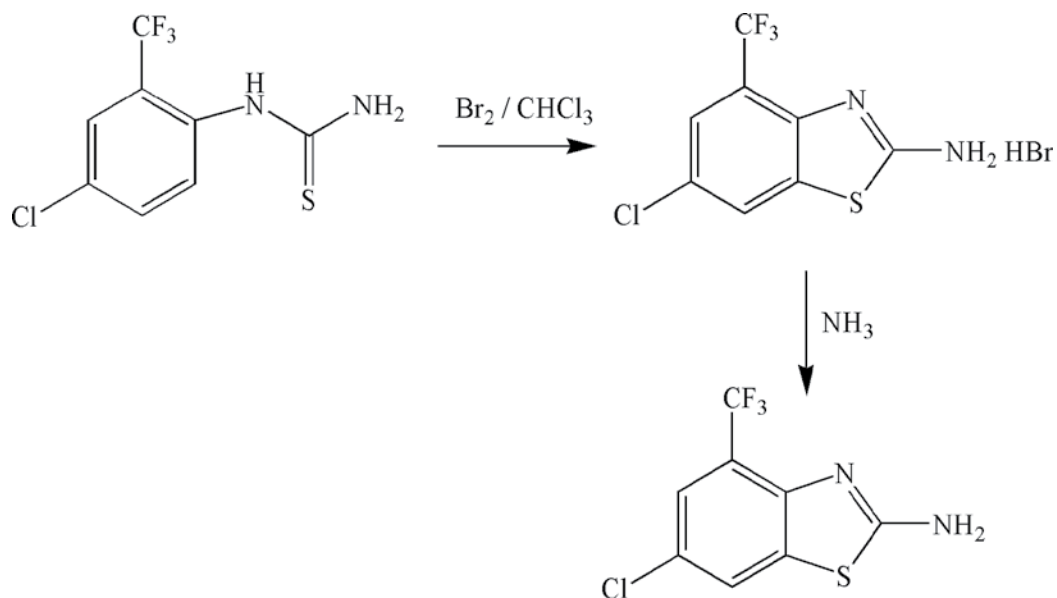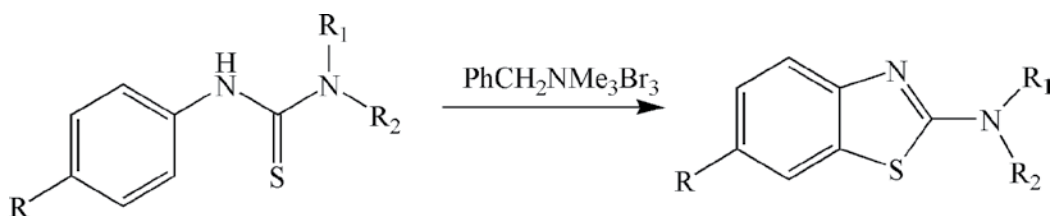
Figure 1. Several *N*-substituted-2-aminobenzothiazole derivatives reported as biologically active compounds and pharmaceutical products.
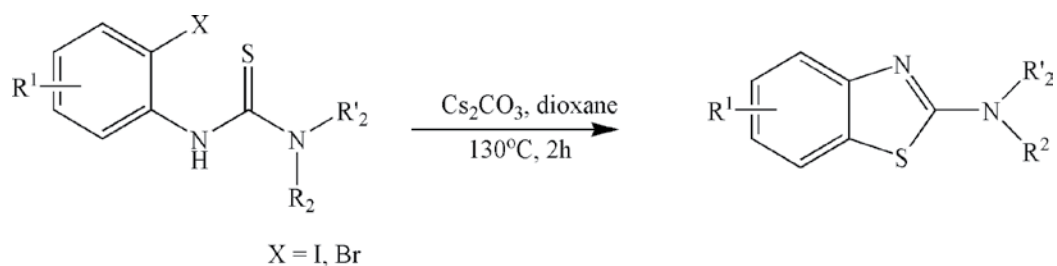

Scheme 1. Hugerschoff synthesis of 2-aminobenzothiazole from 1, 3-diarylthiourea with liquid bromine and chloroform.

**Scheme 2.** Oxidative cyclization of phenylthiourea to give 2-aminobenzothiazole.

Scheme 3. Synthesis of 2-aminobenzothiazoles using benzyltrimethylammoniumtribromide.


Scheme 4. Synthesis of 2-Substituted Benzothiazoles via a Base-Promoted Cyclization.

However, both a ligand and a base are required to promote the reaction, and the substrates are not readily available. It was reported recently a catalytic synthesis of 2-substituted benzothiazoles from thiobenzanilides in the presence of a palladium catalyst through C-H functionalization or C-S bond formation [20].
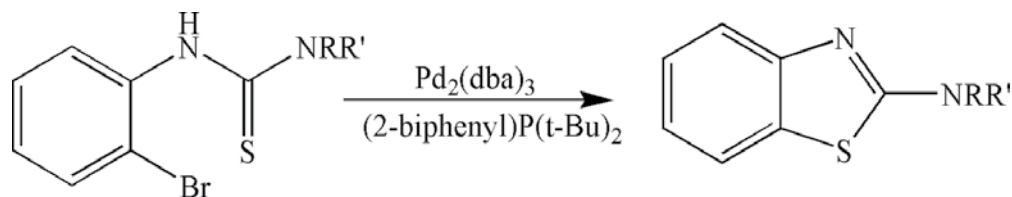
Scheme 5. Synthesis of 2-substituted benzothiazoles through palladium-catalyzed intramolecular cyclization of 2-bromophenylthioureas.
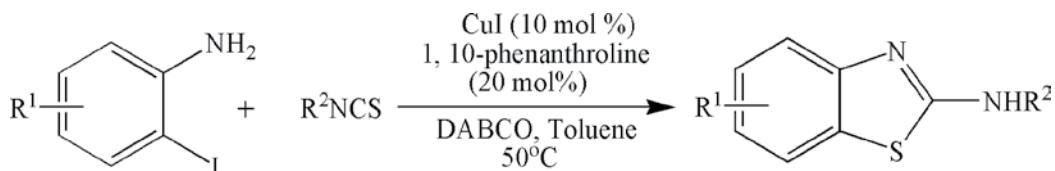
Scheme 6. Copper-catalyzed tandem reaction of 2-iodoaniline with phenyl isothiocyanate to form 2-aminobenzothiazole.

Recently, the transition-metal (copper or iron)-catalyzed one-pot tandem reactions of 2-halobenzenamines with isothiocyanates for the synthesis of 2-aminobenzothiazoles have received considerable attention because of their efficiency and low costs. For example, Wu *et al.* described a copper-catalyzed tandem reaction between 2-halobenzenamines and isothiocyanates using the CuI (10 mol%)/1,10-phenanthroline (20 mol%) catalytic system to prepare 2-aminobenzothiazoles (**Scheme 6**) [21]. Li and Ding's group reported iron-catalyzed tandem reactions of 2-halobenzenamines and isothiocyanates leading to 2-aminobenzothiazoles (**Scheme 7**) [22, 23].
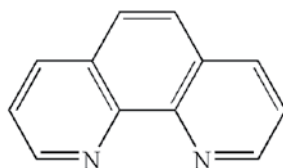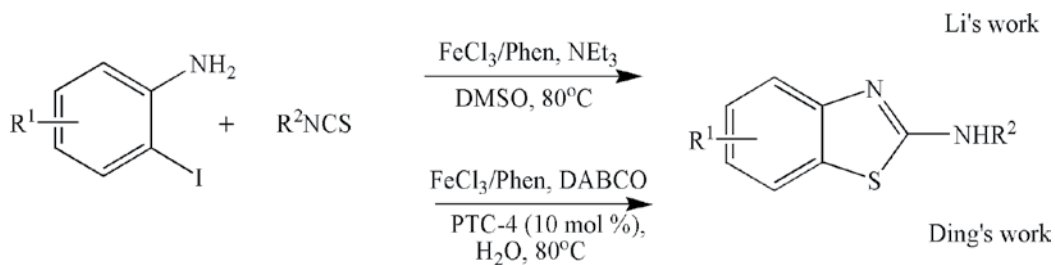
**Scheme 7.** FeCl$_3$-catalyzed tandem reaction of 2-iodoaniline with phenyl isothiocyanate in water to give 2-aminobenzothiazole.

Meanwhile, the ligand-free copper-catalyzed one-pot tandem reactions of 2-halobenzenamines and isothiocyanates were also reported [24, 25]. However, it should be noted that the copper or iron catalyzed one-pot tandem reactions of 2-halobenzenamines with isothiocyanates generally involve organic solvents such as DMSO, DMF, and toluene which are environmentally unfriendly. Moreover, the reactions which are described above might proceed efficiently; they usually suffer from the use of highly toxic and corrosive reagents, high-costing metal catalysts, and specific ligands. There is also possibility to leave toxic traces of metals in the products. More recently, Jiang *et al.* have reported a metal-free synthesis of 2-aminobenzothiazoles from cyclohexanones and thioureas using catalytic iodine and molecular oxygen as the oxidant under mild conditions (**Scheme 8**) [26].
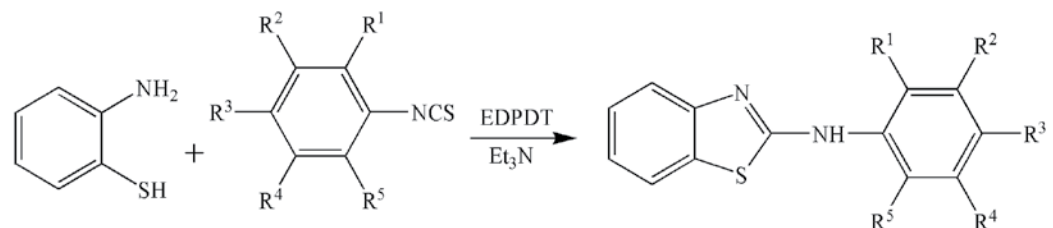
Recently, Patel *et al.* have reported a one-pot procedure for the preparation of 2-aminobenzothiazoles using ditribromide reagent 1,1′-(ethane-1, 2-diyl)dipyridinium bistribromide (EDPBT). In this approach, aryl/alkyl isothiocyanate reacts with *o*-aminothiophenol to form their monothiourea which on desulfurization with EDPBT led to the formation of corresponding 2-aminobenzothiazoles (**Scheme 9**) [27].

Very recently, polymer-supported tribromide has been used as a new solid phase and recyclable catalyst for the one-pot synthesis of 2-(*N*-arylamino)benzothiazole under microwave irradiation (**Scheme 10**) [28].
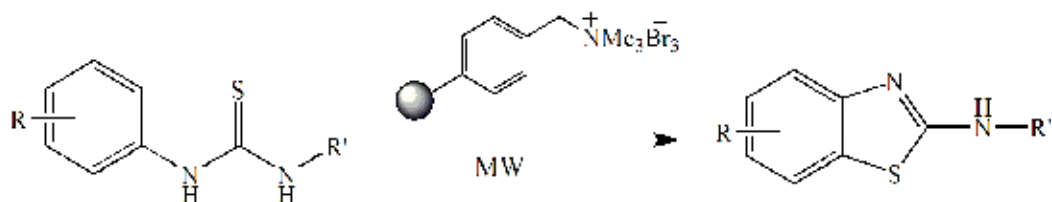
The probable reaction mechanism for the formation of 2-(*N*-arylamino) benzothiazoles through polymer-supported tribromide-mediated intramolecular cyclization of thioureas is given in **Scheme 11**.
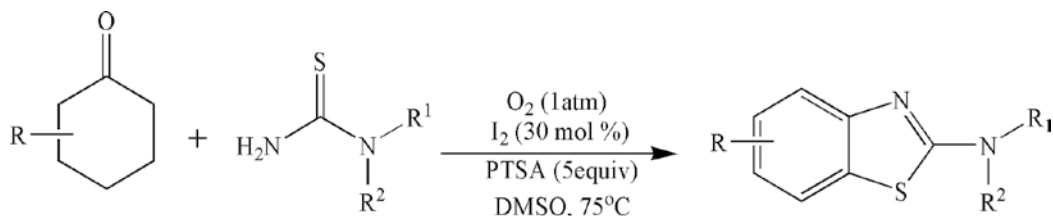

Scheme 8. Metal-free synthesis of 2-aminobenzothiazoles via aerobic oxidative cyclization of cyclohexanones and thioureas.

Scheme 9. One-pot synthesis of 2-aminobenzothiazoles using ditribromide reagent 1, 1′-(ethane-1, 2-diyl)dipyridinium bistribromide (EDPBT).

Scheme 10. One-pot synthesis of 2-(*N*-arylamino)benzothiazoles under microwave irradiation using polymer-supported tribromide.
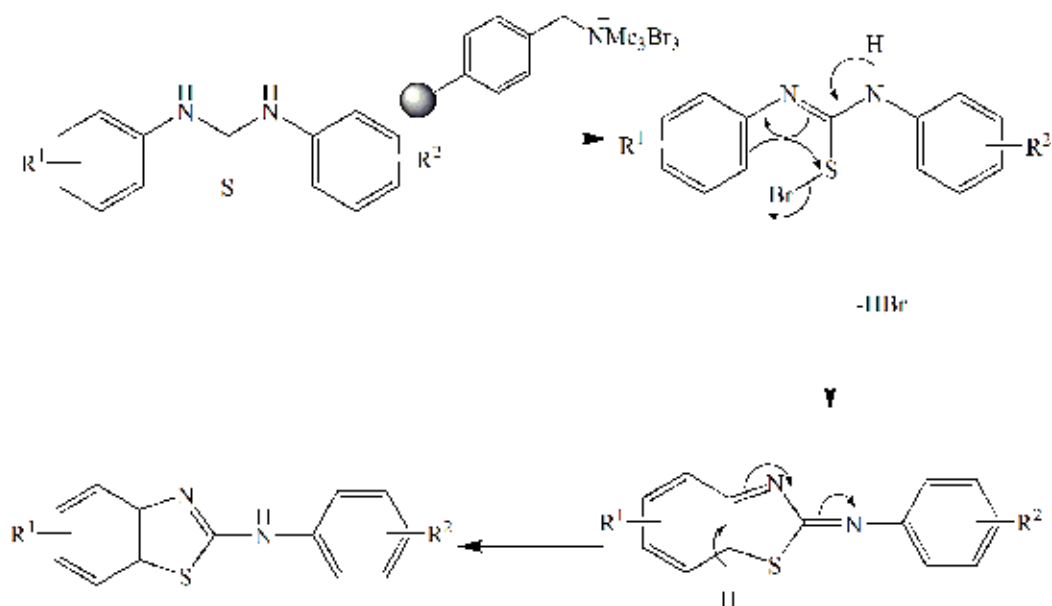

Scheme 11. Plausible reaction mechanism for the formation of 2-(*N*-arylamino) benzothiazoles through polymer supported tribromide–mediated intramolecular cyclization of thioureas.

3. Decomposition of benzoylthioureas

When the reaction of *N,N′*-diphenylthioureas with iodine-alumina as catalyst was carried out, the expected 2-(*N*-arylamino)benzothiazoles were obtained. However, when *N*-substituted-*N′*-benzoylthioureas are treated with the above catalyst, the expected benzothiazoles are not obtained (**Scheme 12**).

Instead, the decomposition of benzoylthioureas to benzamides and thiobenzamides in a single route using iodine-alumina as catalyst under solvent-free condition takes place. When electron donating group, such as methyl or methoxy group, is present at the *para*-position of the aryl group of benzoylthioureas, benzamides are obtained as major product. When electron withdrawing group, such as chlorine or nitro group, is at *para*-position of the aryl group of benzoylthioureas, thiobenzamides are the favored product. Thus, a simple and efficient process
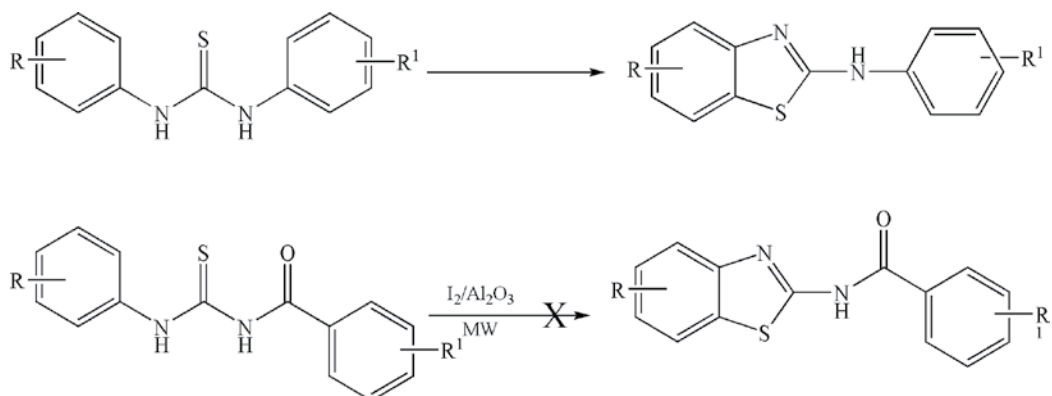
Scheme 12. Reaction of *N,N′*-diphenylthioureas and *N*-substituted-*N′*-benzoylthioureas with iodine-alumina under solvent-free condition

for the conversion of benzoylthioureas to benzamides and thiobenzamides using iodine-alumina as catalyst without any solvent was described (**Scheme 13**) [29].

Amides and thioamides are an important class of building blocks in modern organic synthesis, with broad applications in advanced materials, pharmaceuticals, agrochemicals, and polymers, etc. They are used for the synthesis of various natural products as well as intermediates of organic compounds. Generally, amides are prepared from their corresponding ketoximes by Beckmann rearrangement, and thioamides are prepared by thionation of the corresponding amide analogues by Lawesson's reagent. Liana Allen *et al*. have reported the direct coupling of unactivated carboxylic acids with amines in toluene at 110°C in the absence of catalyst. The use of simple zirconium catalysts at 5.0 mol% loading gave amide formation as little as in 4 h (**Scheme 14**) [30].

Gelens *et al*. have also reported the microwave assistance in the coupling of carboxylic acids with amines. An array of structurally diverse amides was synthesized efficiently by combining (primary and secondary) amines and carboxylic acids in one-pot under solvent-free microwave (MW) conditions (**Scheme 15**) [31].
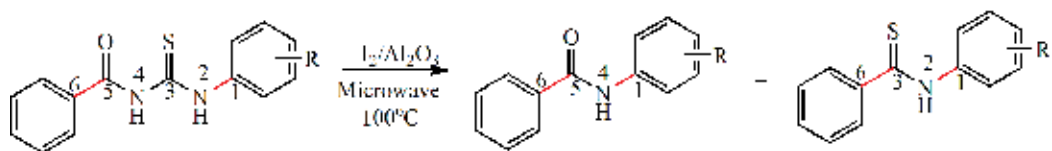
Scheme 13. Decomposition of benzoylthioureas to benzamides and thiobenzamides using iodine-alumina.
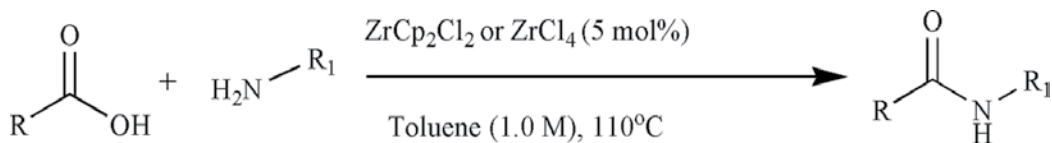

Scheme 14. Direct amide formation from unactivated carboxylic acids with amines using zirconium catalysts.

Very recently, Rajeshwer Vanjari *et al.* have developed a new approach for the synthesis of amides through manganese dioxide-promoted nondirected C-H activation of methylarenes under mild conditions employing *N*-chloroamines as effective coupling partners (**Scheme 16**) [32].

Different synthetic methods have been discovered for the synthesis of thioamides. Among these strategies, thionation of amide analogues with Lawesson's reagent is the most common, but this reaction cannot be classified as an atom economical approach because of crucial limitations: only one oxygen atom is replaced by a sulfur atom, and no other new bond was created. Thus, it is worthwhile to provide a practical and environmentally benign method to synthesize thioamides. Recently, some three component reactions have nicely exploited the use of benzylamine [33], aldehydes [34], and alkyne [35], in combination with elemental sulfur and amine for the synthesis of thioamides (**Scheme 17**).

More recently, Guntreddi *et al.* reported a new decarboxylative strategy for the synthesis of thioamides via a three-component reaction involving arylacetic or cinnamic acids, amines, and elemental sulfur powder, without the need of a transition metal and an external oxidant (**Scheme 18**) [36].
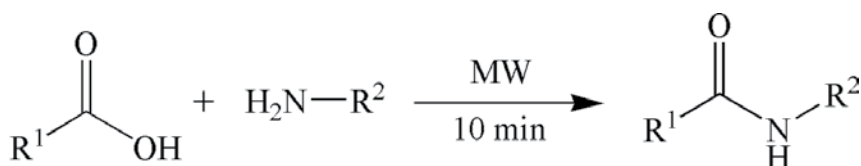
R^1= Aryl, alkyl, containing a chiral center
R^2= Aryl, alkyl, containing a chiral center

Scheme 15. Microwave (MW)-assisted amide formation.
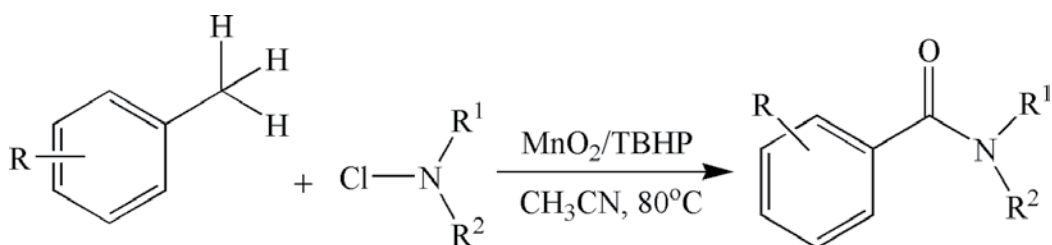
R= Me, OMe, Cl, Br, NO_2
R^1= Benzyi, hexyl, butyl
R^2= Piperidyl, morpholine, Me, H

Scheme 16. Synthesis of amides through manganese dioxide promoted nondirected C-H activation of methylarenes.
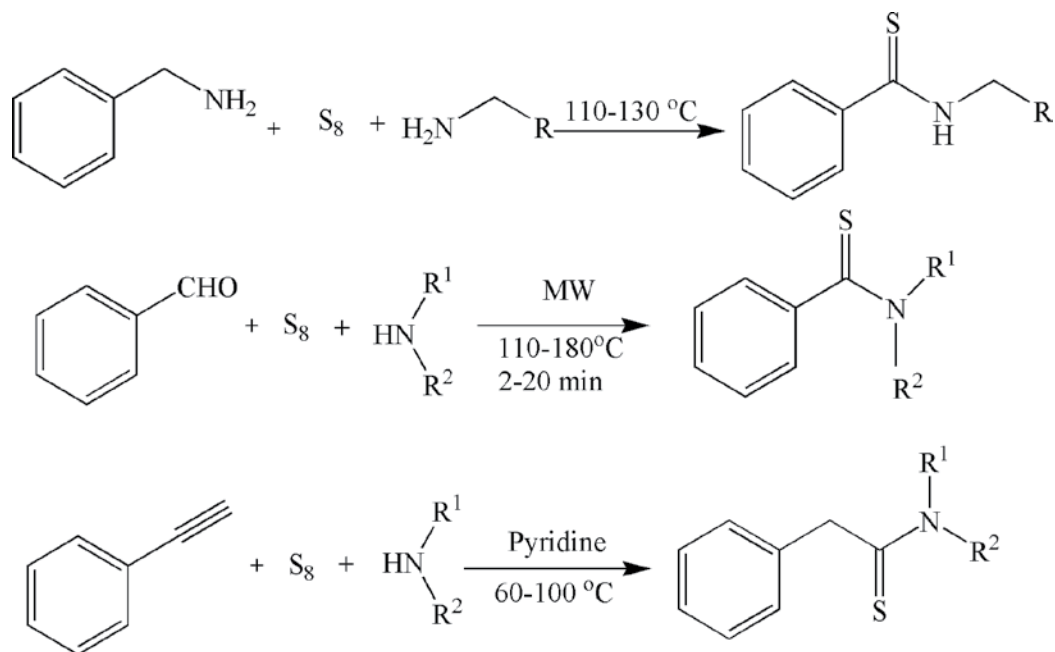
Scheme 17. Multicomponent oxidative coupling into thioamides by elemental sulphur under solvent-free condition.
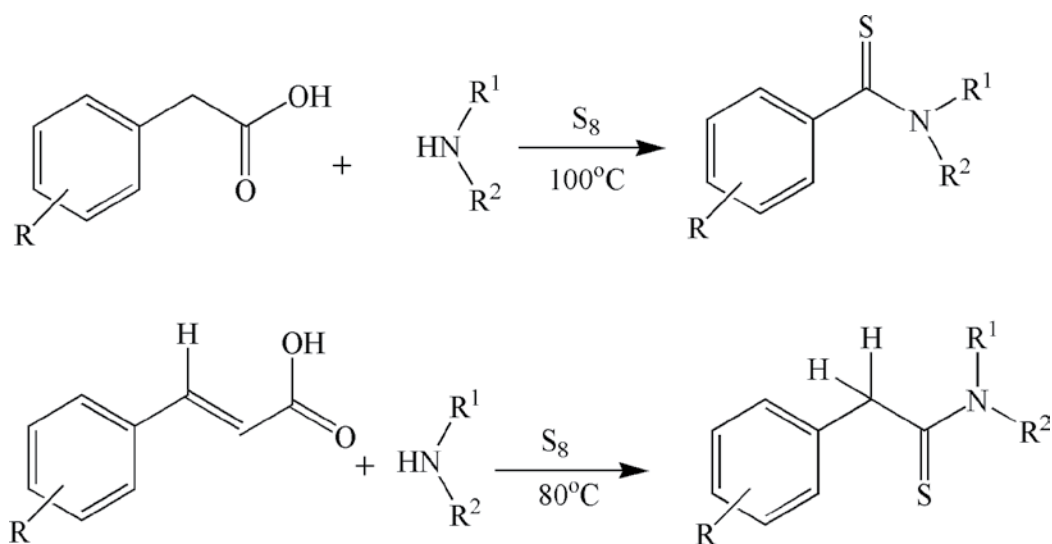
Scheme 18. Synthesis of thioamides via a three-component reaction by decarboxylative method.

The Beckmann rearrangement generally requires a strong acid, high reaction temperature, harsh reaction conditions, and production of unwanted by-products. Several methodologies to check the reaction conditions, such as, in liquid phase, in vapor phase, in supercritical water, and

in ionic liquids have been developed. However, the drawbacks in such methods are the use of toxic solvents, expensive reagents, long reaction times, low yields, and the production of considerable amounts of by-products. Literature survey reveals that there were many reports for the synthesis of amides and its sulfur containing analogue, thioamides; however, there is no report for the simultaneous synthesis of benzamides and thiobenzamides from benzoylthiourea [29].

4. Benzoxazole amides from benzoylthioureas

When *N*-substituted-*N'*-benzoylthioureas are reacted with diacetoxyiodobenzene (DIB) as catalyst, benzoxazole amides are formed; expected benzothiazoles or the decomposition products are not obtained. Thus, when *N*-benzoylthiourea reacts with hypervalent iodine (III) reagent (DIB), instead of molecular iodine, an unexpected cyclized benzoxazole derivative is formed (**Scheme 19**) [37]. Unlike molecular iodine, DIB as catalyst renders the formation of C-O bond in benzoxazole moiety of substituted *N*-benzoxazol-2-yl-amides, instead of the expected C-S bond formation of benzothiazole moiety. Unexpectedly, the reaction follows different pathways leading to C-O bond formation between carbonyl oxygen and *ortho*-carbon of aryl moiety resulting in oxazole ring formation *via* a sequential acylation and deacylation process.

Benzoxazoles are a class of heterocyclic compounds exhibiting therapeutical activities (**Figure 2**), such as, antifungal agents [38–40], cytotoxic compounds [41], as anti-inflammatory agents [42], as HIV-1 protease inhibitor [43], as an antibiotic [44], as *Cp*IMPDH inhibitors [45], non-nucleoside HIV-1 reverse transcriptase inhibitors (NNRTI) [46], and antitumour agents [47].
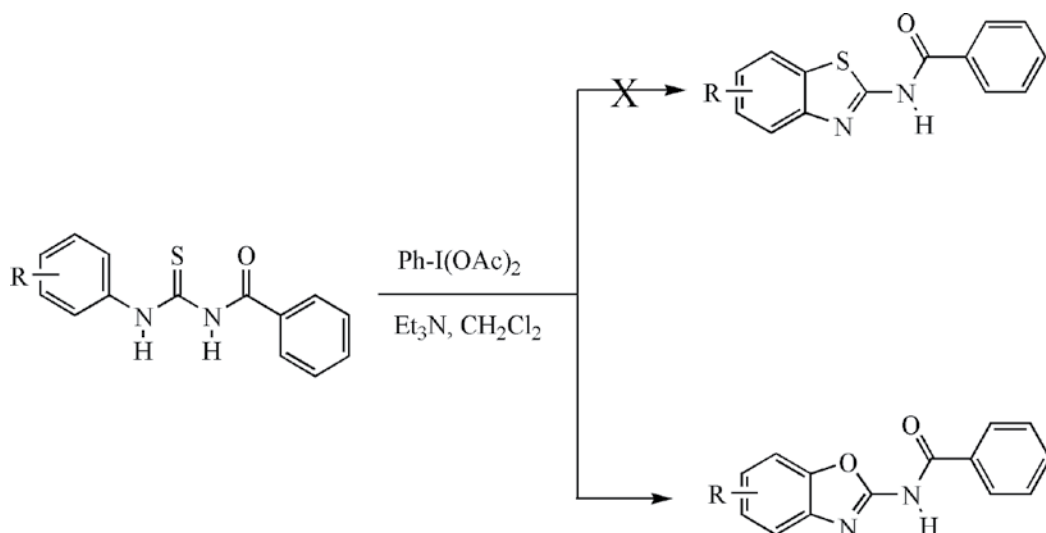
Scheme 19. Synthesis of benzoxazole amides by the reaction of *N*-substituted-*N'*-benzoylthioureas with diacetoxyiodobenzene (DIB) as catalyst.
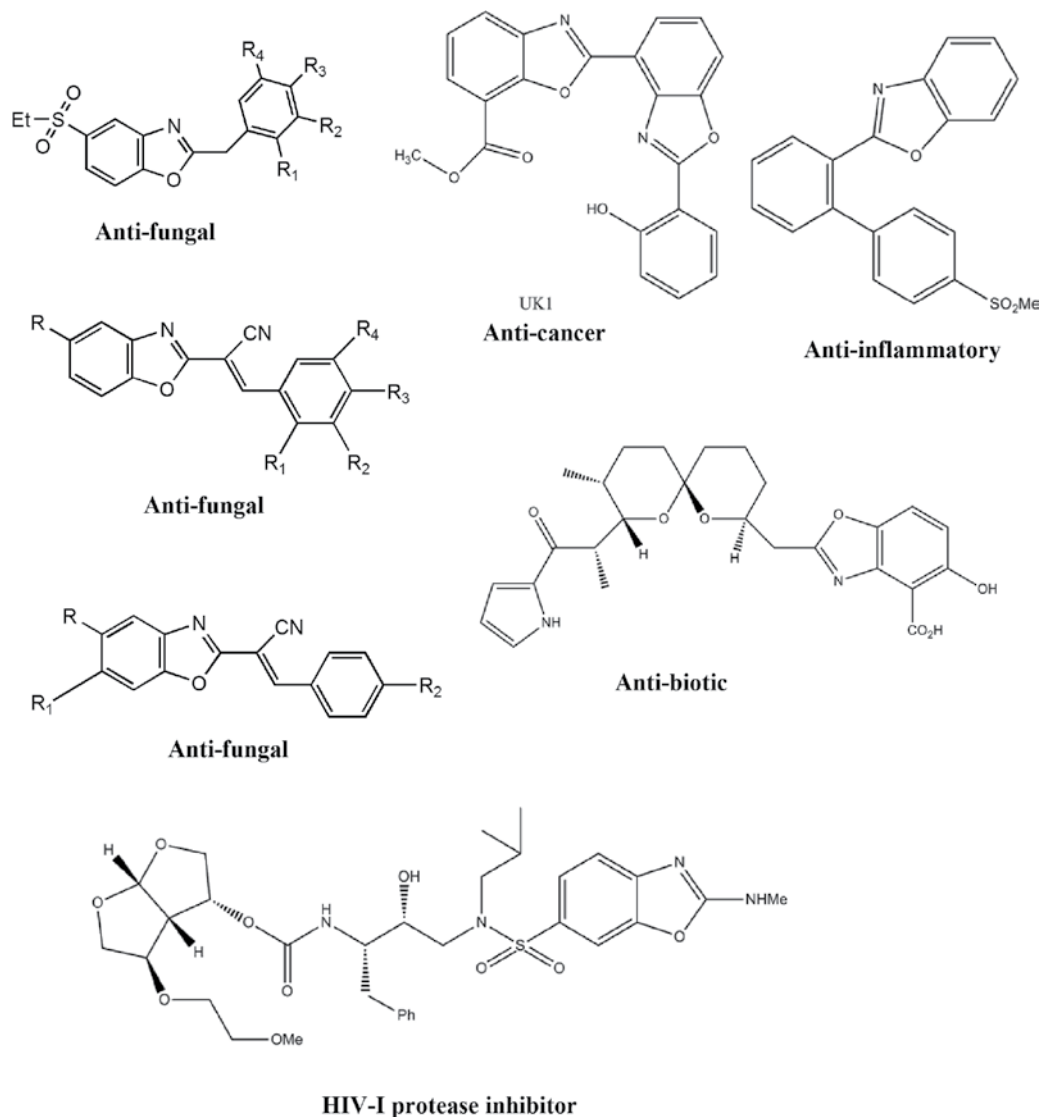
Figure 2. Several benzoxazole derivatives reported as biologically active compounds and pharmaceutical products.

Various methods have been reported in the literature for the synthesis of benzoxazoles starting from 2-aminophenol precursors with carboxylic acid derivatives, such as carboxylic acids, acid chlorides, acid anhydrides, and amides (**Scheme 20**), or by reacting 2-aminophenols with aldehydes followed by oxidation (**Scheme 21**) [48–51].

In most cases, 2-aminophenols are used as the starting materials for the preparation of 2-arylbenzoxazoles. However, the synthesis of *N*-benzoxazol-2-yl-amides is very limited [52] and the synthesis of *N*-benzoxazol-2-yl-amides starting from *N'*-benzoylthiourea using hypervalent iodine(III) reagents (DIB) is recently reported [37].
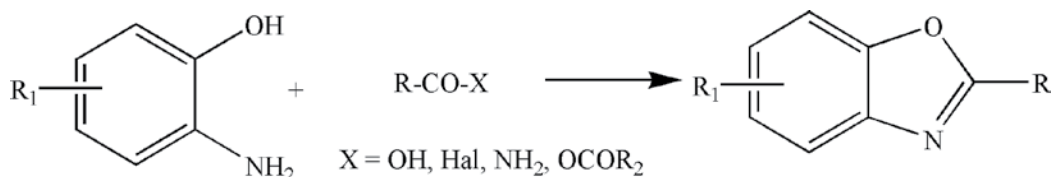
Scheme 20. Synthesis of benzoxazoles from 2-aminophenol with carboxylic acid derivatives, acid chlorides, and amides.
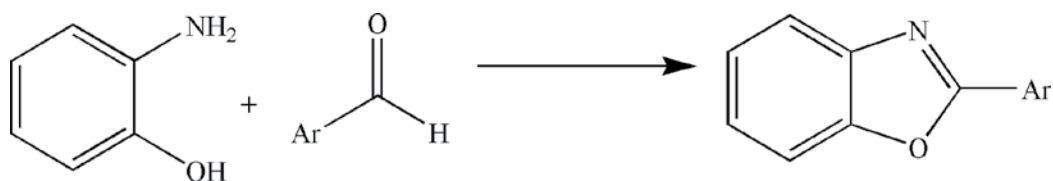
Scheme 21. Synthesis of benzoxazoles from 2-aminophenol with aldehydes followed by oxidation.

5. DFT calculations

With the help of density functional theory (DFT), the electronic structure of organic compounds could be expressed by electron density functional. DFT calculation is recently applied to the study of various reaction mechanisms, *viz.* the reaction mechanisms of the Pd(II)-catalyzed oxidative carbocyclization-alkoxycarbonylation of bisallenes to construct seven-membered carbocycles have been theoretically investigated with the aid of density DFT calculations [53]; the coupling reaction mechanisms of the Rh(III)-catalyzed redox-neutral C7-selective aryl C-H functionalization of indolines with alkynes and alkenes have been theoretically investigated [54]; the mechanism of NHC catalyzed annulation reactions involving an α,β-unsaturated acyl azolium and β-naphthol has been studied using DFT methods [55]; DFT calculations have been performed on Rh(III)-catalyzed phosphoryl-directed oxidative C-H activation/cyclization to investigate the detailed mechanism [56]; DFT calculations were also employed to investigate the energetics of several reaction paths for the Fries rearrangement of aryl formates promoted by boron trichloride [57]; the reactions of hypochlorous acid (HOCl) with ammonia, (di)methyl-amine, and heterocyclic amines have been studied computationally using double-hybrid DFT methods [58]; the mechanisms and chemo- and stereo-selectivities of PBu3-catalyzed intramolec-ular cyclizations of N-allylic substituted α-amino nitriles leading to functionalized pyrrolidines (5-endo-trig cyclization, Mechanism A) and their competing reaction leading to another kind of pyrrolidine (5-exo-trig cyclization, Mechanism B) have been investigated using DFT [59]; a systematic theoretical study has been carried out to understand the mechanism and stereose-lectivity of N-heterocyclic carbene (NHC)-catalyzed intramolecular-crossed benzoin reaction of enolizable ketoaldehyde using DFT calculations [60]. A simple and convenient method for the construction of substituted cycloheptenones from 1-bromoocta-1,7-diene-3-ols has been developed. The reaction involves Pd(0)-catalyzed intramolecular 7-exo-trigcyclization followed by Pd (II)-catalyzed oxidation of cyclic alcohol. The course of the reaction pathway has been evaluated using DFT calculations [61].

5.1. DFT calculations for the formation of benzamides and thiobenzamides

The mechanism for the decomposition of benzoylthioureas to benzamides and thiobenzamides in a single route using iodine-alumina as catalyst under solvent-free condition was studied with DFT calculations; all the structures were optimized by hybrid density functional B3LYP [62, 63] using the segmented all-electron relativistically contracted Def2-TZVP(−df) basis set with the help of ORCA [64]. The DFT calculation shows that the formations of both benzamides and thiobenzamides with by-products, *viz.*, isothiocyanate and isocyanate, respectively, are endothermic. The formation of benzamide and isothiocyanate involves lower energy. Thus, it was found that the formation of benzamide product is a thermodynamically favored reaction although it is observed from the experimental results that both the products are formed, except in *N*-2-pyridinyl-*N'*-benzoylthiourea where only the energetically favored benzamide product is formed [29].

The plausible mechanism for the formation of benzamides and thiobenzamides is shown in **Scheme 22**. To understand the mechanistic pathway, three most probable iodide intermediates **A**, **B**, and **C** formed after reaction with diiodine (I₂) molecule were considered (**Scheme 22** and **Table 1**). The I-I bond in diiodine is often known to be perturbed by thiones and form iodides. The formation of iodide intermediate through oxygen atom **C** is being ruled out because of its
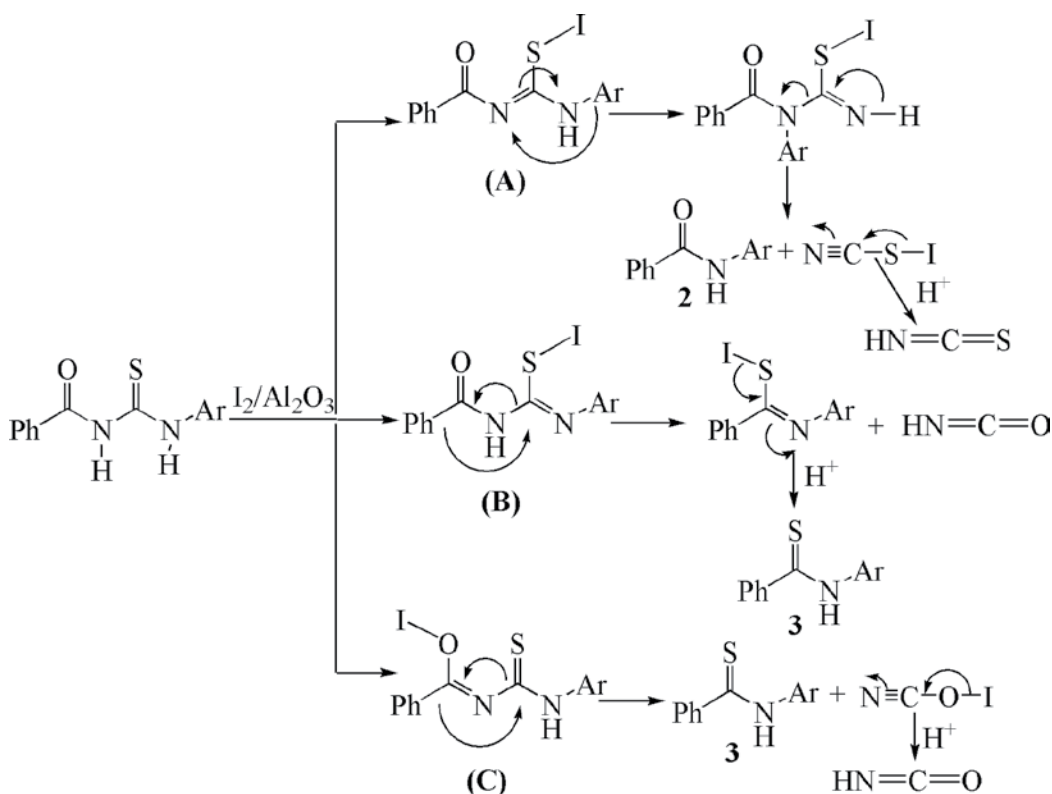
Scheme 22. Plausible mechanism for the formation of benzamides and thiobenzamides.

relatively high energy compared to those of intermediates **A** and **B** (examples of O-I bond formation of diiodine with ketones are not found in the literature).

The results show that the intermediate (**A**) has the lowest energy which indicates that it is the most probable intermediate and the optimized structure is shown in (**Figure 3**). The results further show that for all the reactions theoretically considered, the intermediate (**A**) has the lowest energy, except for *p*-chlorinated molecule, which indicates that it is the most probable intermediate (**Table 1**).

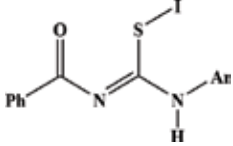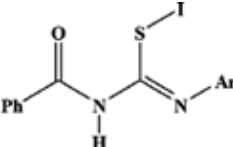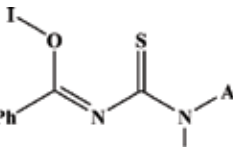| Intermediates	Structure	Relative energy (kcal)
A		0.0
B		0.5
C		35.2

Table 1. Relative energies of different intermediates for parent molecule.
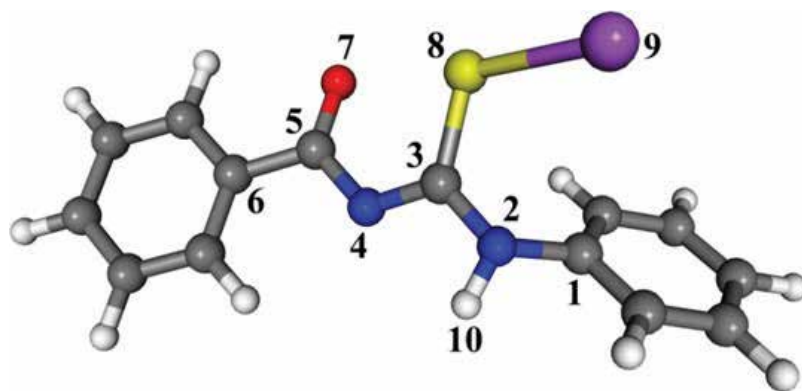
Figure 3. Optimized structure of A.

Intermediates	Mayer bond order				
	C1-N2	N2-C3	C3-N4	N4-C5	C5-C6
A	0.9092	1.1663	1.5143	1.3996	0.9238
B	1.1027	1.8061	0.9953	1.1750	0.9085
C	1.0134	1.1414	1.0373	1.9322	0.9493

Table 2. Mayer bond order for selected bonds (atom numbering is shown in **Figure 3**) for parent molecule.

To study the possibility of breaking the molecular backbone, the strength of different bonds were considered based on the Mayer bond order [65], which indicates a number of electron pairs that constitute a bond. When considering the backbone structure, C1-N2 has the least Mayer bond order in intermediate **A** while C5-C6 has the least bond order in the intermediates **B** and **C** (**Table 2**).

In case of the *p*-chlorinated molecule, an electron withdrawing substituent at the *para*-position of the aryl group, the intermediate **B** is the energetically most favored intermediate (**Table 4**). This indicates that the migration of the phenyl group in *p*-chlorinated molecule to attack the thiocarbonyl carbon is the favored step, which on further rearrangement gives the product thiobenzamide. The proposed steps are supported by the experimental results where the thiobenzamide is the major product. The probable reason for the formation of appreciable amount of the benzamide product, although not the favored step mechanistically, could be that the benzamide product is thermodynamically more stable than the thiobenzamide product. The formation of benzamide occurs through the intermediate **A** by the migration of the aryl group as the C1-N2 bond order is the least in intermediate **A**.

For other substituted molecules also, C5-C6 has the least bond order in the intermediate **B** as mentioned earlier. This explains that the formation of the thiobenzamide product is due to the migration of the phenyl group following the similar steps as in *p*-chlorinated molecule. However, when the electron withdrawing *p*-chlorinated aryl group is replaced by *p*-methylated aryl group, the benzamide product is the major one. The reason for the reaction in this case could be that the formation of benzamide product is preferred by breaking the C1-N2 bond in intermediate **A** than the mechanistically favored step by breaking C5-C6 bond in intermediate **B (**as in *p*-chlorinated molecule). This is so because the intermediate **A** has lower energy than **B** (**Table 3**). It is also interesting to note that when an electron donating group methyl is at the *ortho*-position in the aryl group, the intermediate **A** which has lowest energy has the least bond order at C5-C6 bond. This makes the breaking of C1-N2 bond in intermediate **A** less probable, thus rendering the formation of thiobenzamide product as the major product. Similar result is obtained in *o*-pyridinated molecule.

Thus, the DFT studies showed that the formation of benzamide was due to the migration of the aryl group (in intermediate **A**) while the formation of thiobenzamide may be due to the migration of the phenyl group (in intermediate **B**). It was found that the formation of benzamide product is the thermodynamically favored reaction, although it is observed from the experimental results that both the products are formed, except in *N*-2-pyridinyl-*N'*-benzoylthiourea where only the energetically favored benzamide product is formed.
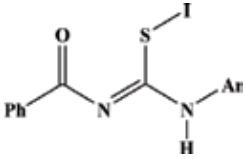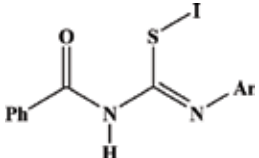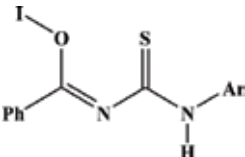
Structure	p-Chlorinated molecule		p-Methylated molecule	
	Intermediate	Relative energy (kcal)	Intermediate	Relative energy (kcal)
	A_p-Cl	0.2	A_p-Me	0.0
	B_p-Cl	0.0	B_p-Me	0.7
	C_p-Cl	35.0	C_p-Me	35.5

Table 3. Relative energies of different intermediates for p-chlorinated and p-methylated molecules.

Intermediates	Mayer bond order				
	C1-N2	N2-C3	C3-N4	N4-C5	C5-C6
p-Chlorinated molecule					
A_p-Cl	0.9138	1.1550	1.5238	1.3918	0.9254
B_p-Cl	1.1197	1.7945	1.0017	1.1714	0.9103
C_p-Cl	1.0194	1.1321	1.0436	1.9265	0.9495
p-Methylated molecule					
A_p-Me	0.9047	1.1728	1.5131	1.4038	0.9261
B_p-Me	1.1200	1.8032	0.9944	1.1719	0.9076
C_p-Me	1.0081	1.1453	1.0359	1.9327	0.9498
o-Methylated molecule					
A_o-Me	0.9585	1.1536	1.5098	1.4015	0.9236
B_o-Me	1.1379	1.7861	0.9979	1.1722	0.9090
C_o-Me	0.9087	1.1397	1.0361	1.9337	0.9413
o-Pyridinated molecule					
A_o-Py	1.0052	1.1535	1.5311	1.3810	0.9264
B_o-Py	1.0588	1.8130	1.0024	1.1710	0.9111
C_o-Py	1.0440	1.1511	1.0501	1.9346	0.9517

Table 4. Mayer bond order for selected bonds for the p-chlorinated, p-methylated o-methylated molecules and the o-pyridinated molecules. (atom numbering is shown in **Figure 3**).

5.2. DFT calculations for the formation of benzoxazoles

Density functional calculations were performed at a B3LYP/Def2-TZVP($-$df) level of theory using ORCA to study the reaction mechanism for the formation of benzoxazole amides from benzoylthioureas in presence of DIB as catalyst and the role of substitution with electron withdrawing/donating group at different positions of the phenyl ring on the reaction. The plausible mechanism for the formation of *N*-benzoxazol-2-yl-amides from benzoylthioureas is shown in **Scheme 18**. The final product benzoxazole amide is formed after a series of acylation and deacylation occurring in tandem, as illustrated in **Scheme 18**, with the formation of a number of intermediates. At first, the acylation occurs due to the formation of carbodiimide from *N′*-benzoylthiourea. During carbodiimide formation, the molecule is oxidized by DIB to give 1 mole each of acetic acid, sulfur atom, and phenyl iodide where iodine is reduced from +3 to +1 oxidation state. There are two possible pathways, namely, Path A and Path B, for the formation of carbodiimide from *N′*-benzoylthiourea through the formation of intermediates A and B, respectively. The attack of sulfur atom of thiocarbonyl on the thiophilic iodine of diacetoxyiodobenzene is initiated by the deprotonation of either of the NH protons lying on either side of the thiocarbonyl group. The deprotonation of N4 atom results in intermediate A, while the deprotonation of N2 atom results in intermediate B. To determine which pathway is the favored one, the relative energies of intermediates A and B were calculated (**Table 5**). It is observed that the intermediate B is the thermodynamically favored intermediate in most of the reactions except for substitution at *ortho*-position with chlorine and at *meta*-position with both electron withdrawing chlorine and donating methyl groups. This shows that the position of substitution plays a bigger role than the type of substituent in determining the pathway to give carbodiimide. It may be mentioned that earlier in our work for iodide intermediate [49], the relative energy of the deprotonated product from N4 atom was slightly less than that obtained from N2 atom. However, the energy difference between the two in the previous work was appreciably small with maximum of 3.0 kcal/mole. In the present case, the difference in relative energy between the two intermediates increases by two fold (**Table 5**) although the deprotonated product from N2 atom generally becomes more stable as shown in mechanistic pathways for the formation of benzoxazole amides (**Scheme 23**).

The carbodiimide thus formed is acylated at carbodiimide carbon which after rearrangement gives the acylated intermediate (**C**). The conversion from the acylated intermediate **C** to the final product here also can follow either of two possible routes: Route 1, which is deacylation by hydrolysis followed by cyclization, to give benzoxazole derivative (**D′**) through oxidation of deacylated product by another molecule of DIB or Route 2, which undergoes cyclization through oxidation of acylated intermediate **C** by another molecule of DIB, to give acylated benzoxazole derivative (**E**) followed by deacylation on hydrolysis. The cyclization to give oxazole ring also is initiated by deprotonation of NH atom as in the first reaction.

To determine which route the reaction follows, one needs theoretical consideration of each step of deacylation then cyclization (Route 1) or cyclization then deacylation (Route 2). One way to determine which route the reaction follows is to compare the energetics of each step undergoing in either route (**Table 6**). Comparison of energies of reactions for the first step through Route 1 (deacylation) and Route 2 (cyclization by oxidation of DIB) shows that the initial deacylation (Route 1) is exothermic and thermodynamically favored over oxazole cyclization through Route 2
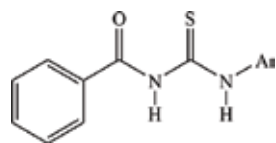
Entry number	Ar	Relative energy of B (kcal/mole)
1		−6.230
2		−7.571
3		−7.236
4		0.952
5		−7.416
6		1.695
7		−7.466
8		0.892
9		−5.000

Table 5. Relative energies of intermediates B with respect to A.
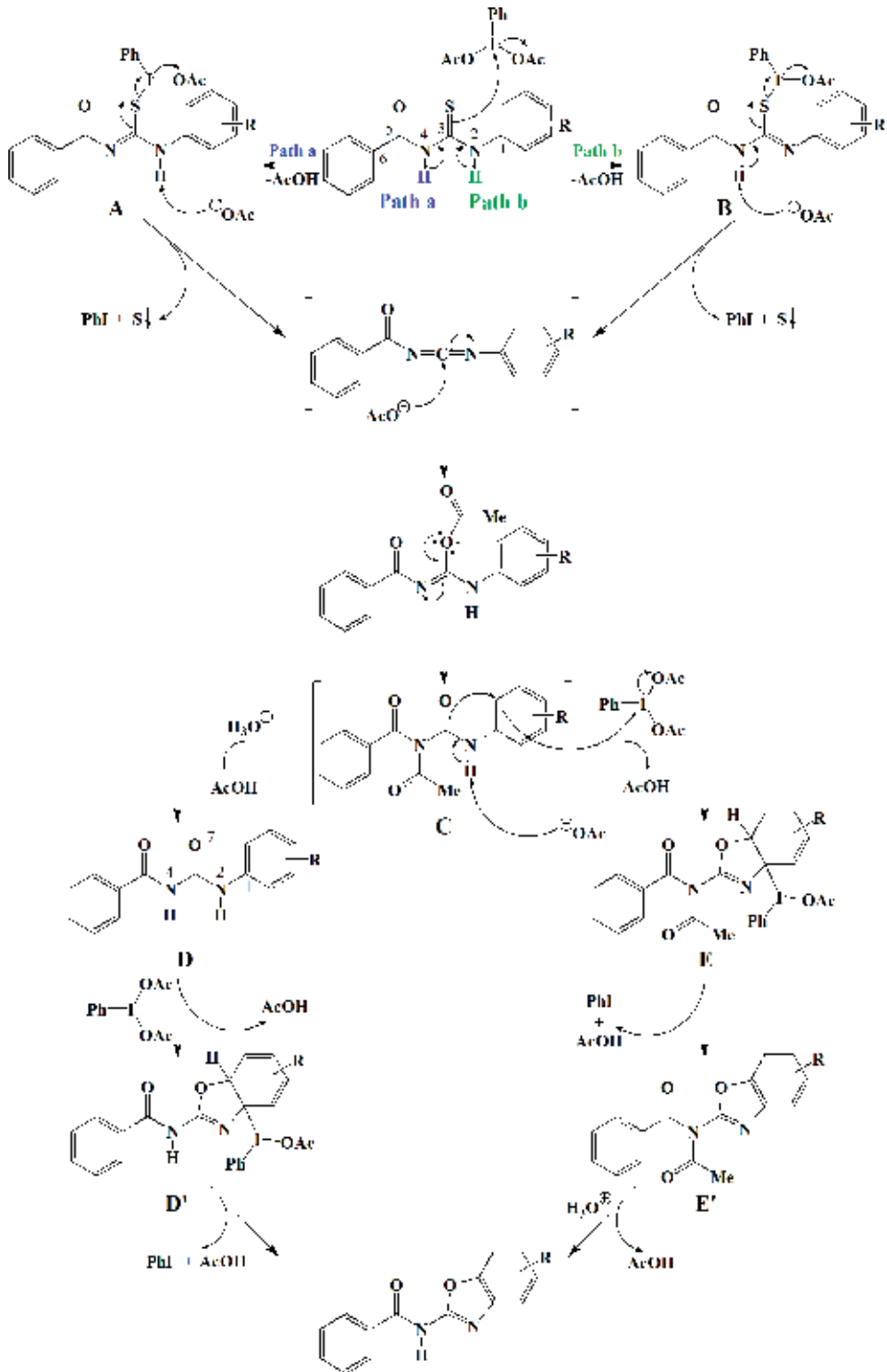
Scheme 23. Mechanistic pathways for the formation of benzoxazole amides.

Entry number	Energy of reaction (kcal/mole)					
	Route 1			Route 2		
	C to D	D to D′	D′ to 2	C to E	E to E′	E′ to 2
1	−22.81	52.02	−79.23	52.23	−84.65	−17.60
2	−24.66	57.52	−81.42	55.53	−86.40	−17.70
3	−24.55	53.96	−81.50	52.12	−86.46	−17.75
4	−24.61	56.30	−79.75	54.34	−84.67	−17.72
5	−24.57	56.41	−80.15	53.78	−84.54	−17.56
6	−24.88	57.55	−79.68	55.48	−85.48	−17.02
7	−24.91	57.46	−80.33	55.33	−85.27	−17.84
8	−28.23	57.48	−81.85	52.68	−86.76	−18.52
9	−25.05	57.63	−80.15	55.72	−85.48	−17.81

Table 6. Energy of reaction through Route 1 and Route 2.

which is endothermic. The Route 1 is favored more on substitution with both electron withdrawing as well as donating groups at all positions, that is, *ortho*-, *meta*- and *para*-positions. Further, it is observed that the deacylation of chlorinated derivative of **C** at *ortho*-position is the most exothermic and the least at *meta*-position. This is because of higher conjugation at *ortho*- and *para*-positions where the electron withdrawing nature of chlorine favors the deacylation more. On the other hand, it is reverse for methylated derivative, that is, the reaction is most exothermic when substituted at *meta*-position and least at *ortho*-position. In case of methylated derivative, the electron donating nature of methyl group disfavors the deacylation when substituted at *ortho*- and *para*-positions where the conjugation is more. On dimethylation, both at *ortho*- and *para*-positions of **C**, the exothermic energy is further reduced. However, the exothermic energy for the dichlorination at *ortho*- and *para*-positions of **C** is less than that for substitution at *ortho*-position although it is higher than those for substitutions at *meta*- and *para*-positions.

The deacylation of **C** gives the deacylated intermediate **D** that has two acidic hydrogen atoms which are bonded to N2 and N4 nitrogen atoms as before. Considering the acidity of the hydrogen atoms, it is found that the hydrogen atom attached to N2 nitrogen atom is more acidic than that attached to N4 atom as is indicated by the Mulliken atomic charges of the hydrogen atoms (**Table 7**). This deprotonation of the proton of N2 atom initiates the attack of carbonyl oxygen O7 atom on *ortho*-carbon of the aryl group (the attack of *ortho*-carbon atom is discussed in detail later), leading to the formation of cyclized intermediate **D′** containing oxazole ring and the reduction of another molecule of DIB from +3 to +1 oxidation state of iodine by the attack of C1 carbon atom of **D** on the iodine of DIB. The attack of O7 atom on *ortho*-carbon and C1 atom on iodine of DIB is such that the two attacks are anti-periplanar. Therefore, the hydrogen attached to the *ortho*-carbon and iodine bonded to C1 atom lie on the same side of the molecular plane.

Upon cyclization to form oxazole ring of **D′**, the aromaticity of the benzene ring is lost as the hybridizations of the attacked *ortho*-carbon as well as that of C1 atom change from sp^2- to sp^3-hybridization. Hence, this cyclization process to give **D′** is endothermic. It is observed that the

| Entry number	Mulliken charge of hydrogen atom bonded to	
	N2	N4
1	0.2982	0.2679
2	0.3002	0.2657
3	0.2984	0.2686
4	0.301	0.2654
5	0.3011	0.2653
6	0.3016	0.2675
7	0.3018	0.2671
8	0.3061	0.2658
9	0.3073	0.2671

Table 7. Mulliken atomic charge of the hydrogen atoms attached to N2 and N4 atoms of D.

energy involved is affected by the substitution with electron withdrawing/donating groups at different positions of the benzene ring. For methyl-substituted derivative, the cyclization energy involved is greatest when substituted at *para*-position and least at *ortho*-position; while for chlorinated derivative, the energy involved is highest at *meta*-position and least at *para*-position.

The aromaticity is regained upon subsequent deprotonation of sp^3-hybridized *ortho*-carbon and bond breaking between C1 carbon and iodine giving the final product with the release of phenyl iodide and acetic acid. This aromatization to give benzoxazole derivative is exothermic (**Table 6**). For both electron-withdrawing chlorine and -donating methyl-substituted derivatives, the exothermic energy is highest when substituted at *ortho*-position and least at *meta*-position.

There is further interesting result from the reaction when there is substitution at the *meta*-position (3′-position) of the starting material as there are two possible products (**Scheme 24**) formed due to presence of two *ortho*-carbon atoms (2′ and 6′ carbon atoms) available for attack. The first product (**F**) is formed due to attack of O7 atom (initiated by deprotonation of N2 proton) on 2′ *ortho*-carbon atom while the second product (**G**) is formed due to attack on 6′ *ortho*-carbon. When considering the Mayer bond order between carbon and oxygen, the O7-C2′ bond of the first product (**F**) is stronger than the O7-C6′ bond of the second product (**G**) for both methylated and chlorinated derivative. However, the first product (**F**) is energetically slightly favored by 0.85 kcal/mole for the methylated derivative, while the second product (**G**) is favored by 0.35 kcal/mole for the chlorinated derivative, although in both derivatives the products have almost same energy. As the products have equivalent energies, it is inferred that both products may be formed for entry 4 (methylated derivative) and 6 (chlorinated derivative).

When *N*-substituted-*N′*-benzoylthioureas are reacted with diacetoxyiodobenzene (DIB) as catalyst, benzoxazole amides are formed; expected benzothiazoles or the decomposition products are not obtained. Unlike molecular iodine, DIB as catalyst renders the formation of C-O bond in benzoxazole moiety of substituted *N*-benzoxazol-2-yl-amides, instead of the expected C-S bond formation of benzothiazole moiety. DFT calculations showed the reaction followed through carbodiimide intermediate. The carbodiimide further undergoes a series of acylation, deacylation, and cyclization in tandem to give the final product, benzoxazole amides.
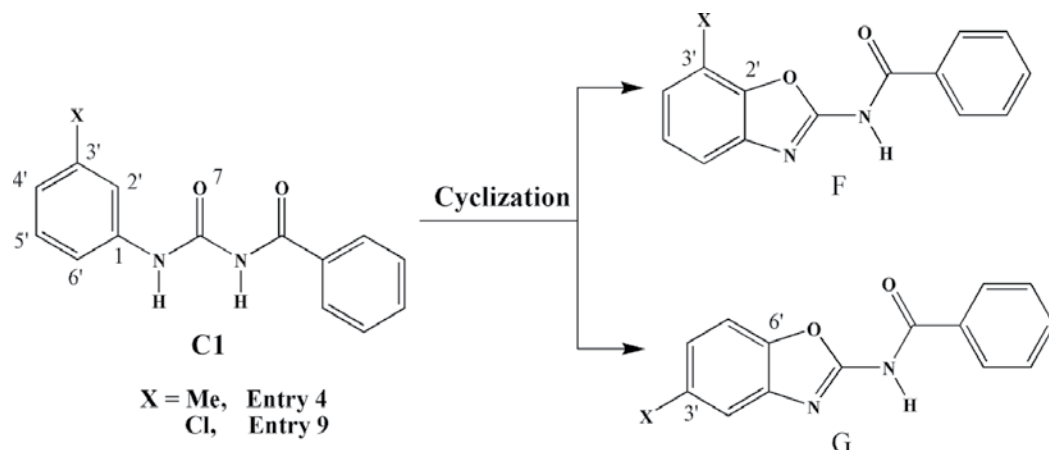
Scheme 24. Two possible products for the *meta*-substituted derivative.

Thus, the density functional calculations showed the reaction followed through carbodiimide intermediate formed by the oxidation of N'-benzoylthiourea by DIB. The carbodiimide intermediate thus formed undergoes a series of acylation and deacylation in tandem, leading to cyclization to form oxazole ring of substituted *N*-benzoxazol-2-yl-amide, due to C-O bond formation as a result of attack of carbonyl oxygen on *ortho*-carbon aryl moiety, instead of the expected C-S bond formation to give benzothiazole moiety.

Author details

Warjeet S. Laitonjam* and Lokendrajit Nahakpam

*Address all correspondence to: warjeet@manipuruniv.ac.in

Department of Chemistry, Manipur University, Imphal, Manipur, India

References

[1] Katritzky AR, Boulton JA. Advances in Heterocyclic Chemistry. Vol. 1-27. New York: Academic Press; 1963-1980

[2] Weissberger A. The Chemistry of Heterocyclic Compounds. Vol. 1-29. New York: Wiley Interscience; 1950-1975

[3] Elderfield RC. Heterocyclic Chemistry. Vol. 1-9. New York: Wiley; 1950-1967

[4] Serdons K, Terwinghe C, Vermaelen P, Van LK, Kung H, Mortelmans L, Bormans G, Verbruggen A. Journal of Medicinal Chemistry 2009;**52**:1428-1437

[5] Bondock S, Fadaly W, Metwally MA. European Journal of Medicinal Chemistry. 2010;**45**: 3692-3701

[6]   Yoshida M, Hayakawa I, Hayashi N, Agatsuma T, Oda Y, Tanzawa F, Iwasaki S, Koyama K, Furukawa H, Kurakata S. Bioorganic & Medicinal Chemistry Letters. 2005;**15**:3328-3332

[7]   Ma D, Xie S, Xue P, Zhang X, Dong J, Jiang Y. Angewandte Chemie, International Edition. 2009;**48**:4222-4225

[8]   Ding Q, He X, Wu J. Journal of Combinatorial Chemistry. 2009;**11**:587-591

[9]   Van Heusden J, Van Ginckel R, Bruwiere H, Moelans P, Janssen B, Floren W, van der Leede BJ, van Dun J, Sanz G, Venet M, Dillen L, Van Hove C, Willemsens G, Janicot M, Wouters W. British Journal of Cancer. 2002;**86**:605-611

[10] Catalano A, Carocci A, Defrenza I, Muraglia M, Carrieri A, Bambeke FV, Rosato A, Corbo F, Franchini C. European Journal of Medicinal Chemistry. 2013;**64**:357-364

[11] McDonnell ME, Vera MD, Blass BE, Pelletier JC, King RC, Fernandez-Metzler C, Smith GR, Wrobel J, Chen S, Wall BA, Reitz AB. Bioorganic & Medicinal Chemistry. 2012;**20**: 5642-5648

[12] Cheah BC, Vucic S, Krishnan AV, Kiernan MC. Current Medicinal Chemistry. 2010;**17**: 1942-1999

[13] Song EY, Kaur N, Park MY, Jin Y, Lee K, Kim G, Lee KY, Yang JS, Shin JH, Nam KY, No KT, Han G. European Journal of Medicinal Chemistry. 2008;**43**:1519-1524

[14] Patel NB, Khan IH, Pannecouque C, De Clercq E. Medicinal Chemistry Research. 2013;**22**: 1320-1329

[15] Patel NB, Khan IH, Rajani SD. European Journal of Medicinal Chemistry. 2010;**45**:4293-4299

[16] Sprague JM, Land AH. In: Elderfield RC, editor. Heterocyclic Compounds. Vol. 5, Chapter 8. New York: Wiley; 1957. pp. 484-721

[17] Jordan AD, Luo C, Reitz AB. The Journal of Organic Chemistry. 2003;**68**:8693-8696

[18] Feng E, Huang H, Zhou Y, Ye D, Jiang H, Liu H. Journal of Combinatorial Chemistry. 2010;**12**:422-429

[19] Benedi C, Bravo F, Uriz P, Fernandez E, Claver C, Castillon S. Tetrahedron Letters. 2003; **44**:6073-6077

[20] Inamoto K, Hasegawa C, Hiroya K, Doi T. Organic Letters. 2008;**10**:5147-5150

[21] Ding Q, He X, Wu J. Journal of Combinatorial Chemistry. 2009;**11**:587-591

[22] Qiu JW, Zhang XG, Tang RY, Zhong P, Li JH. Advanced Synthesis and Catalysis. 2009;**351**: 2319-2323

[23] Ding Q, Cao B, Liu X, Zong Z, Peng YY. Green Chemistry. 2010;**12**:1607-1610

[24] Shen G, Lv X, Bao W. European Journal of Organic Chemistry. 2009:5897-5901

[25] Guo YJ, Tang RY, Zhong P, Li JH. Tetrahedron Letters. 2010;**51**:649-652

[26] Zhao J, Huang H, Wu W, Chen H, Jiang H. Organic Letters. 2013;**15**:2604-2607

[27] Yella R, Patel BK. Journal of Combinatorial Chemistry. 2010;**12**:754-763

[28] Lokendrajit N, Brajakishor CS, Warjeet LS. Journal of Heterocyclic Chemistry. 2015;**52**:267-272

[29] Lokendrajit N, Chipem FAS, Brajakishor CS, Warjeet LS. New Journal of Chemistry. 2015;**39**:2240-2247

[30] Allen CL, Chhatwal RA, Williams JM. Journal of the Chemical Society, Chemical Communications. 2012;**48**:666-668

[31] Gelens E, Smeets L, Sliedregt LAJM, van Steen BJ, Kruse CG, Leurs, R, Orrua RVA. Tetrahedron Letters 2005;**46**:3751-3754

[32] Vanjari R, Guntreddi T, Singh KN. Organic Letters. 2013;**15**:4908-4911

[33] Nguyen TB, Ermolenko L, Al-Mourabit A. Organic Letters. 2012;**14**:4274-4277

[34] Xu H, Deng H, Li Z, Xiang H, Zhou X. European Journal of Organic Chemistry. 2013;**31**:7054-7057

[35] Nguyen TB, Tran MQ, Ermolenko L, Al-Mourabit A. Organic Letters. 2014;**16**:310-313

[36] Guntreddi T, Vanjari R, Singh KN. Organic Letters. 2014;**16**:3624-3625

[37] Lokendrajit N, Chipem FAS, Brajakishor CS, Warjeet LS. Organic & Biomolecular Chemistry. 2016;**14**:7735-7745

[38] Ertan T, Yildiz I, Tekiner-Gulbas B, Bolelli K, Temiz-Arpaci O, Ozkan S, Kaynak F, Yalcin I, Aki E. European Journal of Medicinal Chemistry. 2009;**44**:501

[39] Temiz-Arpaci O, Yıldız Y, Ozkan S, Kaynak F, Akı-Sxener E, Yalcin I. European Journal of Medicinal Chemistry. 2008;**43**:1423

[40] Jauhari PK, Bhavani A, Varalwar S, Singhal K, Raj P. Medicinal Chemistry Research. 2008;**17**:412

[41] Ueki M, Ueno K, Miyadoh S, Abe K, Shibata K, Taniguchi M, Oi SJ. Antibiot. 1993;**46**:1089

[42] Seth K, Garg SK, Kumar R, Purohit P, Meena VS, Goyal R, Banerjee UC, Chakraborti AK. ACS Medicinal Chemistry Letters. 2014;**5**:512-516

[43] Hohlfeld K, Tomassi C, Wegner JK, Kesteleyn B, Linclau B. ACS Medicinal Chemistry Letters. 2011;**2**:461-465

[44] Martin DD, Kotecha NR, Ley SV, Mantegani S, Menéndez JC, Organ HM, White AD, Banks BJ. Tetrahedron. 1992;**48**:7899

[45] Gorla SK, Kavitha M, Zhang M, Chin JEW, Liu X, Striepen B, Makowska-Grzyska M, Kim Y, Joachimiak A, Hedstrom L, Cuny GD. Journal of Medicinal Chemistry. 2013;**56**:4028-4043

[46] Boyer J, Arnoult E, Médebielle M, Guillemont J Unge J, Jochmans D. Journal of Medicinal Chemistry. 2011;**54**:7974-7985

[47] Aiello S, Wells G, Stone EL, Kadri H, Bazzi R, Bell DR, Stevens MFG, Matthews CS, Bradshaw TD, Westwell AD. Journal of Medicinal Chemistry. 2008;**51**:5135-5139

[48] Wang H, Wang L, Shang J, Li X, Wang H, Gui J, Lei AW. Chemical Communications. 2012:76

[49] Shelkar R, Sarode S, Nagarkar J. Tetrahedron Letters. 2013;**54**:6986

[50] Bala M, Verma PK, Sharma U, Kumar N, Singh B. Green Chemistry. 2013;**15**:1687

[51] Mayo MS, Yu X, Zhou X, Feng X, Yamamoto Y, Bao M. The Journal of Organic Chemistry. 2014;**79**:6310

[52] Kim BJ, Kim J, Kim YK, Choi SY, Choo HYP. Bulletin of the Korean Chemical Society. 2010;**31**:1270-1274

[53] Hana L, Org TL. Biomolecular Chemistry. 2017;**15**:5055-5061

[54] Han L, Zhang X, Wang X, Zhao F, Liu S, Liu T. Organic & Biomolecular Chemistry. 2017;**15**:3938-3946

[55] José Aurell M, Domingo LR, Arnó M, Zaragozá RJ. Organic & Biomolecular Chemistry. 2016;**14**:8338-8345

[56] Liu L, Wu Y, Wang T, Gao X, Zhu J, Zhao Y. The Journal of Organic Chemistry. 2014;**79**:5074-5081

[57] Bagno A, Kantlehner W, Kress R, Saielli G, Stoyanov E. The Journal of Organic Chemistry. 2006;**71**:9331-9340

[58] Šakić D, Hanževački M, Smith DM, Vrček V. Organic & Biomolecular Chemistry. 2015;**13**:11740-11752

[59] Zheng L, Tang M, Wang Y, Guo X, Wei D, Qiao Y. Organic & Biomolecular Chemistry. 2016;**14**:3130-3141

[60] Zhang W, Yang W, Wei D, Tang M, Zhu X. Organic & Biomolecular Chemistry. 2016;**14**:6577-6590

[61] Ray JK, Paul S, Ray P, Singha R, Rao DY, Nandi S, Anoop A. New Journal of Chemistry. 2017;**41**:278-284

[62] Becke ADJ. Chemical Physics. 1993;**98**:5648-5652

[63] Lee C, Yang W, Parr RG. Physical Review B. 1988;**37**:785-789

[64] Neese F. WIREs Computational Molecular Science. 2012;**2**:73-78

[65] Mayer I. Chemical Physics Letters. 1983;**97**:270-274

Material and Molecuar Design

Carbon Nanotubes: Molecular and Electronic Properties of Regular and Defective Structures

María Leonor Contreras Fuentes and
Roberto Rozas Soto

Additional information is available at the end of the chapter

http://dx.doi.org/10.5772/intechopen.70934

Abstract

In this chapter, we describe how structural parameters affect the reactivity of single-walled carbon nanotubes through global reactivity descriptors obtained by the DFT methods (B3LYP/6-31G(d) with real frequencies in all cases). First, we investigate regular *armchair*, *chiral*, and *zigzag* nanotubes with bumpy defects (five- and seven-membered rings), finding that regular and defective *zigzag* nanotubes exhibit the greater conductive ability, reactivity, and capacity of nanotubes to be reduced. The bumpy defects favor those properties with greater intensity in *chiral* nanotubes. We also investigate how the properties of *armchair* nanotubes change in the presence of bumpy, haeckelite, Stone-Wales, and zipper defects, and we found that *armchair* nanotubes with zipper defects show greater reactivity and better conducting abilities enhanced by nitrogen doping and longer nanotubes. In addition, for *armchair* nanotubes containing bumpy defects, our results reveal, considering B3LYP-D3 correction, that bumpy defects confer a greater ability to physically adsorb hydrogen, with adsorption energies of 0.32 eV/adsorbed H_2. That value is considered ideal for the reversible adsorption of hydrogen at room temperature and low pressures and therefore favorable for use as a clean energy source. These results contribute to the future design of novel useful materials based in carbon nanotubes.

Keywords: nitrogen-doped carbon nanotubes, conceptual DFT, global reactivity descriptors, hydrogen physisorption energy, saturated nanotubes, nanotube chirality, bumpy defects, zipper defects, haeckelite defects, Stone-Wales defects, conductive ability, *armchair*, *chiral*, *zigzag*, dispersion forces

1. Introduction

Carbon is a very important chemical element, essential for the existence of multiple types of structures. Organic chemistry, a broad and interesting branch of chemistry, in simple terms, is

defined as carbon chemistry and is closely related, for example, to biochemistry and biomedicine. The understanding of the structure-property relations is an important pillar on which the development of these branches of knowledge is based. Thus, exchanging the position of two groups on a molecule of a recommended drug may mean that it becomes a poison. An example is the case of thalidomide disaster [1] where many babies were born with phocomelia (malformation of the limbs) when R-thalidomide, a compound suitable to mitigate some troublesome symptoms of pregnancy, was administered to their mother but contaminated with its enantiomer (compound with the same mirror image, but not superimposable); moreover, the enantiomer, S-thalidomide, has teratogenic effects.

Carbon nanotubes (CNTs) are a family of compounds that, due to their size, composition, surface ratio, and molecular structure, present useful properties. Being lighter than steel, CNTs have a higher tensile strength. They may also be better conductors than copper [2, 3]. In addition, CNTs can penetrate cell membranes without breaking them [4]. Basic nanotube units are six-membered rings of sp^2-hybridized carbon atoms. The diameter of the nanotubes is of great importance in their properties because it modifies the curvature of the surface of the nanotube affecting the distribution of charge density. Also the way these units are arranged, known as chirality of nanotubes, originates conductive or semiconducting nanotubes. It is important to note that here the concept of chirality is not related to the presence of chiral atoms.

Three types of CNTs are known as characterized by the so-called chirality vectors or Hamada indices, as shown in **Figure 1**. CNTs of type (n,n) or *armchair* are metallic; those of type (n,m) or *chiral* and those of type (n,0) or *zigzag* are semiconductors or metallic; *chiral* nanotubes are conductors if the difference n-m is a multiple of 3 [5]. In all these cases, the repeating units are hexagons, and here we call regular CNTs (R) to these nanotubes to differentiate them from other types of CNTs in which there are cyclic units that can be of four, five, seven, or eight members. When present in the nanotubes, these units, different from the hexagons, are known as structural defects. There are different types of structural defects that can be produced by the addition of a pair of carbon atoms. Those having an arrangement (7,5,5,7) are known as bumpy (B) if the defect is repeated in a transverse equidistant form from the ends of the nanotube. If the defect is repeated longitudinally, zipper-type nanotubes (Z) are obtained. **Figure 2** shows the arrangement of nonhexagonal units in some different types of defects. The arrangement (8,4,8,4) represents one of the defects called haeckelite (HK). In addition, the arrangement (5,7,7,5) of the topological defects known as Stone-Wales (SW) is shown. The absence of some atoms (vacancy) or the substitution of some carbon atoms by other elements (doping) is also considered as defects.

The particular structure of the CNTs (mainly the regular ones) can be of a single-wall, SWCNT, or of multiple concentric walls and every day finds new applications in diverse fields of science and technology, and there are a great number of publications and patents which account for it (e.g., see [6–9]). Nanotubes with defects have shown advantages in some fields. For example, doping with nitrogen decreases the toxicity of nanotubes [10] and gives them excellent catalytic properties in oxygen reduction reactions [11, 12]. The bumpy nanotubes present interesting values of hydrogen physisorption energies (0.26 eV/H_2), better than similar regular nanotubes, estimated through theoretical studies based on the density functional theory (DFT) [13]. This physisorption energy value is within the suggested ideal range for using hydrogen as a clean
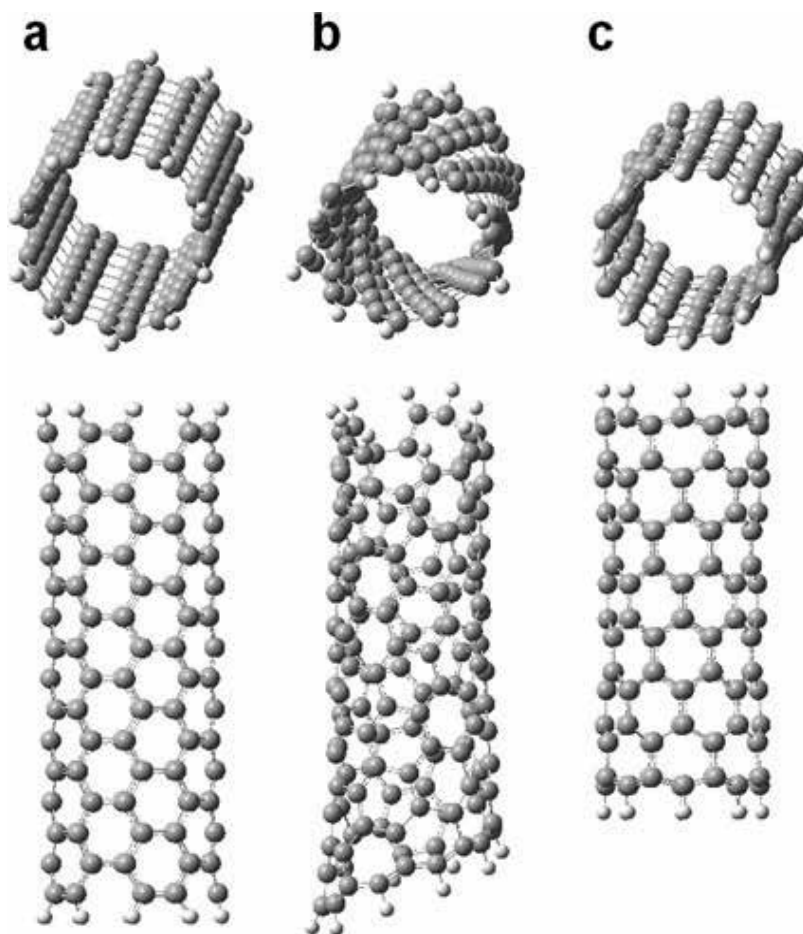
Figure 1. Regular nanotube models of different chirality. Perspective and lateral views for (a) *armchair* (5,5), (b) (*chiral* 6,3), and (c) *zigzag* (8,0) nanotube representations.
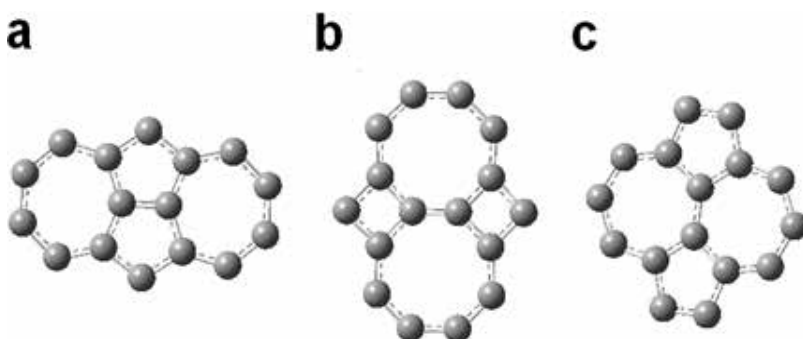

Figure 2. Nanotube defects representation. (a) (7,5,5,7) bumpy and zipper defects; (b) (8,4,8,4) haeckelite defect; and (c) (5,7,7,5) Stone-Wales defect.

energy media [14]. The specialized literature lacks enough information to have a broader perspective of the utility and possible applications of defective nanotubes, despite some interesting isolated results [15, 16].

It is therefore interesting and necessary to evaluate how changes in geometric, structural, topological, or doping parameters can affect properties of stability, conductivity, and chemical reactivity of nanotubes and determine if there is any general tendency to predict or modify specifically their behavior in the search for new applications of these advanced materials.

In this chapter, the effects of chirality, chemisorption, number of defects, and the presence of nitrogen on the reactivity of the regular and defective CNTs are analyzed, and results are obtained confirming the good values of hydrogen physisorption energy. This chapter also discusses how the diameter and length of nanotubes, and the presence of nitrogen and the different types of defects (bumpy, haeckelite, Stone-Wales, and zipper) enhance the molecular and electronic properties of CNTs, particularly *armchair*-type, through molecular global descriptors based on the DFT methods.

2. Methods

Regular and defective nanotubes are built as finite, open, and terminated by hydrogen atoms by using the HyperTube script [17] embedded in Hyperchem [18]. Saturated nanotubes are full exo-hydrogenated. Nitrogen doping is performed by replacing two carbon atoms by nitrogen atoms at an hexagonal ring building a pyrimidine (with the two nitrogen atoms separated by a carbon atom in the way N1-C2-N3) taking care of locating an additional pyrimidine ring opposite to the first one at the same level in the tube. All the structures are fully optimized by the DFT methods at the B3LYP/6-31G(d) level of theory [19, 20] with Jaguar v9.2 [21]. No symmetry restrictions are applied. Energy minima are verified after the harmonic vibrational frequency real values that are obtained by calculations for optimized structures at the same level of theory. Dispersion forces are corrected by means of the DFT-D3 method [22, 23] validated through the DFT nonlocal method [24] as was performed before [25].

The formation energy, E_F, is calculated as follows:

$$E_F = E_{NT} - \sum_{i=1}^{n} n_i E_i \qquad (1)$$

where E_{NT} and E_i are the total energy for the nanotube structure (B3LYP/6-31G(d) full optimized) and for the i elements (for instance, C, H, N), respectively; n_i is the number of each element.

The hydrogen physisorption energy, E_{ph}, is calculated according to expression (2):

$$E_{ph} = E_{(NT+nH_2)} - E_{NT} - nE_{H_2} + vdW \qquad (2)$$

where $E_{(NT+nH_2)}$ and E_{NT} are the total energy for the B3LYP/6-31G(d) full optimized nanotube structure containing the encapsulated hydrogen molecules inside and for the nanotube alone;

E_{H_2} is the total energy for the hydrogen molecule; n is the number of encapsulated hydrogen molecules; and vdW corresponds to the van der Waals interaction correction term accounting for the dispersion forces calculated by DFT-D3 methods [22, 23] as implemented in Jaguar v9.2. Specialized research studies have found B3LYP-D3 as a very accurate method for treating intermolecular interactions [26].

The electronic chemical potential μ is defined [27] as the energy changes of the system with respect to the number of electrons N at a given external potential v(r) defined by the nuclei:

$$\mu = \left(\frac{\partial E}{\partial N}\right)_{v(r)} \tag{3}$$

After applying the finite difference approximation, the Koopmans theorem [28, 30] and the Kohn-Sham principle [29, 31], global reactivity descriptors are calculated according to Eqs. (4)–(7) for the electronic chemical potential, the chemical hardness η, the global electrophilicity index ω, and the softness S, based on conceptual DFT, respectively [27–34]:

$$\mu = (E_{LUMO} + E_{HOMO})/2 \tag{4}$$

$$\eta = (E_{LUMO} - E_{HOMO})/2 \tag{5}$$

$$\omega = \mu^2/2\eta \tag{6}$$

$$S = 1/\eta \tag{7}$$

where E_{LUMO} and E_{HOMO} are the B3LYP/6-31G(d) energies of the frontier orbitals: the lowest unoccupied molecular orbitals and the highest occupied molecular orbitals, respectively. The bandgap, BG, is calculated as the energy difference between the frontier molecular orbitals $E_{LUMO}-E_{HOMO}$.

3. Chirality effect

In this section, we analyze the reactivity of *armchair*, *chiral*, and *zigzag* nanotubes, regular and with bumpy defects, using theoretical DFT methods. We study the effects of both nitrogen doping and the total hydrogenation of nanotubes on the electronic properties.

3.1. Bandgap

The bandgap is the energy difference between the conduction band and the valence band. The smaller is the bandgap, the nanotube tends to have better conductive ability. The regular CNTs (defect free) formed only by six-membered ring units exhibit properties that depend on the ordering of the rings in the nanotube or chirality. Studies with the DFT methods at B3LYP/6-31G(d) for CNTs of similar diameters (between 6.3 and 6.8 Å) and eight carbon-atom layer (cl) of length revealed that the bandgap value decreases in the order: *armchair* (5,5) > *chiral* (6,3) > *zigzag* (8,0) with values 1.77, 1.35, and 0.42 eV, respectively [25]. Nitrogen-doped CNTs

(N-CNTs) in the three mentioned cases show a decrease in the bandgap in the order: *chiral*, *armchair*, and *zigzag* with bandgap values of 1.26, 1.16, and 0.0 eV, respectively. Doped and nondoped *zigzag* nanotubes exhibit the smallest bandgap [25].

CNTs with two bumpy defects and similar dimensions than the mentioned regular CNTs show the following order of bandgap: *armchair* > *zigzag* > *chiral* with values of 1.72, 0.43, and 0.31 eV, respectively. In the case of nitrogen-doped CNTs with bumpy defects, obtained bandgap values increase for *zigzag* and *chiral* nanotubes (0.83 and 0.86 eV, respectively), but decreases for *armchair* nanotubes (1.29 eV) (see 1a in **Table 1**). These results indicate that the bumpy defect decreases the bandgap in the doped and nondoped *chiral* nanotubes. In the *zigzag* and *armchair* nanotubes, the bumpy effect depends on the presence of nitrogen since in both nondoped cases, the presence of the bumpy defect does not affect too much, whereas in the cases of doped *zigzag* and *armchair* nanotubes, the presence of the bumpy defect increases the bandgap. *Armchair* nanotubes with five bumpy defects in their structure, doped and nondoped, decrease the bandgap to 1.17 eV (see 1e in **Table 1**).

The hydrogenation of nanotubes with bumpy defects increases the bandgap to levels between 6.12 and 6.57 eV for two bumpy defects and between 6.37 and 6.79 eV for five bumpy defects. This behavior is expected due to the sp^3 hybridization that makes the structures of the nanotubes similar to each other with a similar electron density distribution (see 2a and 2e in **Table 2**). In all cases, it can be observed that nitrogen decreases the bandgap with values between 5.46 and 5.83 eV.

In other words, in terms of conductive ability, our calculations reveal that both regular and bumpy nanotubes show the same trend: *zigzag* and *chiral* nanotubes have higher conductive

Entry	Reactivity descriptor	Armchair		Chiral		Zigzag	
		0 N	4 N	0 N	4 N	0 N	4 N
with two bumpy defects							
1a	BG	1.72	1.29	0.31	0.86	0.43	0.83
1b	μ	−3.67	−3.25	−3.67	−3.33	−3.49	−3.48
1c	η	0.86	0.64	0.16	0.43	0.21	0.41
1d	ω	7.82	8.19	43.22	12.83	28.52	14.66
with five bumpy defects							
1e	BG	1.17	1.17				
1f	μ	−3.65	−3.64				
1g	η	0.59	0.58				
1h	ω	11.35	11.32				

Table 1. B3LYP/6-31G(d) bandgap ($E_{LUMO}-E_{HOMO}$), BG, electronic chemical potential, μ, chemical hardness, η, and global electrophilicity, ω, in eV, for a series of 32 nitrogen-doped and nondoped *armchair* (5,5), *chiral* (6,3), and *zigzag* (8,0) bumpy nanotubes, with two and five bumpy defects, all of them having a similar diameter (6.3–6.7 Å) and 8 cl of length.

Entry	Reactivity descriptor	Armchair		Chiral		Zigzag	
		0 N	4 N	0 N	4 N	0 N	4 N
with two bumpy defects							
2a	BG	6.29	5.56	6.12	5.62	6.57	5.46
2b	μ	−2.71	−2.10	−2.71	−2.21	−2.71	−1.82
2c	η	3.14	2.78	3.06	2.81	3.28	2.73
2d	ω	1.17	0.79	1.20	0.87	1.12	0.61
with five bumpy defects							
2e	BG	6.53	5.83	6.37	5.79	6.79	5.48
2f	μ	−2.73	−2.28	−2.75	−2.32	−2.88	−2.04
2g	η	3.27	2.92	3.19	2.90	3.39	2.74
2h	ω	1.14	0.89	1.18	0.93	1.22	0.76

Table 2. B3LYP/6-31G(d) bandgap ($E_{LUMO}-E_{HOMO}$) BG, electronic chemical potential μ, chemical hardness η, and global electrophilicity index ω, in eV, for a series of *hydrogenated* nitrogen-doped and nondoped *armchair* (5,5), *chiral* (6,3), and *zigzag* (8,0) nanotubes, with two and five bumpy defects, all of them having a similar diameter (6.3–6.7 Å) and 8 cl of length.

abilities than *armchair* nanotubes. The incorporation of bumpy defects in nanotubes only increases the conductive ability of *chiral* nanotubes (doped or nondoped). Nitrogen doping increases the conductive ability of the three types of regular nanotubes and that of the *armchair* nanotubes with two bumpy defects.

3.2. Chemical potential

The chemical potential μ, is the inverse of electronegativity. It measures the tendency of electrons to escape from an equilibrium system. At higher value of the chemical potential, the molecule behaves as a better electron-donor against an acceptor. In a study of diene and dienophile reactivity in Diels-Alder reactions in the context of conceptual DFT at the B3LYP/ 6-31G(d) level, a compound with μ = −1.85 eV was characterized as electron-donor while another compound with μ = −7.04 eV was considered as electron-acceptor [34].

The values of μ for the regular *armchair*, *chiral*, and *zigzag* nanotubes determined at the same level of theory fluctuate between −3.57 and −3.06 eV. The values of μ for the corresponding nitrogen-doped and nondoped nanotubes with two bumpy defects decrease to −3.67 and −3.25 eV, respectively (the only exception is exhibited by nondoped *zigzag* nanotubes with a μ value of −3.49 eV) and also decrease for *armchair* nanotubes with five defects (see 1b and 1f in **Table 1**). Nitrogen doping slightly increases the value of μ. That means, there is not a very marked difference of chemical potential for nanotubes of different chirality, with or without bumpy defects, doped or nondoped defects. The values of μ are intermediates between the electron-donors and the electron acceptors leaving open the potentiality to behave as electron-donors or electron acceptors.

In the saturated nondoped nanotubes, μ increases to values of −2.88 to −2.71 eV and in the presence of nitrogen doping, μ increases to −1.82 eV being the *zigzag* nanotubes the ones with the greater value of μ (see 2b and 2f in **Table 2**) and likely with a higher ability to be oxidized. Therefore, *zigzag* saturated nitrogen-doped nanotubes could potentially behave as a catalyst in C-H activation reactions [12].

3.3. Hardness

The hardness, η, is a useful reactivity descriptor associated to the resistance of a molecule to exchange electronic density with the environment [27, 34]. It measures the stability of a system. The increase of η is normally associated with a stabilizing process having a negative change of energy.

In the regular nanotubes, η increases in the order: *zigzag* (8,0) > *chiral* (6,3) > *armchair* (5,5), with η values of 0.21, 0.68, and 0.89 eV, respectively, determined at B3LYP/6-31G(d) [25]. When regular *zigzag*, *chiral*, and *armchair* nanotubes are nitrogen-doped, η decreases to values of 0.20, 0.63, and 0.58 eV, respectively [25].

Defective nanotubes exhibit a decrease in η values. The only exception is for doped *zigzag* nanotubes. *Armchair* nanotubes with two bumpy defects reveal the highest values of η (0.64 and 0.86 eV for nitrogen-doped and nondoped nanotubes, respectively) compared to *chiral* and *zigzag* nanotubes with η values between 0.16 and 0.43 eV including nitrogen-doped and nondoped systems. Nitrogen doping increases η in *chiral* and *zigzag* nanotubes, but decreases it in *armchair* nanotubes with two defects. In the *armchair* nanotubes with five defects, η decreases also (0.59 eV) unaffected by the presence of nitrogen doping (see 1c and 1g in **Table 1**). That is, η depends on the chirality. Regular *zigzag* nanotubes are the most reactive. Bumpy defects increase the reactivity of nanotubes (with the exception of doped *zigzag* and *armchair* nanotubes). Nitrogen doping also increases the reactivity of regular nanotubes especially the *armchair* nanotubes and also increases the reactivity of *armchair* nanotubes with bumpy defects. The increase in the number of bumpy defects increases the reactivity of the *armchair* nanotubes.

The saturated nanotubes with two bumpy defects do not show large η differences with chirality (3.06–3.28 eV) nor is it affected too much in nanotubes with five bumpy defects (3.19–3.39 eV). In all cases, nitrogen doping makes η decrease (2.73–2.92 eV) (see 2c and 2 g in **Table 2**) and consequently, increases nanotube reactivity.

3.4. Electrophilicity index

The electrophilicity index ω, as a descriptor of molecular reactivity, gives a measure of the stabilizing energy of a molecule when it acquires some additional amount of electron density from the environment. The value of ω allows to differentiating the power of the molecules that act as electrophiles. Thus, for organic compounds, strong electrophiles are considered to have ω > 1.5 eV and weak electrophiles have ω < 0.8 eV [35]. According to this classification, the CNTs are strong electrophiles since they exhibit ω values that are much higher than 1.5 eV. Also, a higher value of ω may be associated with a greater trend of the compound to be reduced due to its ability to acquire electronic density.

The values of ω for the regular nanotubes were reported to be dependent on chirality and grow in the order: *armchair* (5,5) < *chiral* (6,3) < *zigzag* (8,0), with values of ω of 6.56, 9.42, and 28.43 eV, respectively. Nitrogen doping slightly decreases the ω value in the *armchair* (6.42 eV) and *chiral* (8.46 eV) nanotubes while increases the ω value in *zigzag* nanotubes (30.07 eV) [25]. The bumpy defects increase the value of ω especially in *chiral* nanotubes (43.22 eV). The *armchair* nanotubes with two bumpy defects are the ones with the lowest value of ω (7.82 eV), which rises in nanotubes with five bumpy defects (11.35 eV). Nitrogen-doped nanotubes exhibit lower ω values with the only exception of *armchair* nanotubes with two bumpy defects (8.19 eV) (see 1d and 1h in **Table 1**).

The saturated nanotubes with two and five bumpy defects, independent of the chirality, decrease the values of ω (1.12–1.22 eV). For the nitrogen-doped nanotubes, the value of ω is even lower (0.61–0.93) with values in the range of the weak electrophiles (see 2d and 2h in **Table 2**).

Detailed analysis of the results obtained for this group of regular and bumpy defective nanotubes (with 8 cl of length) reveals that the *zigzag* nanotubes are those that exhibit greater conductive ability. Also the *zigzag* nanotubes are the most reactive and exhibit a great capacity to be reduced, to acquire electronic density, or to be strong electrophiles. The *armchair* nanotubes are at the other end. The presence of nitrogen in *armchair* regular nanotubes increases their conductive ability. The presence of bumpy defects also enhances their reactivity and their ability to be reduced, especially with five bumpy defects. Bumpy defects, in general, increase the conductivity, the reactivity, and the capacity of nanotubes to be reduced, with greater intensity in the *chiral* nanotubes.

The 8 cl saturated nanotubes, regular and with bumpy defects, exhibit a significant decrease in conductive ability counteracted by the presence of nitrogen. Our calculations reveal that they are less reactive and their ability to acquire electronic density or to behave as electron acceptors decreases when compared to unsaturated nanotubes with a quite good consistence within the different reactivity descriptors.

4. Hydrogen adsorption for the carbon nanotubes with defects

Inspired by the unique properties of nanotubes and driven by the idea of contributing to a clean energy source for vehicular use, several authors have studied the possibility of using CNTs as hydrogen transporters [36–40]. Hydrogen may be chemisorbed (covalently attached to carbon atoms) or physisorbed (adsorbed as molecular hydrogen through noncovalent interactions with the nanotube). The results have generated controversy since they have not been reproducible [41, 42]. A reasonable explanation is probably due to the presence of uncontrolled defects in the nanotube that make vary the curvature of the nanotube, the electronic density distribution, and therefore its properties [43]. For example, (7,5,5,7) SW defects increase the ability to adsorb H_2 of the *armchair* (5,5), whereas (5,7,7,5) SW defects decrease the ability to adsorb H_2 of these nanotubes as was established using the DFT methods at the B3LYP/LanL2DZ level [44]. Additionally, the number of defects in the nanotube affects the reactivity [44]. Other

DFT studies for *armchair* (10,10) nanotubes show that SW defects with five- and eight-membered rings have a greater ability to adsorb H_2 than SW defects with five- and seven-membered rings [43], which is also valid for nanotubes of different chirality [43, 45].

SW defects have also been studied in relation to metal-decorated nanotubes and their effects on hydrogen adsorption [46, 47] and also in the study of the interactions with metallic particles and ions [48]. The results obtained for *armchair* (6,6) nanotubes with SW defects at the B3LYP/6-31G(d) level focus on the charge transfer to ions and their relation to the electromigration where the SW defects facilitate the migration of positively charged ions (In^+ and In^{3+}) through the nanotube [48].

In relation to hydrogen storage as a potential source of clean energy, one requirement is to achieve that at least 5.5 wt% of hydrogen [49] can be released under ambient pressure and temperature conditions. For achieving that goal and to favor a reversible H_2 adsorption-desorption process, it is required that the interaction energy CNT-H_2 be of the order of 0.1–0.5 eV/H_2, according to calculations of first principles and to thermodynamic considerations [14, 39, 50, 51].

Hydrogen chemisorption energy is a chirality-dependent exothermic property. *Zigzag* nitrogen-doped and nondoped nanotubes reveal as the most exothermic followed by the *chiral* and *armchair* nanotubes [25]. On the contrary, hydrogen physisorption energies, E_{ph}, exhibit endothermic values. E_{ph} values for saturated, nitrogen-doped *armchair* CNTs obtained by the DFT [B3LYP/6-31G(d)] methods are within the ideal mentioned range (0.26 eV/H_2 for 12 H_2 physisorbed into a (4,4) nanotube) and grow for *chiral* and *zigzag* nitrogen-doped nanotubes [25] in excellent agreement with results obtained for *armchair*, *chiral*, and *zigzag* CNTs by means of the DFT methods that use the local density approximation [37]. In addition to the chirality, the diameter and length of the nanotube affect the nanotube-H_2 interactions. The diameter changes cause the variation in the nanotube curvature affecting the arrangement of the molecular orbitals [4], and the nanotube length variation affects the diffusivity as was determined for drug adsorption [52]. E_{ph} values decrease for nanotubes with a smaller diameter and a larger length (higher number of carbon-atom layers) but increase with the number of adsorbed H_2.

Bumpy defects and nitrogen doping favor interaction with nanotube-H_2. Saturated *armchair* (4,4) nitrogen-doped nanotubes with bumpy defects and 20 cl of length can encapsulate 15 H_2 molecules ($C_{164}N_4H_{210}$ stoichiometry) with a favorable E_{ph} of 0.11 eV/H_2 obtained at the B3LYP/6-31G(d) level [13]. Our calculations, considering dispersion forces correction, reveal that saturated nondoped *armchair* (5,5) nanotubes with bumpy defects and 16 cl of length can encapsulate 44 H_2 molecules (stoichiometry $C_{170}H_{278}$) with a good E_{ph} value of 0.32 eV/H_2. **Figure 3** shows the optimized structure of this system having a hydrogen content of 12 wt%.

The actual available experimental and theoretical information related to hydrogen adsorption in nanotubes indicates that the structural effects that allow obtaining hydrogen physisorption energies within the range considered ideal for the reversible storage of hydrogen (0.1–0.4 eV/H_2 under environmental conditions) are those that favor the nanotube-H_2 electrostatic interactions. Parameters such as the chirality of the nanotube, a suitable diameter and length, and the
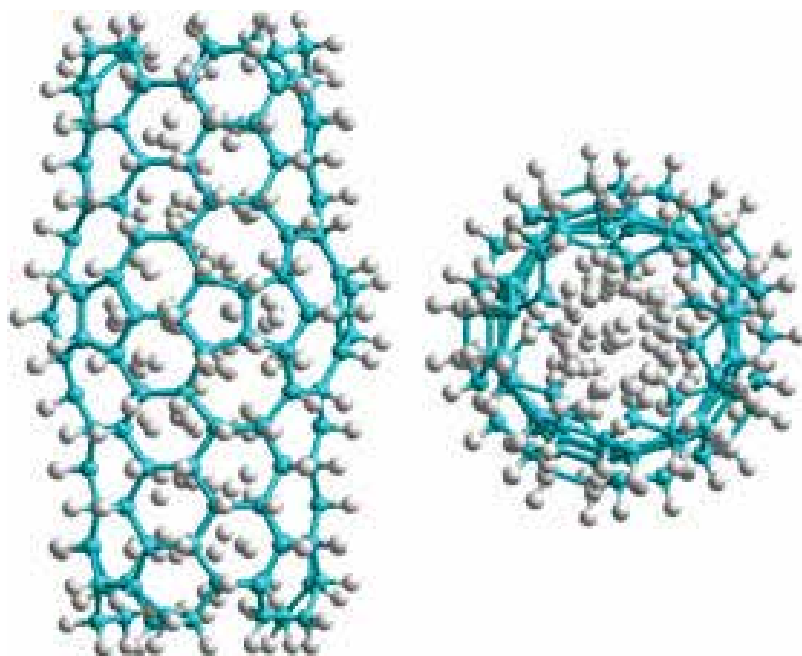
Figure 3. B3LYP/6-31G(d) fully optimized structure of an hydrogenated *armchair* (5,5) bumpy, nondoped nanotube, with 16 cl of length having adsorbed 44 hydrogen molecules (stoichiometry $C_{170}H_{278}$; Eph = 0.32 eV/H_2). Front and lateral views.

presence of defects that generate suitable spaces, as explained above, can be predicted through DFT calculations. However, the use of conceptual DFT reactivity descriptors (μ, η, ω, and S) to correlate or predict hydrogen physisorption energies in nanotubes is not viewed as adequate. Their use is related and manifests mainly in molecular interactions in which there is charge transfer wherein nucleophiles, electrophiles, or species that change their oxidation state take part. A correlation of these descriptors with the hydrogen adsorption efficiency in nanotubes, at this time, could only have limited validity and provided it is used in conjunction with other descriptors such as diameter, length, number of defects, or others to be set.

5. Armchair nanotubes

Nitrogen-doped *armchair* nanotubes are expected to be good catalysts for oxygen reduction reactions compared to their *chiral* and *zigzag* nanotubes because of their particular distribution of electric charge [12, 25]. In this section, we analyze the effect of different types of defects in the reactivity of *armchair* structures by using global descriptors based on the DFT methods. Bumpy, haeckelite, Stone-Wales, and zipper defects are considered (see **Figure 4**). We also analyze the effects of nitrogen doping, the diameter and length of the nanotubes, the number of defects and the charges on the carbon atom adjacent to the two pyrimidine nitrogen atoms.
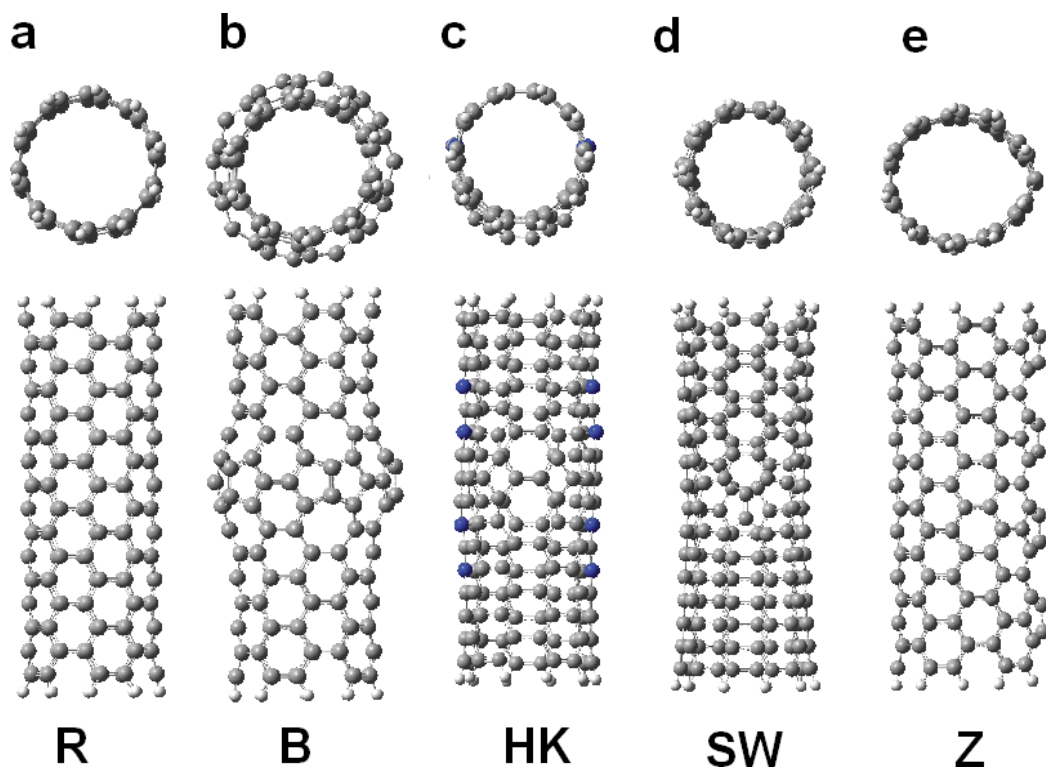
Figure 4. B3LYP/6-31G(d) fully optimized *armchair* (5,5) nanotube structures. Front and lateral views showing (a) regular R; (b) bumpy B, with five defects; (c) haeckelite HK, with one defect doped with eight nitrogen atoms; (d) Stone-Wales SW, with one defect; and (e) zipper Z, with four defects, nanotubes with 16 cl of length each.

5.1. Formation energies

Nitrogen-doped *armchair* nanotubes in all cases show higher values of E_F than nondoped nanotubes, indicating a greater reactivity. The E_F values are calculated according to Eq. (1). A lower value of E_F indicates greater stability. Bumpy nanotubes are the most reactive. Reactivity also increases as the number of defects in the nanotube increases as shown in **Table 3** for 16 cl *armchair* nanotubes (see 3b and 3c). The corresponding stoichiometry is also shown in **Table 3**. Regular nanotubes with smaller diameter are more reactive than those with larger diameter and exhibit E_F values of -0.72 and -1.26 eV, respectively. Defective nanotubes reveal the same trend. For instance, the *armchair* (5,5) and (6,6) nanotubes, both with one bumpy defect exhibit E_F values of -0.67 and -1.18 eV, respectively. The same trend is shown for the *armchair* (5,5) and (6,6) nanotubes with one SW defect (see 3d and 3h in **Table 3**).

5.2. Bandgap and chemical potential

Three groups of *armchair* nanotubes were studied: (1) (5,5) with 16 cl of length (see **Table 4**); (2) (6,6) with 16 cl of length (see **Figure 5**); and (3) (5,5) with 20 cl of length (see **Figure 6**) with bandgap values between 0.54 and 1.27 eV.

Entry	Type	E_F		Stoichiometry	
		0 N	4 N	0 N	4 N
3a	(5,5)-R-16 cl	−0.72	−0.51	C160H20	C156N4H20
3b	(5,5)-B-1D-16 cl	−0.67	−0.45	C162H20	C158N4H20
3c	(5,5)-B-5D-16 cl	−0.31	−0.13	C170H20	C166N4H20
3d	(5,5)-SW-1D-16 cl	−0.59	−0.38	C160H20	C156N4H20
3e	(5,5)-Z-16 cl	−0.57	−0.39	C168H20	C164 N4H20
3f	(6,6)-R-16 cl	−1.26	−1.03	C192H24	C188N4H24
3g	(6,6)-B-1D-16 cl	−1.18	−0.95	C194H24	C190 N4H24
3h	(6,6)-SW-1D-16 cl	−1.14	−0.92	C192H24	C188N4H24

Table 3. B3LYP/6-31G(d) formation energy E_F, in eV, and stoichiometry, for some nitrogen-doped and nondoped *armchair* (5,5) and (6,6) regular, bumpy (with one and five defects), Stone-Wales (with one defect), and zipper nanotubes, all of them having 16 cl of length.

Entry	Type	BG	μ	η	ω	S
4a	R-0N	1.13	−3.57	0.56	11.32	0.89
4b	R-4N	0.85	−3.31	0.42	12.92	1.18
4c	B-1D-0N	1.15	−3.62	0.57	11.39	0.87
4d	B-1D-4N	0.76	−3.28	0.38	14.18	1.32
4e	B-5D-0N	0.89	−3.72	0.45	15.52	1.12
4f	B-5D-4N	0.67	−3.45	0.34	17.71	1.49
4g	SW-1D-0N	0.49	−3.54	0.24	25.78	2.06
4h	SW-1D-4N	0.83	−3.20	0.41	12.43	1.21
4i	Z-0N	1.05	−3.97	0.53	15.00	0.95
4j	Z-4N	0.82	−3.72	0.41	16.86	1.22

Table 4. B3LYP/6-31G(d) bandgap (E_{LUMO}-E_{HOMO}) BG, electronic chemical potential μ, chemical hardness η, and global electrophilicity index ω, in eV, and softness S, in 1/eV, for a series of nitrogen-doped and nondoped *armchair* (5,5) regular, bumpy, Stone-Wales, and zipper nanotubes, all of them having 16 cl of length.

Nitrogen doping increases the CNTs conductive ability both in the regular and defective structures, revealing smaller bandgap values for the nitrogen-doped nanotubes than for the nondoped ones. Defects also increase the conductive ability of *armchair* nanotubes. In the nitrogen-doped (5,5) nanotubes, with 16 cl and 20 cl of length, the zipper nanotubes exhibit the best conductive properties (see 4j in **Table 4** and **Figure 6**) with bandgap values of 0.82 and 0.57 eV, respectively. This behavior of the zipper nanotubes was also observed in doped nanotubes of 8 cl as indicated above with a bandgap value of 0.83 eV (see 1a in **Table 1**). As can be appreciated from the obtained values, increasing the length of the nanotubes increases the nanotube conductive ability.

Figure 5. B3LYP/6-31G(d) values of (a) bandgap ($E_{LUMO}-E_{HOMO}$); (b) electronic chemical potential; (c) chemical hardness; and (d) global electrophilicity index, for nitrogen-doped and nondoped *armchair* (6,6) regular nanotubes, and *armchair* (6,6) defective nanotubes containing one bumpy defect and one Stone-Wales defect, all of them having 16 cl of length.

Chemical potential of the studied nanotubes presents small variations, with values ranging from −3.20 to −3.97 eV. Nitrogen doping, slightly increases the chemical potential of regular and defective *armchair* nanotubes, for the three groups of *armchair* nanotubes, thereby increasing the electron-donor ability of the doped nanotubes, which is consistent with the nitrogen atom electronic characteristics.

5.3. Hardness and softness

The presence of defects decreases the hardness of the (5,5) nanotubes making them more reactive. Nitrogen doping also decreases the hardness of the (5,5) and (6,6) nanotubes of 16 cl,
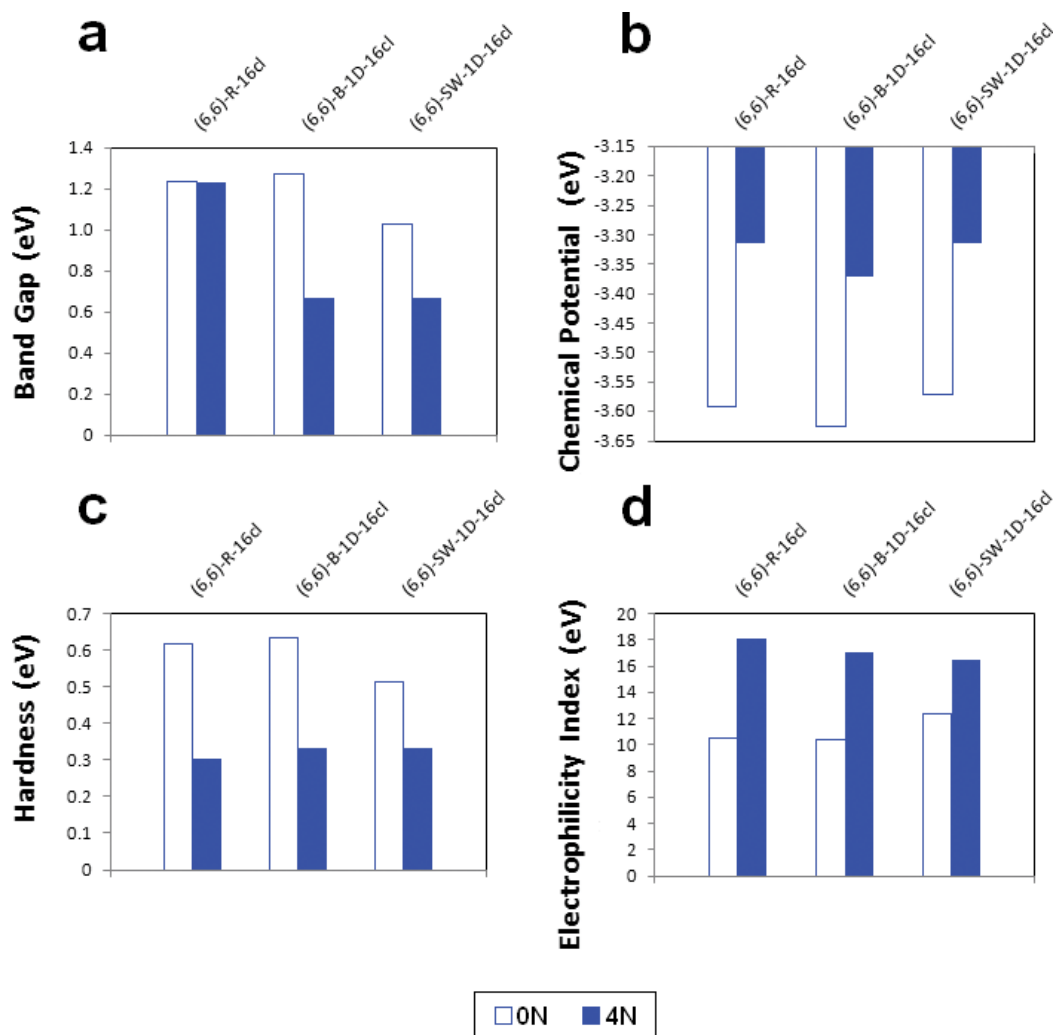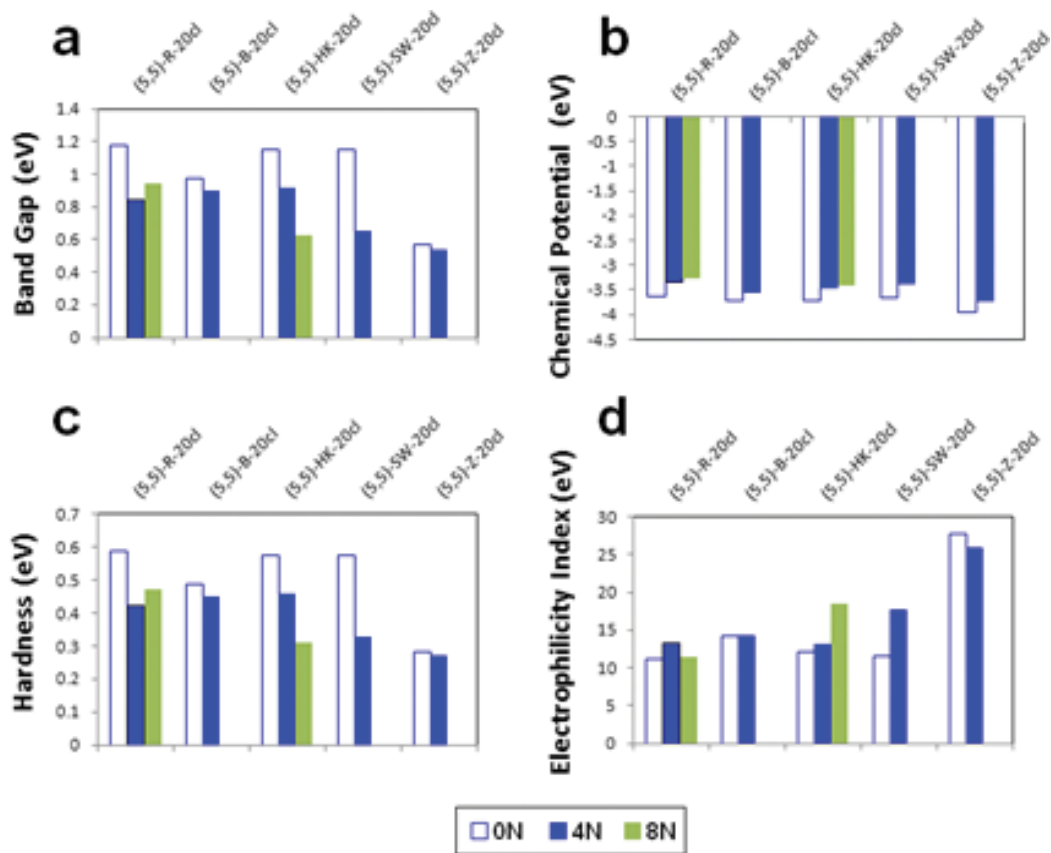
Figure 6. B3LYP/6-31G(d) values of (a) bandgap ($E_{LUMO} - E_{HOMO}$); (b) electronic chemical potential; (c) chemical hardness; and (d) global electrophilicity index, for some nitrogen-doped and nondoped *armchair* (5,5) regular, bumpy, haeckelite, Stone-Wales, and zipper nanotubes, all of them having 20 cl of length.

with the exception of (5,5) nanotubes with one SW defect (see 4h vs. 4g in **Table 4**). For the (5,5) nanotubes of 20 cl, the same previous trends are maintained without exceptions (see **Figure 6**). Nitrogen-doped zipper-defected (5,5) nanotubes of 20 cl are predicted to be the most reactive with a hardness of 0.28 eV. They are more reactive than nitrogen-doped zipper-defected (5,5) nanotubes of 16 cl with a value of hardness of 0.41 eV (see 4j in **Table 4**). The effect of nitrogen doping, the defects, and the length of the nanotube on the nanotube hardness are consistent with the effect of these same structural parameters on the bandgap. The *armchair* nanotubes with zipper defects are perceived as the most reactive nanotubes and the ones having the best conductive ability enhanced by nitrogen doping and longer nanotubes.

Softness, S, is the reciprocal of hardness. A larger value of softness indicates greater ability to hold a charge once acquired by the nanotube. For *armchair* (5,5) nanotubes of 16 cl, the softness varies between 0.87 and 2.06 eV and grows with the defects and with the number of defects. Nitrogen-doped nanotubes have a value of S greater than nondoped nanotubes. The only exception is for nanotubes with one SW defect (see **Table 4**).
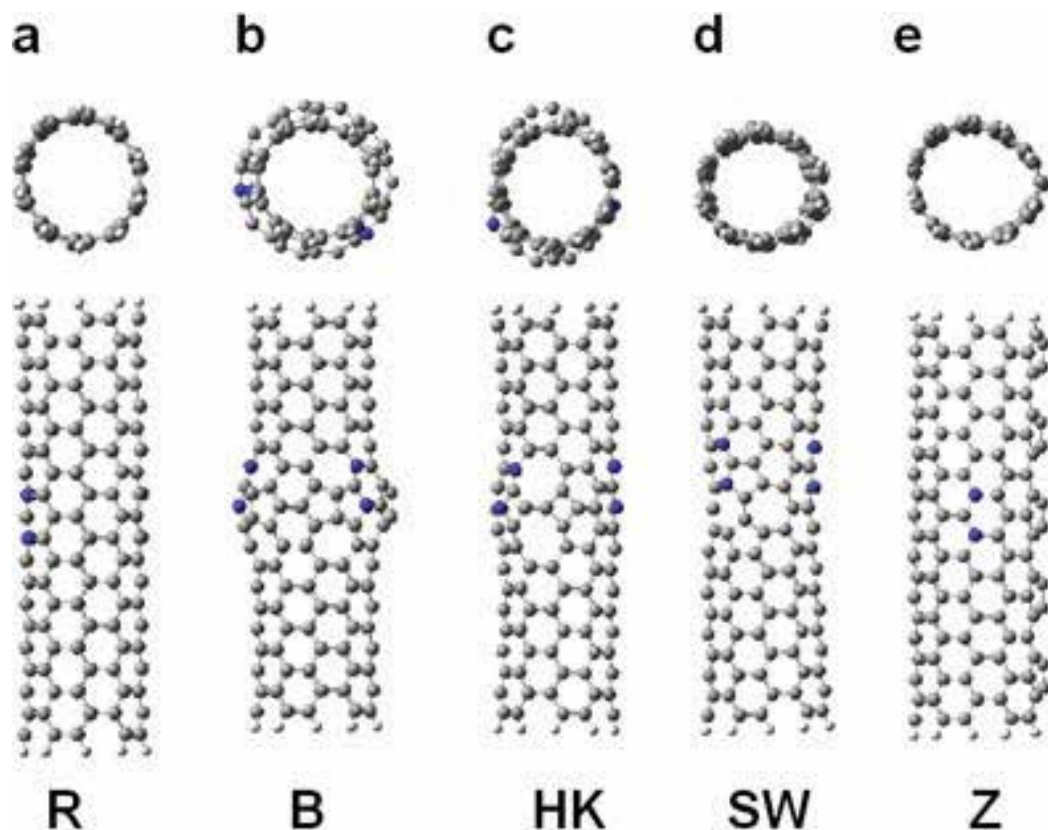
Figure 7. B3LYP/6-31G(d) fully optimized structures of nitrogen-doped *armchair* nanotubes. Front and lateral views showing (a) regular, R; (b) bumpy B, with five defects; (c) haeckelite HK, with two defects; (d) Stone-Wales SW, with two defects; and (e) zipper Z, with five defects, nanotubes with 20 cl of length each.

5.4. Electrophilicity index

The *armchair* (5,5) nanotubes of 16 cl exhibit an ω value of 11.32 eV. The presence of defects in these nanotubes increases the value of ω. The highest value of ω corresponds to the nanotubes with a SW defect (25.78 eV). Nitrogen doping also increases the ω value for regular and defective (5,5) and (6,6) nanotubes except for nanotubes with one SW defect (see **Table 4** and **Figure 5**). The (5,5) nanotubes of 20 cl show the same trend regarding the presence of defects and the nitrogen doping, being highlighted the nanotubes with zipper defects that show the highest values of ω of 27.72 and 25.94 eV for the nondoped and doped nanotubes, respectively (see **Figures 6** and **7**). These high ω values show the great tendency of these nanotubes to acquire electronic density and their high ability to be reduced compared to the other studied nanotubes. This property of *armchair* nanotubes with zipper defects, coupled with their high reactivity and good conductive ability, opens a range of possibilities as advanced materials in the field of electronics or other fields where good electrophiles or catalysts are required in redox reactions.

5.5. Charges

A possible explanation for the reactivity of *armchair* nanotubes with zipper defects may be the charge that develops at the C2 carbon atom that is adjacent to both pyrimidine nitrogen atoms. It has been found to be a feature that allows nitrogen-doped CNTs to behave as good catalysts [11, 12]. Our calculations reveal that the C2 carbon atom Mulliken charge on the nitrogen-doped *armchair* nanotubes with zipper defects reaches a high value of 0.26 e, compared with 0.01 e for the corresponding nondoped nanotubes. In *armchair* nanotubes with bumpy defects, this charge has a value of 0.14 e.

Our results, obtained using the DFT methods, contribute with a ranking of molecular structures of carbon nanotubes according to: (1) their conductive properties, (2) their hydrogen adsorption properties, and (3) their reactivity to charge transfer reactions and redox reactions. We believe that these results will help in the selection of different nanotube structures to be used in a variety of applications that consider materials such as: (1) new polymer composites having conductive properties (biodevices technology); (2) electronic devices (an electronic tongue); (3) energy storage devices; (4) suitable surface functionalized nanotubes for environmental remediation; (5) organic semiconductor-carbon nanotubes composites for separation technology (water purification); (6) catalyst for oxygen reduction reactions; (7) drug delivery systems, imaging and photothermal therapy (biomedicine); and others where tailoring of particular nanotube molecular properties is required.

6. Conclusions

We have performed a systematic study of the reactivity of carbon nanotubes based on various structural parameters by using molecular descriptors obtained by the DFT methods at the B3LYP/6-31G(d) level. Our results confirm that the reactivity of nanotubes depends on their structure. The chirality, the diameter, and the presence of structural, topological, and doping defects significantly modify the reactivity of the nanotubes. The *zigzag* nanotubes, both the regular (defect free) and those with bumpy defects, reveal greater reactivity, better conductive ability, and better behavior as good electrophiles when compared with corresponding *armchair* and *chiral* nanotubes suggesting a high ability to be reduced. Within the *armchair* nanotubes, we highlight those with zipper defects over those with bumpy, haeckelite, and Stone-Wales defects. The *armchair* nanotubes with zipper defects are revealed to be more reactive, with high conductive capacity, good ability to acquire electronic density and to behave as good electrophiles, and potential good catalysts in redox reactions. Nitrogen doping reveals as an important parameter that increases the conductive ability and reactivity of *armchair* nanotubes of different diameter and length. Saturated nanotubes behave as less reactive than unsaturated nanotubes. Saturated *armchair* nanotubes with bumpy defects exhibit favorable values of the hydrogen physisorption energy suggesting a reversible hydrogen adsorption-desorption process at ambient conditions.

These results are valuable to increase the understanding about carbon nanotubes activity and to contribute to the future design of novel useful materials.

To expand the range of applications of carbon nanotubes, an interesting future contribution would be to construct a nanotube-scale of reactivity, based on the values of some reactivity descriptors and their relation with experimental values for some known reactions. The aim of predicting the reactivity of different structures of nanotubes or to be able to designing nanostructures that possess a desired property to obtain advanced materials in a rational way is open.

Acknowledgements

Author details

María Leonor Contreras Fuentes* and Roberto Rozas Soto

*Address all correspondence to: leonor.contreras@usach.cl

Computational Chemistry and Intellectual Property Laboratory, Department of Environmental Sciences, Faculty of Chemistry and Biology, University of Santiago de Chile, USACH, Santiago, Chile

References

[1] Smithells RW, Newman CGH. Recognition of thalidomide defects. Journal of Medical Genetics. 1992;**29**:716-723. Available from: http://www.thalidomide.ca/recognition-of-thalidomide-defects/ [Accessed: 19-07-2017]

[2] Dekker C. Carbon nanotubes as molecular quantum wires. Physics Today. 1999;**52**(5): 22-28. DOI: 0.1063/1.882658

[3] Pastorin G. Crucial functionalizations of carbon nanotubes for improved drug delivery: A valuable option? Pharmaceutical Research. 2009;**26**(4):746-769. DOI: 10.1007/s11095-008-9811-0

[4] Lu X, Chen Z. Curved pi-conjugation, aromaticity, and the related chemistry of small fullerenes (C_{60}) and single-walled carbon nanotubes. Chemical Reviews. 2005;**105**(10): 3643-3696. DOI: 10.1021/cr030093d

[5] Das D, Rahaman H. Carbon Nanotube and Graphene Nanoribbon Interconnects. New York: CRC Press Taylor & Francis Group; 2015. 196 p 9781138822313

[6] Tour JM, Dyke CA, Flatt AK. Bulk separation of carbon nanotubes by bandgap. 2011. US Patent Nr 7,939,047

[7] Howe WR, Hunt JH, Li AW. Nanotube signal transmission system. 2015. US Patent Nr 9,086,523

[8] Huang Y, Fan CQ, Dong H, Wang SM, Yang XC, Yang SM. Current applications and future prospects of nanomaterials in tumor therapy. International Journal of Nanomedicine. 2017;**12**:1815-1825. DOI: 10.2147/IJN.S127349

[9] Yu J, Zhou W, Xiong T, Wang A, Chen S, Chu B. Enhanced electrocatalytic activity of Co@N-doped carbon nanotubes by ultrasmall defect-rich TiO_2 nanoparticles for hydrogen evolution reaction. Nano Research. 2017;**10**(8):2599-2609. DOI: 10.1007/s12274-017-1462-1

[10] Terrones M. Synthesis toxicity and applications of doped carbon nanotubes. Acta Microscópica. 2007;**16**(1–2):33-34. Available from: https://www.ciasem.com/PSD/Cusco2007/images-1/Terrones.pdf [Accessed: 26-07-2017]

[11] Gong KP, ZH D, Xia ZH, Durstock M, Dai LM. Nitrogen-doped carbon nanotube arrays with high electrocatalytic activity for oxygen reduction. Science. 2009;**323**:760-764. DOI: 10.1126/science.1168049

[12] Hu X, Zhou Z, Lin Q, Wu Y, Zhang Z. High reactivity of metal-free nitrogen-doped carbon nanotube for the C—H activation. Chemical Physics Letters. 2011;**503**:287-291. DOI: 10.1016/j.cplett.2011.01.045

[13] Contreras ML, Villarroel I, Rozas R. Hydrogen physisorption energies for bumpy, saturated, nitrogen-doped single-walled carbon nanotubes. Structural Chemistry. 2016;**27**(5): 1479-1490. DOI: 10.1007/s11224-016-0767-0

[14] Singh AK, Yakobson BI. First principles calculations of H-storage in sorption materials. Journal of Materials Science. 2012;**47**:7356-7366. DOI: 10.1007/s10853-012-6551-7

[15] Brozena AH, Leeds JD, Zhang Y, Fourkas JT, Wang Y. Controlled defects in semiconducting carbon nanotubes promote efficient generation and luminescence of trions. ACS Nano. 2014;**8**(5):4239-4247. DOI: 10.1021/nn500894p

[16] Zhu J, Childress AS, Karakaya M, Dandeliya S, Srivastava A, Lin Y, Rao AM, Podila R. Defect-engineered graphene for high-energy- and high-power-density supercapacitor devices. Advanced Materials. 2016;**28**(33):7185-7192. DOI: 10.1002/adma.201602028

[17] Contreras ML, Avila D, Alvarez J, Rozas R. Computational algorithms for fast-building 3D carbon nanotube models with defects. Journal of Molecular Graphics and Modelling. 2012;**38**:389-395. DOI: 10.1016/j.jmgm.2012.05.001

[18] Hypercube Inc. HyperChem Release 7.5. Gainesville; 2003

[19] Becke AD. Density-functional thermochemistry. The role of exact exchange. The Journal of Chemical Physics. 1993;**98**:5648-5652. DOI: 10.1063/1.464913

[20] Lee C, Yang W, Parr RG. Development of the Colle-Salvetti correlation-energy formula into a functional of the electron density. Physical Review B. 1988;**37**:785-789. DOI: 10.1103/PhysRevB.37.785

[21] Schrôdinger LLC. Jaguar version 9.2. New York; 2013

[22] Grimme S, Antony J, Ehrlich S, Krieg H. A consistent and accurate ab initio parametriza-tion of density functional dispersion correction (DFT-D) for the 94 elements H-Pu. The Journal of Chemical Physics. 2010;**132**(15):154104. DOI: 10.1063/1.3382344

[23] Hujo W, Grimme S. Performance of the van der Waals density functional VV10 and (hybrid)GGA variants for thermochemistry and noncovalent interactions. Journal of Chemical Theory and Computation. 2011;**7**(12):3866-3871. DOI: 10.1021/ct200644w

[24] Vydrov OA, Van Voorhis TJ. Nonlocal van der Waals density functional: The simpler the better. The Journal of Chemical Physics. 2010;**133**:244103. DOI: 10.1063/1.3521275

[25] Contreras ML, Cortés-Arriagada D, Villarroel I, Alvarez J, Rozas R. Evaluating the hydrogen chemisorption and physisorption energies for nitrogen-containing single-walled carbon nanotubes with different chiralities: A density functional theory study. Structural Chemistry. 2014;**25**(4):1045-1056. DOI: 10.1007/s11224-013-0377-z

[26] DiLabio GA, Koleini M, Torres E. Extension of the B3LYP–dispersion-correcting potential approach to the accurate treatment of both inter- and intra-molecular interactions. Theo-retical Chemistry Accounts. 2013;**132**:1389. DOI: 10.1007/s00214-013-1389-x

[27] Parr RG, Pearson RG. Absolute hardness: Companion parameter to absolute electronegativ-ity. Journal of the American Chemical Society. 1983;**105**:7512-7516. DOI: 10.1021/ja00364a005

[28] Koopmans T. Über die zuordnung von wellenfunktionen und eigenwerten zu den einzelnen elektronen eines atoms. Physica. 1934;**1**:104-113. DOI: 10.1016/S0031-8914(34)90011-2

[29] Kohn W, Sham LJ. Self-consistent equations including exchange and correlation effects. Physical Review B. 1965;**140**:A1133-A1138. DOI: 10.1103/PhysRev.140.A1133

[30] Parr RG, Yang W. Density-functional theory of the electronic structure of molecules. Annual Review of Physical Chemistry. 1995;**46**:701-728. DOI: 10.1146/annurev.pc.46.100195.003413

[31] Parr RG, von Szentpaly L, Liu S. Electrophilicity index. Journal of the American Chemical Society 1999;**121**:1922-1924. DOI: 10.1021/ja983494x

[32] Toro-Labbé A. Characterization of chemical reactions from the profiles of energy, chemical potential, and hardness. The Journal of Chemical Physics A. 1999;**103**(22):4398-4403. DOI: 10.1021/jp984187g

[33] Gómez-Jeria JS. A new set of local reactivity indices within the Hartree-Fock-Roothaan and density functional theory frameworks. Canadian Chemical Transactions. 2013;**1**:25-55. DOI: 10.13179/canchemtrans.2013.01.01.0013

[34] Domingo LR, Ríos-Gutiérrez M, Pérez P. Applications of the conceptual density func-tional theory indices to organic chemistry reactivity. Molecules. 2016;**21**:748-769. DOI: 10.3390/molecules21060748

[35] Domingo LR, Aurell MJ, Pérez P, Contreras R. Quantitative characterization of the global electrophilicity power of common diene/dienophile pairs in Diels-Alder reactions. Tetra-hedron. 2002;**58**:4417-4423. DOI: 10.1016/S0040-4020(02)00410-6

[36] Dillon AC, Jones KM, Bekkedahl TA, Kiang CH, Bethune DS, Heben MJ. Storage of hydrogen in single-walled carbon nanotubes. Nature. 1997;**386**(6623):377-379. DOI: 10.1038/386377a0

[37] Alonso JA, Arellano JS, Molina LM, Rubio A, Lopez MJ. Interaction of molecular and atomic hydrogen with single-wall carbon nanotubes. IEEE Transactions on Nanotechnology. 2004;**3**(2):304-310. DOI: 10.1109/TNANO.2004.828678

[38] Bilic A, Gale JD. Chemisorption of molecular hydrogen on carbon nanotubes: A route to effective hydrogen storage? The Journal of Physical Chemistry C. 2008;**112**:12568-12575. DOI: 10.1021/jp802104n

[39] Yao Y. Hydrogen storage using carbon nanotubes. In: Marulanda JM, editor. Carbon Nanotubes. 2010. In-the:India. p. 543-562. DOI: 10.5772/39443

[40] Kovalev V, Yakunchikov A, Li F. Simulation of hydrogen adsorption in carbon nanotube arrays. Acta Astronautica. 2011;**68**:681-685. DOI: 10.1016/j.actaastro.2010.09.007

[41] Liu C, Chen Y, CZ W, ST X, Chen HM. Hydrogen storage in carbon nanotubes revisited. Carbon. 2010;**48**:452-455. DOI: 10.1016/j.carbon.2009.09.060

[42] Contreras ML, Rozas R. Nitrogen-containing carbon nanotubes—A theoretical approach. In: Bianco S, editor. Carbon Nanotubes. From Research to Applications. Croatia: InTech; 2011. p. 3-26. DOI: 10.5772/16946 Available from: http://www.intech.open.com/books/carbon-nanotubes-from-research-to-applications/nitrogen-containing-carbon-nanotubes-a-theoretical-approach

[43] Ghosh S, Padmanabhan V. Adsorption of hydrogen on single-walled carbon nanotubes with defects. Diamond & Related Materials. 2015;**59**:47-53. DOI: 10.1016/j.diamond.2015.09.004

[44] Tabtimsai C, Keawwangchai S, Nunthaboot N, Ruangpornvisuti V, Wanno B. Density functional investigation of hydrogen gas adsorption on Fe-doped pristine and Stone-Wales defected single-walled carbon nanotubes. Journal of Molecular Modeling. 2012;**18**(8):3941-3949. DOI: 10.1007/s00894-012-1388-1

[45] Gayathri V, Geetha R. Hydrogen adsorption in defected carbon nanotubes. Adsorption. 2007;**13**(1):53-59. DOI: 10.1007/s10450-007-9002-z

[46] Meng FY, Zhou LG, Shi SQ, Yang R. Atomic adsorption of catalyst metals on Stone–Wales defects in carbon nanotubes. Carbon. 2003;**41**:2009-2025. DOI: 10.1016/S0008-6223(03)00183-0

[47] Shevlin SA, Guo ZX. High-capacity room-temperature hydrogen storage in carbon nanotubes via defect-modulated titanium doping. The Journal of Physical Chemistry C. 2008;**112**:17456-17464. DOI: 10.1021/jp800074n

[48] Simeon T, Balasubramanian K, Welch CR. Theoretical study of the interactions of In[+] and In[3+] with Stone-Wales defect single-walled carbon nanotubes. The Journal of Physical Chemistry Letters. 2010;**1**:457-462. DOI: 10.1021/jz900125e

[49] Targets for onboard hydrogen storage systems for light-duty vehicles. 2009. Available from: http://www.eere.energy.gov/hydrogenandfuelcells/storage/pdfs/targets_onboard_hydro_storage_explanation.pdf. [Accessed 2017–07-24]

[50] Li J, Furuta T, Goto H, Ohashi T, Fujiwara Y, Yip S. Theoretical evaluation of hydrogen storage capacity in pure carbon nanostructures. The Journal of Chemical Physics. 2003; **119**:2376. DOI: 10.1063/1.1582831

[51] Lochan RC, Head-Gordon M. Computational studies of molecular hydrogen binding affinities: The role of dispersion forces electrostatics and orbital interactions. Physical Chemistry Chemical Physics. 2006;**8**:1357-1370. DOI: 10.1039/B515409J

[52] Panczyk T, Wolski P, Lajtar L. Coadsorption of doxorubicin and selected dyes on carbon nanotubes. Theoretical investigation of potential application as a pH-controlled drug delivery system. Langmuir. 2016;**32**:4719-4728. DOI: 10.1021/acs.langmuir.6b00296

Elastic Constants and Homogenized Moduli of Monoclinic Structures Based on Density Functional Theory

Jia Fu

Abstract

Elastic constants and homogenized properties of two monoclinic structures (gypsum and tobermorite) were investigated by first-principles method. The gypsum (chemical formula of $CaSO_4 \bullet 2H_2O$) is an evaporite mineral and a kind of hydration product of anhydrite. Besides, the 11 Å tobermorite model (chemical formula: $Ca_4Si_6O_{14}(OH)_4 \cdot 2H_2O$) as an initial configuration of C-S-H structure is commonly used. Elastic constants are calculated based on density functional theory (DFT), which can also contribute to provide information for investigating the stability, stiffness, brittleness, ductility, and anisotropy of gypsum and tobermorite polycrystals. In addition, based on elastic constants (13 independent constants) of the monoclinic gypsum crystal, the elastic properties of polycrystals are obtained. The bulk modulus B, shear modulus G, Young's modulus E, and Poisson's ration v are derived. Therefore, it is fairly meaningful to study the elastic constants to understand the physical, chemical, and mechanical properties of two monoclinic structures. Elastic constants can be used as the measure criterion of the resistance of a crystal to an externally applied stress. The calculated parameters are all in excellent agreement with reference.

Keywords: DFT calculation, single crystal, nano scale, elastic constants, homogenized moduli

1. Introduction

The density functional theory (DFT) is commonly used to study the crystal structure, lattice energy, the equation of state, the electronic bandgap, and vibration spectra properties [1]. Based on the kinetic energy density functional of Thomas [2] and the exchange-correlation effects of Dirac [3], DFT has been greatly developed by Kohn and Sham (KS) [4], who have established the fundamental approximation theorem on the functional status to describe real

systems by electronic structure calculations. The eigenvalues of KS equations have no physical meaning, and the ionization energy is in the opposite state direction [5]. Moreover, one proposed approach is to introduce the eigenstates to calculate multi-body (many-body calculation) on the basis of Monte Carlo calculations [6] and perturbation theory [7]. The calculation of elastic constants is preceded by full geometry optimization and the stress tensor calculation of a number of distorted structures at the atomic scale. Polycrystalline structure constituted by a single crystal structure contains a variety of information (e.g., orientation) and the properties of a single crystal, such as anisotropy. Within the mechanics of typical crystals structures, the transition from the micro- to the meso-scale (homogenization) and vice versa (localization) can be estimated. Homogenization is an idealized description of a statistical distribution inside the actual heterogeneous material. Once the continuity model is admitted, the concept of homogeneity is deduced from it [8]. For quasi brittle materials, Zhu et al. [9] have formulated the anisotropic model in the framework of Eshelby-based homogenization methods. X-rays diffraction measurement is one of the stress assay test methods in physics field, of which the stress is actually determined by the strain [10]. Diffraction-based stress analysis depends critically on the use of the correct diffraction elastic constants [11]. X-ray method to test the material stress and to obtain elastic constants [12] is commonly based on the Reuss model [13]. Elasticity of single crystal and mechanical properties of polycrystalline material have been closely integrated. Various calculations methods are compared to determine homogenized moduli of the polycrystalline material composed of a single crystal, for example, the certain stress of Reuss model [13] and the certain strain of Voigt model [14].

DFT as a first-principles theory and a solid band theory in quantum mechanics has own a great success in linking physical properties and molecular structure, the calculation with exact accuracy but for low computational efficiency for macromolecular structure, which can be used to calculate elastic constants of anisotropic crystals, the monoclinic gypsum, and tobermorite crystals, for example. The chemical formula of gypsum is $CaSO_4 \bullet 2H_2O$, which is an evaporite mineral and a kind of hydration product of anhydrite (chemical formula: $CaSO_4$). Moreover, the 11 Å tobermorite model (chemical formula: $Ca_4Si_6O_{14}(OH)_4 \cdot 2H_2O$) as an initial configuration of C-S-H structure is commonly used. Since Young's modulus parameters of gypsum and C-S-H are important to the multi-scale model [15], elastic constants of the gypsum crystal are investigated. The crystal is monoclinic, with 13 independent constants. For the homogenization of elastic deformation, especially for polycrystalline structures, the traditional Reuss-Voigt-Hill method is used to calculate the elastic moduli of monoclinic structures. Based on the ab initio plane-wave pseudopotential density functional theory method mentioned earlier, we focus on the monoclinic crystals to estimate their homogenized elastic moduli.

2. Theoretical calculation by density functional theory (DFT)

Despite the above advantages of DFT, however, the resolution of a system by Kohn-Sham equations involves difficulties due to an infinite number of electrons. These electrons maybe changed under an effective potential generated by an infinite number of cores or ions.

2.1. Equation of the theoretical approximate solution

From a microscopic point of view, Schrödinger equation describing a periodic crystal system composed of atomic nuclei n in mutual interaction and electron spin σ_i is positioned $\vec{R} = \left\{ \vec{R}_i ; i = 1, \ldots N_n \right\}$ and $\vec{r} = \left\{ \left(\vec{r}_i, \sigma_i \right) ; i = 1, \ldots N_e \right\}$ respectively.

$$H\psi\left(\vec{R},\vec{r}\right) \quad E\psi\left(\vec{R},\vec{r}\right) \tag{1}$$

Hamiltonian, in simple cases, consists of five terms: the kinetic energy of the electrons and nuclei, and the various interactions between them.

$$H - T_N \mid T_e \mid U_{NN} \mid U_{ee} \mid U_{eN} \tag{2}$$

The possible analytical representation and resolution of such a problem become a difficult task due to the limited memory of the computer tools. However, it is possible to reformulate the problem using appropriate theorems and approximations.

The fundamental principle approaches of mean field theory, in particular the DFT, are that any properties of an interacting particle system can be considered as a functional density in the ground state of the system $n_0(r)$. Besides, the scalar function of the position $n_0(r)$ essentially determines the wave functions of the system at the ground state and the excited states. Electronic and mechanical properties of a periodic crystal refer to solid state physics, quantum mechanics, and crystallography.

The crystalline ion movement of the electron is as $\psi\left(\vec{R},\vec{r}\right) = \chi\left(\vec{R}\right)\varphi\left(\vec{R},\vec{r}\right)$ and assumes that the electron mobility (φ) does not depend on the speed nuclei but on their positions.

According to the Born-Oppenheimer or adiabatic approximation [16], the dynamics of the system (electrons and nuclei) is described. The electrons are assumed to react instantly to ionic motion. In electronic coordinates, the nucleus positions are considered as immobile external parameters.

$$\hat{H} - \hat{T}_e \mid \hat{U}_{Ne} \mid \hat{U}_{ee} \mid \hat{U}_{nn} \tag{3}$$

$$\hat{H}_R \varphi_R^\lambda\left(\vec{r}\right) - E^{\overline{R^\infty}}\left(\vec{R}\right)\varphi_R^\lambda\left(\vec{r}\right)\left(\vec{r}\right) \tag{4}$$

where the last term of the Hamiltonian is constant and has been introduced in order to preserve the neutrality of the system and avoid the divergence of the eigenvalues. Clean the ground state of the system for fixed nuclear positions, total energy is given by the formula:

$$E^{BO}\left(\vec{R}\right)\left\langle \varphi_R^0 \left| \hat{H} \right| \varphi_R^0 \right\rangle = \min\left\langle \varphi_R^0 \left| \hat{H} \right| \varphi_R^0 \right\rangle \tag{5}$$

This energy has a surface in the space coordinates that is said to be ionic Born-Oppenheimer surface. The ions move according to the effective potential energy, including Coulomb repulsion and the anchoring effect of the electron, which are as follows:

$$\hat{H}^{BO} = \hat{T}_n + E^{BO}\left(\hat{R}\right) \tag{6}$$

$$\hat{H}^{BO} \chi\left(\vec{R}\right) = E\chi\left(\vec{R}\right) \tag{7}$$

The dissociation degrees of freedom of electrons from those of nucleons, obtained through the adiabatic approximation, are very important, because if the electrons must be treated by quantum mechanics, degrees of freedom of ions in most cases are processed in a conventional manner.

This theorem/approach of Hohenberg and Kohn tries to make an exact DFT theory for many-body systems. This formulation applies to any system of mutually interacting particles in an external potential $V_{ex}\left(\vec{r}\right)$, where the Hamiltonian is written as.

$$\hat{H} = -\frac{\hbar}{2m_e}\sum_i \nabla_i^2 - \sum_i V_{ex}\left(r_i\right) - \frac{1}{2}\sum_{i \neq j}\frac{e^2}{\left|r_i - r_j\right|} \tag{8}$$

DFT and its founding principle are summarized in two theorems, first introduced by Hohenberg and Kohn [17], which refer to the set of potential $V_{ex}\left(\vec{r_i}\right)$ and the density minimizing of Eq. (5).

The total energy of the ground state of a system for interacting electrons is functional (unknown) of the single electron density

$$E_{HK}[n] = T[n] + E_{int}[n] + \int d^3 r V_{ex}(r) + E_{nn}\left(\vec{R}\right) \cdot F_{HK}[n] + \int d^3 r V_{ex}(r) + E_{nn}\left(\vec{R}\right) \tag{9}$$

As a result, the density $n_0(r)$ minimizing the energy associated with the Hamiltonian (9) is obtained and used to evaluate the energy of the ground state of the system.

The principle established in the second theorem of Hohenberg and Kohn specifies that the density that minimizes the energy is the energy of the ground state

$$E^{BO}\left[\vec{R}\right] = \min E\left(\vec{R}, n\left(\vec{r}\right)\right) \tag{10}$$

Because the ground state is concerned, it is possible to replace the wave system function by the electron charge density, which therefore becomes the fundamental quantity of the problem. In principle, the problem boils down to minimize the total energy of the system in accordance with the variations in the density governed by the constraint on the number of particles $\int n(\vec{r})d^3 r = N_e$. In this stage, the DFT can reformulate the problem rather than solve an uncertain functional $F_{HK}(n)$.

2.2. The approximation approach of Kohn-Sham

The approach of Kohn-Sham system substitutes the interacting particles, which obeys the Hamiltonian in Eq. (3), by a less complex system easily solved. This approach assumes that the density in the ground state of the system is equal to that in some systems composed of non-interacting particles. This involves independent particle equations for the non-interacting system, gathering all the terms complicated and difficult to assess, in a functional exchange-correlation $E_{XC}(n)$.

$$E_{KS} = F[n] + \int d^3 r V_{ex}(r) = T_S[n] + E_H[n] + E_{XC}[n] + \int d^3 r V_{ex}(r) \tag{11}$$

T is the kinetic energy of a system of particles (electrons) independently (non-interacting) embedded in an effective potential which is no other than the real system,

$$T_S[n] = \left\langle \psi_{NI} \left| \hat{T}_e \right| \psi_{NI} \right\rangle = \sum_{i=1}^{N_e} \left\langle \varphi_i \left| -\frac{1}{2} \nabla^2 \right| \varphi_i \right\rangle \tag{12}$$

The Hartree energy or energy of interaction is associated with the Coulomb interaction of the self-defined electron density.

$$E_{Hartree}[n] = \frac{1}{2} \int d^3 r d^3 r' \frac{n(r)n(r')}{|r-r'|} \tag{13}$$

$$n(r) = \sum_{i=1}^{N_e} |\varphi_i(r)|^2 \tag{14}$$

Solving the auxiliary Kohn and Sham system for the ground state can be seen as a minimization problem while respecting the density $n(r)$. Apart from orbital function T_S, all other terms depend on the density. Therefore, it is possible to vary the functions of the wave and to derive the variational equation:

$$\frac{\delta E_{KS}}{\delta \varphi_i^*(r)} = \frac{\delta T_S}{\delta \varphi_i^*(r)} + \left[\frac{\delta E_{ex}}{\delta n(r)} + \frac{\delta E_{Hartree}}{\delta n(r)} + \frac{\delta E_{xc}}{\delta n(r)} \right] \frac{\delta n(r)}{\delta \varphi_i^*(r)} = 0 \tag{15}$$

With the constraint of orthonormalization $\left\langle \varphi_i | \varphi_j \right\rangle = \delta_{i,j}$, this implies the form of Kohn-Sham for Schrödinger equations:

$$\left(\hat{H}_{KS} - \varepsilon_i \right) \varphi_i(r) = 0 \tag{16}$$

ε_i represents the eigenvalues, and $\hat{H}_{KS}$ is the effective Hamiltonian H,

$$\hat{H}_{KS}(r) = -\frac{1}{2} \nabla^2 + V_{KS}(r) \tag{17}$$

$$V_{KS}(r) = V_{ex}(r) + \frac{\delta E_{Hartree}}{\delta n(r)} + \frac{\delta E_{xc}}{\delta n(r)} \tag{18}$$

Eqs. (16)–(18) are known equations of Kohn-Sham, the density $n(r)$ and the resulting total energy E_{KS}. These equations are independent of any approximation on the functional $E_{XC}(n)$, resolution provides the exact values of the density and the energy of the ground state of the interacting system, provided that $E_{XC}(n)$ is exactly known. The latter can be described in terms of Hohenberg Kohn function in Eq. (8)

$$E_{xc}[n] = F_{HK}[n] - (T_S[n] + E_{Hartree}[n]) \tag{19}$$

or more precisely,

$$E_{xc}[n] = \left\langle \hat{T} \right\rangle - T_S[n] + \left\langle \hat{V}_{int} \right\rangle - E_{Hartree}[n] \tag{20}$$

This energy is related to potential exchange-correlation $V_{xc} = \frac{\partial E_{xc}}{\partial n(r)}$.

For the exchange-correlation functional, the only ambiguity in the approach of Kohn and Sham (*KS*) is the exchange-correlation term. It is subject to functional approximations of local or near local order of density that said energy E_{KS} can be written as

$$E_{xc}[n] = \int n(r)\varepsilon_{xc}([n], r)d^3r \tag{21}$$

where $\varepsilon_{xc}([n], r)$ is the exchange-correlation energy per electron at point r, it depends on $n(r)$ in the vicinity of r. These approximations have made enormous progress in the field.

1. The approximation of the local density (LDA)

   The use of the local density approximation (LDA) in which the exchange-correlation energy $E_{xc}^{LDA}[n]$ is another integral over all space, assuming that $\varepsilon_{xc}([n], r)$ is the exchange-correlation energy per particle of a homogeneous electron gas of density n

   $$E_{xc}^{LDA}[n] = \int n(r)\varepsilon_{xc}^{bom}[n(r)]d^3r = \int n(r)\left\{\varepsilon_x^{bom}[n(r)] + \varepsilon_c^{bom}[n(r)]\right\}d^3r \tag{22}$$

   The exchange term $E_x^{bom}[n(r)]$ can be expressed analytically, while the correlation term is computed accurately using the Monte Carlo by Ceperley Alder [18] and then set in different shapes [19].

   This approximation has been particularly checked to deal with non-homogeneous systems.

2. The generalized gradient approximation (GGA)

   The generalized gradient approximation (GGA) involves the local density approximation providing a substantial improvement and better adaptation to the systems. This approximation is equal to the exchange-correlation term only as a function of the density. A first approach (GEA) was introduced by Kohn and Sham then used by the authors of Herman et al. [20].

This notion of GGA is the choice of functions, which allows us a better adaptation to wide variations so as to maintain the desired properties. The energy is written in its general form [21]:

$$E_{xc}^{GGA}[n] = \int n(r)\varepsilon_{xc}[n, |\nabla_n|, \ldots]d^3r = \int n(r)\varepsilon_x^{bom}(n)F_{xc}[n, |\nabla_n|, \ldots]d^3r \tag{23}$$

where ε_x^{bom} is the exchange energy of an unpolarized density $n(r)$ system. There are many forms of F_{XC}, the most used are those introduced by Becke [22] and Perdew [23, 24].

2.3. Parameters of Bloch theorem and Brillouin zone

Different states of the Schrödinger equation for an independent particle in a system. By Kohn and Sham equations, responding to eigenvalue equation is as:

$$\hat{H}_{eff}(r)\psi_i(r) = \left[-\frac{\hbar^2}{2m}\nabla^2 + V_{eff}(r)\right]\psi_i(r) = \varepsilon_i\psi_i(r) \tag{24}$$

where the electrons are immersed in an effective potential $V_{eff}\left(\vec{r}\right)$.

The effective potential has the periodicity of the crystal and may be expressed using Fourier series, in a periodic system:

$$V_{eff}(r) = \sum_m V_{eff}(G_m)\exp(iG_m r) \tag{25}$$

G_m is the reciprocal lattice vector:

$$V_{eff}(G) = \frac{1}{\Omega_{sell}} \int_{\Omega_{sell}} V_{eff}(r)\exp(-iG_m r)dr \tag{26}$$

where Ω_{sell} is the volume of the original mesh.

As the translational symmetry, it is that states are orthogonal and conditioned by the limits of the crystal (infinite volume). In this case, the Eigen functions of *KS* are governed by the Bloch theorem: they have two quantum numbers: the wave vector *k* in the Brillouin zone (*BZ*) and the band index *i*, and this can be expressed by a product of a plane wave *exp.(ik, r)* and a periodic function:

$$\begin{aligned} \psi_{i,k}(r) &= \exp(ik, r)u_{i,k}(r) \\ u_{i,k}(r+R) &= u_{i,k}(r) \\ R &= \sum n_i a_i, n_i = 1 \ldots N_i \end{aligned} \tag{27}$$

where *R* is the vector of direct space defined by a_i with $i \in \{1, 2, 3\}$ and N_i is the number of primitive cells in each direction ($N_i \to \infty$ in the case of perfect crystal).

Solving Eq. (24) is equivalent to increase the periodic function $u_{i,k}(r)$, in a database-dependent functions points $k : \left\{ \phi_j^k(r) | j = 1 \ldots N_{bas}(k) \right\}$:

$$u_{i,k}(r) = \sum_j C_i^j \phi_j^k(r) \tag{28}$$

where ϕ_j^k is the wave function developed in a space of infinite dimensions; this means that j should be in principle infinite. But, in practice, we work with a limited set of basic functions, which imply that the description of ϕ_j^k will approximate. That the selected database simply solves the system:

$$\sum_{m'} H_{m,m'}(k) C_{i,m'}(k) = \varepsilon_i(k) C_{i,m}(k)$$

$$H_{m,m'}(k) = \left\langle \varphi_{m,k}^j \left| \hat{H}_{eff} \right| \varphi_{m,k}^j \right\rangle \tag{29}$$

where each point is a set of k eigenstates, the label having $i = 1, 2, \ldots$ obtained by diagonalization of the Hamiltonian in Eq. (29).

It is necessary to integrate the points k in the Brillouin zone. For a function $f_i(k)$ where i defines the band index, the average value is

$$\overline{f_i} = \frac{1}{N_k} \sum_k f_i(k) \rightarrow \frac{\Omega_{cell}}{(2\pi)^d} \int_{BZ} f_i(k) dk \tag{30}$$

Ω_{cell} is the cell volume of the original mesh in the real space and $(2\pi)^d / \Omega_{cell}$ of the cell volume of the Brillouin zone are determined using a sampling points k. Several election procedures exist for these points. Particularly those of Baldereschi [25], Chadi and Kohen [26], and Monkhorst and Pack [27] are the most frequently used.

3. Elastic constants and homogenized moduli of monoclinic structure

According to the crystal theory [28], any crystal lattice system contains six independent variables, namely the cell side length a, b, and c; unit cell angle α, β, and γ. Generally, the crystal under a certain deformation, temperature, and pressure can be described by the corresponding six-dimensional deformation tensor. The temperature and pressure will cause cell-deformed configuration tensor as

$$X^{P,T} = \begin{bmatrix} a_x^{P,T} & a_y^{P,T} & a_z^{P,T} \\ b_x^{P,T} & b_y^{P,T} & b_z^{P,T} \\ c_x^{P,T} & c_y^{P,T} & c_z^{P,T} \end{bmatrix} = \begin{bmatrix} a_x^{0,0} & a_y^{0,0} & a_z^{0,0} \\ b_x^{0,0} & b_y^{0,0} & b_z^{0,0} \\ c_x^{0,0} & c_y^{0,0} & c_z^{0,0} \end{bmatrix} \left(\begin{bmatrix} 1 & 0 & 0 \\ 0 & 1 & 0 \\ 0 & 0 & 1 \end{bmatrix} + \begin{bmatrix} \alpha_1(P,T) & \alpha_6(P,T) & \alpha_5(P,T) \\ \alpha_6(P,T) & \alpha_2(P,T) & \alpha_4(P,T) \\ \alpha_5(P,T) & \alpha_4(P,T) & \alpha_3(P,T) \end{bmatrix} \right) \tag{31}$$

$$\text{where } \begin{bmatrix} a_x^{P,T} & a_y^{P,T} & a_z^{P,T} \\ b_x^{P,T} & b_y^{P,T} & b_z^{P,T} \\ c_x^{P,T} & c_y^{P,T} & c_z^{P,T} \end{bmatrix} \text{ and } \begin{bmatrix} \alpha_1(P,T) & \alpha_6(P,T) & \alpha_5(P,T) \\ \alpha_6(P,T) & \alpha_2(P,T) & \alpha_4(P,T) \\ \alpha_5(P,T) & \alpha_4(P,T) & \alpha_3(P,T) \end{bmatrix} \text{ separately represent the cell}$$

configuration tensor and the deformation tensor at temperature T (K) under the pressure P (GPa).

3.1. Calculation of elastic constants for single crystal structure

A multi-particle electronic structure satisfies the Schrödinger equation. As in [29], Kohn-Sham equation as an approximation to simplify Schrödinger equation is described. For crystal composed by vibrator with the vibration frequency w_i, the total Helmholtz free energy is

$$F = E + \sum_i F_i^{th} = U + \sum_i \frac{1}{2}\hbar w_i + k_B T \sum_i In\left(1 - e^{-\frac{\hbar w_i}{k_B T}}\right) \tag{32}$$

Helmholtz free energy can be calculated for all the thermodynamic quantities. DFT-QHA (quasi-harmonic approximation) is a precise calculation method to calculate thermodynamic properties of solid materials elastic constants and Debye temperature with the accurate predictions.

According to the theory of elasticity, under the isothermal strain, the elastic modulus of Helmholtz free energy can be described by the form of the Taylor expansion, of which the coefficients of the polynomial are the elastic coefficient:

$$\rho_0 F\left(\eta_{ij}, T\right) = \rho_0 F\left(\eta_{ij}, T\right) + \frac{1}{2}\sum_{ijkl} c_{ijkl}^T \eta_{ij}\eta_{kl} + \dots + \frac{1}{n!}\sum_{ijkl\dots} c_{ijkl\dots}^T \eta_{ij}\eta_{kl}\dots \tag{33}$$

where η_{ij}, η_{kl}, and η_{mn} are the coefficients of Lagrange deformation tensor, c_{ijkl}^T is the isothermal first-order elastic coefficients, and $F\left(\eta_{ij}, T\right)$ is the Helmholtz free energy.

The components of the stress tensor can be extracted by $\sigma_i = \sum_{j=1}^{6} c_{ij}\varepsilon_j$ after the applied strain, the total energy variation of the system can be expressed as

$$\Delta E = \frac{V}{2}\sum_{i=1}^{6}\sum_{j=1}^{6} c_{ij}e_i e_j \tag{34}$$

The second-order elastic coefficients can be obtained by the coefficient of the second-order Taylor expansion of Helmholtz free energy with the strain,

$$c_{ijkl}^T = \rho_0 \frac{\partial^2 F\left(\eta_{ij}, T\right)}{\partial\eta_{ij}\partial\eta_{kl}} \tag{35}$$

Here, strain and thermodynamics deformation are symmetric. There is only six independent deformation tensor in the nine-dimensional deformation tensor. LCEC is a second-order linear combination of independent elastic coefficients corresponding to Helmholtz free energy coefficient under some deformation mode [30, 31]. For all directions under monoclinic crystals, if a strain is added, the corresponding simultaneous equations can be solved to determine all elastic coefficients.

3.2. The energy-volume relationship of the monoclinic crystal

Deformation tensors to calculate independent C_{ij} constants of monoclinic crystal are listed in **Table 1**.

For monoclinic crystal, elastic constants include C_{11}, C_{22}, C_{33}, C_{12}, C_{13}, C_{23}, C_{44}, C_{55}, C_{66} C_{15}, C_{25}, C_{35}, and C_{46}; the strain energy-volume relation and elastic moduli of monoclinic symmetry based on $E\text{-}V$ method can be obtained. The calculated $E\text{-}\delta$ points are fitted to second-order polynomials $E(V, \delta)$. For all strains, different strain forms δ are taken to calculate the total energies E for the strained crystal structure. By applying a series of δ strain amplitude, the independent elastic constants of monoclinic crystal by these simultaneous $\Delta E\text{-}\delta$ equations can be obtained.

Deformation tensor	$\Delta E\text{-}V$ relation of LCEC	LCEC
$e = (\delta, \delta, 0, 0, 0, 0)$	$\frac{\Delta E}{V_0} = \left(\frac{c_{11}}{2} + c_{12} + \frac{c_{22}}{2}\right)\delta^2$	$c_{11} + c_{22} + 2c_{12}$
$e = (0, \delta, \delta, 0, 0, 0)$	$\frac{\Delta E}{V_0} = \left(\frac{c_{22}}{2} + c_{23} + \frac{c_{33}}{2}\right)\delta^2$	$c_{22} + c_{33} + 2c_{23}$
$e = (\delta, 0, \delta, 0, 0, 0)$	$\frac{\Delta E}{V_0} = \left(\frac{c_{11}}{2} + c_{13} + \frac{c_{33}}{2}\right)\delta^2$	$c_{11} + c_{33} + 2c_{13}$
$e = (0, 0, 0, \delta, \delta, 0)$	$\frac{\Delta E}{V_0} = \left(\frac{c_{44}}{2} + c_{45} + \frac{c_{55}}{2}\right)\delta^2$	$c_{44} + c_{55} + 2c_{45}$
$e = (\delta, 0, 0, 0, 0, \delta)$	$\frac{\Delta E}{V_0} = \left(\frac{c_{11}}{2} + c_{16} + \frac{c_{66}}{2}\right)\delta^2$	$c_{11} + c_{66} + 2c_{16}$
$e = (0, \delta, 0, 0, 0, \delta)$	$\frac{\Delta E}{V_0} = \left(\frac{c_{22}}{2} + c_{26} + \frac{c_{66}}{2}\right)\delta^2$	$c_{22} + c_{66} + 2c_{26}$
$e = (0, 0, \delta, 0, 0, \delta)$	$\frac{\Delta E}{V_0} = \left(\frac{c_{33}}{2} + c_{36} + \frac{c_{66}}{2}\right)\delta^2$	$c_{33} + c_{66} + 2c_{36}$
$e = (\delta, \delta, \delta, 0, 0, 0)$	$\frac{\Delta E}{V_0} = \left(\frac{c_{11}}{2} + \frac{c_{22}}{2} + \frac{c_{33}}{2} + c_{12} + c_{13} + c_{23}\right)\delta^2$	$c_{11} + c_{22} + c_{33} + 2c_{12} + 2c_{13} + 2c_{23}$
$e = \left(\delta, -\delta, \delta^2/(1 - \delta^2), 0, 0, 0\right)$	$\frac{\Delta E}{V_0} = \left(\frac{c_{11}}{2} - c_{12} + \frac{c_{22}}{2}\right)\delta^2$	$c_{11} + c_{22} - 2c_{12}$
$e = \left(\delta, \delta^2/(1 - \delta^2), -\delta, 0, 0, 0\right)$	$\frac{\Delta E}{V_0} = \left(\frac{c_{11}}{2} - c_{13} + \frac{c_{33}}{2}\right)\delta^2$	$c_{11} + c_{33} - 2c_{13}$
$e = \left(\delta^2/(1 - \delta^2), \delta, -\delta, 0, 0, 0\right)$	$\frac{\Delta E}{V_0} = \left(\frac{c_{22}}{2} - c_{23} + \frac{c_{33}}{2}\right)\delta^2$	$c_{22} + c_{33} - 2c_{23}$
$e = \left(\delta^2/(1 - \delta^2), 0, 0, 2\delta, 0, 0\right)$	$\frac{\Delta E}{V_0} = 2c_{44}\delta^2$	$4c_{44}$
$e = (\delta, 0, 0, 0, 2\delta, 0)$	$\frac{\Delta E}{V_0} = \left(\frac{c_{11}}{2} + 2c_{15} + 2c_{55}\right)\delta^2$	$c_{11} + 4c_{55} + 4c_{15}$
$e = (\delta, 0, 0, 0, -2\delta, 0)$	$\frac{\Delta E}{V_0} = \left(\frac{c_{11}}{2} - 2c_{15} + 2c_{55}\right)\delta^2$	$c_{11} + 4c_{55} - 4c_{15}$
$e = (0, \delta, 0, 0, 2\delta, 0)$	$\frac{\Delta E}{V_0} = \left(\frac{c_{22}}{2} + 2c_{25} + 2c_{55}\right)\delta^2$	$c_{22} + 4c_{55} + 4c_{25}$
$e = (0, 0, \delta, 0, 2\delta, 0)$	$\frac{\Delta E}{V_0} = \left(\frac{c_{33}}{2} + 2c_{35} + 2c_{55}\right)\delta^2$	$c_{33} + 4c_{55} + 4c_{35}$

Table 1. Deformation tensors to calculate independent elastic constants of monoclinic crystal [30, 31].

3.3. Homogenization of monoclinic polycrystals by RVH estimation

Stress-strain relation in an orthotropic monoclinic crystal can be defined by the independent elastic stiffness parameters [32]:

$$
\begin{bmatrix} \sigma_{11} \\ \sigma_{22} \\ \sigma_{33} \\ \sigma_{12} \\ \sigma_{13} \\ \sigma_{23} \end{bmatrix} = \begin{bmatrix} c_{11} & c_{12} & c_{13} & 0 & c_{15} & 0 \\ c_{12} & c_{22} & c_{23} & 0 & c_{25} & 0 \\ c_{13} & c_{23} & c_{33} & 0 & c_{35} & 0 \\ 0 & 0 & 0 & c_{44} & 0 & c_{46} \\ c_{15} & c_{25} & c_{35} & 0 & c_{55} & 0 \\ 0 & 0 & 0 & c_{46} & 0 & c_{66} \end{bmatrix} \begin{bmatrix} \varepsilon_{11} \\ \varepsilon_{22} \\ \varepsilon_{33} \\ \gamma_{12} \\ \gamma_{13} \\ \gamma_{23} \end{bmatrix}
\tag{36}
$$

where σ represents the normal stress and shear stress in each direction (unit: nN/nm^2); ε and γ are the normal strain and shear strain in each direction, respectively.

The homogenized elastic properties of polycrystals can be calculated, of which elastic moduli and Poisson's ratio can be obtained by calculating Voigt and Reuss bounds and averaging term as [32]

$$
G_V = \frac{1}{15}[c_{11} + c_{22} + c_{33} + 3(c_{44} + c_{55} + c_{66}) - (c_{12} + c_{13} + c_{23})]
\tag{37}
$$

$$
\begin{aligned}
G_R = 15\{4\big[&(c_{33}c_{55} - c_{35}^2)(c_{11} + c_{22} + c_{12}) + (c_{23}c_{55} - c_{25}c_{35})(c_{11} - c_{12} - c_{23}) \\
&+ (c_{13}c_{35} - c_{15}c_{33})(c_{15} + c_{25}) + (c_{13}c_{55} - c_{15}c_{35}) \cdot (c_{22} - c_{12} - c_{23} - c_{13}) \\
&+ (c_{13}c_{25} - c_{15}c_{23})(c_{15} - c_{25}) + f\big]/\Omega + 3\big[g/\Omega + (c_{44} + c_{66})/(c_{44}c_{66} - c_{46}^2)\big]\}^{-1}
\end{aligned}
\tag{38}
$$

$$
B_V = [c_{11} + c_{22} + c_{33} + 2(c_{12} + c_{13} + c_{23})]/9
\tag{39}
$$

$$
\begin{aligned}
B_R = \Omega\big[&(c_{33}c_{55} - c_{35}^2)(c_{11} + c_{22} - 2c_{12}) + (c_{23}c_{55} - c_{25}c_{35})(2c_{12} - 2c_{11} - c_{23}) \\
&+ (c_{13}c_{35} - c_{15}c_{33}) \cdot (c_{15} - 2c_{25}) + (c_{13}c_{55} - c_{15}c_{35})(2c_{12} + 2c_{23} - c_{13} - 2c_{22}) \\
&+ 2(c_{13}c_{25} - c_{15}c_{23})(c_{25} - c_{15}) + f\big]^{-1}
\end{aligned}
\tag{40}
$$

$$
f = c_{11}(c_{22}c_{55} - c_{25}^2) - c_{12}(c_{12}c_{55} - c_{15}c_{25}) + c_{15}(c_{12}c_{25} - c_{15}c_{22}) + c_{25}(c_{23}c_{35} - c_{25}c_{33})
\tag{41}
$$

$$
g = c_{11}c_{22}c_{33} - c_{11}c_{23}^2 - c_{22}c_{13}^2 - c_{33}c_{12}^2 + 2c_{12}c_{13}c_{23}
\tag{42}
$$

$$
\begin{aligned}
\Omega = 2[&c_{15}c_{25}(c_{33}c_{12} - c_{13}c_{23}) + c_{15}c_{35}(c_{22}c_{13} - c_{12}c_{23}) + c_{25}c_{35}(c_{11}c_{23} - c_{12}c_{13})] \\
&- [c_{15}^2(c_{22}c_{33} - c_{23}^2) + c_{25}^2(c_{11}c_{33} - c_{13}^2) + c_{35}^2(c_{11}c_{22} - c_{12}^2)] + gc_{55}
\end{aligned}
\tag{43}
$$

For monoclinic crystal structure, elastic constants include C_{11}, C_{22}, C_{33}, C_{12}, C_{13}, C_{23}, C_{44}, C_{55}, C_{66} C_{15}, C_{25}, C_{35}, and C_{46}. The criteria for mechanical stability are given by Wu [32]:

$$
c_{ij} > 0 (i = 1, 2, 3, 4, 5, 6)
\tag{44}
$$

$$
(c_{44}c_{66} - c_{46}^2) > 0
\tag{45}
$$

$$\left(c_{33}c_{55} - c_{35}^2\right) > 0 \tag{46}$$

$$\left(c_{22} + c_{33} - 2c_{23}\right) > 0 \tag{47}$$

$$[c_{11} + c_{22} + c_{33} + 2(c_{12} + c_{13} + c_{23})] > 0 \tag{48}$$

$$\left[c_{22}\left(c_{33}c_{55} - c_{35}^2\right) + 2c_{23}c_{25}c_{35} - c_{23}^2c_{55} - c_{25}^2c_{33}\right] > 0 \tag{49}$$

$$\{2[c_{15}c_{25}(c_{33}c_{12} - c_{13}c_{23}) + c_{15}c_{35}(c_{22}c_{13} - c_{12}c_{23}) + c_{25}c_{35}(c_{11}c_{23} - c_{12}c_{13})]$$
$$- \left[c_{15}^2\left(c_{22}c_{33} - c_{23}^2\right) + c_{25}^2\left(c_{11}c_{33} - c_{13}^2\right) + c_{35}^2\left(c_{11}c_{22} - c_{12}^2\right)\right] + gc_{55}\} > 0 \tag{50}$$

Young's modulus and Poisson's ratio can be rewritten based on the Voigt-Reuss-Hill approximation [33]. In terms of the Voigt-Reuss-Hill approximations [34], $M_H = (1/2)(M_R + M_V)$, M refers to B or G. Thus, Young's modulus E and Possion's ratio μ are obtained as

$$E = \frac{9BG}{3B + G} = \frac{9(B_V/2 + B_R/2)(G_V/2 + G_R/2)}{3(B_V/2 + B_R/2) + (G_V/2 + G_R/2)} \tag{51}$$

$$\mu = \frac{3B - 2G}{2(3B + G)} = \frac{3(B_V/2 + B_R/2) - 2(G_V/2 + G_R/2)}{6(B_V/2 + B_R/2) + 2(G_V/2 + G_R/2)} \tag{52}$$

Then, Voigt-Reuss-Hill average [32] will be determined, and Young's modulus can be calculated.

4. Modeling and homogenized elastic moduli of gypsum structure

4.1. Nanoscale modeling of monoclinic crystals

4.1.1. Nanoscale modeling of monoclinic gypsum crystal

The gypsum morphology is monoclinic, and the initial lattice is as $a = 5.677\mathring{A}$, $b = 15.207\mathring{A}$, $c = 6.528\mathring{A}$, $\alpha = \beta = 90°$, and $\gamma = 118.49°$, its structure is monoclinic with space group I 2/a [35].

In **Figure 1**, the gypsum crystal can be summarized as follows: (1) the two hydrogen atoms of water molecules formed weak hydrogen bonds with the O atoms of Ca and S polyhedra; (2) a stacking sequence of CaO_8 and SO_4 chains in the (010) plane alternates with water layers along the b-axis; and (3) in (010) plane, the sulfate tetrahedra and CaO_8 polyhedra alternate to form edge-sharing chains along [100] and zigzag chains along [001] direction [36] (**Table 2**).

4.1.2. Nanoscale modeling of monoclinic 11 Å tobermorite crystal

Hamid model [37] as the 11 Å tobermorite (formula: $Ca_4Si_6O_{14}(OH)_4·2H_2O$) as an initial configuration is commonly used. The morphology is monoclinic, and the initial lattice is [37]: $a = 6.69$ Å, $b = 7.39$ Å, $c = 22.779$ Å, $\alpha = \beta = 90°$, and $\gamma = 123.49°$, space group P21. Modeling of 11 Å tobermorite is shown in **Figure 2**.

In **Figure 2(a)**, the 11 Å tobermorite crystal can be summarized as follows: (1) the structure is basically a layered structure. (2) The central part is a Ca-O sheet (with an empirical formula:
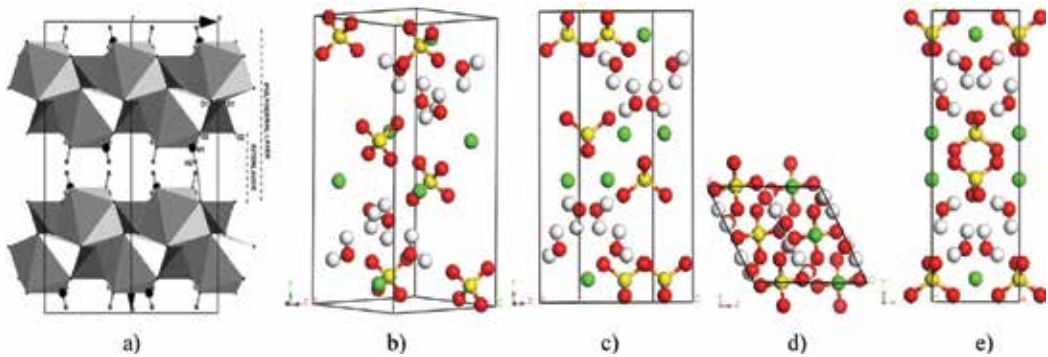
Figure 1. Modeling of gypsum crystal. (a) Gypsum structure [36] along [001]; (b) the real cell; (c) in x-direction; (d) in y-direction; and (e) in z-direction.

Atom	x	y	z	Occupancy rate	Uiso or Ueq
Ca	0.5000	0.0786	0.2500	1.00	1.00
S	0.0000	0.0787	0.7500	1.00	1.00
O1	−0.0384	0.1326	0.5512	1.00	1.00
O2	0.2429	0.0215	0.8347	1.00	1.00
Ow	0.3784	0.1825	0.4554	1.00	1.00
H1	0.2504	0.1615	0.5009	1.00	1.00
H2	0.4022	0.2435	0.4900	1.00	1.00

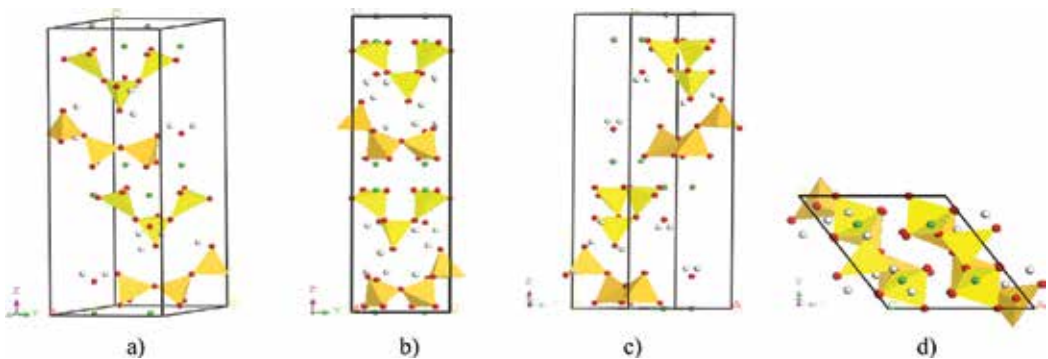**Table 2.** Atomic coordinates and displacement parameters of gypsum [36].

Figure 2. Modeling of 11 Å tobermorite crystal. Silicate chains, calcium octahedral, and oxygen atoms are shown as yellow tetrahedra, green spheres, and red spheres. (a) 11 Å Tob monoclinic crystal; (b) in x-direction; (c) in y-direction; and (d) in z-direction.

CaO_2, of which the oxygen in CaO_2 also includes that of the silicate tetrahedron part). (3) Silicate chains envelope the Ca-O sheet on both sides. (4) Ca^{2+} and H_2O are filled between individual layers to balance the charges. The infinite layers of calcium polyhedra are parallel to

(001), with tetrahedral chains of wollastonite-type along b and the composite layers stacked along c and connected through the formation of double tetrahedral chains [38]. Atomic coordinates and displacement parameters are seen in **Table 3**.

4.2. Initial conditions and elastic constants of monoclinic crystals

4.2.1. Initial conditions and elastic constants of gypsum

The initial conditions are as follows: the pressure region of 0–1 GPa is used. Besides, a plane-wave basis set and ultrasoft pseudopotentials using GGA are used with a plane-wave cutoff energy of 400 eV. Brillouin zone is $6 \times 6 \times 4$. Self-consistent convergence of the total energy per atom is chosen as 10^{-4} eV. Elastic constants of monoclinic gypsum crystal under 0–1.0 GPa are shown in **Figure 3**.

Atomic species	X	Y	Z	Occupancy rate	Uiso or Ueq	Atomic species	X	Y	Z	Occupancy rate	Uiso or Ueq
Si1	0.7710	0.3830	0.1578	1	0.031	O8	0.7690	0.8430	0.0953	1	0.027
Si2	0.9250	0.7500	0.0721	1	0.030	O9	0.5370	0.7980	0.1968	1	0.036
Si3	0.7720	0.9620	0.1596	1	0.015	O10	0.0040	0.0420	0.2008	1	0.034
O1	0.7740	0.4950	0.0932	1	0.039	O11	0.4330	0.2230	−0.0250	0.5	0.072
O2	0.7620	0.1690	0.1305	1	0.019	O12	0.9490	0.2560	0.0000	1	0.080
O3	0.0020	0.5270	0.2000	1	0.032	O13	0.4300	0.7700	−0.0220	0.5	0.090
O4	0.5360	0.3040	0.1926	1	0.035	Ca1	0.2770	0.4257	0.2083	1	0.024
O5	0.9100	0.7470	0.0000	1	0.034	Ca2	0.7630	0.9160	0.2951	1	0.027
O6	0.2020	0.8870	0.0942	1	0.053	Ca3	0.5620	0.0640	0.0450	0.25	0.038
O7	0.2890	0.4360	0.0940	1	0.076	—	—	—	—	—	—

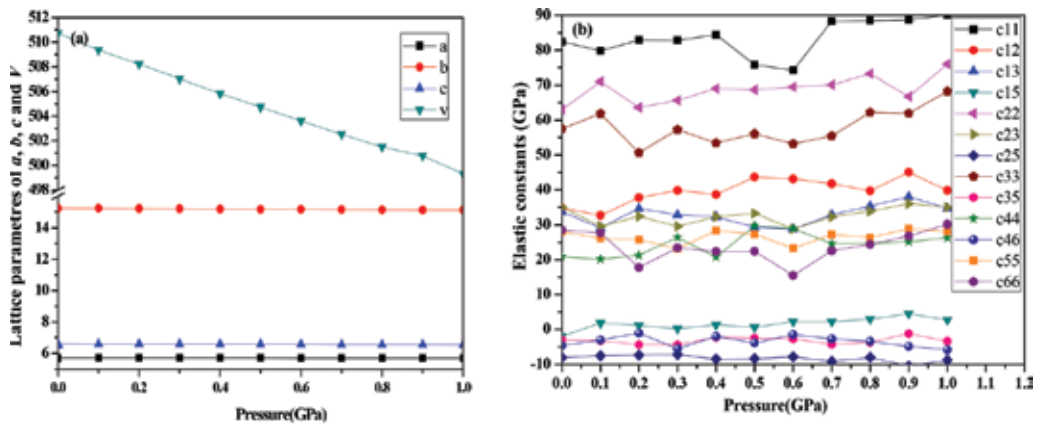**Table 3.** Atomic coordinates and displacement parameters of 11 Å tobermorite [38].

Figure 3. Gypsum monoclinic crystal under pressure 0–1.0 GPa by DFT. (a) Relative change of *a, b, c,* and *V* and (b) elastic constants.

From **Figure 3**, elastic constants at 0 GPa are given as c_{11} = 82.464 GPa, c_{12} = 34.751 GPa, c_{13} = 33.643 GPa, c_{15} = −1.987 GPa, c_{22} = 63.046 GPa, c_{23} = 34.920 GPa, c_{25} = −8.071 GPa, c_{33} = 57.549 GPa, c_{35} = −3.054 GPa, c_{44} = 20.863 GPa, c_{46} = −4.688 GPa, c_{55} = 28.062 GPa, and c_{66} = 28.556 GPa. It is found that the oxygen atom of the water molecule did not change its position or occupancy under pressure conditions. A simple pressure increase at an ambient temperature cannot induce dehydration because of the unchange of water molecular in the gypsum structure within pressure range [36].

Elastic constants of gypsum crystal model based on DFT are calculated, and parameters are detailed in **Table 4**.

4.2.2. Initial conditions and elastic constants of tobermorite

Initial conditions of tobermorite are quite the same with that of gypsum crystal. Elastic constants of 11 Å tobermorite crystal under 0–1.0 GPa are shown in **Figure 4**. Elastic constants are shown in **Table 5**.

A comparisonal results of Shahsavari [39] are provided. Elastic constants at 0 GPa are as follows: c_{11} = 106.63 GPa, c_{12} = 50.37 GPa, c_{13} = 41.09 GPa, c_{15} = −3.50 GPa, c_{22} = 131.67 GPa, c_{23} = 22.78 GPa, c_{25} = −0.78 GPa, c_{33} = 71.45 GPa, c_{35} = −0.83 GPa, c_{44} = 26.03 GPa, c_{46} = −0.02 GPa, c_{55} = 27.61 GPa, and c_{66} = 45.26 GPa. Thus, elastic modulus can be homogenized to compare with the results of LD C-S-H phase in nano-indentation test by Vandamme and Ulm [40].

4.3. Homogenized elastic moduli of typical monoclinic structures

4.3.1. Elastic modulus of monoclinic gypsum structure

Based on elastic constants, the elastic moduli of gypsum at 0 GPa are verified and averaged in **Figure 5**.

P	C_{11}	C_{12}	C_{13}	C_{15}	C_{22}	C_{23}	C_{25}	C_{33}	C_{35}	C_{44}	C_{46}	C_{55}	C_{66}
$10^{-4[36]}$	—	—	—	—	—	—	—	—	—	—	—	—	—
0.0	82.46	34.75	33.64	−1.99	63.05	34.92	−8.07	57.55	−3.05	20.86	−4.69	28.06	28.56
0.1	79.82	32.64	29.2	1.8	71.04	29.61	−7.54	61.88	−3.22	20.13	−3.06	26.19	27.7
0.2	82.93	37.75	34.59	1.09	63.62	32.42	−7.35	50.64	−4.37	21.32	−1.1	25.8	17.8
0.3	82.82	39.77	32.81	0.17	65.64	29.61	−7.23	57.31	−4.45	26.43	−5.57	23.17	23.39
0.4	84.47	38.6	32.25	1.27	69.03	32.31	−8.51	53.41	−2.21	20.8	−2.03	28.41	22.34
0.5	75.84	43.68	29.39	0.57	68.7	33.18	−8.36	56.08	−2.52	29.7	−3.88	27.35	22.4
0.6	74.22	43.11	28.77	2.22	69.52	28.87	−7.81	53.19	−2.68	28.97	−1.49	23.24	15.53
0.7	88.37	41.74	32.85	2.25	70.09	32.28	−9.14	55.48	−4.28	24.66	−2.76	27.25	22.58
0.8	88.53	39.65	35.29	2.96	73.28	33.84	−8.02	62.22	−3.73	24.73	−3.44	26.37	24.39
0.9	88.7	45.09	37.97	4.54	66.78	36.02	−10.4	61.98	−1.2	25.15	−4.92	28.93	26.82
1.0	90.12	39.79	34.63	2.7	75.99	34.92	−8.74	68.31	−3.46	26.32	−5.83	28.15	30.19

Table 4. Elastic coefficient C_{ij} (GPa) of gypsum by DFT.
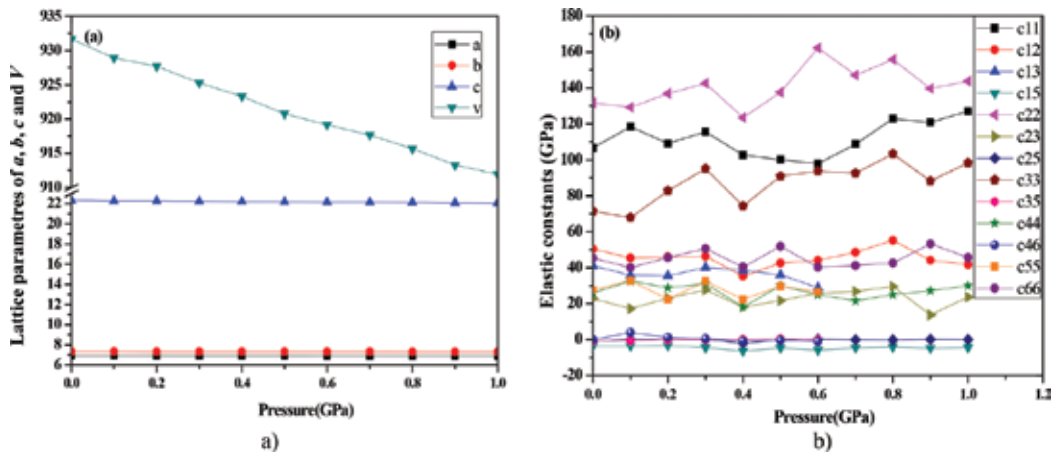
Figure 4. 11 Å tobermorite monoclinic crystal under pressure 0–1.0 GPa by DFT. (a) Relative change of *a*, *b*, *c*, and *V* and (b) elastic constants.

P/GPa	C_{11}	C_{12}	C_{13}	C_{15}	C_{22}	C_{23}	C_{25}	C_{33}	C_{35}	C_{44}	C_{46}	C_{55}	C_{66}
SHA[39]	102.65	41.68	27.70	1.25	125.05	18.83	−4.10	83.80	−3.38	22.90	−11.93	23.25	50.20
0.0	106.63	50.37	41.09	−3.50	131.67	22.78	−0.78	71.45	−0.83	26.03	−0.02	27.61	45.26
0.1	118.37	45.40	35.91	−3.52	129.18	17.19	0.11	67.84	−0.55	32.51	3.90	32.74	40.07
0.2	109.13	45.84	35.63	−3.22	136.79	23.05	0.03	82.75	0.06	28.88	1.21	22.40	45.69
0.3	115.53	46.36	40.17	−4.46	142.59	27.65	−0.04	95.03	0.02	31.08	0.49	32.38	50.57
0.4	102.65	35.38	38.73	−6.32	123.43	18.11	−1.92	74.28	0.05	18.14	−0.83	22.38	40.44
0.5	100.08	42.58	36.10	−4.52	137.56	21.68	−0.26	90.87	0.36	29.92	−0.46	29.66	51.82
0.6	97.87	44.09	28.76	−5.85	162.17	25.77	0.19	93.71	−0.14	24.89	−1.20	26.63	40.26
0.7	108.73	48.60	34.07	−4.55	147.09	26.78	−0.14	92.64	−0.01	21.56	2.06	44.25	41.23
0.8	122.87	55.30	40.62	−4.05	155.75	29.54	−0.25	103.3	−0.57	24.90	0.72	33.31	42.67
0.9	120.77	44.19	45.41	−4.82	139.59	13.68	0.09	88.25	−0.19	27.18	−0.35	26.85	53.22
1.0	127.01	41.78	45.00	−4.47	143.72	23.65	−0.02	98.30	−0.12	29.98	0.71	32.08	45.68

Table 5. Elastic coefficient C_{ij} (GPa) of 11 Å tobermorite by DFT.

As gypsum shows anisotropic compressibility along three crystallographic axes with b > c > a below 5 GPa [44], the pressure region of 0–1.0 GPa is used to verify whether the performance of model under low pressure is stable. Mechanical moduli of gypsum polycrystalline are listed in **Table 6**.

As an acoustic method [41] and mechanical properties [42] have been investigated, according to elastic constants of gypsum crystal [43], elastic moduli by experiment can be calculated, as shown in **Table 6**. Elastic moduli are as follows: G_v = 22.146 GPa, G_r = 19.705 GPa, B_v = 45.521 GPa, B_r = 43.822 GPa, B = 44.672 GPa, G = 20.926 GPa, E = 54.299 GPa, and μ = 0.2974. These results are close to the plane-strain value of Young's modulus by reference
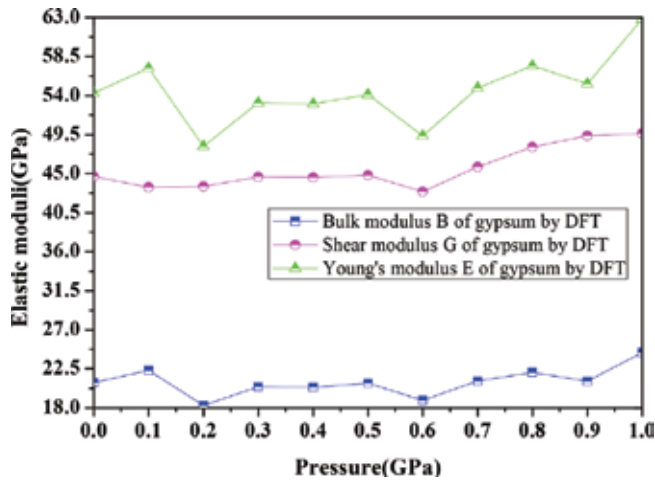
Figure 5. Elastic moduli of gypsum crystal under pressure 0–1.0 GPa.

Pressure (GPa)	G_v (GPa)	B_v (GPa)	G_r (GPa)	B_r (GPa)	B (GPa)	G (GPa)	E (GPa)	μ
Reference [43]	26.5333	39.2556	24.8077	39.2381	25.6705	39.2469	63.2265	0.2315
0.0	22.1459	45.5208	19.7054	43.8224	20.9257	44.6716	54.2985	0.2974
0.1	22.8896	43.9624	21.7569	42.9250	22.3233	43.4437	57.1766	0.2806
0.2	19.1472	45.1906	17.4395	41.9064	18.2934	43.5485	48.1394	0.3158
0.3	21.5041	45.5718	19.3501	43.6675	20.4271	44.6197	53.1678	0.3014
0.4	21.2263	45.9146	19.5324	43.2463	20.3794	44.5805	53.0537	0.3017
0.5	22.1809	45.9026	19.4980	43.7566	20.8395	44.8296	54.1306	0.2988
0.6	19.9615	44.2709	17.7554	41.5818	18.8585	42.9264	49.3486	0.3084
0.7	22.0356	47.5189	20.1833	44.0623	21.1095	45.7906	54.8931	0.3002
0.8	22.7817	49.0659	21.3745	47.0681	22.0781	48.0670	57.4399	0.3008
0.9	22.7399	50.6242	19.4094	48.1542	21.0747	49.3892	55.3510	0.3132
1.0	25.2707	50.3430	23.4785	48.9327	24.3746	49.6379	62.8382	0.2890

Table 6. Mechanical moduli of gypsum polycrystalline by different methods.

[44] E = 50 GPa, μ = 0.45. By comparison of gypsum crystal and CH crystal, axial moduli of gypsum in x, y, and z directions are 57.75, 37.22, and 34.91 GPa, while axial moduli of $Ca(OH)_2$ in x, y, and z directions are 93.75, 93.75, and 42.39 GPa, showing that gypsum crystal is much less anisotropic than hydrogen-bonded layered Ca(OH)2 structure [42].

4.3.2. Elastic modulus of monoclinic tobermorite structure

Based on elastic constants of 11 Å tobermorite crystal using GGA calculation method by DFT, bulk modulus B and shear modulus G are separately calculated by Eqs. (37)–(50) (**Figure 6**).

Elastic moduli at 0 GPa are verified and averaged as G_v = 32.815 GPa, B_v = 59.803 GPa, G_r = 29.908 GPa, B_r = 54.276 GPa, E = 79.512 GPa, and μ = 0.268. Young's modulus is about 79.512 GPa by Reuss-Voigt-Hill estimation, which is close to the simulation result of 89 GPa [45] by Pellenq and result of 78.939 GPa [39] by Shahsavari. Mechanical moduli by different methods are listed in **Table 7**.

However, these values considering the ordered Si-chain at a long range are far away from the nano-indentation experiment performed on the C-S-H phase [40, 46]. It confirms the absence of order at a long range in this phase and that the up-scaling to polycrystals cannot be done with the tobermorite model. Modeling of C-S-H structure with disordered Si chain should be fairly considered.
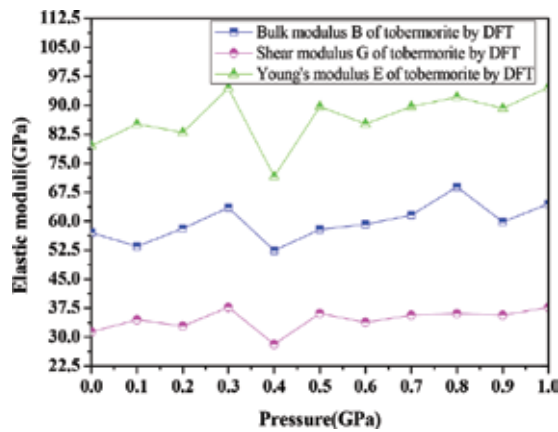

Figure 6. Elastic moduli of 11 Å tobermorite crystal under pressure 0–1.0 GPa.

Pressure (GPa)	B_v (GPa)	B_r (GPa)	G_v (GPa)	G_r (GPa)	B (GPa)	G (GPa)	E (GPa)	μ
Reference [191]	54.2133	51.6976	34.1560	28.9168	52.9555	31.5364	78.9391	0.2516
0.0	59.8066	54.2778	32.8140	29.9063	57.0399	31.3615	79.5121	0.2677
0.1	56.9306	50.1535	35.5205	33.4468	53.5438	34.4843	85.1689	0.2349
0.2	59.7454	56.4236	34.3364	31.4164	58.0846	32.8763	82.9743	0.2619
0.3	64.6138	62.4671	38.7385	36.7029	63.5388	37.7202	94.4669	0.2522
0.4	53.8665	50.9999	30.0678	26.1841	52.4333	28.1257	71.5786	0.2725
0.5	58.8039	56.9635	37.4898	34.7400	57.8831	36.1145	89.6903	0.2417
0.6	61.2236	57.0694	35.3648	32.2837	59.1442	33.8242	85.2259	0.2598
0.7	63.0391	60.0785	37.3432	34.0050	61.5598	35.6744	89.6966	0.2572
0.8	70.3213	67.4998	37.2739	34.9015	68.9022	36.0849	92.1653	0.2771
0.9	61.6837	57.8325	37.8067	33.5164	59.7599	35.6606	89.2325	0.2511
1.0	65.5442	63.4872	38.6855	36.6712	64.5147	37.7292	94.7226	0.2553

Table 7. Mechanical moduli of 11Å tobermorite polycrystalline by different methods.

5. Conclusions

Elastic constants of gypsum and tobermorite structures under a certain pressure region are calculated by DFT method, which has a certain value for both application and reference. Results are as follows:

1. For monoclinic gypsum and tobermorite crystals, elastic coefficients are obtained in 0–1-GPa pressure range to verify the reliability of the model by comparing other literatures.

2. Elastic constants of gypsum single crystal at 0 GPa are given as follows: c_{11} = 82.464 GPa, c_{12} = 34.751 GPa, c_{13} = 33.643 GPa, c_{15} = −1.987 GPa, c_{22} = 63.046 GPa, c_{23} = 34.920 GPa, c_{25} = −8.071 GPa, c_{33} = 57.549 GPa, c_{35} = −3.054 GPa, c_{44} = 20.863 GPa, c_{46} = −4.688 GPa, c_{55} = 28.062 GPa, and c_{66} = 28.556 GPa.

3. Elastic constants of 11Å tobermorite single crystal at 0 GPa are as follows: c_{11} = 106.63 GPa, c_{12} = 50.37 GPa, c_{13} = 41.09 GPa, c_{15} = −3.50 GPa, c_{22} = 131.67 GPa, c_{23} = 22.78 GPa, c_{25} = −0.78 GPa, c_{33} = 71.45 GPa, c_{35} = −0.83 GPa, c_{44} = 26.03 GPa, c_{46} = −0.02 GPa, c_{55} = 27.61 GPa, and c_{66} = 45.26 GPa.

4. Young's modulus of gypsum is about 54.299 GPa. Elastic moduli at 0 GPa are as follows: G_v = 22.146 GPa, G_r = 19.705 GPa, B_v = 45.521 GPa, B_r = 43.822 GPa, E = 54.299 GPa, and μ = 0.297.

5. Young's modulus of 11Å tobermorite is about 79.512 GPa. Elastic moduli at 0 GPa are as follows: G_v = 32.815 GPa, B_v = 59.803 GPa, G_r = 29.908 GPa, B_r = 54.276 GPa, E = 79.512 GPa, and μ = 0.268.

Structural, elastic properties of monoclinic crystals are investigated, and C_{ij} determination is given by DFT method. Reuss-Voigt-Hill estimation has been used for polycrystal structures and can be seen as an intermediate step in the homogenization of elastic properties.

Acknowledgements

Author details

Jia Fu[1,2]*

*Address all correspondence to: fujia@xsyu.edu.cn

1 Xi'an Shiyou University, Xi 'an, China

2 INSA de Rennes, Rennes, France

References

[1] Messaoudi IS, Zaoui A, Ferhat M. Band-gap and phonon distribution in alkali halides [J]. Physica Status Solidi B. 2015;**252**(3):490-495. DOI: 10.1002/pssb.201451268

[2] Thomas LH. The calculation of atomic fields, [C]. Mathematical Proceedings of the Cambridge Philosophical Society. Cambridge University Press. 1927;**23**(05):542-548. DOI: 10.1017/S0305004100011683

[3] Dirac PAM. Note on exchange phenomena in the Thomas atom [J]. Mathematical Proceedings of the Cambridge Philosophical Society. 1930;**26**:376-385. DOI: 10.1017/S0305004100016108

[4] Kohn W, Sham LJ. Self-consistent equations including exchange and correlation effects [J]. Physical Review. 1965;**140**(4A):A1133. DOI: 10.1103/PhysRev.140.A1133

[5] Levy M, Perdew JP, Sahni V. Exact differential equation for the density and ionization energy of a many-particle system [J]. Physical Review A. 1984;**30**(5):2745. DOI: 10.1103/PhysRevA.30.2745

[6] Foulkes WMC, Mitas L, Needs RJ, et al. Quantum Monte Carlo simulations of solids [J]. Reviews of Modern Physics. 2001;**73**(1):33. DOI: 10.1103/RevModPhys.73.33

[7] Aulbur WG, Jönsson L, Wilkins JW. Quasiparticle calculations in solids [J]. Solid State Physics. 1999;**54**:1-218. DOI: 10.1016/S0081-1947(08)60248-9

[8] Luther DIT. Homogenization of Damaged Concrete Meso-Structures Using Representative Volume Elements-Implementation and Application to Slang, Doctoral dissertation. Weimar Germany: Bauhaus-University; 2005

[9] Zhu QZ, Kondo D, Shao JF. Micromechanical analysis of coupling between anisotropic damage and friction in quasi brittle materials: Role of the homogenization scheme. International Journal of Solids and Structures. 2008;**45**(5):1385-1405. DOI: 10.1016/j.ijsolstr.2007.09.026

[10] Behnken H, Hauk V. Berechnung der röntgenographischen Elastizitäts-konstanten (REK) des Vielkristalls aus Einkristalldaten für beliebige Kristallsymmetrie[J]. Zeitschrift für Metallkunde. 1986;**77**:620-626

[11] Gnäupel-Herold T. A software for diffraction stress factor calculations for textured materials[J]. Powder Diffraction. 2012;**27**(02):114-116. DOI: 10.1017/S0885715612000267

[12] Kneer G. Die elastischen Konstanten quasiisotroper Vielkristallaggregate[J]. Physica Status Solidi B. 1963;**3**(9):K331-K335. DOI: 10.1002/pssb.19630030924

[13] Reuss A. ZAMM – Journal of Applied Mathematics and Mechanics/Zeitschrift für Angewandte Mathematik und Mechanik. 1929;**9**(1):49-58. DOI: 10.1002/zamm.19290090104

[14] Voigt W. Lehrbuch Der Kristallphysik Teubner, Leipzig 1910; Reprinted (1928) with an Additional Appendix. Leipzig, Teubner, New York: Johnson Reprint

[15] Kamali-Bernard S, Bernard F. Effect of tensile cracking on diffusivity of mortar: 3D numerical modelling [J]. Computational Materials Science. 2009;**47**:178-185. DOI: 10.1016/j.commatsci.2009.07.005

[16] Born M, Oppenheimer R. Zur quantentheorie der molekeln [J]. Annalen der Physik. 1927;**389**(20):457-484. DOI: 10.1002/andp.19273892002

[17] Hohenberg P, Kohn W. Inhomogeneous electron gas [J]. Physical Review. 1964;**136**(3B): B864. DOI: 10.1103/PhysRev.136.B864

[18] Ceperley DM, Alder BJ. Ground state of the electron gas by a stochastic method[J]. Physical Review Letters. 1980;**45**(7):566. DOI: 10.1103/PhysRevLett.45.566

[19] Perdew JP, Zunger A. Self-interaction correction to density-functional approximations for many-electron systems [J]. Physical Review B. 1981;**23**(10):5048. DOI: 10.1103/PhysRevB.23. 5048

[20] Herman F, Van Dyke JP, Ortenburger IB. Improved statistical exchange approximation for inhomogeneous many-electron systems [J]. Physical Review Letters. 1969;**22**(16):807. DOI: 10.1103/PhysRevLett.22.807

[21] Perdew JP, Burke K. Comparison shopping for a gradient-corrected density functional [J]. International Journal of Quantum Chemistry. 1996;**57**(3):309-319. DOI: 10.1002/(SICI) 1097-461X(1996)57:3.3.CO;2-A.

[22] Becke AD. Density-functional exchange-energy approximation with correct asymptotic behavior [J]. Physical Review A. 1988;**38**(6):3098. DOI: 10.1103/PhysRevA.38.3098

[23] Perdew JP, Wang Y. Accurate and simple analytic representation of the electron-gas correlation energy [J]. Physical Review B. 1992;**45**(23):13244. DOI: 10.1103/PhysRevB.45.13244

[24] Perdew JP, Burke K, Ernzerhof M. Generalized gradient approximation made simple[J]. Physical Review Letters. 1996;**77**(18):3865. DOI: 10.1103/PhysRevLett.77.3865

[25] Baldereschi A. Mean-value point in the Brillouin zone [J]. Physical Review B. 1973;**7**(12): 5212. DOI: 10.1103/PhysRevB.7.5212. DOI: 10.1103/PhysRevB.13.5188

[26] Chadi DJ, Cohen ML. Special points in the Brillouin zone [J]. Physical Review B. 1973;**8**(12): 5747. DOI: 10.1103/PhysRevB.8.5747

[27] Monkhorst HJ, Pack JD. Special points for Brillouin-zone integrations [J]. Physical Review B. 1976;**13**(12):5188

[28] Shao TJ, Wen B, Melnik R, et al. Temperature dependent elastic constants for crystals with arbitrary symmetry: Combined first principles and continuum elasticity theory [J]. Journal of Applied Physics. 2012;**111**:083525. DOI: 10.1063/1.4704698

[29] Bauernschmitt R, Ahlrichs R. Stability analysis for solutions of the closed shell Kohn–Sham equation [J]. The Journal of Chemical Physics. 1996;**104**(22):9047-9052. DOI: 10.1063/1.471637

[30] Catti M. Calculation of elastic constants by the method of crystal static deformation [J]. Acta Crystallographica Section A. 1985;**41**:494-500. DOI: 10.1107/S0108767385001052

[31] Ting TCT. Anisotropic Elasticity-Theory and Applications [M]. Oxford: Oxford University Press; 1996

[32] Wu ZJ, Zhao EJ, Xiang HP, et al. Crystal structures and elastic properties of superhard IrN2 and IrN3 from first principles [J]. Physical Review B. 2007;**76**(5):054115. DOI: 10.1103/PhysRevB.76.054115

[33] Hill R. The elastic behaviour of a crystalline aggregate[J]. Proceedings of the Physical Society. Section A. 1952;**65**(5):349. DOI: 10.1088/0370-1298/65/5/307

[34] Raabe D. Computational Materials Science: The Simulation of Materials Microstructures and Properties. Weinheim: Wiley-VCH; 1998

[35] Knight KS, Stretton IC, Schofield PF. Temperature evolution between 50 K and 320 K of the thermal expansion tensor of gypsum derived from neutron powder diffraction data [J]. Physics and Chemistry of Minerals. 1999;**26**(6):477-483. DOI: 10.1007/s002690050

[36] Comodi P, Nazzareni, et al. High-pressure behavior of gypsum: A single-crystal X-ray study[J]. American Mineralogist. 2008;**93**(10):1530-1537. DOI: 10.2138/am.2008.2917

[37] Hamid SA. The crystal structure of the 11Å natural tobermorite $Ca_{2.25}[Si_3O_{7.5}(OH)_{1.5}]\cdot$ $1H_2O$[J]. Zeitschrift für Kristallographie-Crystalline Materials. 1981;**154**(1–4):189-198. DOI: 10.1524/zkri.1981.154.3-4.189

[38] Merlino S, Bonaccorsi E, et al. The real structure of tobermorite 11Å normal and anomalous forms, OD character and polytypic modifications[J]. European Journal of Mineralogy. 2001;**13**(3):577-590. DOI: 10.1127/0935-1221/2001/0013-0577

[39] Shahsavari R, Buehler MJ, Pellenq RJM, et al. First-principles study of elastic constants and interlayer interactions of complex hydrated oxides: Case study of tobermorite and jennite[J]. Journal of the American Ceramic Society. 2009;**92**(10):2323-2330. DOI: 10.1111/j.1551-2916.2009.03199.x

[40] Vandamme M, Ulm FJ. Nanondentation investigation of creep properties of calcium silicate hydrates[J]. Cement and Concrete Research. 2013;**52**:38-52. DOI: 10.1016/j.cemconres.2013.05.006

[41] Haussuhl S. Elastische und Thermoelastische Eingenschaften von $CaSO_4.2H_2O$ (Gips)[J]. Zeitschrift für Kristallographie. 1960;**122**:311-314. DOI: 10.1515/zkri-1965-1-628

[42] Watt JP. Hashin-Shtrikman bounds on the effective elastic moduli of polycrystals with monoclinic symmetry[J]. Journal of Applied Physics. 1980;**51**:1520-1524. DOI: 10.1063/1.327803

[43] Meille S, Garboczi EJ. Linear elastic properties of 2D and 3D models of porous materials made from elongated objects[J]. Modelling and Simulation in Materials Science and Engineering. 2001;**9**(5):371. DOI: 10.1088/0965-0393/9/5/303

[44] Huang E, Ku J, Lin J, Hu J. Pressure-induced phase transition in gypsum[J]. High Pressure Research. 2000;**17**:57-75. DOI: 10.1080/08957950008200306

[45] Pellenq RJM, Lequeux N, Van Damme H. Engineering the bonding scheme in C-S-H: The iono-covalent framework [J]. Cement and Concrete Research. 2008;**38**(2):159-174. DOI: 10.1016/j.cemconres.2007.09.026

[46] Miller M, Bobko C, Vandamme M, Ulm F-J. Surface roughness criteria for cement paste nanoindentation[J]. Cement and Concrete Research. 2008;**38**:467-476. DOI: 10.1016/j.cemconres.2007.11.014

Multidisciplinary Integration

Application of Density Functional Theory in Soil Science

Jiena Yun, Qian Wang, Chang Zhu and Gang Yang

Additional information is available at the end of the chapter

Abstract

Soil is the basis for life and soil science is regarded as the final frontier; however, as compared to chemistry, physics, biology, and other disciplines, soil science undergoes an obviously slower development and remains almost stagnant in the past few decades, mainly due to two reasons: (1) wrong and outdated perceptions for a large portion of soil researchers; (2) complexity of soil systems that are difficult to characterize by current experimental techniques. Computer simulations have unique advantages to handle complex systems while currently, its role during soil researches is far from being recognized. In this chapter, several examples are given with respect to application of density functional theory (DFT) calculations to soil science, focusing on the adsorption of uranyl ion and SO_2 onto mineral surfaces and reaction mechanisms to form acid rain. In this way, insightful clues at the atomic level are provided for the adsorption, interaction, and reactions regarding soil systems. We believe that computer simulations including DFT are the right key to unravel the complicated processes occurring in soils. More efforts of computer simulations are anticipated for soil science with aim to decipher the experimental results and probe the uncharted principles that may result in a revolutionary in the near future.

Keywords: soil science, computer simulations, density functional theory, interfacial adsorption, reaction mechanism, complex systems

1. Introduction

According to Natural Resources Conservation Service (NRCS), soil is defined as a natural body comprised of solids (mainly minerals and organic matters), liquids, and gases that occurs at the intermediate surface of the Earth, occupies space and is characterized by one or both of the following properties: horizons and layers, which are distinguishable from the initial materials as a result of addition, loss, transfer, and transformation of energy and matter or the ability to

support rooted plants in natural circumstances. Soil constitutes the basis for life and bridges the biosphere, atmosphere, hydrosphere, and geosphere. Despite these facts, apparently less attention has been given to soil science than to other disciplines such as physics, chemistry, and biology. As said by Gardner (the past president of Soil Science Society of America) [1], "not a few people mistakenly perceive that everything worth knowing about soils has already been understood, and all we need to do is merely to apply that knowledge properly. Even knowledgeable scientists assume that principles and theories developed from other disciplines can be applied to the researches of soil science in a straightforward way, requiring little imagination or creativity. In their opinions, soil science is just one of expressions for the applied physics, chemistry, or biology."

The situation of soil science research is alarming. The core concepts of current soil science textbooks remain almost unchanged as compared to those of half a century ago. Obsolete or even incorrect standpoints are a commonplace [2]. Fortunately, a few researchers have recognized such a crisis. On the other hand, because of the complexity of systems and co-function of multiple factors, it seems challenging for experimental techniques to *in-situ* characterize "real" soil properties and processes; in addition, the experimental results from one lab may not be reproducible by others, since soil samples of different areas or even different batches may vary significantly. Computer simulations have unique advantages within this context: (1) probing the various influencing factors one by one; e.g., six factors (identity of heteroatoms, crystallographically distinct T sites, structural alterations, quantity of negative charges, distance from charge centers to metal ions and source of negative charges) were identified to affect the adsorption of metal ions at clay surfaces, and their respective contributions were estimated by density functional theory (DFT) calculations. The quantity of negative charges is the foremost factor that controls the adsorption processes, while other factors in certain circumstances can also play a critical role [3]. The adsorption strengths and numbers of all metal ions increase in a direct proportion to the intensities of electric fields [4]; (2) providing useful and detailed information at the femtosecond scale such as how ions from aqueous solutions diffuse toward to clay surfaces [5]; (3) understanding the adsorption, interaction and reaction processes at the atomic level such as how metal ions interact with surface-O atoms and respond to the increase of electric fields. Based on Hirshfeld, Mulliken, and NBO charge analyses, we found that polarization rather than electrostatic interactions are more likely to result in the pronounced cation-specific effects at clay surfaces [6]; (4) unraveling the exact reaction mechanism by comparing the structural and (especially) activation barriers of competing paths. This can be considered as an extension of (3). There are a plethora of competing reactions occurring in soils; e.g., with DFT calculations, it was clarified that Mn^{4+} rather than Mn^{3+} sites are more reactive for the oxidation of As^{3+} and the oxidation processes are significantly blocked by As^{5+} complexes [7]. A more convictive example is the mechanistic study of Brönsted acid-catalyzed conversion of biomass sugars [8]. More than 120 reaction paths were explored, and the low reactivity and selectivity of glucose conversions were clearly addressed: unlike fructose that prefers to dehydrate at the anomeric O_2H group and initiates a sequence of facile reaction steps toward 5-hydroxymethyl-2-furfural (HMF), the less reactive sites in glucose (O_2H and O_3H) produces levulic acid not involving fructose and HMF intermediates, while the most reactive O_1H site leads to humin precursors or reversion products [8].

The relationship between system size and computational accuracy for representative theoretical levels is shown in **Figure 1**. For huge systems (100,000 or even more atoms), classical methods (Monte Carlo and Molecular Dynamics) seems to be the good choice, although the computational accuracy is relatively low; In contrast, *ab initio* quantum mechanical methods are restricted to relatively small systems (up to several hundred atoms or even fewer atoms) while achieve high accuracy. The computational accuracy of quantum mechanics/molecular mechanics (QM/MM) [9] and semi-empirical methods fall in-between, and QM/MM methods have recently become increasingly popular due to the satisfying computational accuracy (active sites handled by QM methods) and the easy extension to large systems (all atoms except active sites disposed by classical methods). 2013 Noble Prize in Chemistry was awarded to Karplus, Levitt, and Warshel for the development of "multiscale methods for complex systems."

Let us look back to *ab initio* quantum mechanical methods. Strictly speaking, a large portion of DFT methods fall outside this scope; e.g., B3LYP is probably the most popular DFT method and its exchange-correlation functional is written as [10, 11]

$$E_{xc}^{B3LYP} = (1 - a)E_x^{LSDA} + aE_x^{HF} + bE_x^{B88} + cE_c^{LYP} + (1 - c)E_c^{LSDA}$$

where a, b, and c are empirical parameters.

There is a five-rung Jacob's ladder of common density functional approximations, as local spin-density approximation (LSDA), generalized-gradient approximation (GGA), meta-GGA, hyper-GGA, and random phase approximation (PRA-like functionals), see more details in [12]. As far as we know, the most widely density functionals are at GGA (e.g., B3LYP, PBE) and meta-GGA (e.g., M06 L, M06-2X) levels.

Computer simulations, as discussed above, are particularly useful to handle the complex soil systems, and two applications were illustrated in this chapter. Section 2 summarized DFT
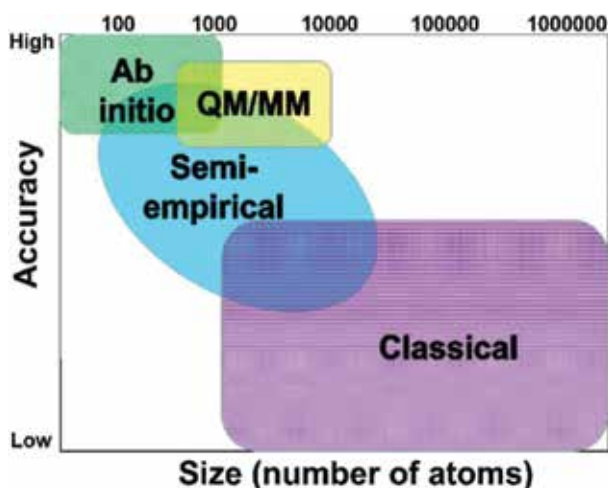

Figure 1. The theoretical landscape regarding to the balance between system size and computational accuracy.

calculated results of uranyl adsorption onto mineral surfaces and Section 3 elaborately discussed DFT calculated results of SO_2 (one of the main precursors for acid rain) adsorption and formation mechanisms of acid rain. In the end, concluding remarks were provided and some suggestions for DFT applications to the future soil researches were presented as well. A more critical role of computer simulations should have played in soil science, and this chapter aims to arouse the attention of general soil researchers regarding to the applications of computer simulations. More efforts in this regard are greatly beneficial to decipher the experimental results and probe the uncharted principles that will result in a revolutionary for soil science in the near future.

2. Uranyl adsorption onto mineral surfaces

Release of radionuclides into the environment seriously threatens the ecosystem and human health, and adsorption of radionuclides onto mineral surfaces significantly affects their migration and transport into the environment [13]. Accordingly, knowledge about the interaction between radionuclides and minerals is essential for the long-term risk assessment of radioactive waste repositories. Uranium is usually present in the uranyl (UO_2^{2+}) form [14, 15] and DFT calculations have been conducted to understand the adsorption of UO_2^{2+} onto mineral surfaces [16–25].

Perron et al. [16] examined UO_2^{2+} adsorption onto rutile(110) surface, the most stable face of natural rutile reported by Jones and Hockey [26, 27]. UO_2^{2+} forms a bidentate inner sphere complex with three H_2O molecules to fill its first hydration shell, see **Figure 2**. There exist two types of surface-O atoms, as O_t (terminal-O) and O_b (bridging-O) that are singly and doubly coordinated, respectively. As a result, a total of three adsorption structures are produced: UO_2^{2+} coordinated to two O_b atoms (bb), two O_t atoms (tt) and both of O_b and O_t atoms (bt). The bb mode is the most preferred and has a lower energy than the bt and tt modes by 5.0 and 13.6 kJ/mol, respectively.

In addition to the $[UO_2(H_2O)_n]^{2+}$ adsorption complexes, other uranyl species containing anionic ligands such as OH^- and CO_3^{2-} also play a critical role in the environmental circumstances. Pan and co-workers [17] investigated the effects of different ligands (H_2O, OH^-, CO_3^{2-}) on the adsorption on rutile(110) surface. Note that only the most stable adsorption mode (bb) has been taken into account therein. The uranyl ion (UO_2^{2+}) interacts more strongly with anionic ligands
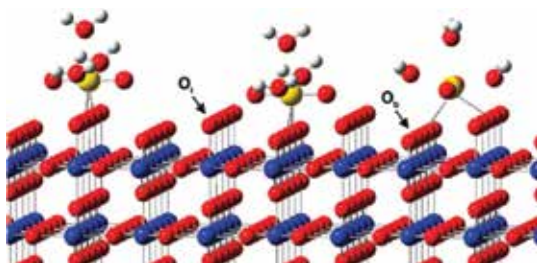

Figure 2. Adsorption structures for uranyl ions on rutile(110) surface: tt (Left), bb (Middle), and bt (Right). U, Ti, O, and H are respectively in yellow, blue, red, and white, and H atoms to saturate surface-O atoms are not shown for clarity.

(OH$^-$ and CO$_3^{2-}$) than H$_2$O in the first coordination sphere. The bond lengths of the U^{6+} center and two O$_b$ atoms are respectively calculated at 2.248 and 2.333 Å for [UO$_2$(H$_2$O)$_3$]$^{2+}$, 2.808 and 2.930 Å for [UO$_2$(OH)$_3$]$^-$, 2.852 and 2.960 Å for [UO$_2$(CO$_3$)$_2$]$^{2-}$, suggesting that the adsorption strengths of the uranyl ion with rutile(110) surface are significantly impaired in the latter two cases. Adsorption of these uranyl complexes on partially hydrated surfaces were then studied, which exhibit stronger interactions and are attributed to the formation of H-bonds between H$_2$O molecules and uranyl ion (UO$_2^{2+}$) that strengthen the adsorption processes.

Kaolinite is the major constituent of sedimentary clay rocks, and adsorption of uranyl species onto its (001) surface [20, 21] and (010) edge surface [22, 23] have been theoretically studied. The adsorption of uranyl species on tetrahedral SiO$_4$ surfaces is thermodynamically unfavorable, with the adsorption energies of inner- and outer-sphere complexes being, respectively, 239 and 206 kJ/mol [20]; in contrast, the adsorption at octahedral AlO$_6$ surfaces is preferred due to the presence of upright (perpendicular to the surface) and lying (parallel to the surface) OH groups. The most stable configuration corresponds to an inner-sphere monodentate complex, where UO$_2^{2+}$ bonds directly to the lying surface-OH group and has an adsorption energy of −155 kJ/mol. Martorell et al. [21] continued to study the adsorption of uranyl ion on the bare and solvated octahedral AlO$_6$ surfaces of kaolinite, where UO$_2^{2+}$ forms two direct bonds with
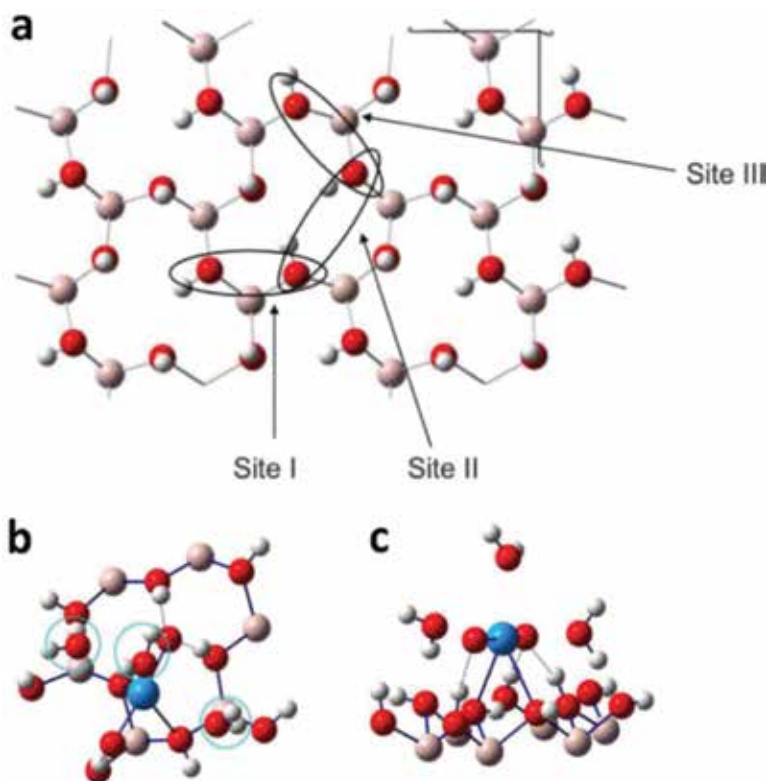

Figure 3. (a) Three sites for uranyl adsorption on gibbsite(001) surface and (b) top and (c) side views of the optimal adsorption complex. U, Al, O, and H are, respectively, in blue, pink, red, and white, and H-bonds are in black dash lines and water molecules are in circles.

the surface-O atoms of deprotonated OH groups. Two different adsorption structures are assigned according to the coordination of surface-O atoms: two surface-O atoms connected to one and two Al atoms are designated to be AlOO (short-bridge site) and AlO-AlO (long-bridge site), respectively. The formation of adsorption complex at the short-bridge site (AlOO) requires an energy of 195 kJ/mol and is obviously less than at the long-bridge site (AlO-AlO, 261 kJ/mol). Thus, the uranyl ion prefers to adsorption at the short-bridge site; furthermore, similar trends for uranyl adsorption remain when including solvent effects by adding a mono-layer of water molecules.

Gibbsite is a primary mineral form of aluminum hydroxide, and adsorption of the uranyl ion onto its (001) surface [18, 24] and edge surface [25] have been investigated, similar to the situation of kaolinite discussed above. **Figure 3a** depicts three potential adsorption sites for uranyl adsorption: Sites I and III hold almost the same O-O distances (about 2.7 Å), while site II shows an apparently elongated O-O distance (about 3.4 Å). Site I represents the lowest-energy adsorption structure (**Figure 3**), and the adsorption structures of sites II and III are less stable with relative energies being 22.2 and 46.3 kJ/mol, respectively. Three H-bonds constructed between surface-OH groups and UO_2^{2+} center as shown in **Figure 3** stabilize the interactions between uranyl ion and gibbsite surfaces.

3. Acid rain

In 1852, Smith demonstrated the relationship between acid rain and atmospheric pollution in Manchester, and after 20 years (i.e., 1872), he coined the term "acid rain." Now acid rain has become a popular term and one of the world's biggest environmental concerns, especially in North America, Europe, and China [28]. Acid rain refers to any form of precipitations with acidic components that fall to the ground from the atmosphere, including rain, snow, flog, hail, or even dust that is acidic. It results mainly from SO_2 and NO_x emissions to the atmosphere and the further transport by wind and air currents, during when SO_2 and NO_x react with water, oxygen, and other substances leading to the formation of sulfuric (H_2SO_4) and nitric (HNO_3) acids. The pH of acid rain is approximately 5.6 and since 1940s, researchers began to recognize its strong impacts on the ecosystem and human health so that soils, freshwaters, forests, and buildings will be damaged. With regard to soils, acid rain inhibits the decomposition of organic matter [29], fixation of nitrogen [30], elution of calcium (Ca^{2+}), magnesium (Mg^{2+}), potassium (K^+), and other nutrients [31]. As a result, soil fertility and microbial activity show an obvious reduction [32]. Geochemical modeling indicated that Ca^{2+} leaching in marble due to acid rain neutralization approximates 0.158 mmol/L, in contrast to 10.5 mmol/L by dry deposition, and the corresponding Cu^{2+} losses in bronze are ca. 0.21 and 47.3 mmol/L, respectively [33].

As aforementioned, SO_2 emissions are one of the principal causes of acid rain and also represent a primary source of atmospheric aerosols, which can lead to respiratory diseases, premature deaths, and even climate changes by affecting the properties of clouds and the balance of solar radiation. Therefore, it is of great significance to convert SO_2 to other less contaminated compounds, and a number of measures to control SO_2 emissions have been

proposed. During 1982–1999, SO_2 emissions have reduced by approximately 65% in Europe and 40% in the United States, and SO_2 emissions in China decline in the late 1990s while again increase after then. DFT calculations provide useful information about the adsorption of SO_2 onto mineral surfaces as well as reaction mechanisms that seem difficult to capture by current experimental techniques [34–45], which are, however, critical to understand the formation of acid rain at the molecular level and to remediate the ecosystem. Clay minerals, such as alumina (Al_2O_3), iron oxides (Fe_xO_y), are good candidates for the adsorption of acid components from acid rain and then convert them into less hazardous compounds. Lo et al. [35] studied the adsorption of SO_2 on clean (100), dehydrated (110), and hydrated (110) surfaces of γ-Al_2O_3, finding that significant adsorption differences exist for the various surfaces and the calculated adsorption energies (-13 to -85 kcal/mol) are consistent with experimental results.

The γ-Al_2O_3(100) surface is composed by bridging-O and five-coordinated Al atoms, and a total of five stable configurations are produced for SO_2 adsorption (**Figure 4**). The feeble interaction between S and surface-O atoms results in the physisorption configuration (CM3) with the S-O distance of 2.915 Å, and the corresponding binding energy is very small (-2.0 kcal/mol). The interaction between O@SO_2 and Al atoms leads to a chemisorption state named CM4, and the O-Al bond distance and adsorption energy are 2.123 Å and -23.9 kcal/mol, respectively. The other three configurations are also ascribed to chemisorption. In CM5, one O@SO_2 atom is coordinated to two Al atoms in the vicinity of an octahedral vacancy, and
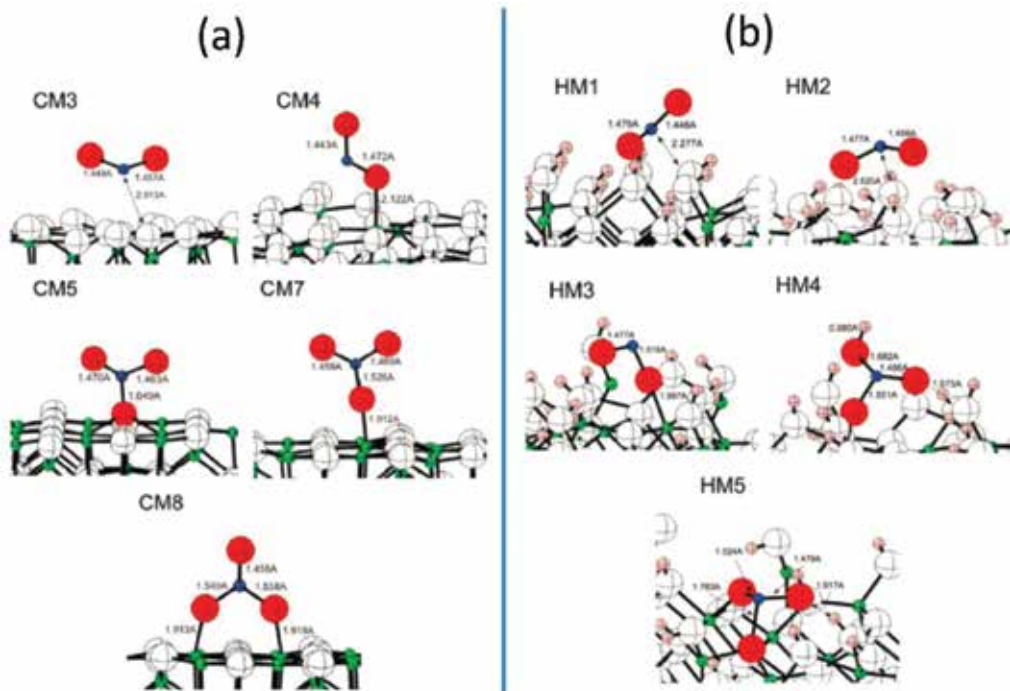

Figure 4. Optimized configurations of SO_2 adsorption on (a) dehydrated (100) and (b) hydrated (110) surfaces of γ-Al_2O_3, where Al, H, O, S, and O attached to S are presented in green, pink, white, blue, and red balls, respectively.

CM7 and CM8 can be considered to generate from CM5 conversion and recombination. As compared to CM5 and CM7, the adsorption configuration CM8 possesses a superior symmetry, and both O@SO_2 atoms participate in the formation of direct bonds with the Al atoms. The adsorption energies of SO_2 are calculated to be −39.2, −15.1, and −45.2 kcal/mol, respectively, for CM5, CM7, and CM8. In consequence, three types of sulfite (SO_3^{2-}) are produced during the adsorption of SO_2 onto γ-Al_2O_3(100) surface. For all adsorption configurations including three with positive adsorption energies (CM1: 1.0 kcal/mol, CM2: 2.7 kcal/mol, and CM6: 21.4 kcal/mol), no direct coupling is detected between S@SO_2 and Al atoms. When γ-Al_2O_3(110) surface is hydrated, five stable adsorption configurations arise that are distinct from dehydrated condition: two physisorption modes (HM1 and HM2) and three chemisorption modes (HM3, HM4, and HM5), see **Figure 4**. HM1 and HM2 are structurally similar in that their S atoms are coordinated to a surface hydroxyl, while the coordination numbers of their Al atoms are different from each other. HM3 is produced by interaction of O@SO_2 atom with five-fold Al sites. HM4 and HM5 contain the sulfite species where the S atom is coordinated with surface-O atoms. The adsorption energies are calculated to be −20.4, −25.3, −31.1, −17.5, and −35.0 kcal/mol, respectively, for HM1, HM2, HM3, HM4, and HM5. In consequence, HM5 with formation of the sulfite species represents the lowest-energy adsorption configuration, which is the same as in dehydrated condition (CM8). Two IR peaks at 1214 and 1349 cm^{-1} are assigned to the sulfate species, which can be been finely interpreted by DFT calculated results.

Goethite (α-FeO(OH)), which can be found in soils and other low-temperature environments, is an iron-bearing hydroxide. Because of the considerable adsorption capacity for organic acids and anions, goethite has also been widely used in environmental remediation and protection [35]. Zubieta et al. [37] investigated the adsorption of SO_2 on partially and fully hydrated (110) surfaces of goethite and obtained eight stable products: six sulfite, one bisulfate, and one sulfate (**Figure 5**). The six adsorption structures containing sulfite species, created only on two types of partially dehydrated goethite surfaces, are further divided into two monodentric mononuclear (MdMn) and four bidentate (Bd) configurations. In the MdMn configurations (I and II), the S-O_{Fe} distances are elongated as compared to the other S-O distances, and they display two symmetrical stretching modes (OSO and OSO$_{Fe}$) centered at ca. 1126 and 976 cm^{-1}. In BdBn configurations (I and II), the two S-O_{Fe} distances are approximately 1.62 Å, and although with similar geometries and stretching modes, the vibrational frequencies deviate significantly from those of MdMn configurations and fall at around 672 and 661 cm^{-1}. In BdPn configurations (I and II), one S-O_{Fe} distance is optimized at 1.75 Å and lengthened as compared to those of BdPn configurations, while the other S-O_{Fe} distance equals 1.55 Å and is obviously contracted. The Bader analyses indicate that all sulfite species carry approximately −1.4 |e| charges.

The bisulfate species is formed when the S atom constructs direct bonds with μ_1-OH (**Figure 5**), which is further stabilized by two H-bonds (1.77 and 1.81 Å). A similar bisulfate species was observed by Liu et al. [35] during the adsorption of SO_2 on γ-Al_2O_3 surfaces. The Bader analyses indicate that the HSO_3 species (bisulfate) carries −0.8 |e| charges. The computational sulfite and bisulfate species have IR spectra that are consistent with experimental results [37, 38]. The sulfate species emerges only when two water molecules are deprived from the (110)
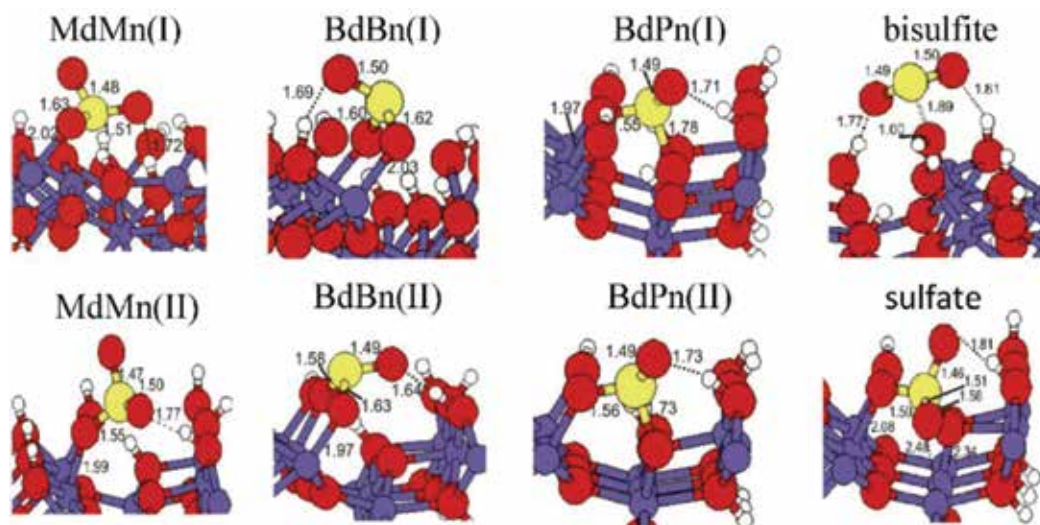
Figure 5. Optimized configurations for the adsorption of SO_2 on partially hydrated goethite(110) surfaces forming the sulfite, bisulfite and sulfate species (violet = Fe, red = O, white = H, yellow = S).

surface of goethite. In this way, two O atoms are singly coordinated and one O atom is three-fold coordinated with the Fe ions of goethite(110) surface. The sulfate species is corroborated by one H-bond (1.81 Å) and carries -1.6 |e| charges according to the Bader charge analyses. A stable sulfite structure can be produced under identical conditions, whereas its adsorption energy is obviously less, indicating that the formation of the sulfate species is significantly preferred.

The adsorption of SO_2 onto the Cu(100), MgO and carbon surfaces was discussed as well, which may provide insightful clues for resembling processes onto mineral surfaces. It was proposed that SO_2 and H_2O are co-adsorbed onto Cu(100) surfaces [30], through the direct coupling of Cu atom with S and O@H_2O atoms. The Cu-O distances ascend in the order of co-adsorption of SO_2 and H_2O < adsorption of only SO_2 << adsorption of only H_2O. Accordingly, the interaction between SO_2 and Cu(100) surface is stronger than that of H_2O, and the co-adsorption of SO_2 conduces to the enhanced interaction of H_2O with Cu(100) surface. At the same time, the Cu-S distance of the co-adsorption configuration is optimized at 2.385 Å and is shorter than that with only SO_2 adsorption. That is, water exhibits a promoting effect for the adsorption of SO_2 on Cu(100) surface, as corroborated by the calculated adsorption energies. Eid and collaborators [41] found that as compared to regular MgO surface, the adsorption capacity of SO_2 at MgO(Fs-center) defects is higher, and MgO(Fs-center) corresponds to an enhanced catalytic activity. With regard to pure carbon materials, SO_2 is physisorbed and van der Waals (vdW) is the driving force therein [42]. When carbon materials are modified with functional groups such as carboxyl, lactone, or/and phenolic hydroxyl, the adsorption strengths of SO_2 are enhanced pronouncedly, especially for the sites at edge surfaces. In addition, these functional groups show little effects on SO_2 adsorption, suggesting that the enhanced adsorption is mainly due to regulation of carbon surface properties.

Adsorption of SO_2 is the first step for the formation of acid rain. According to our preliminary studies, the reaction mechanisms of gas phase and mineral surfaces resemble each other, and hence the gas-phase results are beneficial to understand acid rain formation at mineral surfaces. The reaction of SO_2 and H_2O produces two isomers that have close electronic energies [43]; in addition, the two isomers have apparently lower electronic energies than H_2SO_3. Accordingly, the gaseous SO_2 and H_2O mixture is likely to exist as the $SO_2 \cdot H_2O$ complex rather than H_2SO_3. The activation barrier of SO_2 reacting with H_2O to form H_2SO_3 is so high (146.7 kJ/mol) that it becomes very difficult to produce the sulfite species (H_2SO_3) in gas phase. Five years later, Stirling [44] investigated the hydrolysis of SO_2 in aqueous solutions, finding that hydrated SO_2 forms the bisulfite anion and hydronium ion after overcoming an energy barrier of about 17 kcal/mol, while the one-step formation of H_2SO_3 has not been detected. The orientation of water molecules in the hydration shell of SO_2 implies a more facile formation of the bisulfite anion rather than H_2SO_3 [45], in line with the results of meta-dynamics calculations [46]. When HO_2 participates in the reaction, the S atom constructs a new bond with O@H_2O atom (S-O: 1.716 Å). The energy barrier reduces considerably and equals 56.6 kJ/mol. HO_2 exists widely in the atmosphere and participates in a variety of chemical reactions [47]. In addition to HO_2, a number of computational studies explicitly indicated that acidic substances in the atmosphere play similar catalytic effects and reduce significantly the energy barriers for the hydrolysis of SO_2 [48–50]. The effects of H_2SO_3 and H_2O on the hydrolysis of SO_2 were studied by Liu et al. [48], showing that the energy barriers ascend in the order of $H_2SO_3 + SO_2 \cdot H_2O$ (26.4 kJ/mol) < $H_2O + SO_2 \cdot H_2O$ (84.0 kJ/mol) < $SO_2 \cdot H_2O$ (154.6 kJ/mol). The catalytic effect of H_2SO_3 is obviously more pronounced than that of H_2O. As reflected by NBO analyses, the reactant complexes in presence of sulfurous acid have the enhanced second-order stabilization energies as compared to those with addition of only water molecules, which provides strong supports for the pronounced catalytic effect of H_2SO_3. The kinetic calculations further show that the hydrolysis of SO_2 is a nearly autocatalytic reaction.

Alternatively, acid rain can be formed by release of SO_2 into the atmosphere and oxidization of SO_3, which then reacts with H_2O to form sulfuric acid (H_2SO_4). There are many oxidants that are able to convert SO_2 to SO_3, and Calvert [51] have provided the formation mechanism of sulfuric acid (H_2SO_4)

$$SO_2 + OH \rightarrow HSO_3$$

$$HSO_3 + O_3 \rightarrow SO_3 + HO_2$$

$$SO_3 + H_2O \rightarrow H_2SO_4$$
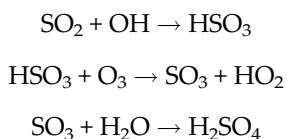
Interaction between SO_2 and the OH radical ($OH^\bullet$) has been addressed by *ab initio* electronic structure calculations [52], and the optimized structure of the $HOSO_2$ radical show differences with that predicted using a small basis set (MP4/6-31G**//HF/3-21G*) [53]: Inclusion of correlation effects results in an increase of S-O distances and OSO angle, whereas the HOS angle shows a substantial decrease. Although geometrically stable at all levels of theory, stability of the $HOSO_2$ radical is estimated to be 104–110 kJ/mol, suggesting that the direct dissociation to SO_3 is almost infeasible. O_3 and H_2O_2 are two oxidizing substances in atmosphere chemistry, and their reaction mechanisms with SO_2 were studied by Jiang et al. [54].

$$SO_2 + O_3 \rightarrow SO_3 + O_2$$

$$SO_2 + H_2O_2 \rightarrow H_2SO_4$$
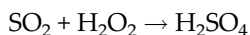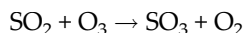
SO_2 and O_3 interact mainly through the S and $O@O_3$ atoms, and their reaction causes the formation of S-O bond (1.708 Å) and the rupture of O-O bond in O_3. This is one-step process and requires to overcome an energy barrier of 46.5 kJ/mol. The reaction of SO_2 with H_2O_2 proceeds via the OH-abstraction mechanism, and two OH radicals generated from the dissociation of H_2O_2 are appended to SO_2 forming H_2SO_4. However, the energy barrier of this reaction is 299.5 kJ/mol, which is extremely difficult to proceed at normal conditions. Chen et al. [46] reported the reaction mechanism between SO_2 and HO_2 and showed that there exist two types of $SO_2 \cdot HO_2$ complexes: one is to combine the terminal $O@HO_2$ and S atoms. In this reaction, the O-S distance decreases from 2.966 Å (the initial complex: $SO_2 \cdot HO_2$) to 1.598 Å while the O-O bond of HO_2 is gradually elongated until broken. The reaction of SO_2 and H_2O is divided into three stages, and the energy barrier of $SO_3 \cdot OH$ formation is so small (1.7 kJ/mol) that can be considered negligible. The final product of this reaction is HSO_4. The other complex is characterized by two types of intermolecular H-bonds that form between the terminal $O@HO_2$ and S atoms and between the $H@HO_2$ and $O@SO_2$ atoms. It is a one-step process and the product for this reaction is $HOSO \cdot O_2$. When a single water is added, it has a combined effect on the overall process, not only accelerating the reaction of generating HSO_4 by reducing the activation barrier of the second step from 48.8 to 44.8 kJ/mol but also inhibiting the reaction between SO_2 and HO_2 to produce HOSO due to blocking the interaction between the $H@HO_2$ and $O@SO_2$ atoms.

It can be seen from the above discussions that the SO_3 and water reaction is an integral section for the formation of acid rain. The direct reaction of SO_3 with one water to produce sulfuric acid (H_2SO_4) requires to overcome a large energy barrier (28.7 kcal/mol) and seems difficult to occur at normal conditions [55–57]. When the second water participates, the energy barrier reduces substantially and the reaction becomes almost barrierless, which is probably due to the formation of a stable six-membered cyclic transition state, see **Figure 6** [58]. The two water molecules transfer their protons in a concerted manner, and a new S-O bond is formed between the newly generated OH and SO_3 fragments. In consequence, multiple reaction pathways may co-exist as illustrated below
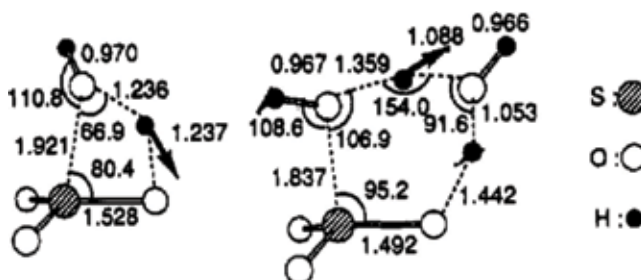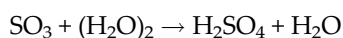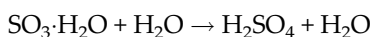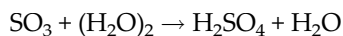

Figure 6. Optimized transition states for the formation of sulfuric acid from SO_3 in presence of one (left) and two (right) water molecules. Arrows indicate the reaction coordinate vectors, and some important distances (Å) and angles (degrees) are shown.

$$SO_3 + (H_2O)_2 \rightarrow H_2SO_4 + H_2O$$

$$SO_3{\cdot}H_2O + H_2O \rightarrow H_2SO_4 + H_2O$$

$$SO_3 + (H_2O)_2 \rightarrow H_2SO_4 + H_2O$$

The energy barriers for the reaction of SO_3 and water clusters $(H_2O)_n$ to form $H_2SO_4{\cdot}(H_2O)_{n-1}$ are calculated to be 28.7, 11.1, and 4.6 kcal/mol for n = 1, 2, 3, respectively [59]. With increase of water numbers, more water molecules are available to solvate and stabilize the charged transition state complexes, which further reduce the energy barriers. That is, it is favorable to hydrolyze SO_3 to form sulfuric acid in presence of sufficient water vapor. The second molecule acts as a good catalyst that promotes proton transfer from water to SO_3, and according to both experimental and theoretical reports, the rate constant of $SO_3 + 2H_2O$ reaction is approximately 10^{-15} $cm^3{\cdot}molecule^{-1}{\cdot}s^{-1}$ [60–62]. HO_2 [63], HCOOH [62, 64], H_2SO_4 [49], HNO_3 [65] can replace the role of the second water molecule and exhibit a similar catalytic effect on the formation of sulfuric acid (H_2SO_4).

4. Concluding remarks

In contrast to the rapid development of chemistry, physics, and biology and other disciplines, soil science remains almost stagnant in the past few decades, and to best of our knowledge, no breakthroughs have been reported for rather a long time. Despite that, no one can deny the vital significance of soil to our life, and soil science has been widely acknowledged as the final frontier.

The slow progresses for soil science, we think, should be attributed to two reasons: (1) wrong and outdated perceptions. A majority of soil researchers mistakenly believe that all knowledge worth knowing about soils has already been understood and no revolutionary progresses would take place; (2) complex systems. Soils are very structurally complicated and there are multiple factors to co-function, which makes it very difficult to characterize by experimental techniques. Computer simulations have unique advantages to handle complex systems, while currently its role in soil science is far from being recognized. In this chapter, two examples are elaborately discussed with regard to application of DFT calculations in soil science: one focuses on the adsorption of uranyl onto mineral surfaces, and the other involves the adsorption of SO_2 onto mineral surfaces and reaction mechanisms to form acid rain. It can be seen from these discussions that DFT calculations are able to provide useful and detailed information about the adsorption, interaction and reactions at the atomic level that greatly promote our understanding about soil science.

With advent of high-performance computing platforms, the same DFT calculation tasks of 10 years ago can now finish within a remarkably shorter time, even if you increase model size (periodic model is also an option), consider solvent effects by adding explicit solvent molecules or/and choose more accurate methods. The methodological developments regarding to DFT calculations have also made remarkable progresses over the recent three decades, and as a result, thermodynamics and reaction barriers can now be predicted with nearly chemical

accuracy (≤1 kJ/mol). In consequence, computer simulations including DFT are the right key to unravel the complicated phenomena and processes occurring within soils; e.g., with DFT calculations, the aggregation mechanisms of "real" soils and the driving force therein were unveiled at an atomic level [6].

In addition to DFT methods, there are a number of other computational methods, such as QM/MM and Molecular Dynamics (MD). The choice of suitable computational methods is strongly recommended. We are pleased to see the birth of the ClayFF force-field [66] that was developed specially for clay minerals and the capability of the ReaxFF force-field [67] to handle reaction mechanisms. The 2013 Noble Prize in Chemistry was awarded to the development of "multiscale methods for complex systems," and now it is time to apply these methods to tackle complex soil systems.

Acknowledgements

Author details

Jiena Yun, Qian Wang, Chang Zhu and Gang Yang*

*Address all correspondence to: theobiochem@gmail.com

College of Resources and Environment and Chongqing Key Laboratory of Soil Multi-Scale Interfacial Process, Southwest University, Chongqing, China

References

[1] Sposito G, Reginato RJ, Luxmoore RJ, editors. Opportunities in Basic Soil Science Research. Madison, Wisconsin, USA: Soil Science Society of America, Inc.; 1992

[2] Li H, Yang G. Rethink the methodologies in basic soil science research: From the perspective of soil chemistry. Acta Pedologica Sinica. 2017;**54**:819-826

[3] Wang Q, Zhu C, Yun JN, Yang G. Isomorphic substitutions in clay materials and adsorption of metal ions onto external surfaces: A DFT investigation. Journal of Physical Chemistry C. 2017;**121**:26722-26732

[4] Li X, Li H, Yang G. Electric fields within clay materials: How to affect the adsorption of metal ions. Journal of Colloid and Interface Science. 2017;**501**:54-59

[5]   Li X, Li H, Yang G. Configuration, anion-specific effects, diffusion, and impact on counterions for adsorption of salt anions at the interfaces of clay minerals. Journal of Physical Chemistry C. 2016;**120**:14621-14630

[6]   Tian R, Yang G, Tang Y, Liu XM, Li R, Zhu HL, Li H. Origin of Hofmeister effects for complex systems. PLoS One. 2015;**10**:e0128602

[7]   Zhu MQ, Paul KW, Kubicki JD, Sparks DL. Quantum chemical study of arsenic(III, V) adsorption on Mn-oxides: Implications for arsenic(III) oxidation. Environmental Science & Technology. 2009;**43**:6655-6661

[8]   Yang G, Pidko EA, Hensen EJM. Mechanism of Brönsted acid-catalyzed conversion of carbohydrates. Journal of Catalysis. 2012;**295**:122-132

[9]   Lundberg M, Kawatsu T, Vreven T, Frisch MJ, Morokuma K. Transition states in a protein environment—ONIOM QM:MM modeling of isopenicillin N synthesis. Journal of Chemical Theory and Computation. 2009;**5**:222-234

[10] Perdew JP. Density-functional approximation for the correlation energy of the inhomogeneous electron gas. Physical Review B. 1986;**33**:8822-8824

[11] Lee C, Yang WT, Parr RG. Development of the Colle-Salvetti correlation energy formula into a functional of the electron density. Physical Review B. 1988;**37**:785-789

[12] Perdew JP, Ruzsinszky A. Fourteen easy lessons in density functional theory. International Journal of Quantum Chemistry. 2010;**110**:2801-2807

[13] Choppin GR. Actinide speciation in the environment. Journal of Radioanalytical and Nuclear Chemistry. 2007;**273**:695-703

[14] Kalsi PK, Tomar BS, Ramakumar KL, Venugopal V. Studies on recovery of uranium from fluoride matrix employing sonochemistry. Journal of Radioanalytical and Nuclear Chemistry. 2012;**293**:863-867

[15] Bieluszka P, Zakrzewska G, Chajduk E, Dudek J. Liquid-liquid extraction of uranium(VI) in the system with a membrane contactor. Journal of Radioanalytical and Nuclear Chemistry. 2014;**299**:611-619

[16] Perron H, Domain C, Roques J, Drot R, Simoni E, Catalette H. Periodic density functional theory investigation of the uranyl ion sorption on the TiO_2 rutile (110) face. Inorganic Chemistry. 2006;**45**:6568-6570

[17] Pan QJ, Odoh SO, Asaduzzaman AM, Schreckenbach G. Adsorption of uranyl species onto the rutile (110) surface: A periodic DFT study. Chemistry - A European Journal. 2012; **18**:1458-1466

[18] Roques J, Veilly E, Simoni E. Periodic density functional theory investigation of the uranyl ion sorption on three mineral surfaces: A comparative study. International Journal of Molecular Sciences. 2009;**10**:2633-2661

[19] Sebbari K, Roques J, Simoni E, Domain C, Perron H, Catalette H. First-principles molecular dynamics simulations of uranyl ion interaction at the water/rutile TiO_2(110) interface. Surface Science. 2012;**606**:1135-1141

[20] Kremleva A, Krüger S, Rösch N. Density functional model studies of uranyl adsorption on (001) surfaces of kaolinite. Langmuir. 2008;**24**:9515-9524

[21] Martorell B, Kremleva A, Krüger S, Rösch N. Density functional model study of uranyl adsorption on the solvated (001) surface of kaolinite. Journal of Physical Chemistry C. 2010;**114**:13287-13294

[22] Kremleva A, Krüger S, Rösch N. Quantum chemical modeling of uranyl adsorption on mineral surfaces. Radiochimica Acta. 2010;**98**:635-646

[23] Kremleva A, Krüger S, Rösch N. Uranyl adsorption at (010) edge surfaces of kaolinite: A density functional study. Geochimica et Cosmochimica Acta. 2011;**75**:706-718

[24] Veilly E, Roques J, Jodin-Caumon M-C, Humbert B, Drot R, Simoni E. Uranyl interaction with the hydrated (001) basal face of gibbsite: A combined theoretical and spectroscopic study. The Journal of Chemical Physics. 2008;**129**:244704

[25] Hattori T, Saito T, Ishida K, Scheinost AC, Tsuneda T, Nagasaki S, Tanaka S. The structure of monomeric and dimeric uranyl adsorption complexes on gibbsite: A combined DFT and EXAFS study. Geochimica et Cosmochimica Acta. 2009;**73**:5975-5988

[26] Jones P, Hockey JA. Infra-red studies of rutile surfaces. Part 1. Transactions of the Faraday Society. 1971;**67**:2669-2678

[27] Jones P, Hockey JA. Infra-red studies of rutile surfaces. Part 2—Hydroxylation, hydration and structure of rutile surfaces. Transactions of the Faraday Society. 1971;**67**:2679-2685

[28] Larssen T, Lydersen E, Tang DG, He Y, Gao JX, Liu HY, Duan L, Seip HM, Vogt RD, Mulder J, Shao M, Wang YH, Shang H, Zhang XS, Solberg S, Aas W, Okland T, Eilertsen O, Angelf V, Li QR, Zhao DW, Xiang RJ, Xiao JS, Luo JH. Acid rain in China. Environmental Science & Technology. 2006;**40**:418-425

[29] Calace N, Fiorentini F, Petronio BM, Pietroletti M. Effects of acid rain on soil humic compounds. Talanta. 2001;**54**:837-846

[30] Purvaja R, Ramesh R, Ray AK, Rixen T. Nitrogen cycling: A review of the processes, transformations and fluxes in coastal ecosystems. Current Science. 2008;**94**:1419-1438

[31] Singh A, Agrawal M. Acid rain and its ecological consequences. Journal of Environmental Biology. 2008;**29**:15-24

[32] Koptsik GN, Koptsik SV, Dan A. Pine needle chemistry near a large point SO_2 source in Northern Fennoscandia. Water, Air, and Soil Pollution. 2001;**130**:929-934

[33] Livingston RA. Acid rain attack on outdoor sculpture in perspective. Atmospheric Environment. 2016;**146**:332-345

[34] Lo JMH, Ziegler T, Clark PD. SO_2 Adsorption and transformations on γ-Al_2O_3 surfaces: A density functional theory study. Journal of Physical Chemistry C. 2010;**114**:10444-10454

[35] Liu H, Chen T, Frost RL. An overview of the role of goethite surfaces in the environment. Chemosphere. 2014;**103**:1-11

[36] Zubieta CE, Fortunato LF, Belelli PG, Patricia G, Ricardo M. Theoretical study of SO_2, adsorption on goethite(110) surface. Applied Surface Science. 2014;**314**:558-563

[37] Zhang X, Zhuang G, Chen JM, Wang Y, Wang X, An ZS, Zhang P. Heterogeneous reactions of sulfur dioxide on typical mineral particles. The Journal of Physical Chemistry. B. 2006;**110**:12588-12596

[38] Goodman AL, Li P, Usher CR, Grasslan VH. Heterogeneous uptake of sulfur dioxide on aluminum and magnesium oxide particles. The Journal of Physical Chemistry. A. 2001;**105**:6109-6120

[39] Wei X, Dong CF, Chen ZH, Huang JY, Xiao K, Li XG. Insights into SO_2 and H_2O co-adsorption on Cu(100) surface with calculations of density functional theory. Transactions of the Nonferrous Metals Society of China. 2015;**25**:4102-4109

[40] Sierraalta A, Bermudez A, Rosa-Brussin M. Density functional study of the interaction of Cu^+ ion-exchanged zeolites with H_2O and SO_2 molecules. Journal of Molecular Catalysis A: Chemical. 2005;**228**:203-210

[41] Eid KM, Ammar HY. Adsorption of SO_2, on Li atoms deposited on MgO(100) surface: DFT calculations. Applied Surface Science. 2011;**257**:6049-6058

[42] Liu X, Sun F, Qu ZB, Gao JH, Wu SH. The effect of functional groups on the SO_2, adsorption on carbon surface I: A new insight into noncovalent interaction between SO_2, molecule and acidic oxygen-containing groups. Applied Surface Science. 2016;**369**:552-557

[43] Bandyopadhyay B, Kumar P, Biswas P. Ammonia catalyzed formation of sulfuric acid in troposphere: The curious case of a base promoting acid rain. The Journal of Physical Chemistry. A. 2017;**121**:3101-3108

[44] Stirling A. SO_2 hydrolysis: Ab initio MD study of the formation of bisulfite ion. Journal of Computer Chemistry, Japan. 2013;**12**:38-42

[45] Brown RE, Barber F. Ab initio studies of the thermochemistry of the bisulfite and the sulfonate ions and related compounds. The Journal of Physical Chemistry. 1995;**99**:8071-8075

[46] Chen X, Tao C, Zhong L, Gao Y, Yao W, Li SJ. Theoretical study on the atmospheric reaction of SO_2, with the HO_2, and $HO_2 \cdot H_2O$ complex formation HSO_4, and H_2SO_3. Chemical Physics Letters. 2014;**608**:272-276

[47] Ehhalt DH, Dorn HP, Poppe D. The chemistry of the hydroxyl radical in the troposphere. Proceedings of the Royal Society of Edinburgh. 1990;**97**:17-34

[48] Liu J, Fang S, Bing Q, Tao FM, Liu JY. Theoretical study of the auto-catalyzed hydrolysis reaction of sulfur dioxide. Computational & Theoretical Chemistry. 2016;**1076**:11-16

[49] Torrent-Sucarrat M, Francisco JS, Anglada JM. Sulfuric acid as autocatalyst in the formation of sulfuric acid. Journal of the American Chemical Society. 2012;**134**:20632-20644

[50] Hazra MK, Francisco JS, Sinha A. Hydrolysis of glyoxal in water-restricted environments: Formation of organic aerosol precursors through formic acid catalysis. The Journal of Physical Chemistry. A. 2014;**118**:4095-4105

[51] Calvert JG. SO_2, NO and NO_2 Oxidation Mechanisms: Atmospheric Considerations. Oxford: Butterworth-Heinemann; 1984

[52] Moore-Plummer PL, Wu RC, Flenner JJ. Ab initio investigation of the gas phase reaction $SO_2 + H_2O \rightarrow SO_2OH$ radical. Molecular Physics. 2002;**100**:1847-1853

[53] Nagase S, Hashimoto S, Akimoto H. Bisulfite and peroxybisulfate radicals studied by ab initio calculation and matrix isolation technique. The Journal of Physical Chemistry. 1988; **92**:641-644

[54] Jiang SD, Wang ZH, Zhou JH, Wen ZC, Cen KF. A quantum chemistry study on reaction mechanisms of SO_2 with O_3 and H_2O_2. Journal of Zhejiang University. Science. A. 2009; **10**:1327-1333

[55] Chen TS, Plummer PLM. Ab initio MO investigation of the gas-phase reaction sulfur trioxide + water. fwdarw. sulfuric acid. The Journal of Physical Chemistry. 1985;**89**:3689-3693

[56] Morokuma K, Muguruma C. Ab initio molecular orbital study of the mechanism of the gas phase reaction $SO_3 + H_2O$: Importance of the second water molecule. Journal of the American Chemical Society. 1994;**116**:299-301

[57] Hofmann M, Schleyer PVR. Acid rain: Ab initio investigation of the H_2O.cntdot.SO_3 complex and its conversion to H_2SO_4. Journal of the American Chemical Society. 1994; **116**:4947-4952

[58] Morokuma K, Muguruma C. Ab initio molecular orbital study of the mechanism of the gas phase reaction $SO_3 + H_2O$: Importance of the second water molecule. Journal of the American Chemical Society. 1994;**116**:10316-10317

[59] Larson LJ, Kuno M, Tao FM. Hydrolysis of sulfur trioxide to form sulfuric acid in small water clusters. The Journal of Chemical Physics. 2000;**112**:8830-8838

[60] Reiner T, Arnold F. Laboratory investigations of gaseous sulfuric acid formation via $SO_3 + H_2O + M \rightarrow H_2SO_4 + M$: Measurement of the rate constant and product identification. The Journal of Chemical Physics. 1994;**101**:7399-7407

[61] Wang X, Jin YG, Suto M, Lee LC. Rate constant of the gas phase reaction of SO_3 with H_2O. The Journal of Chemical Physics. 1988;**89**:4853-4860

[62] Long B, Long ZW, Wang YB, Tan XF, Han YH, Long CY, Qin SJ, Zhang WJ. Formic acid catalyzed gas-phase reaction of H_2O with SO_3 and the reverse reaction: A theoretical study. ChemPhysChem. 2012;**13**:323-329

[63] Gonzalez J, Torrent-Sucarrat M, Anglada JM. The reactions of SO_3 with HO_2 radical and H_2O. HO_2 radical complex. Theoretical study on the atmospheric formation of HSO_5 and H_2SO_4. Physical Chemistry Chemical Physics. 2010;**12**:2116-2125

[64] Hazra MK, Sinha A. Formic acid catalyzed hydrolysis of SO_3 in the gas phase: A barrierless mechanism for sulfuric acid production of potential atmospheric importance. Journal of the American Chemical Society. 2011;**133**:17444-17453

[65] Long B, Chang CR, Long ZW, Wang YB, Tan XF, Zhang WJ. Nitric acid catalyzed hydrolysis of SO_3, in the formation of sulfuric acid: A theoretical study. Chemical Physics Letters. 2013;**581**:26-29

[66] Cygan RT, Liang JJ, Kalinichev AG. Molecular models of hydroxide, oxyhydroxide, and clay phases and the development of a general force field. The Journal of Physical Chemistry. B. 2004;**108**:1255-1266

[67] Pitman MC, van Duin ACT. Dynamics of confined reactive water in smectite clay-zeolite composites. Journal of the American Chemical Society. 2012;**134**:3042-3053

Edited by Gang Yang

Density functional theory (DFT) ranks as the most widely used quantum mechanical method and plays an increasingly larger role in a number of disciplines such as chemistry, physics, material, biology, and pharmacy. DFT has long been used to complement experimental investigations, while now it is also regarded as an indispensable and powerful tool for researchers of different fields. This book is divided into five sections that include original chapters written by experts in their fields: "Method Development and Validation," "Spectra and Thermodynamics," "Catalysis and Mechanism," "Material and Molecular Design," and "Multidisciplinary Integration." I would like to express my sincere gratitude to all contributors and recommend this book to both beginners and experienced researchers.

IntechOpen